DISCRETE ELEMENT MODELING FOR FLOWS OF GRANULAR MATERIALS

LIM WEE CHUAN ELDIN

NATIONAL UNIVERSITY OF SINGAPORE

2006

DISCRETE ELEMENT MODELING FOR FLOWS OF GRANULAR MATERIALS

BY

LIM WEE CHUAN ELDIN

(M.Eng., B.Eng. (Hons.), NUS)

A THESIS SUBMITTED

FOR THE DEGREE OF DOCTOR OF PHILOSOPHY

DEPARTMENT OF CHEMICAL AND BIOMOLECULAR ENGINEERING

NATIONAL UNIVERSITY OF SINGAPORE

2006

ACKNOWLEDGEMENTS

I would like to thank the National University of Singapore for providing financial support in the form of a research scholarship during my Ph.D. studies and the award of the President's Graduate Fellowship during the year in which this thesis was written. I would also like to acknowledge the overall supervision of this project by my research supervisor, Associate Professor Wang Chi-Hwa.

The opportunity provided by my research supervisor and our collaborator Professor Aibing Yu for me to be attached to the Centre for Simulation and Modelling of Particulate Systems (SIMPAS) at the University of New South Wales during the initial phase of this research project is gratefully acknowledged.

I also thank Professor John Bridgwater from the Department of Chemical Engineering at Cambridge University for helpful discussions via video-conferencing on the subject of granular attrition which subsequently led to the formulation of a theoretical approach for modeling bulk granular attrition.

The helpful suggestions provided by Professor Sankaran Sundaresan of the Department of Chemical Engineering at Princeton University on our work on voidage wave instabilities are also much appreciated.

All computational work described here was performed at the Supercomputing and Visualisation Unit of the National University of Singapore.

TABLE OF CONTENTS

SUMMARY

The pneumatic transports of solid particles in both vertical and horizontal pipes were studied numerically using the Discrete Element Method (DEM) coupled with Computational Fluid Dynamics (CFD). In the vertical pneumatic conveying simulations, the dispersed flow and plug flow regimes were obtained at different gas velocities and solid concentrations. Similarly, the homogeneous flow, stratified flow, moving dunes and slug flow regimes in horizontal pneumatic conveying were also reproduced computationally. Solid concentration profiles showed a symmetrical but non-uniform distribution for dispersed flow and an almost flat distribution for plug flow. The profile for stratified flow showed higher solid concentration near the bottom wall while that for slug flow was flat. Hysteresis in solid flow rates was observed in vertical pneumatic conveying near the transition between the dispersed and plug flow regimes. Solid flow rates were more sensitive towards the coefficient of friction of particles and the pipe walls.

Pneumatic transport through an inclined and vertical pipe in the presence of an electrostatic field was studied using CFD-DEM simulations coupled with a simple electrostatic field model. The eroding dunes and annular flow regimes in inclined and vertical pneumatic conveying respectively were reproduced computationally. In the presence of a mild electrostatic field, reversed flow of particles was seen in a dense region close to the bottom wall of the inclined conveying pipe and forward flow in the space above. At sufficiently high field strengths, complete backflow of solids may be observed. A higher inlet gas velocity would be required to sustain a net positive flow along the pipe at the expense of a larger pressure drop. The time required for a steady

state to be attained was longer when the electrostatic field strength was higher. Finally, a phase diagram for inclined pneumatic conveying systems was proposed.

An empirical model for bulk granular attrition was proposed and investigated. The attrition process occurring in various types of systems was modeled with a diffusion type equation. The model reproduced much of the experimentally observed behavior and numerical simulation results. This might suggest similarities between the process of bulk granular attrition and diffusion of material. A comparison of the model with the well-established Gwyn correlation provided insights on the general success of such a power-law type correlation in describing granular attrition behavior.

The nature of one-dimensional voidage waves in a liquid fluidized bed subjected to external perturbations and exhibiting instabilities was investigated both experimentally and numerically. Voidage waves consisting of alternating regions of high and low solid concentrations were observed to form and travel in a coherent manner along the fluidized bed. Solid particles moved upwards when a dense phase of the wave passed through their positions and settled downwards otherwise. The voidage waves are traveling waves with dense and dilute phases being convected along the bed. However, the motion of individual particles was highly restricted to a small region. A diffusive type of behavior was observed where particles drifted gradually away from their initial positions within the bed. This type of motion was adequately described by a simple dispersion model used in the present study.

Keywords: Discrete Element Method, Computational Fluid Dynamics, Pneumatic Conveying, Electrostatic Effects, Granular Attrition, Vibrated Liquid-Fluidized Bed

LIST OF TABLES

LIST OF FIGURES

LIST OF SYMBOLS

$c_{d0,i}$	drag coefficient
d	distance to pipe wall
D	dispersion coefficient
E	electric field strength
E_y	electric field strength component in the wall-normal direction
E_z	electric field strength component in the axial direction
$\mathbf{f}_{c,ij}$	contact force
$\mathbf{f}_{cn,ij}$	normal component of contact force
$\mathbf{f}_{ct,ij}$	tangential component of contact force
$\mathbf{f}_{d,ij}$	viscous contact damping force
$\mathbf{f}_{dn,ij}$	normal component of viscous contact damping force
$\mathbf{f}_{dt,ij}$	tangential component of viscous contact damping force
$\mathbf{f}_{f,i}$	fluid drag force
$\mathbf{f}_{f0,i}$	fluid drag force in absence of other particles
$\mathbf{f}_{E,i}$	electrostatic force
$\mathbf{f}_{Ep,i}$	electrostatic force due to charged particles
$\mathbf{f}_{Ew,i}$	electrostatic force due to charged pipe walls
F	source term due to fluid-particle interaction
g	gravitational acceleration
I_i	moment of inertia
k_y	dimensionless wavenumber
L	characteristic length
m_i	particle mass

n	number of particles in a computational cell
$\mathbf{n}_i$	unit vector in normal direction
N	number of particles
P	fluid pressure
q	equilibrium charge on the pipe wall
Q	particle charge
$\mathbf{r}$	position vector of particle
r	average distance of particles to the pipe wall
r_{ij}	distance between particles
$\mathbf{R}_i$	radius vector from particle centre to a contact point
$Re_{p,i}$	Reynolds number based on particle diameter
t	time
$\mathbf{t}_i$	unit vector in tangential direction
T	granular temperature
$\mathbf{T}_{ij}$	torque
$\mathbf{u}_i$	fluid velocity
$\bar{u}$	mean horizontal velocity component
$\mathbf{v}_i$	particle velocity
$\mathbf{v}_t$	terminal velocity
$\bar{v}$	mean vertical velocity component
z	dimensionless coordinate along the axis of pipe in experimental setup

Greek Symbols

α_s	particle concentration at a given pixel measured by ECT
α	solid concentration
$\delta_{n,ij}$	displacements between particles in normal direction
$\delta_{t,ij}$	displacements between particles in tangential direction
Δt	simulation time step
ΔV	volume of a computational cell
ε_i	local average porosity
ε_o	permittivity of free space
$\kappa_{n,i}$	spring constant for normal collisions
$\kappa_{t,i}$	spring constant for tangential collisions
λ	linear charge density along the pipe wall
λ_y	wavelength
λ'_y	dimensionless wavelength
Λ	ratio of electrostatic force to gravitational force
μ_f	fluid viscosity
$\eta_{n,i}$	viscous contact damping coefficients in normal direction
$\eta_{t,i}$	viscous contact damping coefficients in tangential direction
ρ_f	fluid density
ρ_p	particle density
θ	geometrical variable
χ	empirical parameter
ω_i	angular velocity

CHAPTER 1 INTRODUCTION

Gas-solid systems are commonly encountered in the chemical and petrochemical, food and mineral processing and pharmaceutical industries. Their applications include fluid catalytic cracking, drying operations, mixing and granulation and the transport of granular material and fine powders through pipelines. In particular, the pneumatic transport of granular material is a common operation frequently employed to transport solid particles from one location to another. Some of the advantages associated with this method of solid transportation include relatively high levels of safety, low operational costs, flexibility of layout, ease of automation and installation and low maintenance requirements. On the other hand, one of the main disadvantages of pneumatic transport is the occurrence of attrition of the granular material, especially at high conveying velocities. This may result in severe degradation of product quality in certain industrial applications and possibly unpredictable changes in flow behaviors within the conveying pipelines. Depending on the system geometry, gas velocities and material properties of the solid particles to be transported, such transportation processes can take place in different modes usually referred to as dense or dilute phase conveying. The former involves transportation of the solids as dense clusters or slugs and is usually the preferred method for handling solids which are sensitive to abrasion as shear and collisional forces arising within the solid material are generally lower. In comparison, the latter mode where particles are dispersed as a suspension in the gas is known to be a more stable mode with lower fluctuations and excursions in gas pressures.

It has been well established in previous experimental work done in our laboratory that different flow regimes can arise under different operating conditions in pneumatic conveying of granular materials. Rao *et al.* (2001) applied a non-invasive technique known as Electrical Capacitance Tomography (ECT) to the study of pneumatic conveying in horizontal pipes and past a 90^{o} smooth elbow. At high air superficial velocities, a homogeneous flow regime where particle concentration was evenly distributed throughout the interior of the conveying pipe was observed while at lower velocities, particles were observed to move in the form of small dunes along the bottom of the pipe. These were referred to as the homogeneous and moving dunes flow regimes respectively. At still lower air velocities, particles were mainly transported as clouds above a concave settled layer. Finally, a slug flow regime where particles traveled as solid slugs intermittently through the pipe was observed as the air superficial velocity was decreased further. These different flow regimes could be identified based on the temporal variation of the cross-sectional averaged solids concentration obtained by single-plane ECT measurements. Furthermore, propagation velocities of patterns could also be obtained by cross-correlation of twin-plane ECT data. Zhu *et al.* (2003) studied the same pneumatic conveying process in vertical and inclined pipes using ECT. The various flow regimes identified included the dispersed, slugging and annular capsule flow regimes. The first was characterized by low particle concentration at the wall and in the core of the pipe but slightly higher concentration at a small distance away from the wall. On the other hand, the slugging flow regime consisted of two alternating patterns with high particle concentration occurring in the wall region and at the core intermittently and the annular capsule flow regime involved stationary capsules of particles with an annular structure and particles being brought from one capsule to the next.

Despite the apparent simplicity of this type of transport process, the ability to predict the flow behavior of both gas and solid phases during a typical operation or even the modes in which the transportation would take place remains a challenging task. Traditionally, researchers have applied a fluid mechanics approach towards the analysis of such systems by treating the gas and solid phases as two interpenetrating continua. However, it is well recognized that in order for such an approach to be successful, the solid rheology relating stress to rate of deformation must be known. To this end, a substantial amount of work has been done in the development of rheological models and constitutive equations for describing granular flow behavior, an example of which is the kinetic theory for granular flow. However, in the presence of an interstitial fluid such as in pneumatic conveying and gas fluidization systems, the ability of continuum models to predict with a reasonable level of accuracy the various complex behavior and phenomena commonly observed in physical experiments is limited at best. This difficulty encountered with using continuum models to describe gas-solid systems stems from the presence of different length and time scales associated with the two phases present. Any form of local averaging technique performed to resolve this difficulty would be at the expense of the ability to describe structures and motions at the finest scales which are usually most significant to the overall hydrodynamics of the system but which would have been inevitably sacrificed during the averaging process.

One possible alternative approach to the modeling of gas-solid systems is to apply a discrete model to describe the motion of solid particles. This type of model can be based only on the most fundamental laws of motion without any special

assumptions or simplifications. Akin to Molecular Dynamics simulation, such a discrete model would be capable of resolving the dynamics and motion at the length and time scales of individual particles while possibly preserving the macroscopic characteristics of the system. With the advent of supercomputing facilities in recent years, this approach has been gaining much popularity for numerical studies of granular flow behavior. And when coupled appropriately with Computational Fluid Dynamics techniques to describe an interstitial fluid phase, the resulting combined model may potentially be used for the numerical simulation of any general gas-solid systems.

It is also well recognized that a common and sometimes hazardous phenomenon associated with pneumatic transport systems is the generation of electrostatic charges via triboelectrification. In general, electrostatic charges may be generated from frictional and collisional interactions between solid particles and the pipe wall during transportation. The resulting electric field produced, fluid flow field and solid distribution are intricately linked in a complex and as yet poorly understood manner giving rise to various flow behaviors observed by many research workers. However, to date, a general theory for such pneumatic transport systems which unifies the electrodynamics, fluid and granular dynamics concepts for such systems is still lacking in the literature. There has also been no report of experimental investigations which attempt to establish the fundamental inter-relationships between these components and flow behaviors observed. In the presence of an electric field which is generated naturally during the pneumatic transport process through triboelectrification, it may be expected that electric forces would have direct effects on solid flow behavior, giving rise to other unexpected or anomalous flow regimes

(Yao *et al.*, 2004). Further to this, the flow profile of the interstitial fluid is also expected to be affected significantly by the altered solid flow pattern. As such, a complex relationship exists between the three components of such a gas-solid system, the nature and implications of which are far from being understood. Electrostatic charging effects affect and are in turn indirectly affected by both the solid and gas phases. Such effects presumably become more significant and important as the scale of operation increases. In particular, electrostatic charge accumulations are often the root cause of industrial accidents and fatalities.

The next aspect of pneumatic transport systems which is of considerable industrial concern is the attrition or breakage of particles during transportation. Such phenomena degrade the quality of final products formed such as those from pharmaceutical plants and so are usually very much undesirable. It is not difficult to deduce that particle attrition normally occurs when the granular materials are transported at high speeds along the transportation lines and so a possible way of preventing such occurrences is to apply a low gas velocity. However, in most industrial practices, a compromise usually has to be reached, often in an arbitrary and empirical manner, between causing attrition and degradation of final products at high conveying velocities and plugging of the transportation lines otherwise. This is an important reflection of the inadequacy of our current knowledge for such multiphase flow systems and the complex relationships between the various phases present in such systems.

This project describes the application of the Discrete Element Method coupled to Computational Fluid Dynamics for the numerical study of pneumatic conveying of

granular materials through vertical, horizontal and inclined pipes both in the absence and presence of electrostatic effects. The attrition of granular materials during pneumatic conveying about a sharp bend and the phenomenon of voidage wave instability in a vibrated liquid fluidized bed were also investigated using the same numerical method. In the following chapters of this thesis, a review of the scientific literature in areas relevant to this project will first be provided in Chapter 2. This is followed by a description in Chapter 3 of the rationale for various aspects of the work carried out in this project in relation to those which have been completed and published in the literature by other research workers. The details of the computational method and experimental procedures used in this project and a discussion of the results obtained will be presented in Chapters 4 and 5 of this thesis respectively. Finally, a conclusion summarizing the work completed in this research project is provided in Chapter 6.

CHAPTER 2 LITERATURE REVIEW

This research focuses on the development and application of a computational model for simulating various types of granular flow systems. The approach used in the model involves applying particle dynamics simulation to a dispersed particulate phase and Computational Fluid Dynamics techniques to a continuous fluid phase with appropriate coupling between the two to account for physical interactions between the two phases. Although the two individual components of the model, namely particle dynamics and Computational Fluid Dynamics, are well established methods for simulating particle and fluid motions respectively, the application of a combined model towards multiphase granular systems is a relatively new concept. This chapter gives a review of the relevant literature on particle dynamics simulation and illustrates some applications completed by various research workers.

2.1 Discrete Element Method

Particle dynamics simulation has become a popular tool for investigation of granular flow systems. It has the capability of providing the investigator with a complete set of information of the system under investigation, some of which may be difficult or even impossible to obtain experimentally. In particular, the Discrete Element Method (DEM) originally developed by Cundall and Strack (1979) for describing the mechanical behavior of assemblies of discs and spheres, has been successfully applied by many research workers in various areas of engineering interests. The authors validated the method by simulating the movement of an assembly of discs placed between vertical and horizontal plates subjected to forces. The force vector plots obtained from the simulation were compared with those

obtained experimentally by other research workers using photoelastic analysis. The comparisons were largely qualitative in nature and based on visual observations. Nonetheless, it was shown that the correspondence between the numerically and experimentally obtained force vector plots was sufficiently good for DEM to qualify as a valid tool for fundamental research into the behavior of granular assemblies.

Dallimore and McCormick (1996) developed a model of a planetary ball mill using DEM to predict grinding media motion. They considered four methods of modeling collision forces between particles, namely the Kelvin model, modified Kelvin model, Maxwell model and Elastic/Plastic yield model. The Kelvin model was originally used by Cundall and Strack (1979) in their development of DEM and simulation of a granular assembly. It considers each impact force to be a function of both the linear overlap and relative velocity of approach of the two particles. On the other hand, the modified Kelvin model considers the collision force to consist of an elastic force proportional to the volume of overlap and a damping force proportional to both the velocity of approach and instantaneous area of impact:

$$f_n = K_n \delta vol + C_n v_n \delta a \tag{2.1}$$

where K_n and C_n are the spring and dashpot coefficients respectively, δvol is the volume of overlap, v_n is the relative approach velocity and δa is the instantaneous area of impact.

The two Kelvin type models described above effectively represent collision forces between particles using a spring and dashpot in parallel. The Maxwell model uses a spring and dashpot placed in series for this purpose and so constrains the elastic and damping forces to be of equal magnitude:

$$f_n = K_n \delta n = C_n v_n \quad (2.2)$$

where δn is the linear overlap.

In the elastic/plastic yield model, the contact stress is allowed to vary linearly with normal overlap up to a critical stress level and remains constant beyond this critical stress level. The impact force is calculated from the stress level and instantaneous contact area. The Maxwell model was found to be suitable only for modeling entirely inelastic collisions and thus was inappropriate for simulating ball milling processes. Based on a comparison of the impact force distribution predicted using the remaining three models and that measured experimentally using a force transducer, the modified Kelvin model was chosen as the most appropriate model for subsequent studies. Milling experiments were conducted in a planetary mill with steel vials of diameter 0.064 m and depth 0.015 m and chrome steel balls of diameter 0.0127 m to investigate the effect of mill speed on the progression of the Ni/CuO displacement reaction. 8 milling balls and a 3 g stoichiometric mixture of Ni and CuO powders were used. The mill speeds considered were 240, 270, 300 and 330 rpm. These same conditions were also used in computer simulations of the milling process using the modified Kelvin model for calculating collision forces. The simulation predicted that increasing mill speed caused a proportionally larger increase in impact collisions which dissipate more than 4×10^{-3} J of energy. It also appears that the distribution of the impact collision energies did not significantly affect the propagation of the Ni/CuO displacement reaction over the range of mill speeds investigated.

Drake and Walton (1995) performed computer simulations of spheres flowing down an inclined glass-walled channel and successfully reproduced profiles of mean velocity, bulk density, particle rotations and fluctuating quantities measured with a high-speed camera in physical experiments. The particles used in the experiments were 6 mm diameter spheres and the channel was a 3.7 m long, 0.5 m deep, 6.7 mm wide chute inclined at 42.75^{o} to the horizontal. The flow was analyzed using a 16 mm high-speed camera operating at 1440 frames per second. The computer simulation performed made use of DEM with a simple fluid drag force model to account for the effects of fluid drag. The value of the spring constant used in the model was 38000 N m^{-1} for computational efficiency even though this parameter was experimentally determined to be 380000 N m^{-1}. The time step used was 1.31×10^{-5} s and drag coefficient measured experimentally for single particles was 3.4 ± 2.2. The time evolution of profiles of the mean downchute velocity, bulk density and mean in-plane rotations obtained from the simulations agreed well with those obtained from the physical experiments. The simulated flows were slightly slower and more compact than the physical flows and the authors attributed this to the simple fluid drag force model used in their simulations. Subsequently, periodic boundary conditions were applied and statistics of fluctuating quantities were generated for comparisons with the physical experiments. The fluctuating downchute and bed-normal velocities were observed to be anisotropic, especially in low-bulk density and high-shear regions of the flow. This was because particles tend to acquire larger fluctuating velocities in the direction of the mean flow velocity than in the other components. These features of the fluctuating quantities were observed in both the simulated and physical flows.

Zhou *et al.* (1999) modified the original DEM by introducing a rolling friction torque in order to study the effect of rolling friction coefficient on the formation of a sandpile. The number of particles simulated was 1000 and two-sized spheres with diameters equal to 10 mm or 3 mm were used respectively. The time step used was 1.5×10^{-5} s for the large spheres and 4×10^{-6} s for the small spheres. A typical simulation started with the random generation of spheres in a small vertical cylindrical tube resting on a flat horizontal surface. The spheres were allowed to settle under gravity to form a packing and then the tube was raised at a speed of 0.015 m s^{-1} to allow the spheres to spread and form an unconfined heap on the surface. It was observed that a large rolling frication coefficient gave rise to a large angle of repose of the particles while no distinct heap could be formed if the rolling friction coefficient was too small. Physical experiments were also carried out using glass beads of diameters 6 mm or 10 mm. The photographs of heaps formed during the experiments were seen to resemble those obtained from the simulations.

2.2 Numerical Applications

Numerical modeling of pneumatic conveying and other gas-solid systems plays an important role in improving our understanding of such systems. One of the commonly used approaches to pneumatic conveying modeling is the Eulerian/Lagrangian method where particles are tracked in a Lagrangian frame of reference either individually or as groups with identical properties known as parcels (Tashiro *et al.*, 1997; Huber and Sommerfeld, 1998). An alternative approach has been Computational Fluid Dynamics (CFD) with two-fluid continuum models to represent the gas and solid phases as two interpenetrating continua (Levy, 2000). Further, the technique of particle dynamics simulation such as DEM as reviewed in

the previous section coupled to CFD has also been widely used for investigations of gas-solid systems.

Tsuji *et al.* (1992) carried out numerical simulations of horizontal pneumatic conveying of solid particles using DEM. A linear spring-dashpot-friction slider model was used to calculate particle-particle and particle-wall contact forces and the Ergun's equation was used for evaluating the fluid drag force. Particle motion was treated three-dimensionally while fluid motion was one-dimensional. The geometry of the conveying pipe simulated had a diameter of 50 mm and length of 800 mm. Periodic boundary conditions were applied to the ends of the relatively short pipe whereby particles leaving the outlet were re-introduced at the inlet. This facilitated the use of smaller numbers of particles in the simulation and a corresponding shorter computational time. Two different cases with 500 and 1000 particles respectively were considered. The density and diameter of the particles used were 1000 kg m^{-3} and 10 mm respectively. The various parameters found in the contact force model such as the stiffness and damping coefficients were estimated from known material properties such as the Young's modulus (3×10^9 Pa) and Poisson ratio (0.33) using a Hertzian contact model. The coefficient of friction used for simulating sliding motion between particles was 0.3. Two gas velocities, 1.7 m s^{-1} and 2.4 m s^{-1}, were applied separately to investigate the effects of the conveying gas velocity on the solid motion. Finally, a time step of 2×10^{-5} s, estimated by the authors to be sufficiently small to ensure stability of their code without incurring high computational costs, was used in the simulations. The results showed that particles moved in the form of plugs in the horizontal conveying pipe, creating a wave-like motion similar to gas-liquid slug flow. With 1000 particles, a stationary layer of particles was formed on the bottom of

the pipe. The plug swept up these stationary particles in front of itself and left behind a layer of these particles during its motion through the pipe. The plug velocity was generally different from the gas velocity and increased with increasing gas velocity. The values obtained were compared with those measured in experiments done using 3 mm particles and found to be in good agreement. The authors mentioned that the real values of particle diameter used in the experiments were not used in the numerical simulations because of CPU time and memory constraints. However, the plug motion obtained from the simulation and visualized in the form of a video was realistic in comparison with experimental observations. In contrast, when 500 particles were simulated, all particles settled to form the stationary layer and no plug motion was observed.

Tsuji *et al.* (1993) subsequently applied the same approach as Tsuji *et al.* (1992) to the simulation of a two-dimensional fluidized bed. 2400 particles with diameters 4 mm and density 2700 kg m^{-3} were used. The spring constant in the spring-dashpot-friction slider model of DEM was set to be 800 N m^{-1}. This value was smaller than that of the actual aluminium particles which the authors used in their experiments so as to allow a reasonably large time step of 2.0×10^{-4} s to be used in the simulation. The coefficients of friction and restitution were 0.3 and 0.9 respectively. Gas was simulated to be introduced from a 10 mm nozzle at the center of the container base and a range of superficial gas velocities from 2.0 m s^{-1} to 2.6 m s^{-1} were considered. It was shown that at 2.0 m s^{-1}, the bed of particles expands without circulation. At 2.4 m s^{-1}, bubbles were generated within the bed which allow mixing of particles and at 2.6 m s^{-1}, bubbles were observed to form periodically at the nozzle and rise to the surface of the bed. These fluidization behaviors were qualitatively similar to those observed

in actual experiments using aluminium particles. The frequency of pressure fluctuations extracted from the simulation was also in good agreement with those obtained experimentally but the amplitude of the fluctuation was less satisfactory.

Xu and Yu (1997) carried out an investigation on the gas fluidization system studied by Tsuji *et al.* (1993). The numerical method used was also a combined CFD and DEM approach. In contrast with the unrealistic stiffness coefficient used by the previous workers, Xu and Yu (1997) used 50000 N m^{-1} as the spring constant in their application of DEM. In addition, the authors included a predictor-corrector scheme in the numerical integration of Newton's Law to evaluate particle motion so as to achieve higher numerical stability while applying a reasonably large time step of 1.5×10^{-5} s. The fluid drag force model used was that developed by Di Felice (1994) in comparison with the Ergun's equation used by previous workers. They tested the validity of their proposed model by attempting to establish the relationship between superficial gas velocity and pressure drop across the fluidized bed. The simulation results obtained indicated four stages of fluidization where the bed changed from an initial fixed bed configuration to an incipient fluidization stage and finally a fully fluidized stage before undergoing a defluidization process where the gas velocity was decreased gradually. The hysteretic nature of pressure drop variation with superficial gas velocity normally associated with a fluidization and defluidization process was successfully reproduced in the simulation. Typical fluidization behaviors and flow patterns relating to bubble formation and slugging were also observed from the numerical outputs.

Mikami *et al.* (1998) developed a simulation model for wet powder fluidization to investigate cohesive powder behavior. To take into account inter-particle cohesive interactions due to liquid bridging, a regression expression for the liquid bridge force was developed as a function of the dimensionless liquid bridge volume and the separation distance based on numerical solutions of the Laplace-Young equation. A two-dimensional bed containing 14000 spherical particles of diameter 1 mm and 0.27 wt% moisture content was simulated. The fluidized bed was supposed to have six inlet nozzles and the superficial gas velocity applied was 1.2 m s^{-1}. For the case of a noncohesive powder, realistic simulations of bubble formation, coalescence, eruption and particle circulation were obtained. With a wet powder, formation of agglomerates could be observed. The pressure fluctuation of the wet powder bed was also larger than that of the noncohesive bed due to the accumulation of energy by liquid bridges. When the gas velocity was decreased below the respective minimum fluidization velocities, the bed voidage for the case of wet particles was higher than that of dry particles and this was attributed to support by the wall by liquid bridges.

The simulation code developed by Mikami *et al.* (1998) was subsequently modified by Kaneko *et al.* (1999) by incorporating energy balance and reaction rate equations to study particle and fluid dynamics in a polyolefin reactor. The modified simulation model accounted for the polymerization reaction kinetics, temperatures of individual particles and gas-solid heat exchange to provide information on the mechanism of hot spot formation in the fluidized bed. A total of 14000 or 28000 particles with diameters of 1 mm were used. From the simulation results for the temperature profiles of the particles and gas obtained, a steep gradient of bed

temperature was found near the bed bottom and an almost constant profile in the area above. With the use of a perforated distributor, a dead zone of particles appeared at the corner of the distributor where particle and gas temperatures increased continuously. In contrast, no high temperature zone was present when a porous plate distributor was used. The random mixing of particles was also found to be important for the non-uniformity of temperatures. This would be critical for smooth and safe operations of polyolefin synthesis reactors especially when the heat of reaction is high.

Xu *et al.* (2000) applied their Combined Continuum and Discrete Model (CCDM) to study the strongly localized particle motion in a packed bed caused by lateral gas blasting. The model used was similar to that used by Xu and Yu (1997) for the study of gas fluidization. The geometry in this case consisted of a rectangular bed of dimension 1.0 × 0.3 × 0.004 m with a jet slot of 0.02 m flushed with the right wall 0.09 m above the bottom of the bed. 10000 spherical particles of diameters 4 mm were simulated and the time step used was 2.0×10^{-5} s. Based on the pressure drop against gas velocity profile obtained from the simulations, four regions could be identified and these were namely the fixed bed, raceway, fluidization and a second raceway region. The authors mentioned that the similarity and transition between the raceway and fluidization phenomena supported the argument that fluidization and raceway formation were two manifestations of gas-solid interactions in a packed bed. The formation of a raceway did not change the bed structure significantly as particles in the bed adjusted themselves in response to the disturbance. The raceway was characterized by a central high void region and a clockwise circulating particle region near the raceway boundary. When the magnitude of the gas velocity exceeded a

critical value, a transition from raceway to fluidization occurred. A microdynamic analysis of the gas-solid flows in raceway formation and fluidization showed that large interparticle forces occurred around the raceway boundary and propagated into the particle assembly in a complex manner. On the other hand, large drag forces were found above the roof of the raceway, indicating that the roof was supported by fluid drag forces.

Han *et al.* (2003) carried out a study to simulate the attrition of salt particles during pneumatic conveying through three straight pipes and two bends. The simulation was performed in a two-dimensional domain by combining DEM, CFD and an attrition model. The solid particles were initially given a monodispersed size distribution each with a diameter of 0.5 mm. During the attrition process, particles which attained sizes smaller than 10^{-4} m were removed from the simulation domain artificially for simplification purpose. Particle size decreased with increasing number of passes through the pneumatic conveying system. It was observed that the shape of the cumulative size distribution of particles obtained after nine passes was similar to that obtained from experiments. The size range of particles tended to a narrow range as the number of passes increased. Furthermore, the influence of the inlet gas velocity on particle breakage was found to be higher than the influence of the solids loading ratio. This was also consistent with previously reported experimental observations.

More recently, Xiang and McGlinchey (2004) also developed a two-dimensional mathematical model for simulating particle motion in dense phase pneumatic conveying using a combined CFD-DEM approach. A finite difference method and the semi-implicit method for pressure-linked equations (SIMPLE)

scheme was employed with a staggered grid configuration to integrate the Navier-Stokes equations to simulate the gas phase. A nonlinear spring and dashpot model was employed in the DEM model for describing force-displacement relationships. A total of 40000 particles of diameter 3 mm were simulated to flow in a horizontal pipe of length 8 m and internal diameter 8 cm. The authors also undertook experimental work to verify their simulations. Pressure transducers were used to provide information about plug formation and development for comparisons. The formation and motion of plugs observed in the numerical simulations were observed to be similar to those seen in the physical experiments. Good agreement was also observed in terms of pressure drops across the pneumatic conveying pipe.

2.3 Electrostatic Effects

The generation of electrostatic charges due to continuous and frequent collisions and friction between the granular material being transported and the walls of the conveying pipes, also referred to as the electrification of particles, is an unavoidable and usually undesirable phenomenon in most dry particulate systems. In addition to being a safety hazard, the buildup of electrostatic charges within a pneumatic conveying system may cause deviations in performance of the system from that for which it was originally designed. The occurrence of unexpected flow patterns of the granular material within the conveying pipes is an example of the significance of such electrostatic effects. Joseph and Klinzing (1983) examined the phenomenon of choking in vertical pneumatic transport in the presence of electrostatics using a 0.0254 m diameter Plexiglas tube and 150 μm diameter glass particles. It was mentioned that electrostatic effects should be minimized in the design of pneumatic conveying systems as these have an adverse effect on the optimal operating

conditions. In particular, they showed that the pressure drop at choking conditions and the required gas velocity at minimum pressure drop in vertical pneumatic conveying were higher in the presence of electrostatic forces. These were accompanied with violent pressure fluctuations and increased power requirements for the pneumatic transport operation. The pressure fluctuations could indicate the onset of the slugging transition both in the presence and absence of electrostatics.

Zhang *et al.* (1996) reported that the addition of an anti-static agent (Larostat powder) caused cohesive particles belonging to Group C in the Geldart classification scheme to behave similarly to Group A and B particles. A Laser Doppler Anemometer system was used to measure particle velocity, fluctuating velocity, size and extent of agglomeration or cluster formation of particles in a circulating fluidized bed system. Two test samples consisting of 750 g of shale particles and 742.5 g of shale particles mixed with 1% Larostat powder were used in the experiments respectively. Larostat powder is a cationic surfactant made of about 60% soyadimethylethyl-ammonium and 40% ethasulfate added to reduce the tendency for static buildup at the particle surface. The Larostat particles also acted as slip agents by lowering the friction between particles and between particles and the wall. For pure shale particles, it was found that an annular boundary region formed adjacent to the pipe wall. At low superficial gas velocities, reversal flow of particles was observed at the wall boundary while at high superficial gas velocities, the particle velocity profiles were parabolic in shape. In contrast, with 1% Larostat powder at low superficial gas velocities, no reversal flows were observed and at high superficial gas velocities, the mean particle velocity profiles were almost flat. This resulted in a plug flow pattern with almost no specific wall regions. As such, the addition of the Larostat powder had

reduced interparticle forces significantly leading to flatter particle velocity profiles. Similar types of trend were observed for the particle fluctuating velocity and turbulence intensity profiles in the absence and presence of the Larostat powder. Furthermore, the agglomeration of pure shale particles became dominant beyond a critical superficial gas velocity, resulting in significant increase in the average particle size. This was attributed to the increase in the frequency of collisions of particles, local eddies and streaming of particles at higher gas velocities. With the addition of 1% Larostat powder, only an insignificant amount of agglomerates was formed and the overall average particle size was reduced significantly. As such, the shale particles which belonged to Group C have been made to behave in a similar manner as Group A and B particles.

Al-Adel *et al.* (2002) have also emphasized the importance of considering electrostatic effects in analyzing gas-solid flows in their study of radial segregation of particles in vertical risers. However, the quantitative characterization of electrostatic effects on granular behaviors in any dry particulate systems remains a major challenge to experimentalists. This stems from the fact that the hydrodynamics associated with interactions between the gas and solid phases are interlinked with the effects of electrostatics such that any resulting flow behaviors are the composite effects of both. It is practically impossible in physical experiments to isolate the effects of electrostatics for a quantitative analysis of such effects on flow behaviors by controlling to a sufficiently high level of precision the amount of electrostatic charges which can be allowed to develop in a particular section of a system.

Numerical simulations may provide a viable alternative to the study of electrostatic effects in granular flow systems. Klinzing (1986) used a continuum model which incorporated electrostatic but not frictional forces to analyze the ability of particles to form clusters during pneumatic transport and showed that clustering tendency increased in the presence of electrostatic forces and was strongly influenced by particle size. Al-Adel *et al.* (2002) were able to characterize the extent of lateral segregation of particles arising solely from static electrification in flow through a vertical riser by numerical simulations using a continuum model. The model consisted of steady state axial momentum balances for the gas and particle phases, the Poisson equation for the electric potential and the steady state radial momentum balance for the particle phase. The mechanism of hydrodynamically driven segregation could be deliberately and fully suppressed by choosing appropriate closures for their particle-phase pressure. At steady state, a radially non-uniform particle volume fraction distribution was obtained. It was shown that the model reproduced important qualitative features of riser flows such as core-annular particle distribution, annular particle downflow at low riser gas velocities and annular upflow at high gas velocities. The numerical results obtained were comparable with experimental data reported in the literature.

Watano *et al.* (2003) proposed a two-dimensional DEM model for analysis and prediction of particle electrification and showed that the electrification of particles during pneumatic conveying depended on the number of particle collisions against the pipe wall and the normal component of the impact velocities. Spherical PMMA particles with diameters 300 μm were used in their experimental study. The pneumatic conveying system consisted of a 36 mm pipe of length 2 m. It was

observed that the specific charge of particles decreased with an increase in the initial particle load while the specific charge increased with an increase in the air velocity. The same phenomena were obtained from the DEM simulations performed. As such, the authors concluded that the vertical component of the impact velocity could be effectively used to predict particle electrification in a pneumatic conveying system. The DEM model was subsequently extended by Watano (2006) to carry out three-dimensional simulations of the same phenomenon of particle electrification during pneumatic conveying. The mechanism for the above experimental observations could then be extracted from the simulations. The number of collisions between particles increased with an increase in the initial loading which in turn led to a decrease in the number of particle-wall collisions. Since electric charging arose mainly from the latter, the specific charge of particles decreased with initial loading.

The presence of electrostatic effects were unnecessary for the formation of most flow regimes observed by Rao *et al.* (2001) and Zhu *et al.* (2003) experimentally. In particular, it seems that the so called annular capsule and eroding dunes flow in, respectively, vertical and inclined pneumatic conveying do not arise in the presence of purely hydrodynamic effects only. In the former, the solids distribution exhibited a core-annular structure with particles being concentrated against the walls of the vertical pipe leaving a relatively empty core region at the center while in the latter, erosion of dunes occur due to backflow of solids from the tails of individual dunes along the inclined pipe. There seemed to be either an anomalous attractive force towards the walls of the vertical pipe leading to severe radial segregation of the granular material or an exceptionally large amount of friction at the lower walls of the inclined pipe such as to cause dune erosion. As with the

previous studies carried out by other research workers, these observations suggest that electrostatic effects play an important role in gas-solid flow systems.

2.4 Granular Attrition

Attrition of solid particles is a commonly encountered but usually undesirable occurrence in processes involving granular material. For example, attrition of particles in fluidization and pneumatic transport systems is an issue of considerable industrial concern and research efforts have been devoted to the understanding and quantification of this phenomenon. However, granular attrition is also a complex and poorly understood process for which no general theory currently exists. The most popular approach taken by a number of research workers in deriving theoretical models for granular attrition processes has been through the application of a chemical kinetics analogy. The success of this approach has been limited so far. Paramanathan and Bridgwater (1983b) used an annular shear cell to examine the attrition of various types of particulate solids such as molecular sieve beads, various forms of sodium chloride and sodium carbonate. They reported that a simple first order kinetics model where the rate of disappearance of particles in a given size interval due to breakage is proportional to the weight of particles present gives limited agreement with experimental results. This was largely due to anomalously high initial attrition rates which cannot be satisfactorily accounted for by the model. They proposed a modified first order kinetics model with three parameters where the rate of attrition depends on the deviation from attrition at infinite strain. However, it was found that this three-parameter model was not suitable for describing attrition of some of the materials tested in their annular shear cell experiments and no significant benefits in terms of modeling accuracy could be obtained even at the expense of having an additional

parameter in the model. They suggested that this might be due to inherent inaccuracies in the theory used.

Ayazi Shamlou *et al.* (1990) carried out experiments on attrition of soda glass beads in a gas fluidized bed and proposed a model which states that the rate of attrition is first order with respect to the total initial mass of intact particles and about 0.8th order with respect to time. The apparatus used was a 14 cm diameter by 100 cm high cylindrical column constructed of Perspex. The fluidizing gas was air with a superficial velocity into the bed of 1.1 – 1.3 m s^{-1} giving a linear velocity through each hole in the range 80 – 94 m s^{-1}. The bed material consisted of agglomerates prepared from narrowly classified soda glass beads with a mean size of 75 μm. The experimental data obtained showed a nonlinear rate of increase in the mass of fines generated as a function of time. The relatively high rate of fines formation during the initial period of fluidization was due to the loss of sharp corners and edges of the attriting particles. This led to rounding of all particles, after which the rate of attrition tended towards a constant. The rate coefficient in their proposed model depended upon the relative magnitudes of the forces acting on the particles and the limiting cohesive strength of a single particle. Specifically, it increased with increasing gas velocity and decreasing concentration of the binder used initially to form the agglomerates.

Cook *et al.* (1996) performed attrition tests in a circulating fluidized bed and selected a second order kinetics model as one which best fit their experimental data. The diameter and height of the fluidized bed used were 0.0762 m and 3 m respectively. Two groups of lime samples with mass mean diameters of 903 μm and

1764 μm respectively were used. Air was used as the fluidizing gas at superficial gas velocities of 1.54 – 2.69 m s^{-1} and 2 – 5 m s^{-1} for the two samples respectively. The model used may be interpreted to describe attrition as a process whose driving force is the deviation of the weight of solids remaining in a bed raised to the second power from the corresponding squared minimum weight required for attrition to become negligible. This minimum weight is generally a strong function of gas velocity and may also be dependent on material properties and other operating conditions and so has to be determined experimentally before the model may be used for making any theoretical predictions. Furthermore, the authors mentioned that the second order kinetics model may only be applicable where elutriation of fines takes place, as in the experiments they conducted.

The most successful and versatile model for describing granular attrition so far has been the empirical formulation due to Gwyn (1969) which states that the weight fraction of particles attrited is proportional to the shear strain (or equivalently, time, under constant strain rate conditions) raised to a certain power. Bridgwater (1987) found the formulation to be more satisfactory for describing attrition of high density polyethylene in an annular shear cell than a first order kinetics model. High density polyethylene particles with sizes 710 – 1000 μm were used with a strain of 75 cell revolutions being employed at a cell speed of 5 min^{-1}. It was observed that the attrition of the polymers increased monotonically with stress and strain with the initial rate being high and then decreasing substantially. A first order fit to the kinetics data obtained was found to be unsatisfactory while the Gwyn formulation provided a sounder way of unifying the data. However, though mostly successful, the Gwyn formulation is not without limitations. Bridgwater (1987) commented that Gwyn's

formulation is incomplete in the sense that it implies an infinite initial attrition rate at zero shear strain and also allows the amount of attrited material to increase without bound at large strains.

Neil and Bridgwater (1994; 1999) also found the same formulation to describe well their experimental data for attrition of molecular sieve beads, heavy soda ash and tetra-acetyl-ethylene-diamine particles in various systems such as the annular shear cell, fluidized bed and screw pugmill. Each of these devices had a different mechanical action on the materials. In particular, the annular shear cell modeled the breakage occurring in a failure zone of a deforming powder and permitted the stress and strain to be determined and controlled. They noted that for some materials, a first order breakage law was satisfactory after the initial period of attrition but for others it was never appropriate. On the other hand, the Gwyn formulation, which was empirical in its origin, was most effective in describing the rate of attrition. The product size distribution was well described by the Schuhmann formulation and this provided a means of modifying the Gwyn approach. For any one material, there was little variation in the value of the Gwyn parameter between different equipment.

Despite the general success of the Gwyn formulation in describing the characteristic behavior of particle attrition reported by several research workers, Ghadiri *et al.* (2000) observed deviations of their experimental results from the Gwyn formulation under some operating conditions such as at high normal stress loads. They carried out annular shear cell experiments using porous silica catalyst beads with sizes in the range 2.0 – 2.36 mm. The annulus of the shear cell used was 20 mm wide having inner and outer diameters of 120 and 160 mm respectively. Four values

of stresses, 25, 50, 100 and 200 kPa were applied in the experiments with the speed of the shear cell fixed at approximately 1.4 rpm. For the low normal loads of 25 and 50 kPa, the fraction of broken material increases with the shear strain according to Gwyn's formulation. However, for relatively high normal stress levels such as at 100 and 200 kPa, this trend was only maintained at strains lower than about 10 while the attrition data appeared to depart from the Gwyn formulation at large shear strains. As such, the authors concluded that the Gwyn formulation did not provide an adequate description of the process of attrition in an annular shear cell.

Boerefijn *et al.* (2000) provided a review on the attrition of fluid catalytic cracking (FCC) catalysts. They reported that the level of attrition in an FCC unit is a function of the interactions between various features such as surface burrs, cracks and shells of the particles, particle properties and structure and the hydrodynamic regimes prevailing in the unit. The bulk test method has been designed to reproduce the hydrodynamic regime on a smaller scale for assessment of the attrition propensity of particles. On the other hand, single-particle impact testing can also be used to evaluate the attrition propensity of particulate solids and allows various mechanisms of attrition to be investigated in detail. The authors analyzed attrition in jets in fluidized beds and showed that bulk tests may not be easily applicable to attrition occurring in large-scale operations.

Werther and Hartge (2004) presented a modeling approach which is able to handle most important aspects of industrial fluidized bed reactors. The relationship between catalyst attrition, solids recovery in the reactor system and chemical performance of the fluidized bed reactor was described. This modeling approach was

applied to a fictitious first-order reaction in which the fluidized bed is equipped with different solids recovery systems including one single-stage cyclone, several cyclones in parallel and two- and three-stage cyclone systems. The bed particle size distribution develops under the combined influences of catalyst attrition and efficiency of solids recovery and the simulations performed reveal that it might take months for an equilibrium particle size distribution to be established and the reactor to reach a quasi-steady state of operation. The authors concluded that the model presented takes proper account of the relevant effects and so may be helpful for solution of practical problems in industry.

2.5 Liquid Fluidization

Liquid-solid fluidization systems have evolved from its early industrial application as a way of separating solids of different sizes in the mining industry to its present day usage in hydrometallurgy, food technology, biochemical processing and water treatment. In a liquid fluidized bed, a suspension of solid particles is supported by a fluid flowing upwards through a porous base plate. At low fluid flow rates, the bed is quiescent and the fluid flows through the interstitial spaces between the particles. When the fluid flow is increased, the drag force acting on the particles increases until it exactly balances their net gravitational force. The so called minimum fluidization then occurs at the point where the particles are totally supported by the fluid. Further increase in fluid flow can lead to bed expansion and subsequently voidage instabilities over the entire bed.

In practice, fluidized beds show different regimes of hydrodynamic behavior above the minimum fluidization velocity. The stable, uniform and homogenous state

of fluidization is seldom found in practical applications. For example, gas fluidized beds are usually very unstable with excess gas rising up in the form of bubbles. On the other hand, it is well established that liquid fluidized beds exhibit more stable fluidization behaviors but may develop a type of instability known as voidage wave instability under certain conditions. Such instabilities are of considerable interests to many researchers and have been studied using both experimental and theoretical approaches.

El-Kaissy and Homsy (1976) presented the first statistically significant measurements of the propagation properties of voidage waves in fluidized beds. The experiments were conducted in a Plexiglas column of 2.22 × 7.62 cm cross-section and 1.22 m high containing a 10.16 cm deep packed bed of 0.51 cm diameter particles. The data acquisition system was a photodetection package composed of a light box, photodiode box and signal conditioner. Quantitative measures of the amplitude, velocity of propagation and dominant frequency were obtained for a range of flow rates as a function of height above the distributor. It was found that in the initial stages of growth, voidage waves grew exponentially with height with a growth rate which was a function of flow rate and bead size. This was in accordance with the qualitative predictions of linear stability theory. Subsequently, a loss of coherence and attenuation of amplitude was observed followed by another region of exponential growth or a pinching off of the wave to form circular structures. This suggested that bubbles could form from instability waves. This might imply that bubbles in gas fluidized beds were a result of the same instability of the state of uniform fluidization.

Didwania and Homsy (1981) also carried out experimental work on liquid fluidized beds to identify the various fluidization regimes and the transition points between them using flow visualizations and local voidage fluctuation measurements and to obtain quantitative information on the continuum length and time scales of particle motion. The experiments were carried out in a Plexiglas column of 30 × 3.15 cm cross-section and 180 cm height containing a 30 cm packed bed of glass beads of 0.059 cm diameter. Flow visualizations were carried out using 35 mm still photography and video tape recording. The studies showed that the state of motion in a liquid fluidized bed was complex and the flow had distinct regimes with characteristic features. These regimes included wavy flow, wavy flow with transverse structures, fine-scale turbulent flow and bubbling states. The transition points between these regimes were sharp and without hysteresis. In particular, the observation of bubbling states in liquid fluidized beds at high flow rates and low density ratio was new in this study.

Ham *et al.* (1990) set out in their experimental work to determine if stable, uniform fluidization at velocities above minimum fluidization could be attained, to characterize the stable regime and to compare experimentally determined characteristics to those predicted by linear stability theory. The apparatus used was a cylindrical glass tube of 0.782 cm inner diameter. The ratios of bed diameter to particle diameter were constrained to fall within the range 10 to 50 so that wall effects could be neglected while maintaining resolution of the measurement technique. A light extinction technique was applied for detecting instability waves. The basic principle was that the amount of light attenuation by particles in the suspension was a function of the particle concentration. Fluctuations in the intensity of light transmitted

could therefore be correlated with fluctuations in local void fraction. The light source used was a 5 mW He-Ne laser and the detector was a photodiode. It was reported that a qualitative agreement with the prediction from linear stability theory was obtained. A gap between minimum fluidization and the onset of the wavy instability was observed where a stable fluidized state could be obtained.

Nicolas *et al.* (1996) focused on the first wavy instability of liquid fluidized beds to examine the nature of such unstable flows in their experimental work. In particular, the response of the instability to a localized harmonic forcing was analyzed. The fluidized bed apparatus was similar to that used by Ham *et al.* (1990) and consisted of a 2 m vertical cylindrical glass tube with an inner diameter of 6.97 mm containing glass spheres with a mean diameter of 685 μm. Instability waves were recorded with a CCD camera connected to a real time digital imaging system and spatio-temporal plots, also termed characteristic diagrams of the instability, were then constructed. The wave instability was shown to follow a harmonic localized forcing whereas the unforced instability presented a broad power spectrum. When the forcing was small, the instability amplitude was found to increase along the bed height, suggesting that the behavior of the bed was dictated by an external forcing. As such, the instability was convective in nature. In a subsequent work, Nicolas *et al.* (1999) applied the light attenuation technique using a He-Ne laser beam as light source to carry out a more quantitative study of the amplification of perturbations up the suspension. The amplitudes of unstable modes were found to saturate and the associated waveform could be described as a succession of concentration dips and plateaus. The wave seemed to be symmetrical about the concentration minimum and could be well fitted by a cnoidal wave. The solid phase viscosity and pressure in the

two-phase model were deduced from the shape of the saturated wave and it was concluded that a Newtonian description of the stress tensor of the solid phase may not be valid.

More recently, Duru *et al.* (2002) performed experimental investigations on the primary wave instability of liquid fluidized beds. They showed that the voidage disturbance reached a nonlinearly saturated shape after its initial growth. They related the saturated shape to the unknown solid phase viscosity and pressure functions of a simple two-phase model with a Newtonian stress tensor for the solid phase and found the scaling laws and particle concentration dependence for these two quantities. The fluidized bed apparatus used was a straight vertical cylindrical glass tube of height 1.8 m mounted on a rigid support structure. Different tubes with different inner diameters were used. The bed to particle diameter ratio was chosen to be smaller than 25 in order to ensure that the instability remained one-dimensional but larger than 10 in order to avoid particle arching effect. The method of light attenuation was applied for particle volume fraction measurements whereby a linear photodiode was used to detect the transmitted light from a 25 mW He-Ne stabilized laser through the suspension. By performing long-time averages of the data obtained with periodic forcing applied at the base of the fluidized bed, the growth of one-dimensional voidage waves up the bed to their saturated finite amplitude were observed. These saturated waves had a well-defined shape with flat peaks of high particle concentrations and narrow troughs of low concentrations. In contrast to the finding of Nicolas *et al.* (1999) described earlier, the simplest two-phase model of a fluidized bed with a Newtonian stress tensor was found to be quite satisfactory for describing these one-dimensional voidage waves.

In addition to the various experimental studies reviewed above which have been carried out on the phenomenon of voidage wave instability in liquid fluidized beds, a limited number of theoretical investigations have also been reported in the literature. Homsy *et al.* (1980) explored the ability of two-fluid continuum equations to quantitatively describe the features of the experiments completed by El-Kaissy and Homsy (1976). By formulating and solving a linear stability problem, the proposed theory was found to be capable of describing consistently the propagation of small amplitude instability waves in fluidized beds reported in the earlier experimental work. The authors also used the experimental data to deduce values of various material constants appearing in the constitutive equation used.

Nicolas *et al.* (1994) investigated theoretically the stability of a fluidized bed with respect to spatially growing disturbances and looked for conditions under which a transition between convective and absolute instabilities could be identified. They derived a general linearized equation for the small perturbation of particle volume fraction, otherwise known as a wave hierarchy equation, and investigated linear stability using the mathematical framework of open flow theory. Two classes of spatially evolving flows, convectively and absolutely unstable flows, were found. In the former, the fluidized bed behaved as a spatial noise amplifier of incoming perturbation whereas in the latter, the instability had an intrinsic behavior and the perturbation grew both temporally and spatially. Spatial and temporal analyses gave the same result for the growth of the wave in the vicinity of the stability threshold but results from the two types of analyses differed otherwise. The authors stated that this showed that spatial analysis provided an accurate description of the spatial growth of

the wave and thus could yield a precise comparison with experimental observations. Another important result from the theoretical analyses was the possibility of absolutely unstable flow but the question of whether such a type of instability can be observed in practice remains open.

CHAPTER 3 RESEARCH APPROACH

An understanding of the differences in physics between the various flow regimes found in pneumatic conveying of granular material may be important to actual industrial or commercial applications with regards to the optimality of operation, ease of control and extent of damage inflicted on the solid particles as well as the conveying lines. Despite the large number of work reported on gas-solid systems, there have been relatively fewer attempts at modeling the various flow regimes in vertical, horizontal and inclined pneumatic conveying systems. The ability to predict the flow behaviors of both gas and solid phases during a typical pneumatic conveying operation or the modes in which the transportation would take place remains limited. As such, the objective of this study was to apply the technique of combining DEM with CFD to the numerical simulation of pneumatic conveying of granular material in vertical, horizontal and inclined pipes. The emphasis had been on reproducing computationally the different types of solid flow patterns and behaviors observed experimentally under different operating conditions. A two-dimensional CFD-DEM program code was developed in-house during the initial stages of the present study.

3.1 Pneumatic Conveying

The geometry of the pneumatic conveying system and type of particles used in the present simulations were based on the experimental work of Rao *et al.* (2001) and Zhu *et al.* (2003) (Table 3.1) so that a meaningful comparison between the simulation and experimental outputs can be made. The gas velocities considered in this study

Table 3.1 Material properties and system parameters

Shape of particles	Spherical
Type of particles	Polypropylene
Number of particles	500, 1000, 1500, 2000
Particle diameter, d	2.8×10^{-3} m
Particle density, ρ_p	1123 kg m^{-3}
Spring constant in force model, κ	5.0×10^{3} N m^{-1}
Viscous contact damping coefficient, η	0.02, 0.35
Coefficient of restitution	0.1, 0.9
Coefficient of friction	0.3
Cohesion, c	0.0
Coefficient of rolling friction, μ_r	5.0×10^{-5} m
Gas density, ρ_f	1.205 kg m^{-3}
Gas viscosity, μ_f	1.8×10^{-5} N s m^{-2}
Pipe diameter	0.04 m
Pipe length	1.0 m
Pipe inclination	45^o, 90^o
Computational cell size	4 mm × 4 mm
Simulation time step, Δt	10^{-7} s

were in the ranges 14 m s^{-1} – 24 m s^{-1} and 10 m s^{-1} – 30 m s^{-1} for the vertical and horizontal pneumatic conveying simulations respectively because these would include all the flow regimes observed via Electrical Capacitance Tomography measurements by Rao *et al.* (2001) and Zhu *et al.* (2003) for the two systems. The numbers of particles used were 500, 1000, 1500 and 2000 corresponding to overall solid concentrations α, of 0.08, 0.16, 0.24 and 0.32 respectively where α is defined as the overall volume fraction of particles divided by the volume fraction of particles at maximum packing which is generally taken to be 0.64. The equivalent coefficient of restitution represented by the viscous contact damping coefficient selected for the present study was found by conducting a numerical experiment similar to that used by Xu and Yu (1997). A single particle was simulated to fall from rest under the effects of gravity and rebound from a flat surface. The coefficient of restitution was then given by $\sqrt{\frac{h}{h_o}}$ where h_o and h are the maximum heights of the particle above the surface before and after the collision respectively. The value obtained was insensitive to h_o and a value of 1 m was used for this quantity for all subsequent calibration of the viscous contact damping coefficient to the coefficient of restitution. Without loss of generality, the same values of the coefficients of friction and restitution as shown in Table 3.1 were used for both particle-particle and particle-wall interactions. The flow patterns from the numerical simulations were then compared qualitatively with the experimental observations of Rao *et al.* (2001) and Zhu *et al.* (2003).

In all simulations performed, particles were first allowed to settle freely under gravity for 0.5 s and form a packing at the 'bottom' of a vertical pipe or a heap in a horizontal pipe before gas flow was initiated. Periodic boundary conditions were

applied to the solid phase to simulate an open flow system while a uniform gas velocity profile was maintained at the inlet. Particles which were carried out of the conveying pipe by the flowing gas were simulated to re-enter from the inlet of the pipe with the same velocities and radial positions. The main advantage of this method was the possibility of simulating a very long conveying pipe using a significantly smaller computational domain which leads to more efficient utilization of computing resources.

3.2 Electrostatic Effects

During pneumatic conveying, solid particles gain electrostatic charges as a result of repeated collisions and impacts against other particles and with the walls of the conveying pipe. The amount of charge transferred between two contacting bodies during impact depends on the potential difference between the two bodies, which in turn depends on their surface work functions and the image charge effect (Matsusaka and Masuda, 2003). In addition, the large group of charged particles within a conveying line gives rise to an electric field that can also influence the total potential difference through what is known as the space charge effect. It may be expected that a comprehensive mathematical model which incorporates such effects would be necessary for a detailed transient simulation of the electrification of particles starting from uncharged ones. Such a model is beyond the scope of the present study. Instead, it is assumed that the pneumatic conveying system has been operated beyond the transient state of electrification such as to reach a dynamic state of electrostatic equilibrium (Yao *et al.*, 2005). The amount of charge carried by the particles as well as the walls of the pipe then remains fairly constant with respect to time. The total

electrostatic force acting on each particle may then be written as the sum of electrostatic forces due to charges carried by other particles and the pipe walls.

$$\mathbf{f}_{E,i} = \mathbf{f}_{Ep,i} + \mathbf{f}_{Ew,i} \tag{3.1}$$

where $\mathbf{f}_{Ep,i}$ and $\mathbf{f}_{Ew,i}$ are the electrostatic forces due to other charged particles and the pipe walls acting on particle i respectively.

The electrostatic force arising from charges carried by other particles may be calculated by assuming each particle to be a constant point charge.

$$\mathbf{f}_{Ep,i} = \sum_{\substack{j=1 \\ j\neq i}}^{N} \frac{Q^2}{4\pi\varepsilon_o r_{ij}^2}\mathbf{n}_i \tag{3.2}$$

where Q is the constant charge assumed to be carried by all particles, ε_o is the permittivity of free space, r_{ij} is the distance between particles i and j and $\mathbf{n}_i$ is the unit normal vector in the direction of the line joining the two particle centers.

Such calculations, typical of molecular dynamics simulations, are expected to be computationally intensive and impractical for large numbers of particles. Yao *et al.* (2005) carried out experiments using the same pneumatic conveying setup and type of particles as those used by Rao *et al.* (2001) and Zhu *et al.* (2003) shown in Table 3.1. They found experimentally that the electrostatic force acting on particles by the charged pipe wall is at least three orders of magnitude larger than that due to other charged particles. The former was typically of the same order of magnitude as the weight of each particle. As such, the latter effect was assumed to be of secondary importance in determining the hydrodynamics and flow patterns of the granular material within the pneumatic conveying system. The amount of charge carried by each particle was also found to be in the range $1.0 \times 10^{-9} - 3.0 \times 10^{-9}$ C. In order to

verify the claim that interparticle electrostatic interactions are negligible compared with those between particles and walls, a number of simulations for pneumatic conveying through a 45^{o} inclined pipe were carried out in the initial phase of the present study using equation (3.2) to calculate interparticle electrostatic forces. The amounts of charge prescribed to be carried by each particle, Q, at the beginning of each simulation were 1.0×10^{-9} C, 2.0×10^{-9} C, 3.0×10^{-9} C and 5.0×10^{-9} C. The inlet gas velocity used was 3 m s^{-1} and all other pertinent parameters are as given in Table 3.1. Figures 3.1a, b, c and d show typical flow patterns of the granular material in a 45^{o} inclined pneumatic conveying pipe for each of the cases respectively. It may be observed that the flow patterns in such a system are indeed insensitive to the charge carried by each particle within the system. It was also found from the calculations that the average electrostatic force acting on each particle during the pneumatic conveying process for the cases Q = 2.0×10^{-9} C and 5.0×10^{-9} C was about 5.0×10^{-9} N and 1.0×10^{-8} N respectively while the weight of each particle was about 1.3×10^{-4} N. This showed quantitatively that electrostatic effects due to charged particles are indeed negligible compared with other types of forces which are of similar orders of magnitude as the weight of the particles in the present system. Such effects may be important for fine powders where the weight of each particle is very small or for granular materials which can be charged to significantly higher extents.

Figure 3.2 shows a map of particle charge-to-mass ratios as a function of particle sizes for various types of particles reported by other research workers. In comparison, the charge-to-mass ratio for the 2.8 mm polypropylene particles used in the present experimental and numerical studies is comparable with those observed for

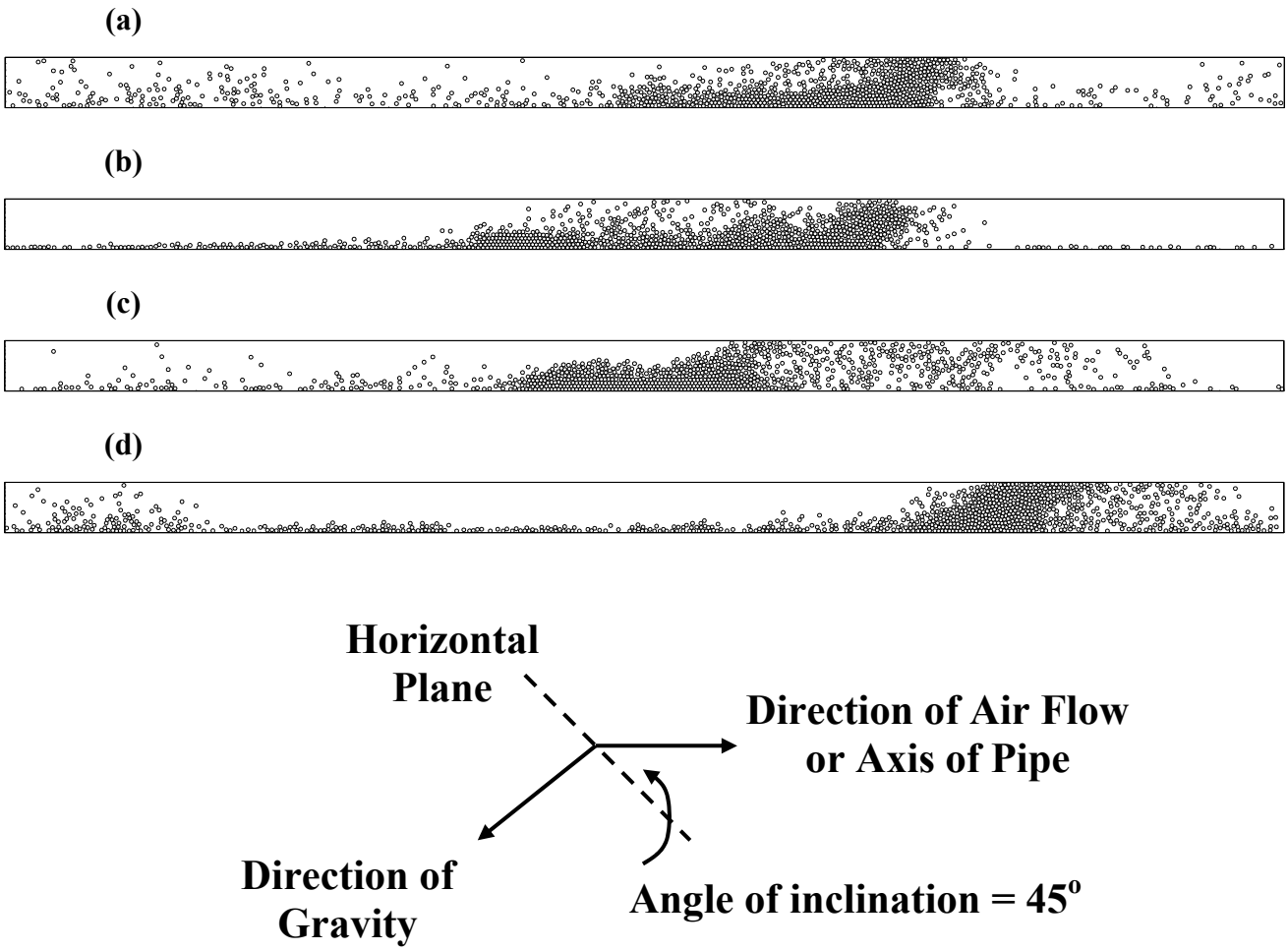

Figure 3.1 Pneumatic conveying through a pipe inclined at 45° to the horizontal with an inlet gas velocity of 3 m s^{-1}, α = 0.16 and (a) Q = 1.0×10^{-9} C (b) Q = 2.0×10^{-9} C (c) Q = 3.0×10^{-9} C (d) Q = 5.0×10^{-9} C. Here, the inclined pipes are presented horizontally with the direction of gravity relative to the pipe axis as indicated in the inset. Gas flow is from left to right.

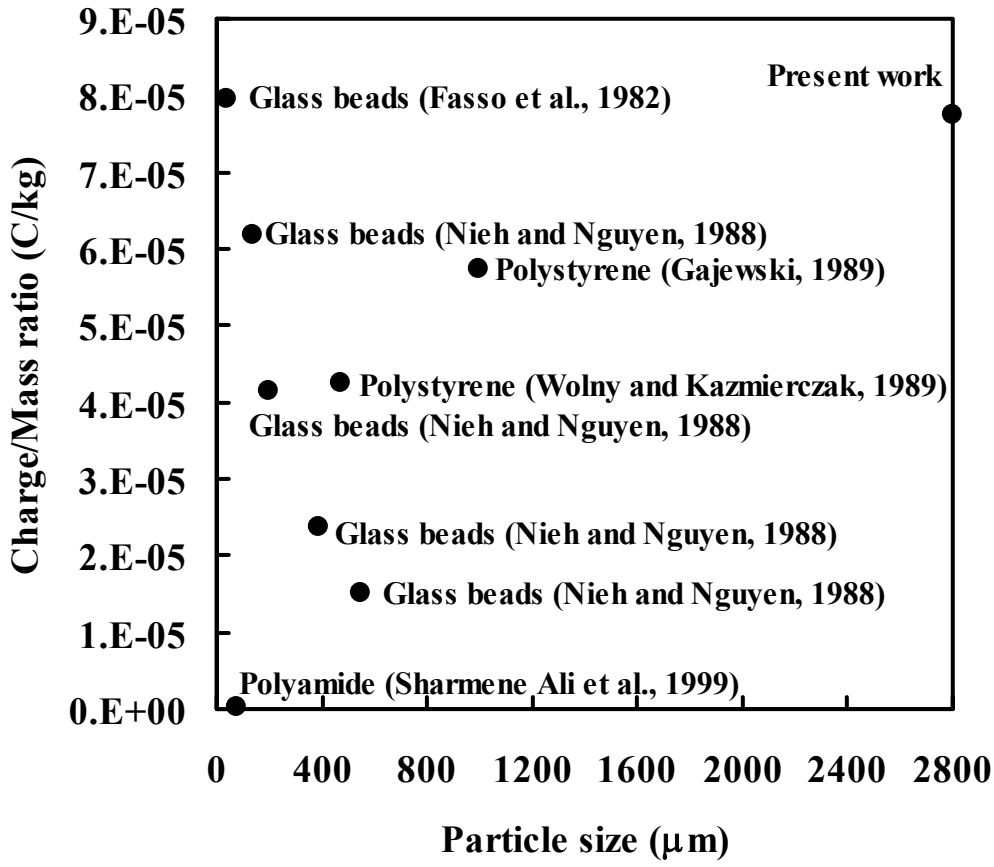

Figure 3.2 Map of particle charge-to-mass ratio as a function of particle size

other types of particles. There is no well-defined criterion available in the literature for neglecting van der Waals or inter-particle electrostatic forces. However, the present particles used are much more massive. This may also provide an explanation for the above observation that flow patterns are insensitive to the charge carried by each particle and electrostatic forces between particles are much smaller than their weight. Similarly, the type of pipe wall material used in a pneumatic conveying system has also been observed to have an effect on the amount of electrostatic charge generated within the system. However, the amount of studies which have been carried out on this aspect has been quite limited. Yao *et al.* (2004) measured the current induced on a copper pipe used in a pneumatic conveying system which has been covered with different types of polymer films such as polyvinyl chloride (PVC) and polyethylene (PE). The induced current represents the total amount of charge which has been accumulated on the polymeric material. It was reported that both the induced current and the magnitude of its fluctuations were larger when the pipe wall was covered with PVC than PE. In an earlier study by Ally and Klinzing (1985), it was also found that the type of pipe wall material also affected the charge-to-mass ratio of particles conveyed through the pipe. Table 3.2 shows a summary of the experimental results for various types of pipe wall and particle material reported by them. It may be expected that charges induced on a pipe wall made of a conductive material may be more easily conducted away while those induced on an insulating material may tend to be accumulated. Zhu *et al.* (2004) have reported that the presence of electrostatic charges residing on pipe walls may have some perturbation effects on ECT measurements when low gas velocities are used. However, this aspect of tomographic measurements is currently still being investigated by various research workers and no conclusive remarks are available at this point.

Table 3.2 Charge-to-mass ratios of particles conveyed through various types of pipes (Ally and Klinzing, 1985)

Pipe material	Particle material	Particle size (μm)	Particle charge-to-mass ratio (C/kg)
Copper	P004 glass	75	2.2×10^{-2}
	P008 glass	150	3.6×10^{-3}
	Crushed glass	314	5×10^{-6}
	Plexiglas	145	5×10^{-4}
Plexiglas	P004 glass	75	3×10^{-3}
	P008 glass	150	5×10^{-4}
	Plexiglas	145	3.5×10^{-3}
	Cu	196	2.5×10^{-3}
Glass	Cu	196	2.2×10^{-1}
	Plexiglas	145	6.5×10^{-2}

In pneumatic conveying through inclined or horizontal pipes, the lower walls of the pipe are charged to a significantly larger extent than the upper walls due to the larger amount of collisions and traction from solid particles (Yao *et al.*, 2005). In the present study, such a charging condition is assumed to exist. This gives rise to a net electrostatic force of attraction (due to opposite polarities with charges assumed to reside on particles) in the wall-normal direction towards the bottom wall of the inclined pipe on all charged particles within the system. As the angle of inclination of the pneumatic conveying pipe is increased, it may be expected that the upper walls would experience a larger amount of collisions from particles and thus be charged to a larger extent. This aspect of pipe wall charging in inclined pneumatic conveying has not been investigated previously and does not fall within the scope of the present study. In contrast, all walls of a vertical pipe may be charged to the same extent due to almost equal amount of collisions from solid particles in such a configuration. The net electrostatic force acting on a particle by a charged pipe wall in this case then depends on the relative proximity of the particle to each wall within the system. In the present work, a dimensionless quantity Λ depicting the ratio of the electrostatic force arising from the charged pipe wall to the gravitational force exerted on each particle, $\mathbf{f}_{Ew,i}/m_i g$, is defined. In other words,

$$f_{Ew,i} = \Lambda m_i g \tag{3.3}$$

The value of Λ is varied over a reasonable range and its effects on solid velocity and solid fraction profiles, pressure drops and reversed flow behavior in pneumatic conveying through an inclined pipe under the condition of electrostatic equilibrium are investigated numerically. The case of pneumatic conveying through a vertical pipe is considered as a special case with pipe inclination of 90^o. The consideration of the state of electrostatic equilibrium and the numerical study of flow pattern formation

and flow behaviors in a pneumatic conveying system under such conditions have not been attempted before to date.

3.3 Granular Attrition

As reviewed in the previous chapter of this thesis, theoretical models for bulk granular attrition based on chemical kinetics analogies or their variants may be limited in their capabilities to describe granular attrition processes quantitatively. It was verified during the initial phase of the present study that first order kinetics model gives poor fitting with all experimental data reported by other research workers. As such, the first order kinetics model does not bear the true physics of a bulk granular attrition process. This is also the reason for the use of various kinetic models of different rate orders by different research workers for fitting with their own experimental data. It was also verified in this study that models derived based on more complex kinetics than those mentioned to be inadequate as well. A general and coherent theory of granular attrition capable of unifying all experimental data collected to date using various types of material, systems and operating conditions is still lacking in the literature. Here, a novel approach to the modeling of granular attrition by treating such processes as analogs to mass diffusion is proposed.

During granular attrition, the weight fraction of large particles decreases while that of small particles increases (Figure 3.3). Weight fraction of particles shifts from large sizes towards smaller sizes and never in the opposite direction, much like the diffusion of material down a concentration gradient in the continuum sense. As such, it is proposed to treat the process of bulk granular attrition as the diffusion of weight

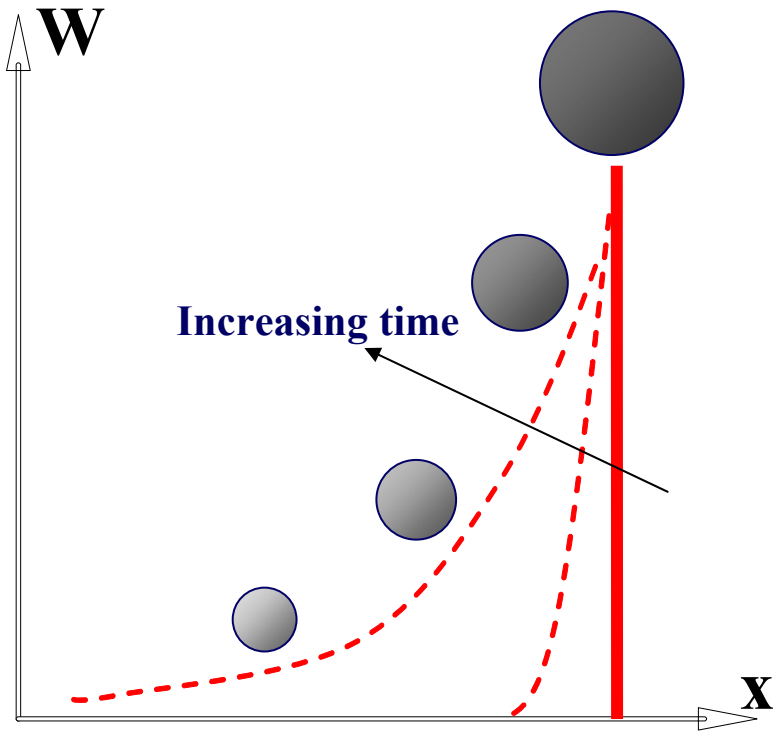

Figure 3.3 Changes in particle size distribution with time in the presence of granular attrition. Analogy with changes in concentration profiles during diffusion of material

fraction of granular materials in particle-size space:

$$\frac{\partial W}{\partial t} = D\frac{\partial^2 W}{\partial x^2} \tag{3.4}$$

where W(x, t) is the weight fraction of particles, t is attrition time, x is a dimensionless particle size defined as $\frac{d}{d_o}$, d_o and d are parameters characterizing the size of intact and attrited particles respectively and may be taken to be their diameters, D would be referred to as attrition diffusivity and may be interpreted to be a measure of the attritability of particles. Accordingly, a plot of W against x at a particular time t would correspond to the particle size distribution of the entire population of particles at that instant of time. There is no relation between W and d by definition. In a physical experiment or computer simulation, the particle size distribution evolves naturally as a result of attrition and so the weight fraction of particles for each size range changes continuously with time. The boundary conditions to be applied are W(0, t) = 0, W(1, t) = 1 and W(x, 0) = 0. The essential features include the requirements that no particle achieves zero size as a result of attrition at any point in time, a constant availability of intact particles and the absence of any attrited particles at the start of the attrition process. The condition W(1, t) = 1 holds true approximately if the amount of intact particles is much larger than that of attrited particles. This can be maintained by continuous feeding of intact particles in a continuous operation or during the initial stages of a batch operation where only a small amount of attrition has occurred. The corresponding solution to equation (3.4) may then be written as (Appendix A):

$$W = \frac{2}{\pi}\sum_{n=1}^{\infty}\frac{(-1)^n}{n}\left\{\exp\left[-(n\pi)^2 Dt\right]-1\right\}\sin(n\pi x) \tag{3.5}$$

The weight fraction of particles which has undergone attrition at time t, denoted W', is then the integral of W in the interval x = 0 to 1 (Appendix B):

$$W' = \frac{4}{\pi^2} \sum_{\substack{n=1 \\ (n \text{ odd})}}^{\infty} \frac{1}{n^2} \left\{ 1 - \exp\left[- (n\pi)^2 Dt \right] \right\} \tag{3.6}$$

Equation (3.6) is correlated with experimental data reported in the literature for various types of systems, operating conditions and granular material using the attrition diffusivity as the fitting parameter. A physical interpretation of this parameter will then be proposed.

The proposed diffusion model is a macroscopic, empirical equation which has the potential to be used for predicting bulk granular attrition behavior. The applicability of this model for correlating with existing experimental data obtained from fluidized bed and annular shear cell experiments will be investigated. It may be noticed that such experiments involved relatively slow attrition processes conducted over long time periods. On the other hand, it is also necessary to verify the applicability of the diffusion model towards attrition processes where particle breakages occur over very short time scales but producing comparable extents of attrition as those observed in experiments. To this end, computer simulations are used to "create" such an attrition process from the microscopic or particle-level scale by combining the CFD-DEM model with an appropriate attrition model and its bulk behavior is subsequently analyzed using the diffusion model. Attrition of individual particles based on operating conditions at the single particle scale, such as the impact velocity of each particle, is modeled. This would provide an independent and rigorous test of the validity of the diffusion model for attrition occurring over short time scales.

As for the previous studies on pneumatic conveying, the system geometry simulated here consists of a 1.0 m vertical conveying pipe of diameter 0.04 m containing 1000 spherical particles with initial diameters of 2.8 mm. The coefficient of restitution of the particles was varied in the range 0.06 – 0.4 to investigate its effect on the extent of attrition. Periodic boundary conditions were applied to simulate an open flow system such that particles which were carried out of the conveying pipe by the flowing air were simulated to re-enter from the inlet of the pipe with the same velocities and radial positions. The flow of air and particles with application of periodic boundary conditions was carried out for 5 s of physical time during which the solid particles cycled through the pipe segment numerous times and reached a fully developed flow state. A sharp bend in the system was then simulated by the imposition of a wall at the upper end of the vertical pipe while shifting the position of the outlet to the side wall. The DEM algorithm checks for collision between each particle and the pipe walls and among particles at every time step. Upon the detection of particle-wall or particle-particle collision, the normal component of the velocity of the particle relative to the wall or other particle is determined and used as the impact velocity for determination of fragment sizes. Attrition can result from both interaction between particles and between particles and wall. The number of particle fragments formed upon collision and attrition was then recorded.

3.4 Liquid Fluidization

Bubbles are important features in fluidized beds for inducing solid motion and promoting mixing. However to date, the origin of bubbles is still not well understood. They are conjectured to evolve from secondary instabilities which in turn are believed to appear due to primary voidage wave instabilities. As such, investigations on such

voidage waves are essential to providing us with a fundamental understanding of bubble formation. Here, both CFD-DEM simulations and experimental investigations using the technique of Particle Image Velocimetry will be applied to study the phenomenon of voidage wave formation and propagation in a vibrated liquid fluidized bed. The geometry used in the CFD-DEM simulations is discussed below while the experimental setup and procedures used will be described in the next chapter of this thesis.

The geometry of the liquid fluidization system simulated in this study follows that of the experimental setup discussed in the following chapter and consists of a pseudo three-dimensional narrow channel of 2 cm width and 1.0 mm thickness containing 2500 glass beads as the solid phase and water as the interstitial fluid. It was deemed justifiable to carry out a pseudo three-dimensional simulation of the fluidization system as the physical structures of interest in this case are one-dimensional traveling voidage waves. Feng *et al.* (2004) applied periodic boundary conditions to the front and rear walls of a rectangular fluidized bed with two side walls in their numerical study of particle mixing and segregation behaviors. This was to reduce wall effects and allow three-dimensional motion of particles without the use of a large number of particles. This aspect of the simulation was considered to be important to the particular phenomenon being investigated as it has been previously reported that the packing structure of a bed of particles is strongly dependent on the size of those particles which constitute the bed (Yang *et al.*, 2000). However, the fluidized bed system of interest in the present study is basically a geometrically constrained type of system which may be viewed upon as a pseudo one-dimensional bed. Such type of bed is essential for the observation of traveling voidage waves

which propagate along the 'single' dimension of the bed and do not exhibit any transverse structures along a second dimension. The good agreement between various experimentally observed and numerically simulated characteristics of such voidage waves, as will be shown in the rest of this thesis, also indicates that the pseudo three-dimensional CFD-DEM model applied in the present study is sufficiently adequate for capturing most of the physics associated with such phenomena.

Each glass bead had a diameter of 1.0 mm and density of 2500 kg m^{-3}. The coefficients of friction and restitution used were 0.3 and 0.9 respectively. The base of the fluidization system was allowed to undergo simple harmonic motion when desired in order to facilitate the study of the effects of external perturbations on the stability of the bed. This is the first computational study of vibrated liquid fluidized beds whereby the external forcing (in the form of an oscillating base) imposed experimentally in previous (Duru *et al.*, 2002) and the present work is also incorporated as part of the simulation. This reproduces the physical conditions present in such experiments in a realistic manner and thus facilitates corresponding studies of the underlying physics through this approach. The amplitude and frequency applied when a vibrating base was simulated were 1.5 times the diameter of a glass bead (i.e. 1.5 mm) and 2 Hz respectively so as to have a basis for comparison with actual experimental observations. The superficial velocities of the liquid used were 0.018 m s^{-1} and 0.030 m s^{-1}. In simulations involving an oscillating base, the moving piston was assumed not to impart a significant amount of momentum to the fluid (Duru *et al.*, 2002) and the superficial velocities used were maintained at a constant value.

CHAPTER 4 COMPUTATIONAL AND EXPERIMENTAL

4.1 Discrete Element Method

The translational and rotational motions of individual solid particles are governed by Newton's laws of motion:

$$m_i \frac{d\mathbf{v}_i}{dt} = \sum_{j=1}^{N} \left(\mathbf{f}_{c,ij} + \mathbf{f}_{d,ij} \right) + m_i \mathbf{g} + \mathbf{f}_{f,i} \tag{4.1}$$

$$I_i \frac{d\boldsymbol{\omega}_i}{dt} = \sum_{j=1}^{N} \mathbf{T}_{ij} \tag{4.2}$$

where m_i and $\mathbf{v}_i$ are the mass and velocity of particle i, N is the number of particles in contact with this particle, $\mathbf{f}_{c,ij}$ and $\mathbf{f}_{d,ij}$ are the contact and viscous contact damping forces respectively, $\mathbf{f}_{f,i}$ is the fluid drag force due to an interstitial fluid, I_i is the moment of inertia of particle i, $\boldsymbol{\omega}_i$ is its angular velocity and $\mathbf{T}_{ij}$ is the torque arising from contact forces which will cause the particle to rotate.

Contact and viscous contact damping forces have to be calculated using force-displacement models which relate such forces to the relative positions, velocities and angular velocities of the colliding particles. In the present work, the linear force-displacement model was implemented for the calculation of these collision forces. With such a closure, interparticle collisions are modeled as compressions of a perfectly elastic spring while the inelasticities associated with such collisions are modeled by the damping of energy in the dashpot component of the model. Collisions between particles and a wall may be handled in a similar manner but with the latter not incurring any change in its momentum. In other words, a wall at the point of contact with a particle may be treated as another particle but with an infinite amount

of inertia. The normal ($f_{cn,ij}$, $f_{dn,ij}$) and tangential ($f_{ct,ij}$, $f_{dt,ij}$) components of the contact and damping forces are calculated according to the following equations:

$$\mathbf{f}_{cn,ij} = -\kappa_{n,i}\boldsymbol{\delta}_{n,ij} \tag{4.3}$$

$$\mathbf{f}_{ct,ij} = -\kappa_{t,i}\boldsymbol{\delta}_{t,ij} \tag{4.4}$$

$$\mathbf{f}_{dn,ij} = -\eta_{n,i}\left(\mathbf{v}_r \cdot \mathbf{n}_i\right)\mathbf{n}_i \tag{4.5}$$

$$\mathbf{f}_{dt,ij} = -\eta_{t,i}\left\{\left(\mathbf{v}_r \cdot \mathbf{t}_i\right)\mathbf{t}_i + \left(\boldsymbol{\omega}_i \times \mathbf{R}_i - \boldsymbol{\omega}_j \times \mathbf{R}_j\right)\right\} \tag{4.6}$$

where $\mathbf{f}_{cn,ij}$, $\mathbf{f}_{dn,ij}$ and $\mathbf{f}_{ct,ij}$, $\mathbf{f}_{dt,ij}$ are the normal and tangential components of the contact and viscous contact damping forces respectively, $\kappa_{n,i}$, $\boldsymbol{\delta}_{n,ij}$, $\mathbf{n}_i$, $\eta_{n,i}$ and $\kappa_{t,i}$, $\boldsymbol{\delta}_{t,ij}$, $\mathbf{t}_i$, $\eta_{t,i}$ are the spring constants, displacements between particles, unit vectors and viscous contact damping coefficients in the normal and tangential directions respectively, $\mathbf{v}_r$ is the relative velocity between particles and $\mathbf{R}_i$ and $\mathbf{R}_j$ are the radius vector (from particle center to a contact point) for particles i and j respectively. If $\left|f_{ct,ij}\right| > \left|f_{cn,ij}\right| \tan\phi$ then 'slippage' between the two contacting surfaces is simulated by a Coulomb-type friction law, $\left|f_{ct,ij}\right| = \left|f_{cn,ij}\right| \tan\phi$ where $\tan\phi$ is analogous to the coefficient of friction.

4.2 Fluid Drag Force

In a multiphase system such as the gas-solid pneumatic conveying system considered in this study, interactions between the two phases take the form of fluid drag forces on the solid particles exerted by the interstitial fluid and arise from velocity differences between the two phases. In this study, the model due to Di Felice (1994) which is applicable over a wide range of particle Reynolds numbers was used for evaluating the fluid drag force term in equation (4.1). As this empirical model was developed by fitting with previously reported experimental data for both fixed and fluidized beds, it was assumed that the various interaction effects such as those due to

particle collisions, which must necessarily be present in the physical experiments used for correlation, have been incorporated empirically in the model. As such, these effects are not further computed explicitly through a separate set of equations in the present simulations. In the literature, this same fluid drag force model has been applied for numerical simulations of gas-solid flow in fluidized beds (Xu and Yu, 1997; Xu *et al.*, 2000) and realistic results in comparison with actual experiments have been obtained. Following Xu *et al.* (2000), the modified equations in this model are shown as follows:

$$\mathbf{f}_{f,i} = \mathbf{f}_{f0,i}\varepsilon_i^{-(\chi+1)} \tag{4.7}$$

$$\mathbf{f}_{f0,i} = 0.5 c_{d0,i}\rho_f \pi R_i^2 \varepsilon_i^2 \left|\mathbf{u}_i - \mathbf{v}_i\right|\left(\mathbf{u}_i - \mathbf{v}_i\right) \tag{4.8}$$

$$\chi = 3.7 - 0.65\exp\left[-\frac{\left(1.5 - \log_{10} \mathrm{Re}_{p,i}\right)^2}{2}\right] \tag{4.9}$$

$$c_{d0,i} = \left(0.63 + \frac{4.8}{\mathrm{Re}_{p,i}^{0.5}}\right)^2 \tag{4.10}$$

$$\mathrm{Re}_{p,i} = \frac{2\rho_f R_i \varepsilon_i \left|\mathbf{u}_i - \mathbf{v}_i\right|}{\mu_f} \tag{4.11}$$

where $\mathbf{f}_{f0,i}$ is the fluid drag force on particle i in the absence of other particles, χ is an empirical parameter, ε_i is the local average porosity in the vicinity of particle i, $c_{d0,i}$ is the drag coefficient, $\mathrm{Re}_{p,i}$ is the Reynolds number based on particle diameter, ρ_f is the fluid density, μ_f is the fluid viscosity and $\mathbf{u}_i$ is the fluid velocity of the computational cell in which particle i is located.

4.3 Rolling Friction Model

It is well recognized that rolling against a contacting surface is a common state of motion of solid particles in addition to pure translational or rotational motions. This arises when the translational velocity of a particle is exactly equal but opposite in direction to the tangential velocity due to rotation at the point of contact such as to give rise to a 'no-slip' condition between the two surfaces. In the presence of only sliding frictional effects simulated by the Coulomb friction law, a particle in such a state of motion tends to preserve its kinetic energy for unrealistically long traveling times and distances. As such, a rolling friction model which simulates resistances against rolling motion in terms of a torque which opposes this 'no-slip' rotation of a particle may be essential for an accurate representation of such motions. Zhou *et al.* (1999) found that implementation of such a rolling friction model in DEM is necessary for realistic simulations of particle heap formation with angles of repose comparable with experimental observations. They advocated the following angular velocity-independent rolling friction model due to Beer and Johnson (1976):

$$\mathbf{M}_i = \mu_r \mathbf{f}_{cn,ij} \tag{4.12}$$

where $\mathbf{M}_i$ is the torque which opposes rotation of the particle and is opposite in direction to that of its angular velocity, μ_r is the coefficient of rolling friction. This rolling friction model was similarly incorporated into DEM in this study to ensure realistic simulations of particle motions and dynamics.

4.4 Numerical Integration

The numerical procedure for particle dynamics simulation involves alternating between integration of Newton's second law and the force-displacement model. In order to enhance the numerical stability of the code, the well known Verlet algorithm

(Verlet, 1967) commonly used in Molecular Dynamics simulation was used for time integration of Newton's law and evaluation of particle positions and velocities. The equations involved in this algorithm are given as follows:

$$\mathbf{x}_i(t+\Delta t) = -\mathbf{x}_i(t-\Delta t) + 2\mathbf{x}_i(t) + \frac{\mathbf{F}_i(t)}{m_i}\Delta t^2 \tag{4.14}$$

$$\mathbf{v}_i(t+\Delta t) = \frac{\mathbf{x}_i(t+\Delta t) - \mathbf{x}_i(t-\Delta t)}{2\Delta t} \tag{4.15}$$

where $\mathbf{x}_i$ is the position vector of particle i represented by Cartesian coordinates, $\mathbf{F}_i$ is the total force acting on the particle equal to the sum of all terms on the right hand side of equation (4.1) and Δt is the time step used.

4.5 Computational Fluid Dynamics

The motion of the continuum gas phase is governed by the Navier-Stokes equations with an additional source term in the momentum equation to represent the reaction force acting on the fluid by the particles. For all simulations carried out in this study, the gas phase is assumed to be incompressible.

$$\frac{\partial \varepsilon}{\partial t} + \nabla \cdot (\varepsilon \mathbf{u}) = 0 \tag{4.16}$$

$$\frac{\partial (\rho_f \varepsilon \mathbf{u})}{\partial t} + \nabla \cdot (\rho_f \varepsilon \mathbf{u}\mathbf{u}) = -\varepsilon \nabla P + \nabla \cdot (\mu_f \varepsilon \nabla \mathbf{u}) + \rho_f \varepsilon \mathbf{g} - \mathbf{F} \tag{4.17}$$

where **u** is the velocity vector, ε is the local average porosity, P is the fluid pressure and **F** is the source term due to fluid-particle interaction. No turbulence models are included for solution of the turbulent kinetic energy and dissipation terms as this would involve numerical solution of an extra set of partial differential equations which would increase the computational requirements significantly. The emphasis of the work carried out in this study is on the flow behavior of solid particles and the

resulting flow patterns and regimes formed. The inherent assumption made is that turbulence effects in the fluid phase have minimal influence on solid flow behavior.

In the present study, the numerical solution of the Navier-Stokes equations was carried out using the first order upwind difference scheme for discretizing the convection term, the central difference scheme for the diffusion term and the SIMPLE method (Patankar, 1980) for pressure prediction. The computational domain was divided into uniform 4 mm × 4 mm grid cells and all quantities such as velocities and pressure were assumed constant over each cell. The source term **F** for a particular computational cell was calculated by summing the fluid drag forces on all particles present within that cell:

$$\mathbf{F} = \frac{\sum_{i=1}^{n} \mathbf{f}_{f,i}}{\Delta V} \tag{4.18}$$

where ΔV is the volume of a computational cell and n is the number of particles present in the cell.

4.6 Porosity Calculation

Fluid drag forces are strong functions of porosity values. The local average porosity ε_i in the neighborhood of a particle as applied in equation (4.7) of the Di Felice model is defined as the porosity value within the computational cell in which the particle is residing. This is normally calculated by taking 1.0 minus the ratio of the total volume of all particles found within the computational cell to that of the cell (Mikami *et al.*, 1998). Two approaches are used to calculate the porosity of a computational cell. First, a particle is usually defined to be completely in a computational cell as long as its center is located within the space enclosed by the

boundaries of the cell while errors arising from particles lying only partially within a cell have largely been neglected (Tsuji *et al.*, 1992). Secondly, only the partial volumes of particles which are included in a computational cell are taken into account when the particles are located over the cell boundaries (Xu and Yu, 1997; Kaneko *et al.*, 1999). Obviously the second approach is more accurate and should be used. On the other hand, the first approach is also attractive because it can reduce the computational effort involved. The first approach was employed in the present work. However, it has been modified in order to meet the need for accuracy and efficiency, as described below.

In CFD, the sizes of computational cells have to be small for fine resolution of the fluid flow pattern. On the other hand, as illustrated in Figure 4.1, a small computational cell has the effect of magnifying the abovementioned errors associated with porosity calculation as the proportion of particle volumes which lie outside the cell but which have been assumed to be within the cell is large. To resolve this issue in a computationally efficient manner, a modification to the conventional method of porosity calculation is proposed in this study. The size of computational cells used is kept minimal but larger than the characteristic size of a single particle, in accord with the idea of local averaging for all fluid properties. However, the local average porosity in the vicinity of a particle ε_i is calculated from the ratio of volumes of all particles located within the computational cell under consideration as well as those located in the immediate neighboring eight cells (Figure 4.1) to the total volume of these nine cells (equation 4.19). This allows the use of small computational cells to ensure accurate CFD calculations without compromising the accuracies of porosity estimations at the same time.

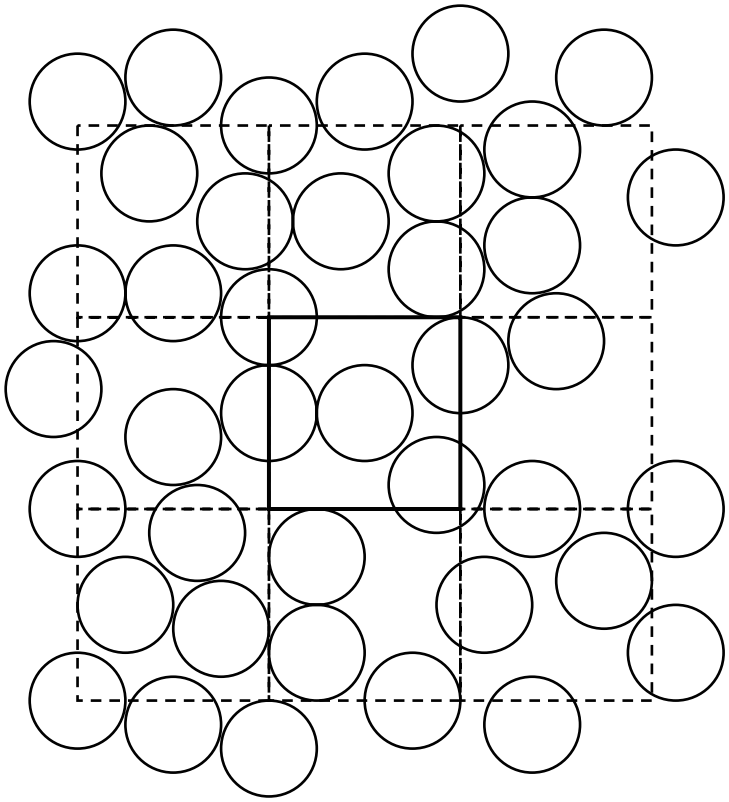

Figure 4.1 Computational cells used in the calculation of local porosity. The surrounding eight cells are included in the calculation of the porosity value for the central cell.

$$\varepsilon = 1 - \frac{\sum_{i=1}^{k} V_i}{9\Delta V} \tag{4.19}$$

where k is the total number of particles in nine computational cells for a two-dimensional system and V_i is the volume of particle i. In both equations (4.18) and (4.19), the volume of a computational cell ΔV is calculated based on a pseudo-three-dimensional geometry assumption whereby the 'thickness' of the computational domain in the spanwise direction is assumed to be equal to the particle diameter used.

4.7 Attrition Model

The Ghadiri's attrition model accounts for two different mechanisms of attrition, namely chipping and fragmentation with the former occurring at impact velocities between 4 m s^{-1} and 13 m s^{-1} and the latter above 13 m s^{-1}. It is assumed in this model that daughter particles produced by attrition of mother particles are spherical. The respective equations for calculating particle sizes produced by the two mechanisms are (Han *et al.*, 2003):

$$d_s = \left(\alpha_f \frac{\rho_s H v_s^2 d_{so}^4}{K_c^2} \right)^{\frac{1}{3}} \tag{4.20}$$

$$(3 - \zeta') \ln\left(\frac{d_s}{d_{so}} \right) = \ln \lambda' + \zeta' \ln\left(\frac{\rho_s H v_s^2 d_{so}}{K_c^2} \right) \tag{4.21}$$

where α_f is a proportionality factor, d_s is the diameter of the smaller part of a particle after impact, d_{so} is the diameter of the mother particle before impact, H is the material hardness, v_s is the particle impact velocity, λ' and ζ' are parameters that are determined experimentally and K_c is the critical stress intensity factor. The various empirical parameters found in the model determine the sizes of particle fragments upon attrition while the occurrence of the attrition process itself depends only on the

impact velocity. In the absence of experimental values for these parameters, arbitrary but reasonable values have been selected to simplify the equations to the following form (Han *et al.*, 2003):

$$d_s = \left(2\times10^{-4}\rho_s v_s^2 d_{so}^4\right)^{\frac{1}{3}} \tag{4.22}$$

$$2\ln\left(\frac{d_s}{d_{so}}\right) = \ln\left(2\times10^{-4}\rho_s v_s^2 d_{so}\right) \tag{4.23}$$

4.8 Experimental Setup of Liquid Fluidization System

The fluidized bed apparatus used in this study consisted of four major components: a vertical cylindrical column, rotameters, centrifugal pump and liquid tank. The experimental setup is shown schematically in Figure 4.2. The cylindrical column was a glass tube of 2 cm diameter and 1 m height. The bed was fluidized by water at ambient condition. During experiments, the bed was clamped in position to maintain it vertical and straight. A centrifugal pump was used to circulate the water from the liquid tank through rotameters to the bed in a closed loop.

The bed suspension was supported by a specially designed piston, which consisted of a 2 mm thick sintered stainless steel plate with 50 μm orifice holes. These small orifice holes ensured a large pressure drop and uniform distribution of flow (Ham *et al.*, 1990). The piston could be set to oscillate vertically at a given frequency and amplitude driven by a stepper motor. Such a piston-distributor setup would allow examination of the response of the bed towards external perturbations. The amplitude of the piston was carefully chosen as 1.5 times the particle diameter to avoid close packing in the near distributor region (Duru *et al.*, 2002).

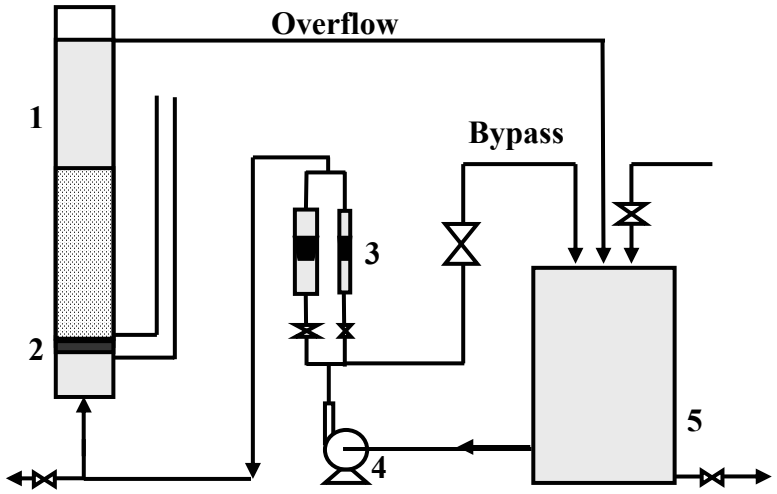

Figure 4.2 Schematic diagram of the liquid fluidized bed setup: 1. Vertical cylindrical bed; 2. Piston-like distributor; 3. Rotameters; 4. Centrifugal pump; 5. Liquid tank.

The ratio of bed to particle diameters should be greater than 10, but not exceed 25 to ensure smooth propagation of one-dimensional voidage wave structures along the bed (Ham *et al.*, 1990; Duru *et al.*, 2002). In the present study, the granular material used was glass beads of density 2500 kg m^{-3} and diameter 1 mm ($u_{mf} \approx 0.01$ m s^{-1}). The corresponding bed to particle diameter ratio was then 20. The column was filled with glass beads up to a height of 12 cm and fluidized by water at flow velocities in the range 0.018 – 0.030 m s^{-1}. External harmonic perturbations were introduced into the bed by oscillating the piston-distributor with an amplitude of 1.5 mm and frequencies in the range 1 – 2 Hz. Typically, four regimes could be observed during experiments: packed, worming, planar wave and turbulent regimes. The scope of the present study was limited to the planar wave regime.

Solid concentrations were determined using a light scattering method at various bed levels. The basic principle of this technique is that under column backlighting conditions, the light intensity transmitted through the bed suspension varies strongly as a function of solid concentration. Here, a stabilized He-Ne laser (25 mW) was used as the light source and a low-energy photodiode (Newport, USA) was used to detect the transmitted intensity signals.

The velocity field data of the bed was obtained using a PowerView Particle Image Velocimetry (PIV) system from TSI Company (Figure 4.3). The column was placed inside a square glass tube of dimensions 2.7 cm × 2.7 cm to facilitate more accurate measurements using the PIV system. NewWave Nd:Yag lasers operating at ~15 mJ/pulse were introduced from the side wall of the square tube to illuminate particles near the central region of the column. Images of the illuminated particles

were acquired by a TSI PowerView camera (2K × 2K resolution) at an angle perpendicular to the laser sheet. The PIV sampling frequency did not match the vibrating frequency of the moving piston. To overcome this problem, the PIV system was operated under external trigger mode with a sampling frequency of 5 Hz. The motions of particles in one full oscillation cycle of the base could then be extracted from the images captured.

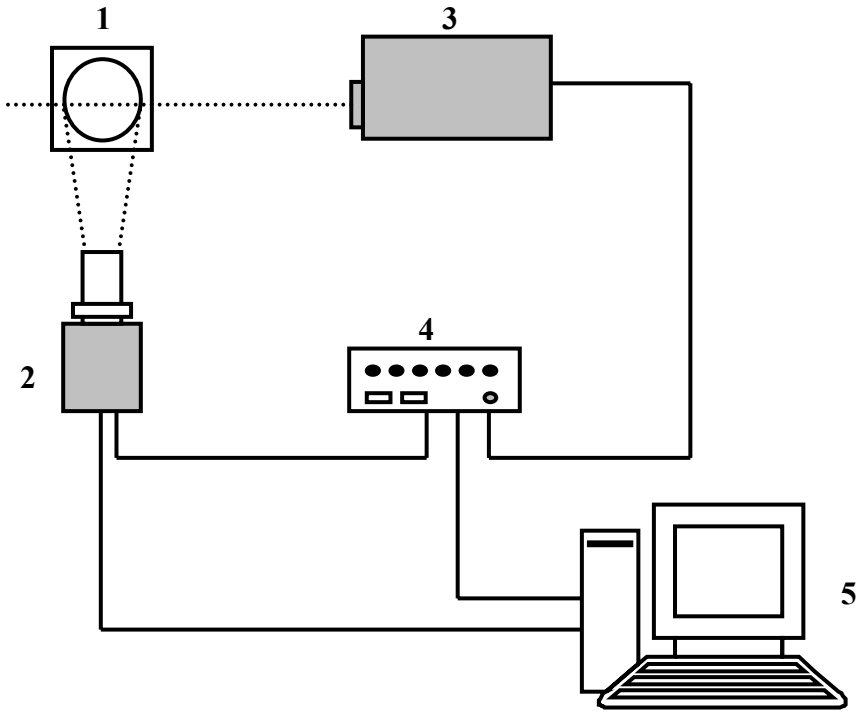

Figure 4.3 Schematic diagram of velocity data acquisition system (PIV system): 1. Test section; 2. PIV camera; 3. New Wave Nd:Yag laser; 4. TSI synchronizer; 5. Computer for data post-processing.

CHAPTER 5 RESULTS AND DISCUSSION

5.1 Vertical Pneumatic Conveying

The combined CFD-DEM model described in the previous chapter was first used for the numerical simulation of pneumatic conveying of granular material in a vertical pipe. From the simulation outputs obtained, two distinct types of flow regimes could be identified. Figure 5.1 shows the case where the solid concentration was 0.08 and the gas velocity was 14 m s^{-1}. Particles are seen to be distributed throughout the entire length of the pipe. This kind of flow pattern, known generally as dispersed flow, persisted for the 10 s of physical time simulated during which particles cycled through the pipe numerous times. In contrast, Figure 5.2 shows the case where α = 0.16 at the same gas velocity. There seems to be a tendency for particles to cluster together and be re-dispersed again into a homogeneous suspension intermittently. This indicates that the operating conditions applied may correspond to an unstable flow regime which oscillates between that of dispersed flow and plug flow continuously. When α was increased further to 0.24 and 0.32, the clusters of particles formed during the transportation process remained stable throughout the entire simulation time. Figures 5.3 and 5.4 show that particles in these cases move in the form of a single large plug along the conveying pipe. Generally, it is known from previous experimental work reported in the literature that the dispersed flow regime is usually dominant at high gas velocities and low solid concentrations while the plug flow regime is observed otherwise. At a gas velocity of 24 m s^{-1}, the simulation outputs for α = 0.08 and 0.16 presented in Figures 5.5 and 5.6 respectively show that both cases exhibit dispersed flow while those using α = 0.24 and 0.32 exhibited plug

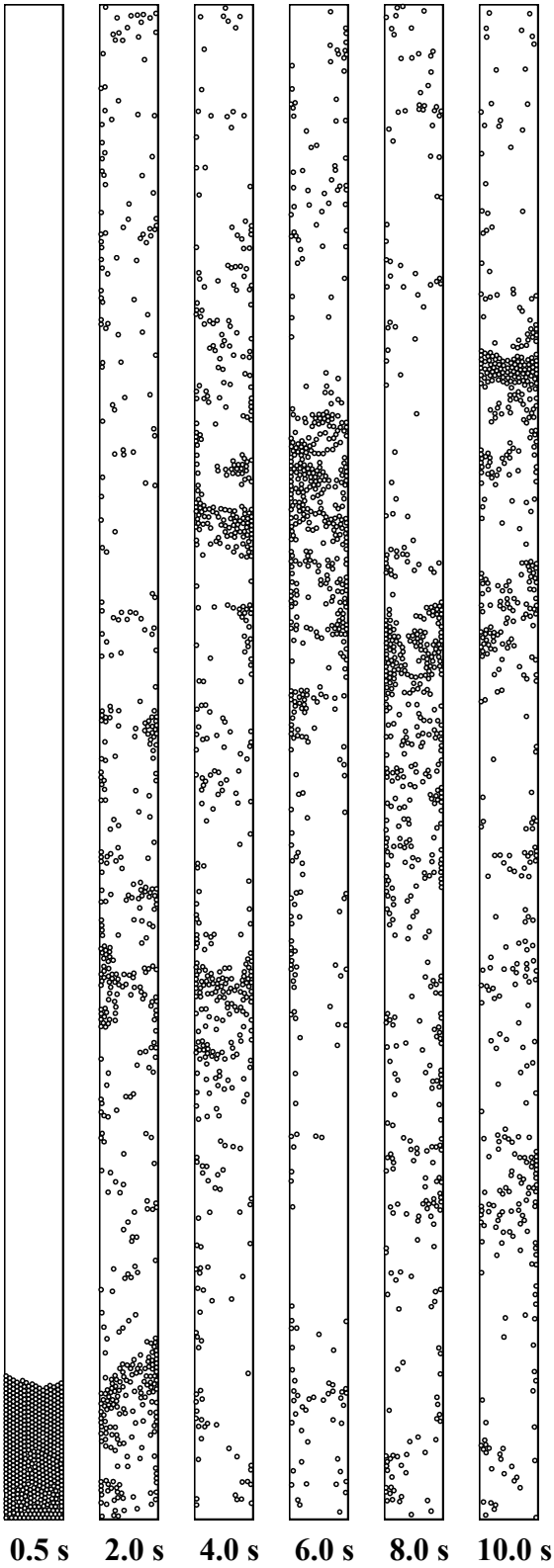

Figure 5.1 Vertical pneumatic conveying in the dispersed flow regime with $\alpha = 0.08$ (500 particles) and gas velocity 14 m s^{-1}

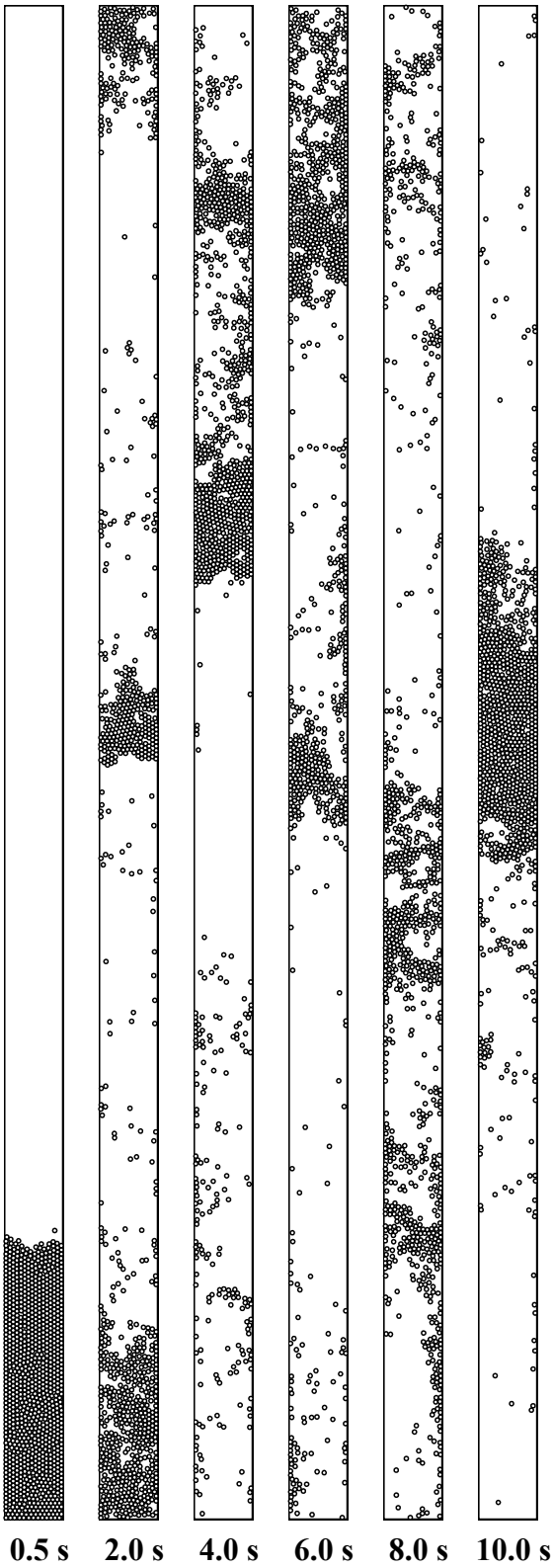

Figure 5.2 Vertical pneumatic conveying showing transition between the dispersed and plug flow regimes with α = 0.16 (1000 particles) and gas velocity 14 m s^{-1}

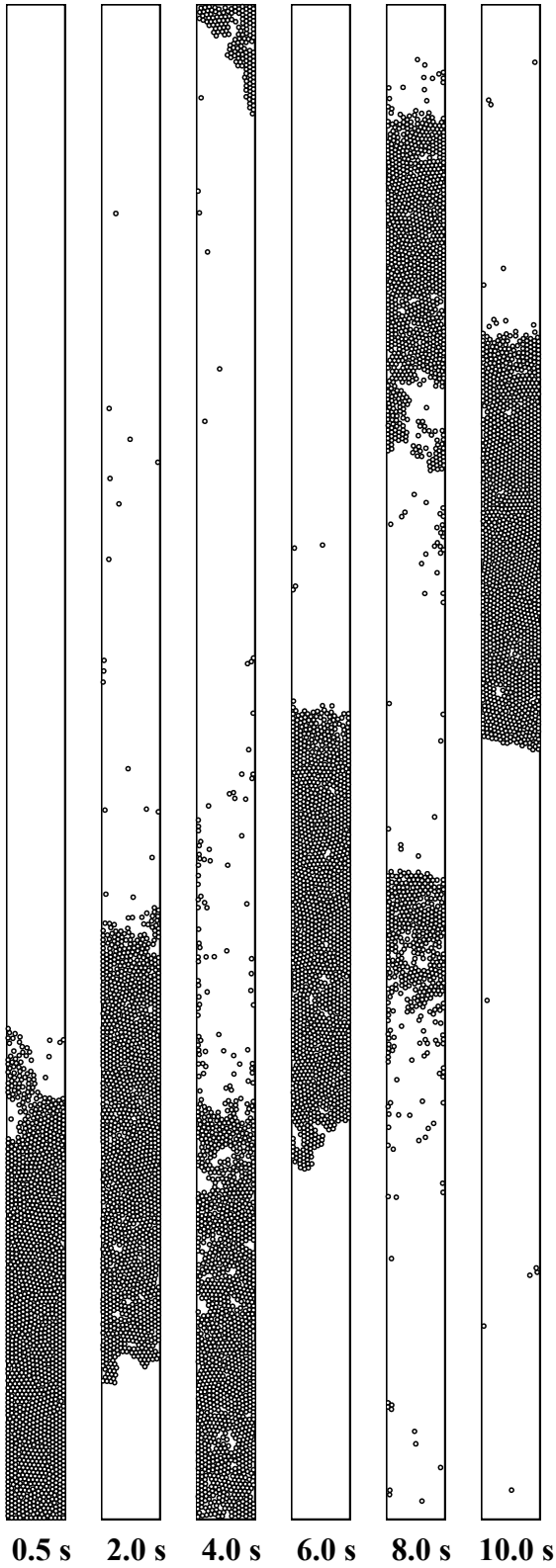

Figure 5.3 Vertical pneumatic conveying in the plug flow regime with $\alpha = 0.24$ (1500 particles) and gas velocity 14 m s^{-1}

Figure 5.4 Vertical pneumatic conveying in the plug flow regime with $\alpha = 0.32$ (2000 particles) and gas velocity 14 m s^{-1}

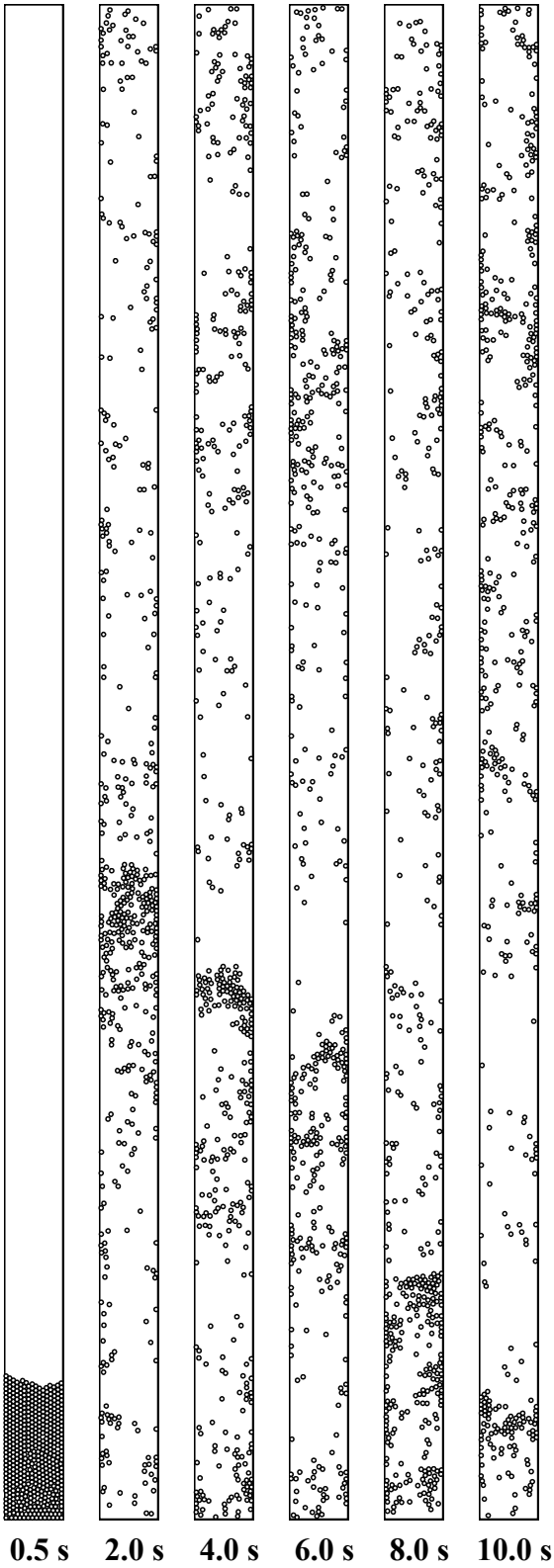

Figure 5.5 Vertical pneumatic conveying in the dispersed flow regime with $\alpha = 0.08$ (500 particles) and gas velocity 24 m s^{-1}

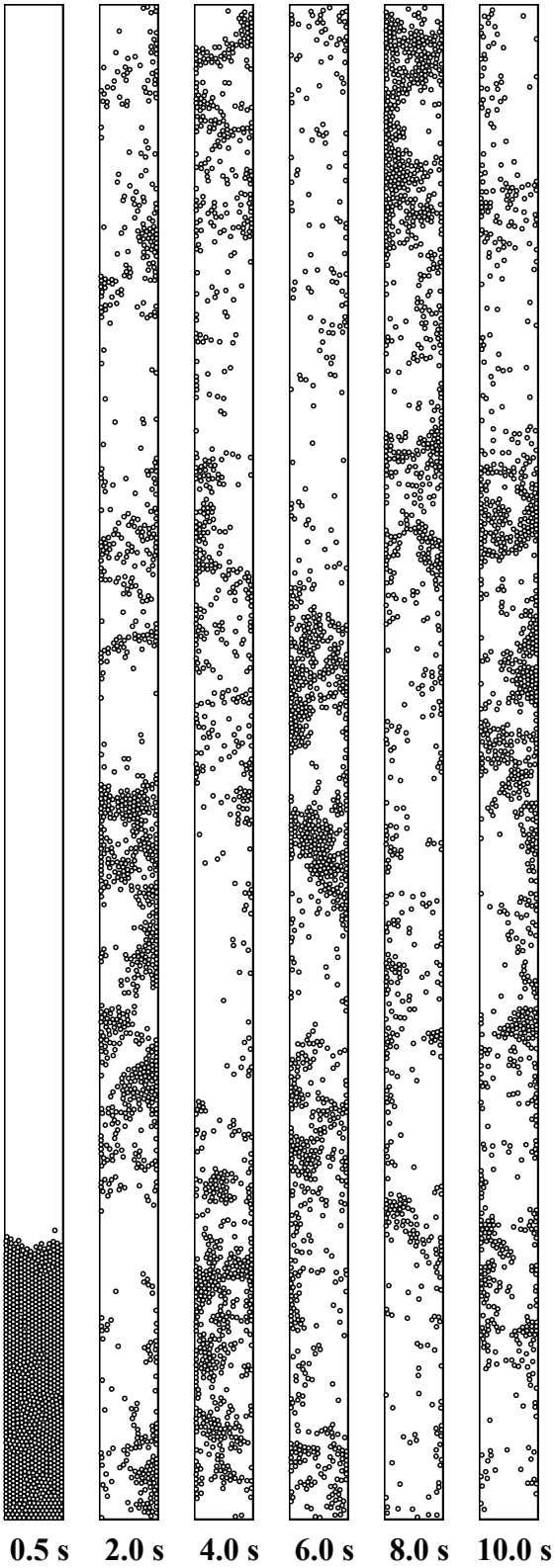

Figure 5.6 Vertical pneumatic conveying in the dispersed flow regime with $\alpha = 0.16$ (1000 particles) and gas velocity 24 m s^{-1}

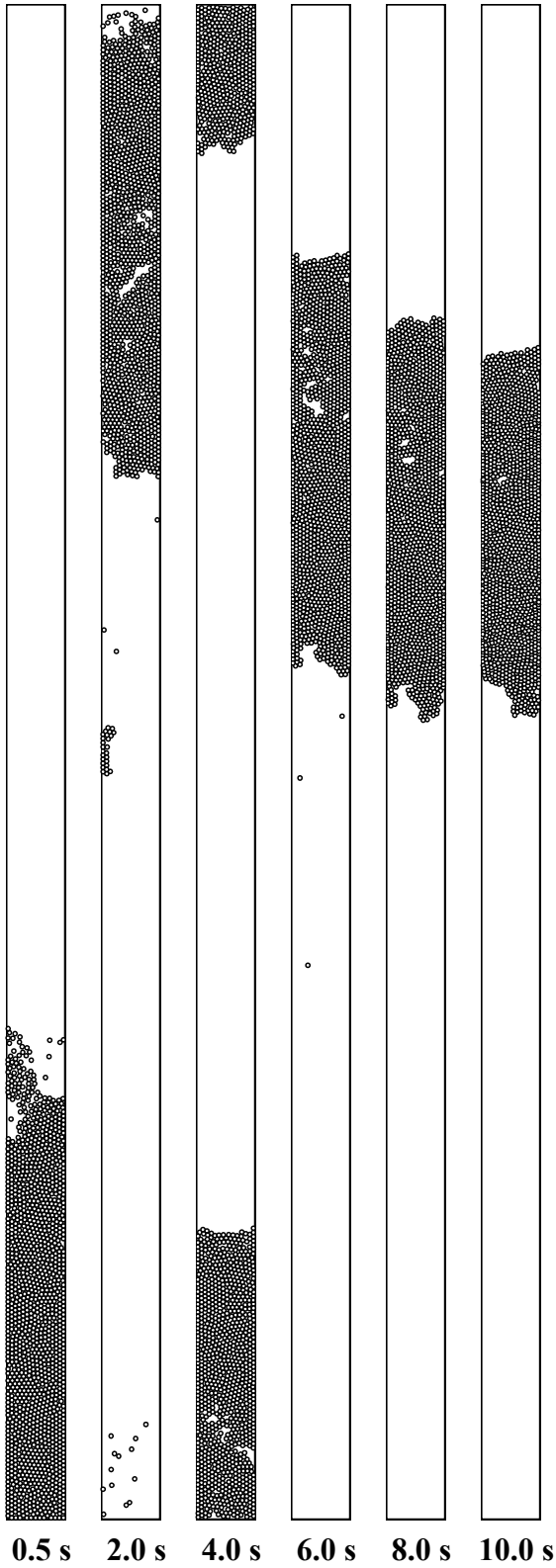

Figure 5.7 Vertical pneumatic conveying in the plug flow regime with $\alpha = 0.24$ (1500 particles) and gas velocity 24 m s^{-1}

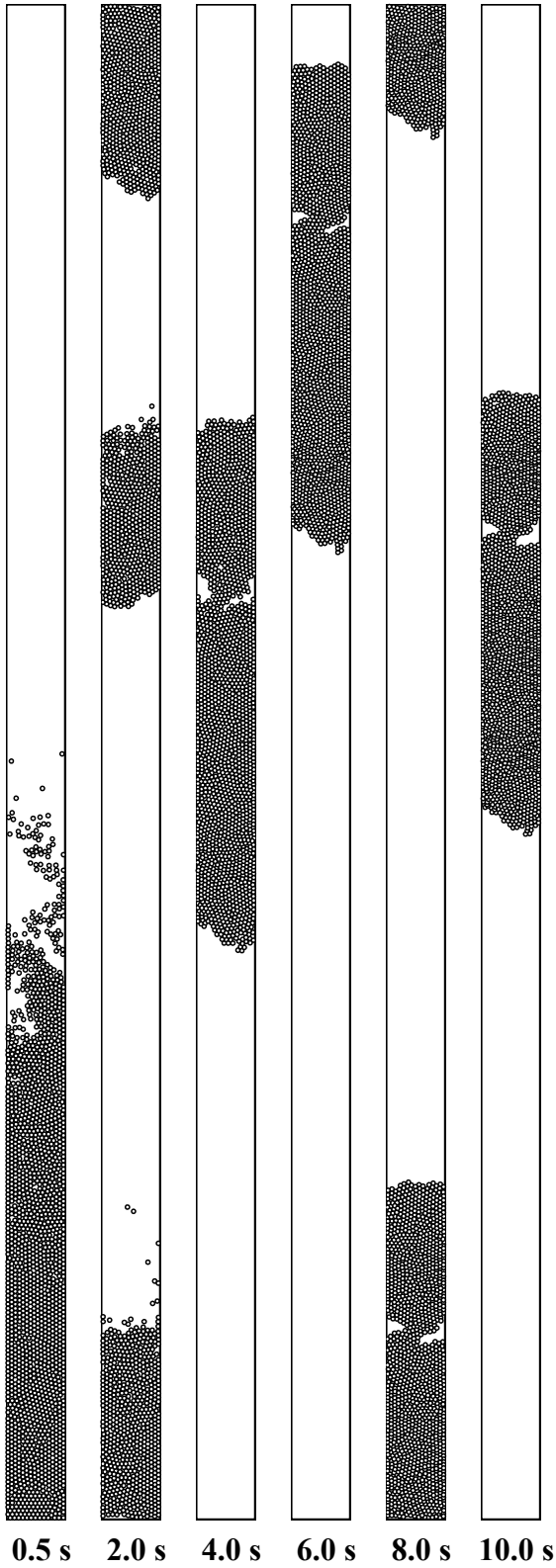

Figure 5.8 Vertical pneumatic conveying in the plug flow regime with $\alpha = 0.32$ (2000 particles) and gas velocity 24 m s^{-1}

flow (Figures 5.7 and 5.8). The simulations with α = 0.08 representing vertical pneumatic conveying at a relatively low solid concentration verified the general experimental observation that the dominant flow regime encountered under such conditions was dispersed flow even at the lowest gas velocity of 14 m s^{-1} considered. The case with α = 0.16 has shown a transition from an unstable plug flow regime to a dispersed flow regime when the gas velocity was increased from 14 m s^{-1} to 24 m s^{-1}. On the other hand, at high solid concentrations of 0.24 and 0.32 represented by the use of 1500 and 2000 particles respectively in the simulation, the plug flow regime remained dominant even up to the gas velocity of 24 m s^{-1}. These general observations and trends with respect to the types of flow regimes observed under different operating conditions and their transitions agree well with the experimental observations of Zhu *et al.* (2003). This is also the first successful direct simulation of these two important flow regimes frequently observed in pneumatic conveying in vertical pipes and the procedure used involved varying the gas velocity and solid concentration only, much like what would be done in a physical experiment. Other flow regimes which have been observed experimentally, such as the moving annular capsules described by Zhu *et al.* (2003) and ring or half-ring flow regimes observed by Yao *et al.* (2004) may have arisen due to the effects of electrostatics and the present study may be a good starting point for further explorations into such effects in pneumatic conveying systems.

The solid concentration profiles for both flow regimes were obtained by dividing the space in the conveying pipe into long strips parallel to the length of the pipe and calculating the solid concentration within each strip. It was observed that this spatially averaged solid concentration profile became invariant with time after a

sufficiently long simulation time, indicating the attainment of a fully developed flow state. The time required also corresponded to that required for the solid flow rate to reach a steady value. This latter point would be elaborated in a later section. Figures 5.9 and 5.10 show the solid concentration profile for the dispersed ($\alpha = 0.08$) and plug ($\alpha = 0.32$) flow regimes at various gas velocities respectively. It may be observed that, contrary to the name of the regime and the qualitative observations which can be made from the instantaneous snapshots of the simulation, the solid concentration profile for dispersed flow shows a symmetrical but non-uniform distribution with higher solid concentrations near the walls and a minimum near the center of the pipe. This may be due to the effects of inelastic collisions with the walls which leave particles lying in the vicinity of the walls. On the other hand, the solid concentration profile for the plug flow regime is uniform and flat across the section of the pipe. This is due to the fact that particles in such a regime are closely packed together into a single large plug which moves much like a rigid body along the conveying pipe. For each of these regimes studied, the solid concentration profiles do not seem to be significantly affected by the actual velocity of the gas used.

5.2 Horizontal Pneumatic Conveying

The simulation outputs for horizontal pneumatic conveying showed a few other types of flow patterns in addition to those observed in vertical pneumatic conveying. These arise mainly due to gravitational effects which cause particles to settle towards the bottom wall of the conveying pipe. At a low solid concentration of 0.08 represented by 500 particles and conveying gas velocity of 10 m s^{-1}, the flow pattern observed in Figure 5.11 resembles that of dispersed flow in vertical pneumatic

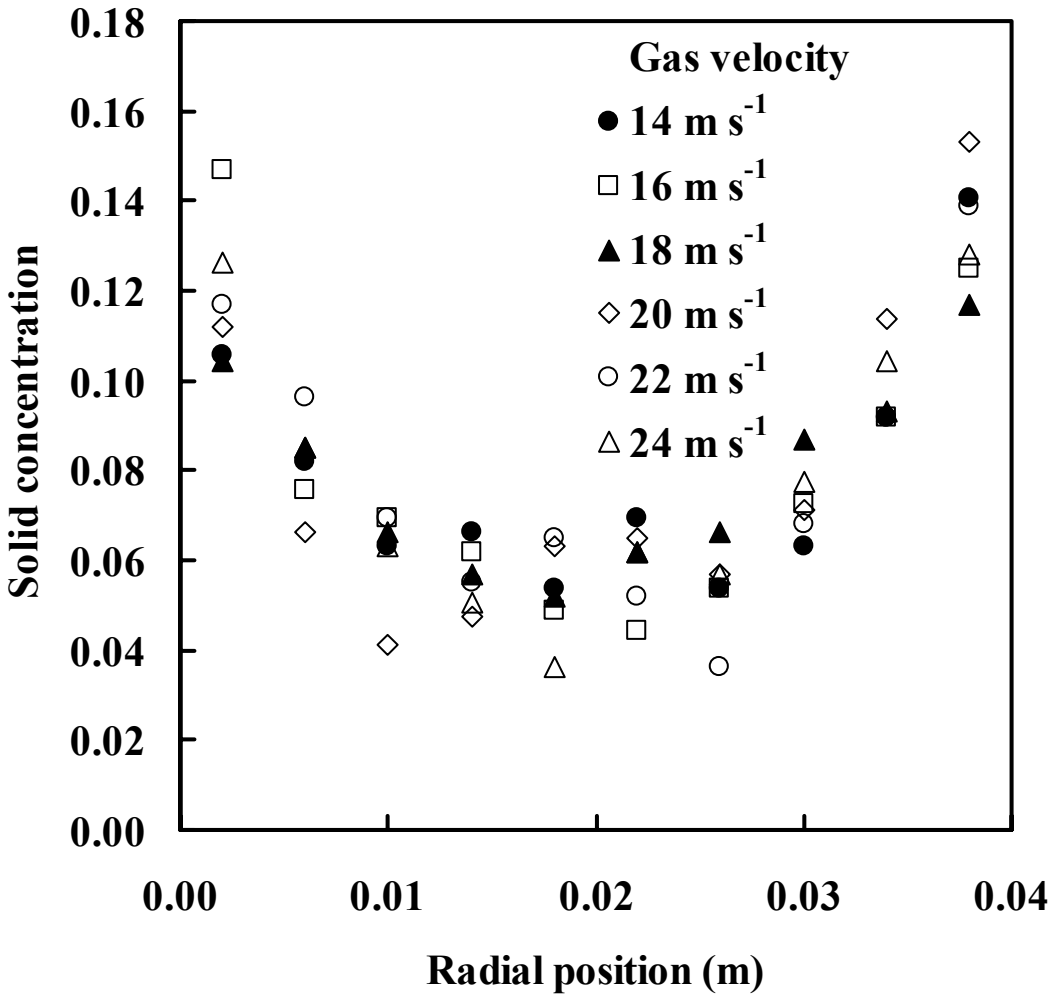

Figure 5.9 Solid concentration profile for the dispersed flow regime in vertical pneumatic conveying (α = 0.08) at various gas velocities showing symmetry and minimum near the pipe center

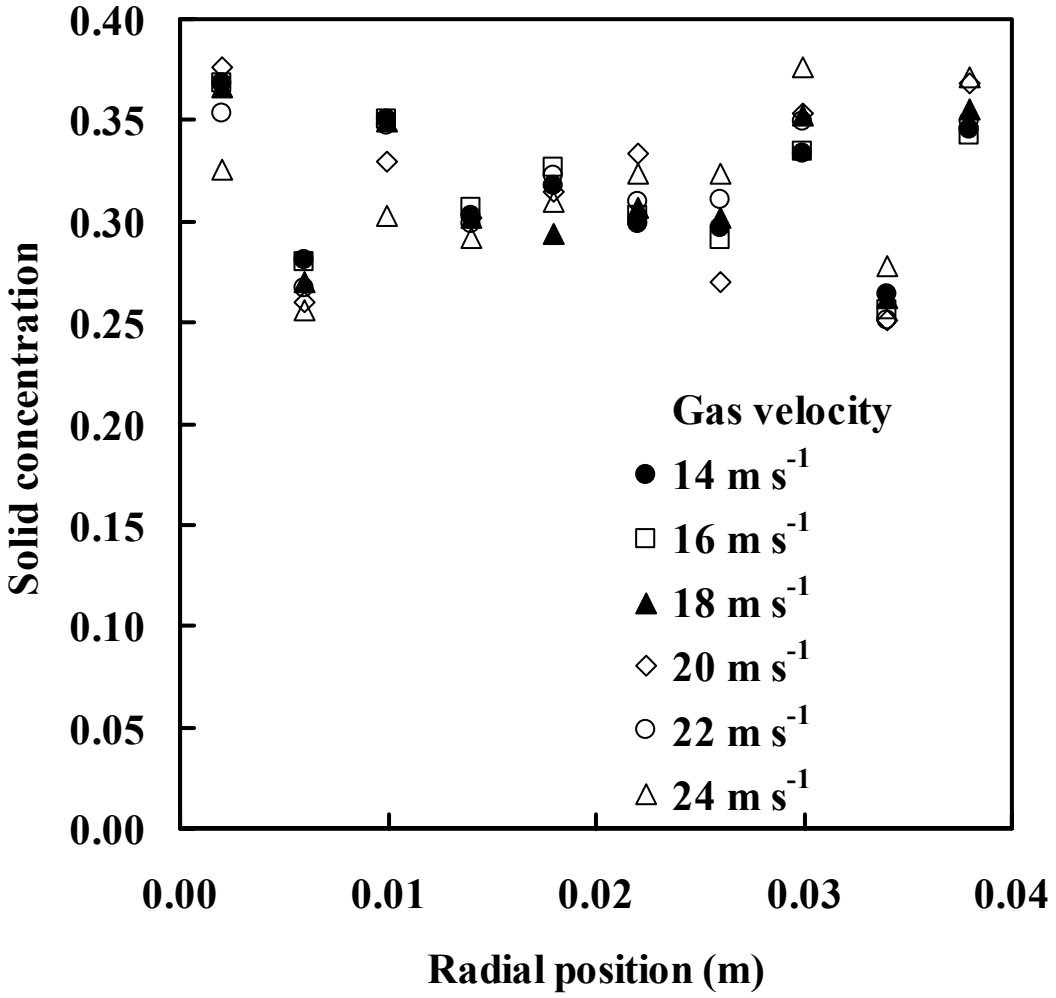

Figure 5.10 Solid concentration profile for the plug flow regime in vertical pneumatic conveying (α = 0.32) at various gas velocities showing a flat distribution

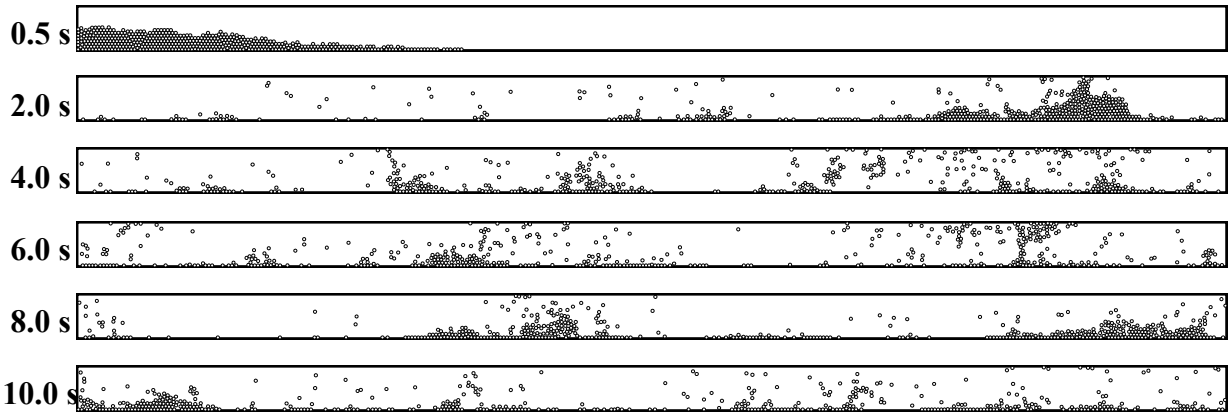

Figure 5.11 Horizontal pneumatic conveying in the stratified flow regime with $\alpha = 0.08$ (500 particles) and gas velocity 10 m s^{-1}

conveying but due to the effects of gravitational settling as mentioned, a thin layer of particles is formed along the lower pipe wall. There exists a gradient in the concentration of particles in the vertical direction with higher concentration of particles near the lower pipe wall and vice versa. This flow regime was also observed under similar operating conditions experimentally and is known as the stratified flow regime (Rao *et al.*, 2001). With α = 0.16, it can be seen in Figure 5.12 that the previously observed thin settled layer of particles has become larger clusters which move along the lower wall by traction. The individual clusters do not seem to have a tendency to combine together nor be dispersed into suspension but remain quite stable throughout the entire simulation time. A large portion of the particles is still transported in suspension above these moving clusters. Following the experimental work of Rao *et al.* (2001), this is referred to as the moving dunes flow regime. In contrast, at the highest solid concentrations of 0.24 and 0.32 considered in the present simulation using 1500 and 2000 particles respectively, particles tend to be transported in the form of a single large cluster reminiscent of plug flow in vertical pneumatic conveying (Figures 5.13 and 5.14). This may be a result of clustering of multiple adjacent moving dunes to form a stable large plug which spans the entire cross-section of the conveying pipe. This kind of flow pattern was similarly observed in physical experiments done at high solid concentrations and low gas velocities and was called the slug flow regime. When the gas velocity was increased to 30 m s^{-1} in the present simulation, it can be seen in Figures 5.15 and 5.16 that the original stratified and moving dunes flow regimes observed with α = 0.08 and 0.16 respectively have transformed into a homogeneous flow pattern. Most of the particles are now transported in suspension along the pipe and seem to be distributed throughout the

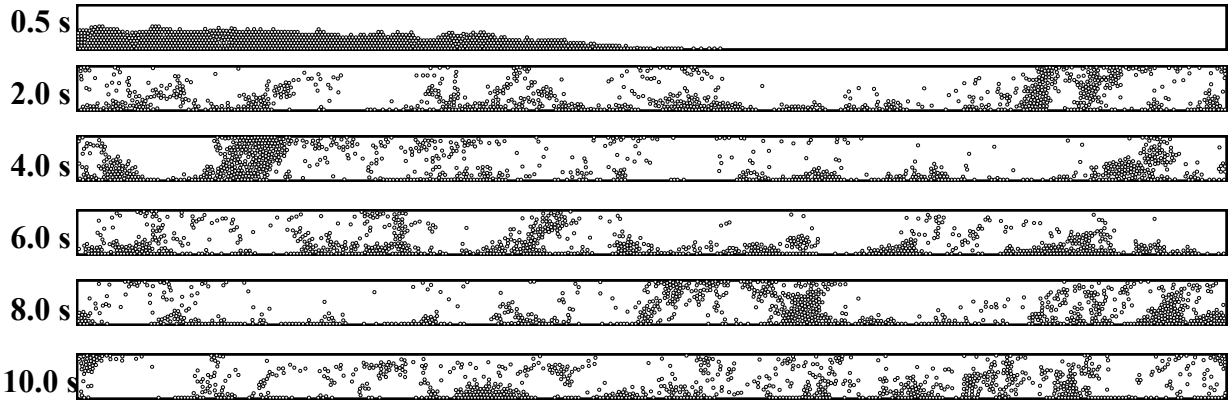

Figure 5.12 Horizontal pneumatic conveying in the moving dune flow regime with $\alpha = 0.16$ (1000 particles) and gas velocity 10 m s^{-1}

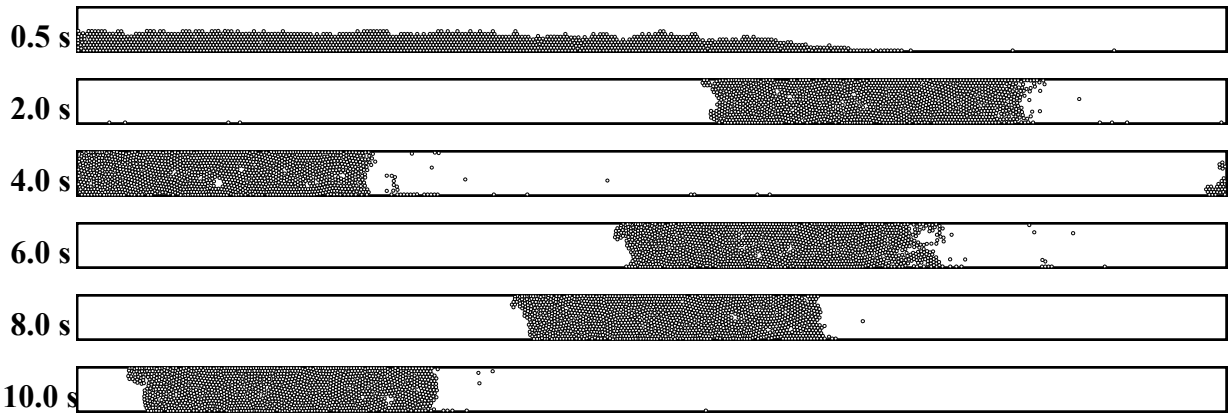

Figure 5.13 Horizontal pneumatic conveying in the slug flow regime with $\alpha = 0.24$ (1500 particles) and gas velocity 10 m s^{-1}

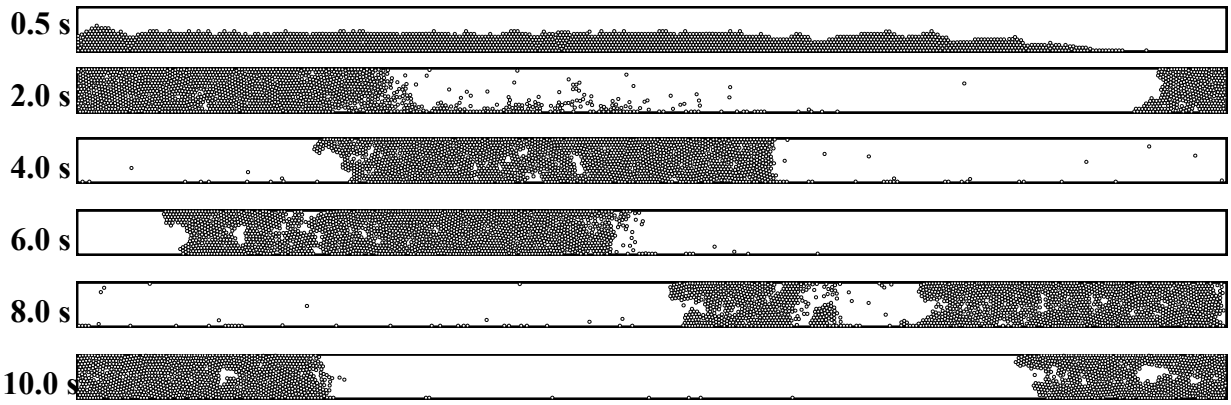

Figure 5.14 Horizontal pneumatic conveying in the slug flow regime with $\alpha = 0.32$ (2000 particles) and gas velocity 10 m s^{-1}

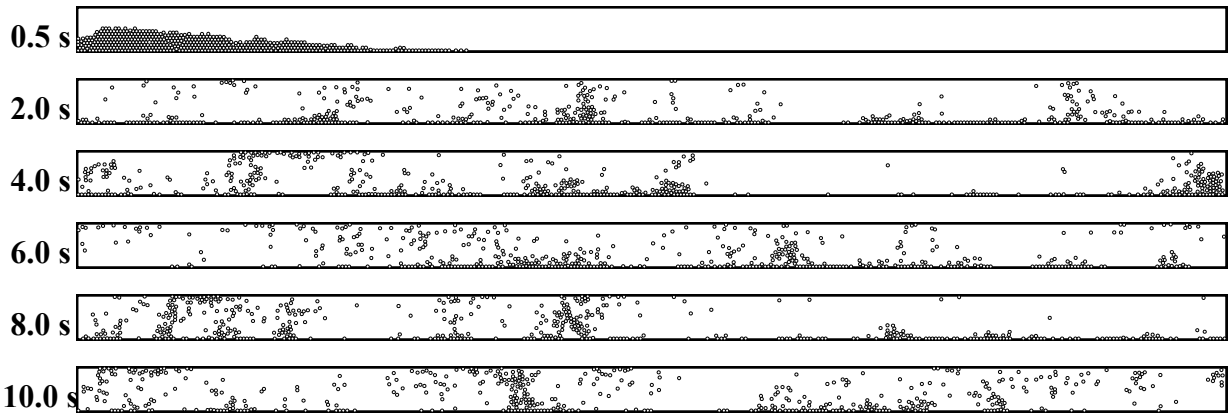

Figure 5.15 Horizontal pneumatic conveying in the homogeneous flow regime with $\alpha = 0.08$ (500 particles) and gas velocity 30 m s^{-1}

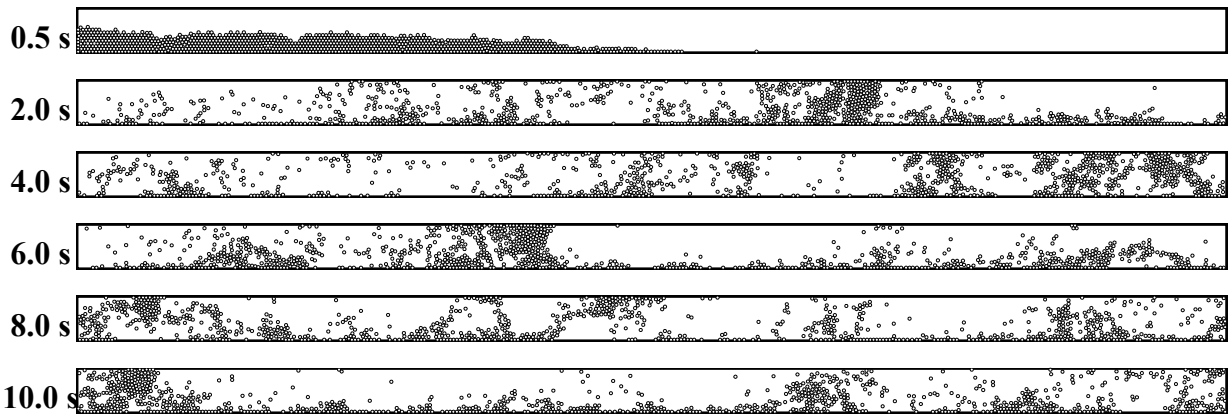

Figure 5.16 Horizontal pneumatic conveying in the homogeneous flow regime with $\alpha = 0.16$ (1000 particles) and gas velocity 30 m s^{-1}

entire length of the conveying line. The relative effect of gravitational settling is lower due to the higher conveying velocity resulting in minimal non-homogeneity in particle distribution. However, cases where α = 0.24 and 0.32 showed that the slug flow regime remained as the dominant regime at these high solid concentrations up to the gas velocity of 30 m s^{-1}. As with the vertical pneumatic conveying simulations, these different flow regimes do not seem to have been reproduced computationally previously. Tsuji *et al.* (1992) simulated a type of slug flow in a horizontal pipe which they referred to as plug flow. However, other types of flow regimes and in particular the moving dunes, have only been observed in physical experiments so far. It may not even be possible in principle to reproduce this type of flow pattern computationally using two-fluid continuum models.

The solid concentration profiles for two representative regimes in horizontal pneumatic conveying, stratified flow (α = 0.08) and slug flow (α = 0.32), were similarly computed for a quantitative comparison of the effects of gravitational settling mentioned earlier on the resulting solid distribution. Figure 5.17 shows quantitatively that the solid concentration is higher near the bottom wall of the horizontal pipe when particles are conveyed in the stratified flow regime, corresponding to the qualitative observations made from the simulation snapshots seen previously. By comparison with the solid concentration profile for dispersed flow in vertical pneumatic conveying, the effect of gravitational settling has caused the profile to change from a symmetrical distribution to an unsymmetrical one. In contrast, the solid concentration profile for slug flow (Figure 5.18) is seen to be very similar to that for plug flow in vertical pneumatic conveying. This fits well with the

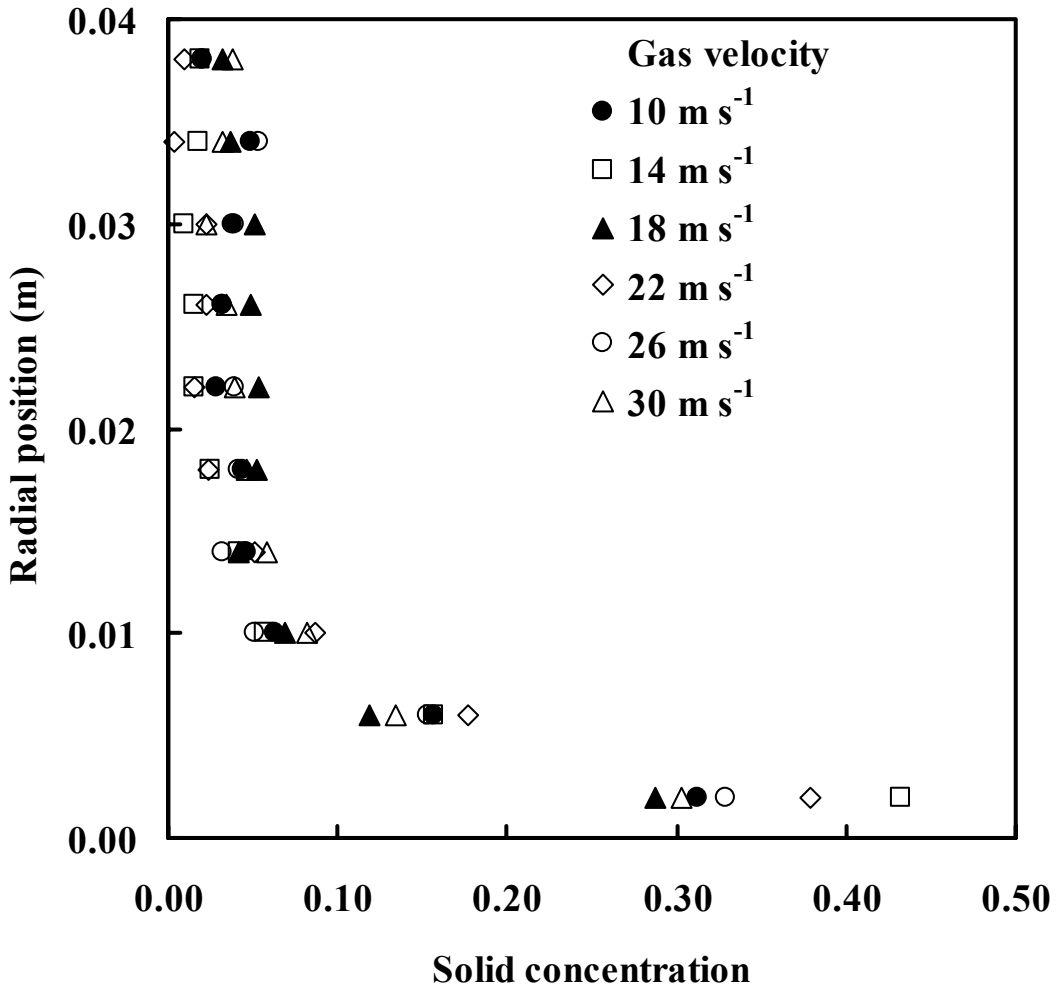

Figure 5.17 Solid concentration profile for the stratified flow regime in horizontal pneumatic conveying (α = 0.08) at various gas velocities showing non-symmetry and higher solid concentration near the bottom wall

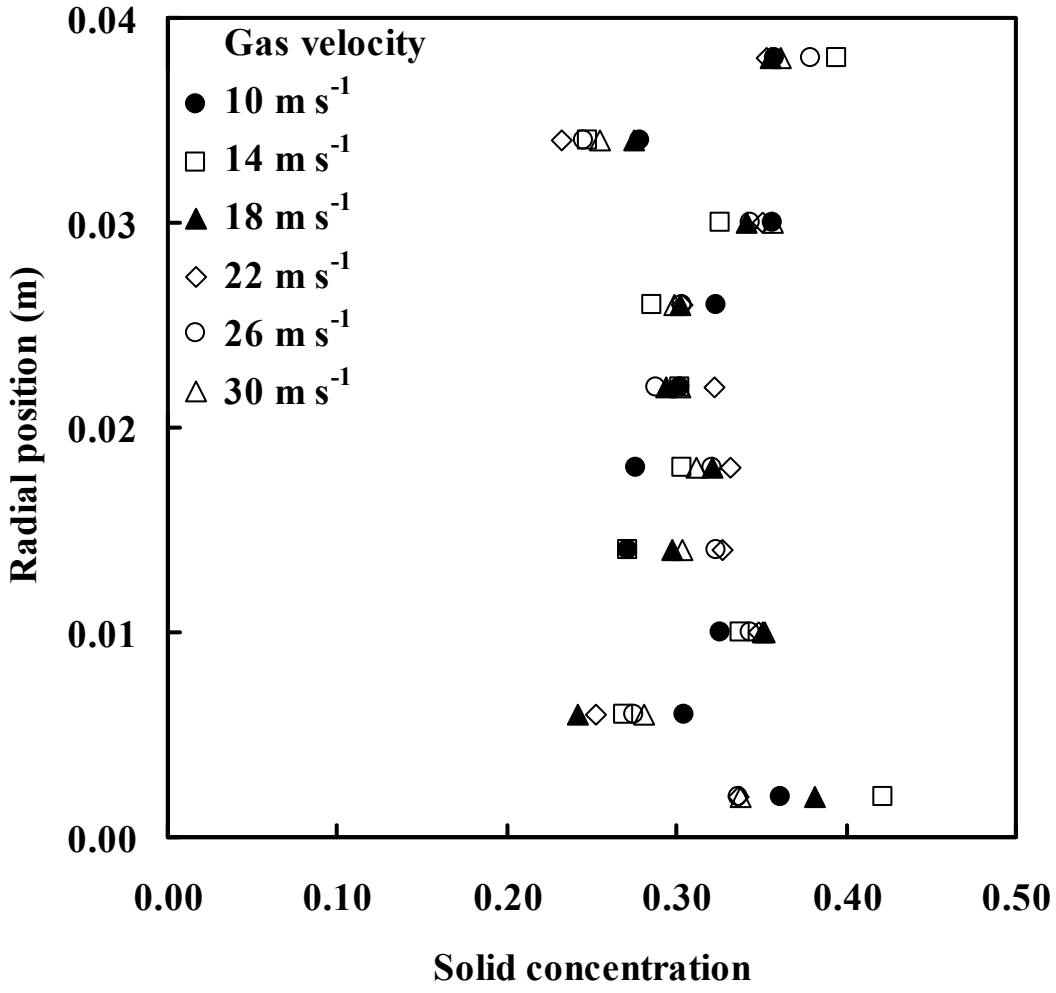

Figure 5.18 Solid concentration profile for the slug flow regime in horizontal pneumatic conveying (α = 0.32) at various gas velocities showing a flat distribution (Order of coordinates is different from Figure 5.9 to aid in visualization)

fact that particles are carried in the form of a single large plug in both cases. When this occurs in a horizontal pipe, the effect of gravity does not alter the solid concentration profile to any significant extent. As with the previous cases for vertical pneumatic conveying, the solid concentration profiles for each type of flow regime at different gas velocities are similar for the range of velocities investigated.

5.3 Phase Diagrams

The different flow regimes in vertical and horizontal pneumatic conveying arising from the use of different operating conditions can be represented in the form of phase diagrams as shown in Figures 5.19 and 5.20 respectively. Dashed lines in the figures separate approximately the regions representing different flow regimes while dashed circles enclose regions where transition between two adjacent flow regimes might be taking place. In vertical pneumatic conveying, the dispersed flow regime is dominant at high gas velocities and low solid concentrations while the plug flow regime is dominant otherwise (Figure 5.19). This is also generally true for horizontal pneumatic conveying except at low gas velocities and solid concentrations where the effects of gravitational settling of particles result in the formation of the moving dunes and stratified flow regimes (Figure 5.20). Intermediate values of gas velocities where transitions between the moving dunes and homogeneous flow regimes (MD/H) and between the stratified and homogeneous flow regimes (S/H) are similarly approximated by regions enclosed within the dashed circles in Figure 5.20.

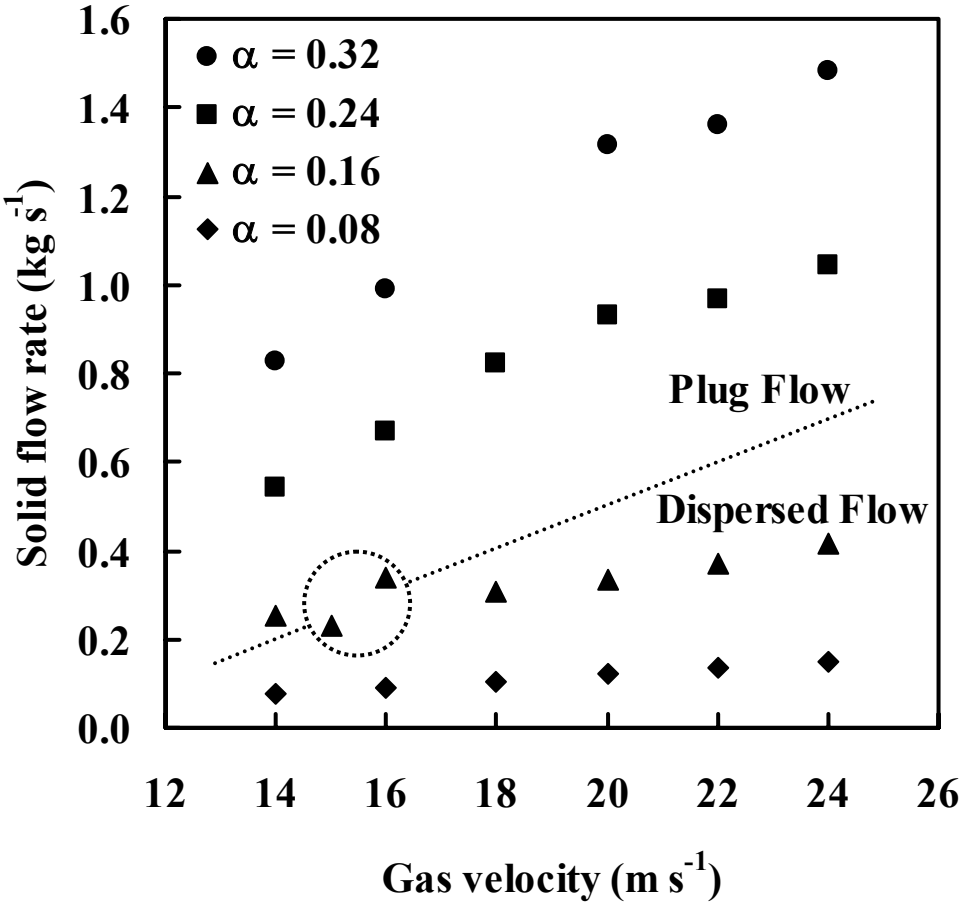

Figure 5.19 Phase diagram for vertical pneumatic conveying. Dashed lines separate approximately regions representing different flow regimes while dashed circles enclose regions where transition between two adjacent flow regimes might be taking place. The dispersed flow regime is dominant at high gas velocities and low solid concentrations while the plug flow regime is dominant otherwise.

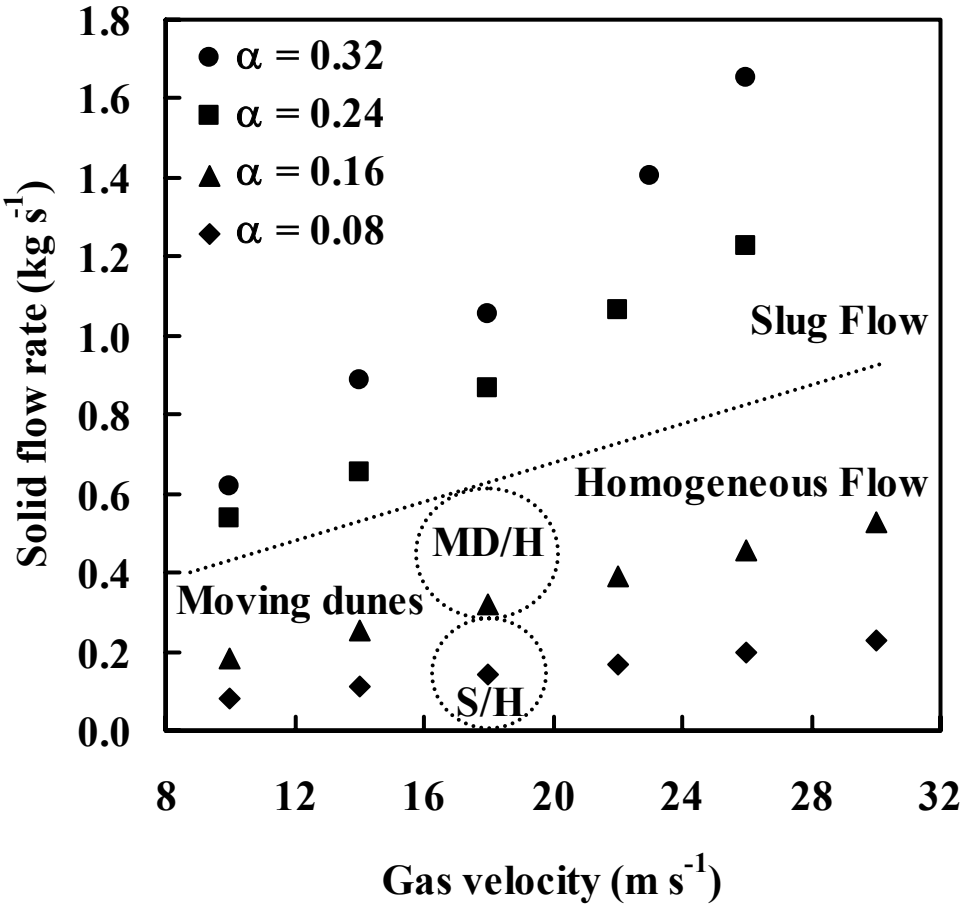

Figure 5.20 Phase diagram for horizontal pneumatic conveying. Homogeneous flow is dominant at high gas velocities and low solid concentrations. The effects of gravitational settling result in the formation of the moving dunes and stratified flow regimes at low gas velocities and solid concentrations. MD/H and S/H denote transitions between moving dunes and homogeneous flow and between stratified and homogeneous flow respectively.

5.4 Solid Flow Rate

Figures 5.21 and 5.22 show respectively the transient development of the solid flow rates in vertical and horizontal pneumatic conveying at various gas velocities and for the case of $\alpha = 0.16$. The flow rates increase sharply from an initial value of zero at time 0.5 s when gas flow is initiated and reach a steady value after about 3 s of physical time. Flow rate profiles at other solid concentrations are similar to those presented and are not shown for the sake of brevity. As mentioned in an earlier section, the attainment of a time invariant solid concentration profile corresponded with that of a steady state defined by a constant solid flow rate. In view of this point and in consideration of the high computational demands of the present study (each simulation case shown earlier requires between 1 and 3 weeks of computer time on a Linux cluster with Pentium Xeon 3.06 GHz processors), it was deemed justifiable to simulate for a relatively short physical time of 10 s in each case before quantitative characterization of each flow regime was carried out.

As may be seen from Figure 5.21 for vertical pneumatic conveying, the case where the gas velocity was equal to 15 m s^{-1} resulted in a lower solid flow rate than that at 14 m s^{-1}. This was attributed previously to an unstable flow regime occurring near the transition between dispersed and plug flow. The apparent hysteresis in the solid flow rate was investigated further by tracking the variation of solid flow rate with respect to time as the gas velocity was increased (or decreased) from an initially low value of 14 m s^{-1} (or correspondingly high value of 18 m s^{-1}) to a high value of 18 m s^{-1} (or low value of 14 m s^{-1}) past the point where transition was expected to occur.

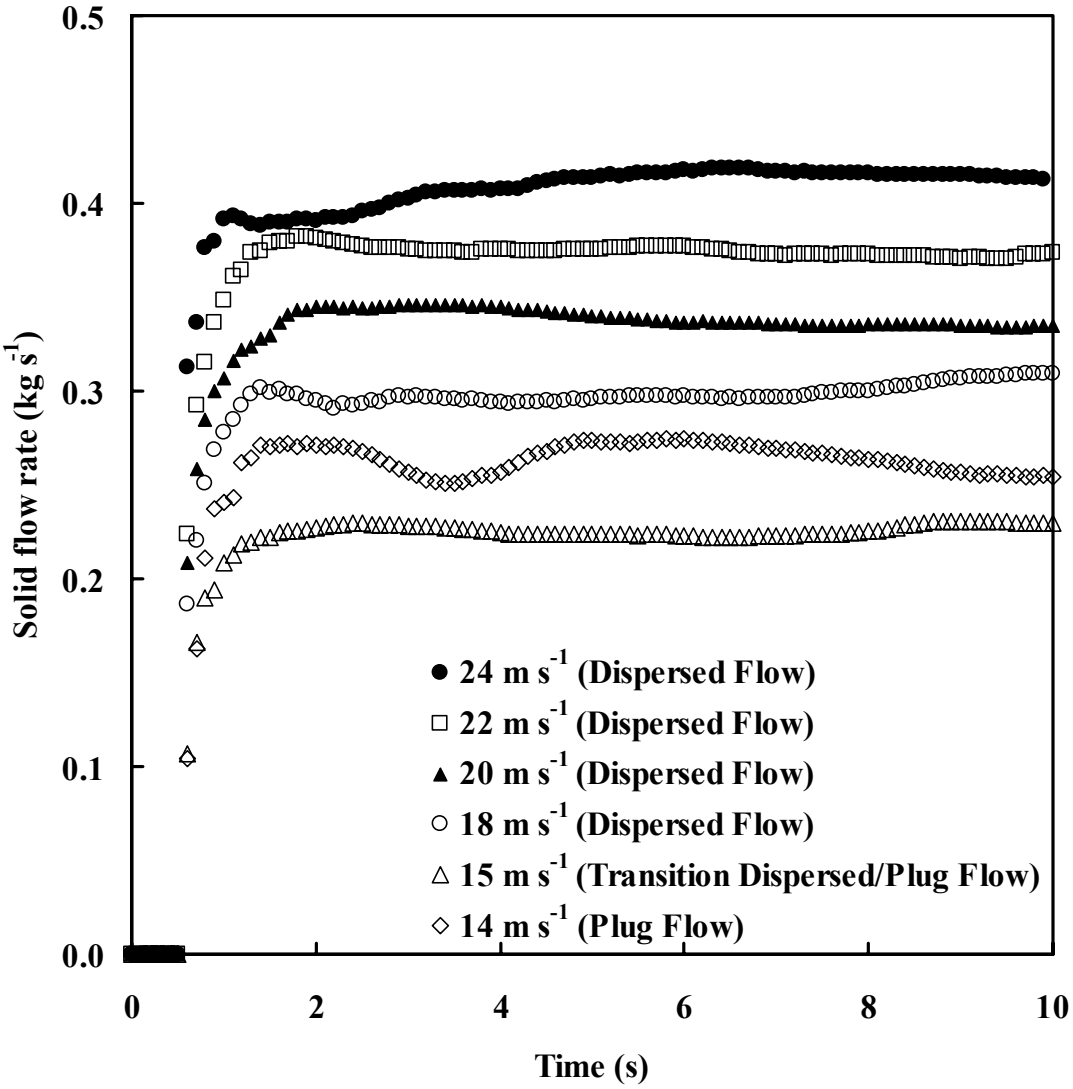

Figure 5.21 Transient development of solid flow rates at various gas velocities in vertical pneumatic conveying. Steady state is reached after about 3 s of physical time. Each simulation is performed for 10 s before quantitative characterization of each flow regime is carried out.

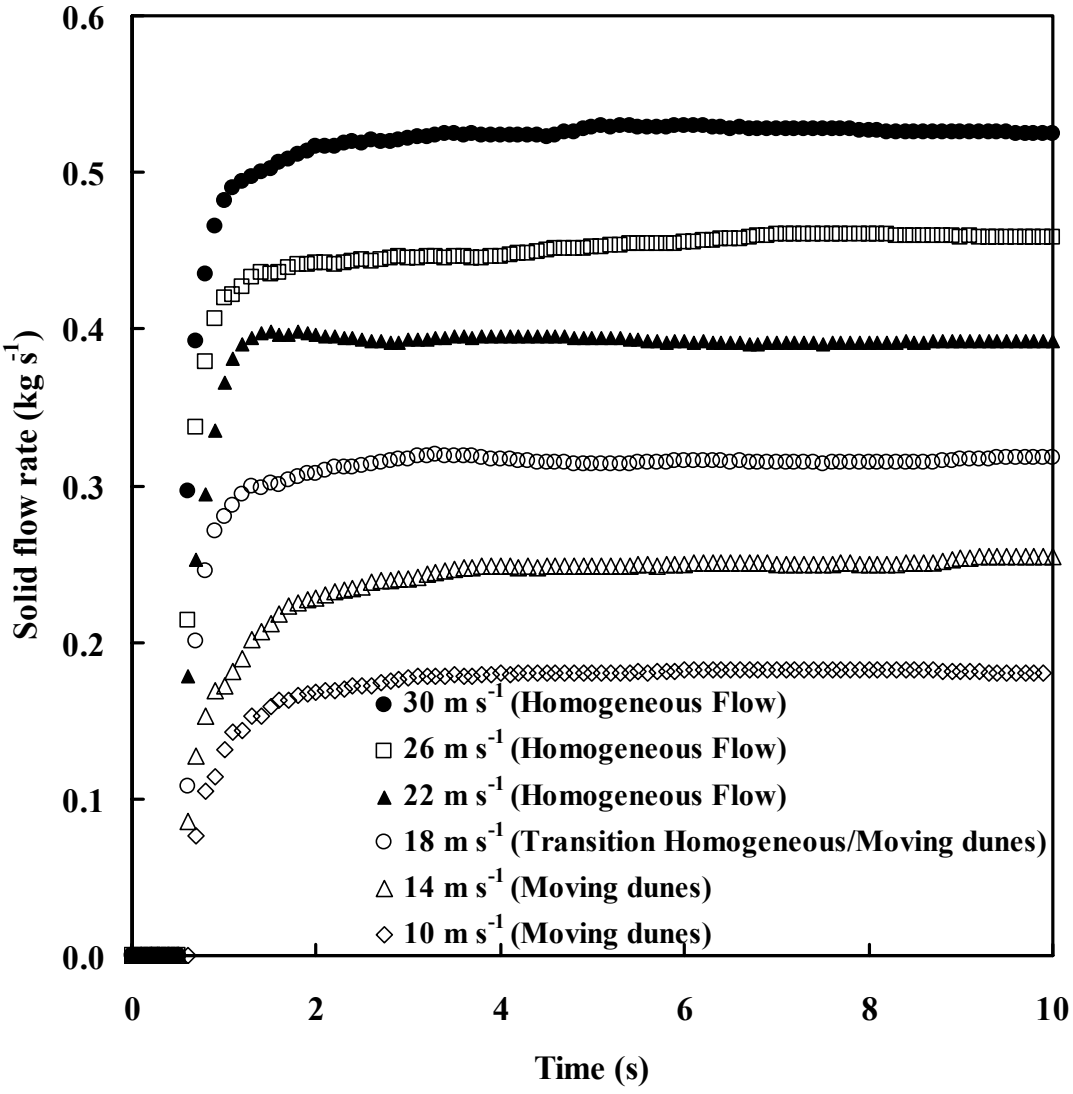

Figure 5.22 Transient development of solid flow rates at various gas velocities in horizontal pneumatic conveying. Steady state is reached after about 3 s of physical time. Each simulation is performed for 10 s before quantitative characterization of each flow regime is carried out.

The system was first allowed to reach a steady state with the initial gas velocity used in the usual manner before changes in gas velocity were implemented in the form of step increases (or decreases) of magnitude 0.5 m s^{-1} at one second intervals. Figure 5.23 shows that the time variations of solid flow rates for the two cases described exhibit hysteresis. The start (and end) point of one graph does not correspond to the end (and start) point of the other in terms of solid flow rate values obtained. As such, in the range of gas velocity values where hysteresis occurs, there might be more than one solid flow rate value which the system can undertake and this may be the reason for the previously observed anomalous values in the phase diagram of Figure 5.19 and steady state solid flow rates in Figure 5.21. In general, transitions between flow regimes in pneumatic conveying systems seem to be complex processes which are path dependent and sensitive to the specific operating conditions used.

5.5 Sensitivity Analyses

The parameters deemed to be important in any typical discrete element simulation include the spring constant, viscous contact damping coefficient and coefficient of friction used in the force-displacement model. The spring constant determines the stiffness of the spring used in modeling interparticle or particle-wall collisions and so is an indication of the hardness of the colliding entities. On the other hand, the viscous contact damping coefficient determines the amount of energy lost during a collision in analogy with the way energy is damped in a dashpot and so affects the elasticity of collisions. Finally, the coefficient of friction is a representation of surface roughness for both particles and pipe walls. Although these parameters are related to physical and material properties of the particles and pipe walls for the

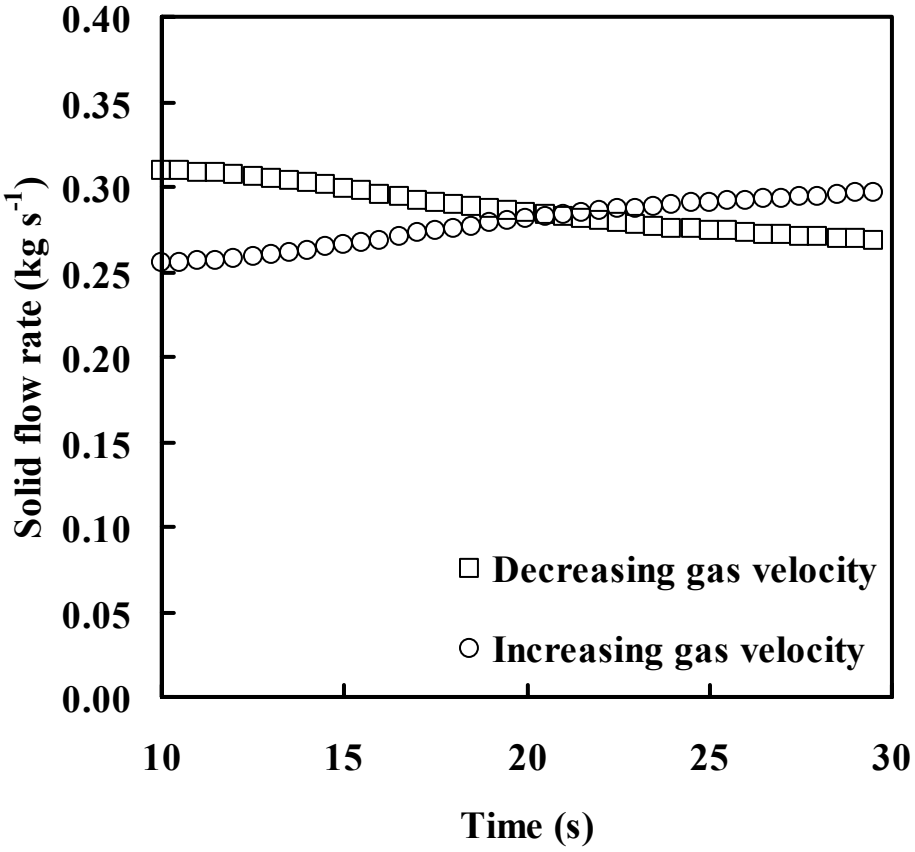

Figure 5.23 Time variation of solid flow rate in vertical pneumatic conveying for varying gas velocities. Hysteresis occurs in the range of gas velocity values where transition between two flow regimes may be taking place.

specific system considered here, their values are not readily available in the literature. As such, the investigation of the influence of these parameters on the qualitative features of flow patterns obtained was deemed an important component of this study and this was carried out through simple sensitivity analyses during the initial phase of this work. It was found that the simulation results obtained in terms of the solid flow pattern at different gas velocities were insensitive to the three parameters in the range of values $10^3 – 10^4$ N m^{-1} for the spring constant, 0.20 – 0.35 for the viscous contact damping coefficient (equivalently 0.3 – 0.1 for the coefficient of restitution) and 0.2 – 0.8 for the coefficient of friction. The narrow range of the coefficient of restitution considered here was necessary to preserve the type of flow regime observed. The solid flow pattern may be altered when the value of the coefficient of restitution is set to be outside this range. Otherwise, the flow regime observed was independent of this particular material property of the solid particles. Thus, the specific parameter values selected for subsequent detailed simulation studies as presented in Table 3.1 previously were assumed to have negligible effects on the formation of the various flow regimes described earlier and these would have been the results of complex gas-solid interactions reproduced realistically with the combined CFD-DEM model developed in this study.

The quantitative influences of the coefficient of friction and viscous contact damping coefficient were investigated by comparing the steady state solid flow rates obtained at different values of these parameters. The system geometry and operating conditions which were kept constant throughout this analysis included the vertical pipe configuration, gas velocity of 14 m s^{-1} and overall solid concentration $\alpha = 0.16$ (1000 particles). Table 5.1 shows that the coefficient of friction has a marginal

influence on the steady state solid flow rate. As the surface roughness of the particles and walls increases, the solid flow rate achieved decreases monotonically but only marginally. As mentioned earlier, the flow regimes were qualitatively similar in the range of values shown. In contrast, Table 5.2 shows that the coefficient of restitution does not seem to have a direct effect on the solid flow rate within the range of values investigated. When the coefficient of restitution was increased from 0.1 to 0.2, 0.3 and 1.0, the solid flow rate does not vary monotonically but instead decreased from 0.255 to 0.211 and 0.208 and then increased to 0.226 respectively. The flow patterns obtained are also insensitive to this parameter in the range 0.1 – 0.3. An example of a flow pattern obtained with a parameter value outside this range is shown in Figure 5.24. Other conditions such as gas velocity of 14 m s^{-1} and $\alpha = 0.16$ (1000 particles) were kept identical to those used for simulating the plug flow regime shown in Figure 5.2. Figures 5.24a and b show qualitatively the flow patterns observed at the end of a 10 s simulation when the values for the coefficient of restitution used were 0.1 (corresponding to the last snapshot of Figure 5.2) and 1.0 respectively. It may be seen that particles form small clusters throughout the pipe but not a single large plug in the latter case. As such, the plug flow regime may not exist at high values of coefficient of restitution and a low value such as that used throughout the present study is necessary to reproduce computationally both the dispersed and plug flow regimes observed in vertical pneumatic conveying.

Table 5.1 Effect of coefficient of friction on solid flow rate

Coefficient of friction	Solid flow rate (kg s^{-1})
0.3	0.255
0.4	0.238
0.5	0.237
0.6	0.237
0.8	0.225

Table 5.2 Effect of coefficient of restitution on solid flow rate

Coefficient of restitution	Solid flow rate (kg s^{-1})
0.1	0.255
0.2	0.211
0.3	0.208
1.0	0.226

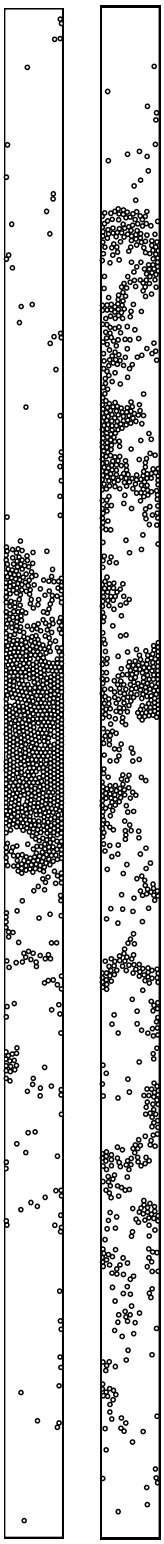

Figure 5.24 Comparisons of flow patterns obtained in vertical pneumatic conveying (gas velocity 14 m s^{-1}, α = 0.16) for values of coefficient of restitution equal to (a) 0.1 and (b) 1.0. Particles in the latter case do not show a tendency to cluster into a single large plug.

5.6 Electrostatic Effects

As discussed in Chapter 3 of this thesis, it has been reported in previous experimental studies that various types of solid flow patterns can arise in pneumatic conveying systems (Rao *et al.*, 2001; Zhu *et al.*, 2003). The presence of electrostatic effects may also give rise to additional anomalous flow patterns (Wang *et al.*, 2000; Yao *et al.*, 2004). Such flow patterns have not been reproduced using numerical simulations to date. In a recent study, Yao *et al.* (2005) proposed the concept of electrostatic equilibrium for pneumatic conveying systems which refers to the state where the amount of charge accumulated on solid particles and pipe walls achieves a steady value after a sufficiently long period of operation. Based on the above seemingly disparate information published by the various research workers, the following conceptual idea was formulated with a view towards integrating the individual ideas into one larger concept. During pneumatic conveying, solid particles which are originally uncharged undergo a transient stage of electrification, the duration of which may be relatively short compared with subsequent operation times. Once a state of electrostatic equilibrium is reached, electrostatic forces between fully charged particles and pipe walls act to establish various anomalous solid flow patterns which remain stable over long periods of time. The objective of this study was thus to investigate the influences of different extents of electrostatic effects on flow pattern formation and flow behaviors in pneumatic conveying through inclined and vertical pipes under the conditions of electrostatic equilibrium. This has not been attempted before in the literature so far.

5.6.1 Flow Patterns

The combined CFD-DEM model described in the previous section was first used for the numerical simulation of pneumatic conveying of granular material through an inclined pipe when no electrostatic forces were present. Figure 5.25a shows that under such normal operating conditions, solid particles are transported as a cluster which slides along the bottom wall of the conveying pipe. Following the convention used in the previous sections, this type of flow pattern is referred to as the moving dunes regime. It may also be observed from the scale for the axial velocities of the particles that most particles are moving in the direction of the air flow. However, when the value of the parameter Λ representing the ratio of electrostatic to gravitational force was increased to 0.5 in the simulation, a small amount of reversed flow behavior could be observed in particles moving along the bottom wall (Figure 5.25b). The axial velocities of particles in the main dune are smaller compared with those achieved in the absence of electrostatic forces while particles in smaller dunes are seen to flow in the opposite direction down the inclined pipe. As a result, the main dune picks up particles in front as it slides forward and loses particles at its tail due to backflow. This type of flow pattern was observed previously in experiments conducted by Zhu *et al.* (2003) and was called the eroding dunes regime. The present study is the first report of the successful reproduction of this type of flow regime through numerical simulations. As Λ is increased further to 1.0 and 2.0 while maintaining the gas inlet velocity constant at 3 m s^{-1}, it may be seen from Figures 5.25c and d respectively that practically all particles within the conveying pipe now exhibit reversed flow behavior. Based on this observation, the following mechanism

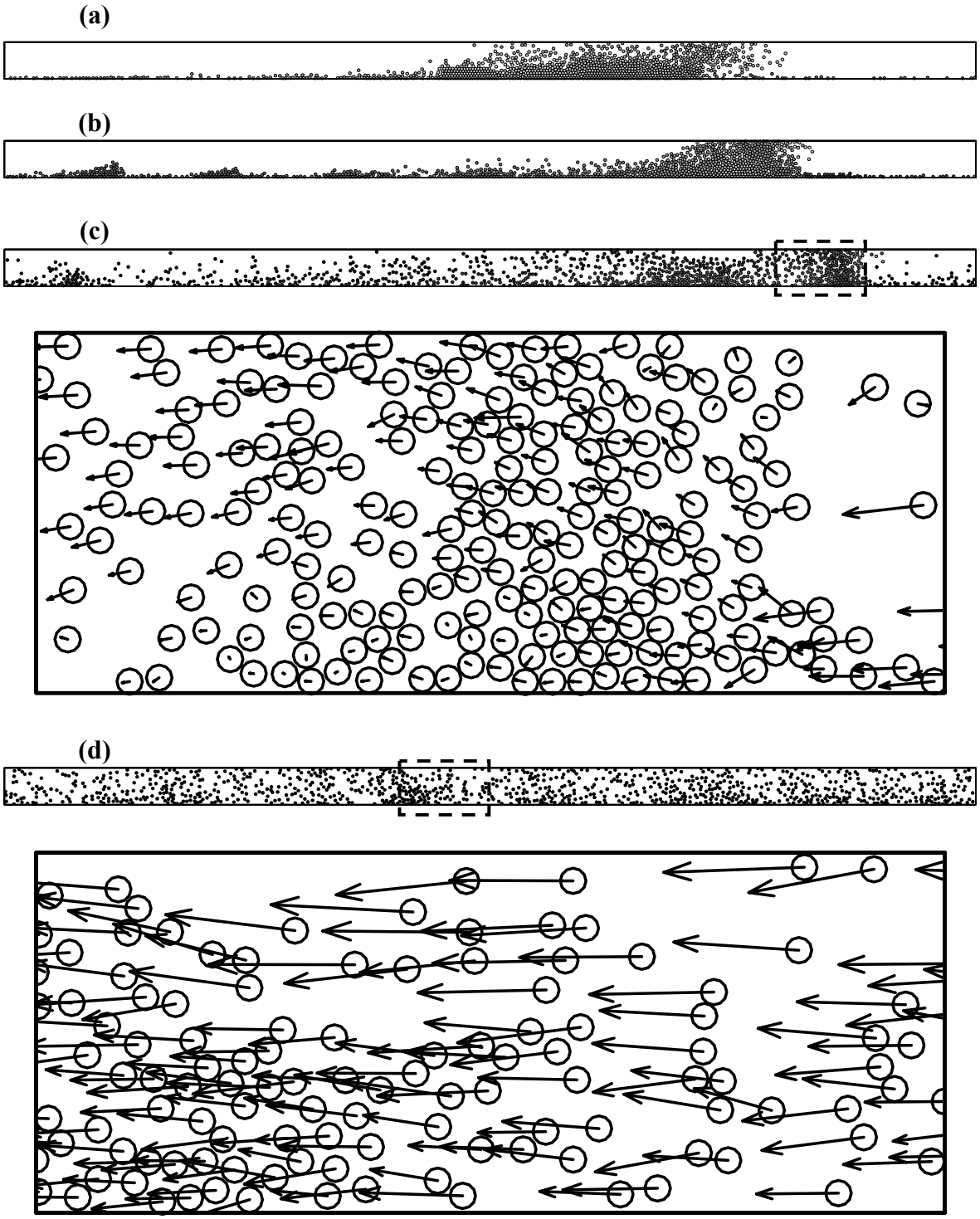

Figure 5.25 Pneumatic conveying through a pipe inclined at 45^{o} to the horizontal with an inlet gas velocity of 3 m s^{-1}, α = 0.16 (1000 particles) and (a) Λ = 0.0 (b) Λ = 0.5 (c) Λ = 1.0 (d) Λ = 2.0. The range for the scale is -3 m s^{-1} (black) to 3 m s^{-1} (white). The insets to (c) and (d) show the enlarged image of the respective sections enclosed in dashed boxes. The orientation of the pipe relative to the direction of gravity and the horizontal plane and the direction of gas flow may be inferred from the inset to Figure 3.1. Particle velocity vectors are indicated to illustrate the reversed flow behavior.

for the occurrence of reversed flow is proposed: (a) When the effect of electrostatics is increased during pneumatic conveying through an inclined pipe, particles become more strongly adhered onto the lower pipe wall in the presence of stronger electrostatic forces (b) The effective frictional forces become larger and the tendency for reversed flow behavior is increased (c) This leads to the occurrence of reversed flow. This confirms the significant effects that electrostatic forces can have on the flow behavior in pneumatic conveying through inclined pipes. Furthermore, the structure of the dunes may be disrupted in the presence of a relatively strong electrostatic field such as in Figure 5.25c where a small amount of particles are flowing backwards in the space above the dunes, forming a dilute solids phase. This effect of the electrostatic field on the disruption of flow patterns of solids becomes even more acute when Λ is increased to 2.0 in Figure 5.25d where the moving dunes or eroding dunes regimes are no longer identifiable. Instead, the distribution of particles now seems to resemble the dispersed flow regime, usually encountered in vertical or horizontal pneumatic conveying at high gas velocities or low solid concentrations, but with solids flowing backwards in the present case.

Figure 5.26 shows the flow patterns obtained at the same set of values of Λ as those used in the simulations shown in Figure 5.25 but with a higher gas velocity of 5 m s^{-1}. The same trend of a reduction in solid axial velocities following an increase in electrostatic effects may also be observed. In cases where the gas velocity is sufficiently high to sustain a forward flow of solids (Figures 5.26a, b, c), a greater amount of solid deposition is seen to occur with an increase in Λ due to stronger electrostatic forces of attraction towards the lower wall. An interesting difference in

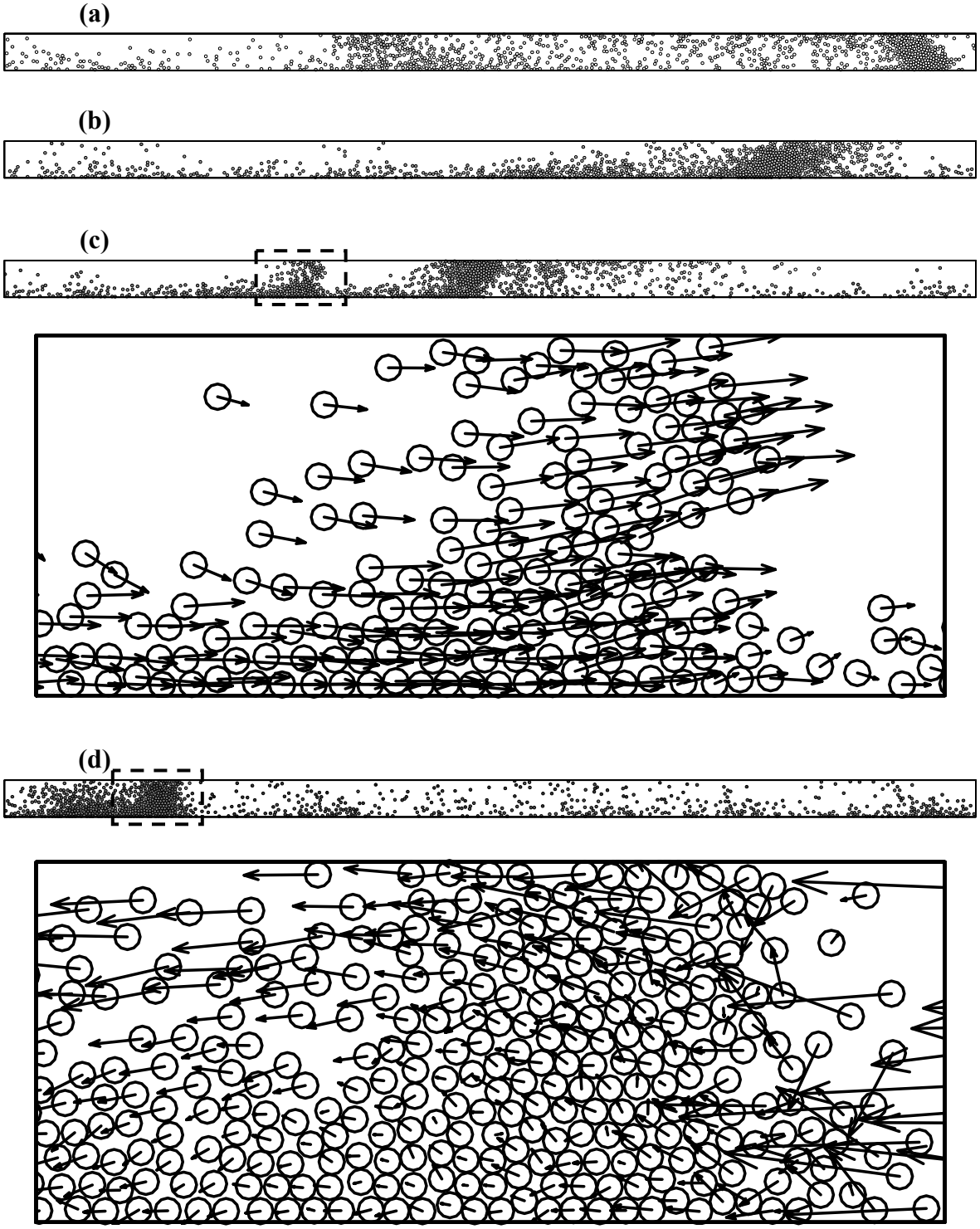

Figure 5.26 Pneumatic conveying through a pipe inclined at 45^{o} to the horizontal with an inlet gas velocity of 5 m s^{-1}, α = 0.16 and (a) Λ = 0.0 (b) Λ = 0.5 (c) Λ = 1.0 (d) Λ = 2.0. The range for the scale is -5 m s^{-1} (black) to 5 m s^{-1} (white). The insets to (c) and (d) show the enlarged image of the respective sections enclosed in dashed boxes. The orientation of the pipe relative to the direction of gravity and the horizontal plane and the direction of gas flow may be inferred from the inset to Figure 3.1. Particle velocity vectors are indicated to illustrate the reversed flow behavior.

flow patterns compared with those presented in the previous figure is that the eroding dunes regime is still clearly identifiable at Λ = 2.0 (Figure 5.26d) where almost complete reversed flow of solids is already taking place. This reveals the complex interactions between hydrodynamics and electrostatics involved in producing a particular flow regime under a specific set of operating conditions and further substantiates the importance of considering the effects of electrostatics in all experimental or numerical investigations of dry granular flow processes.

5.6.2 Solids Velocity

Figure 5.27a shows quantitatively the effects of an electrostatic field on the solid axial velocity profile within the conveying pipe. The data presented are spatially averaged velocities for a fully developed flow and have been normalized with respect to the inlet gas velocity of 3 m s^{-1}. The solid velocity profiles in the upper half of the pipe are similar for cases where an electrostatic field is absent or weak. On the other hand, solid velocities are generally lower in the lower half of the pipe in the presence of an electrostatic field. This shows that the influence of a charged lower wall at this solid concentration is only confined to the lower part of the conveying pipe when the strength of the field is mild. A small amount of reversed flow occurs along the lower wall where the solid velocities can be seen to be slightly negative. This implies that a gas velocity of 3 m s^{-1} is just sufficient to maintain a positive flow of solids under the condition Λ = 0.5. In contrast, the solid velocity profiles for cases of Λ = 1.0 and 2.0 shown in Figure 5.27b indicate complete reversed flow of solids. As such, electrostatics can be the sole determining factor in causing reversed flow in pneumatic conveying of granular materials through inclined pipes.

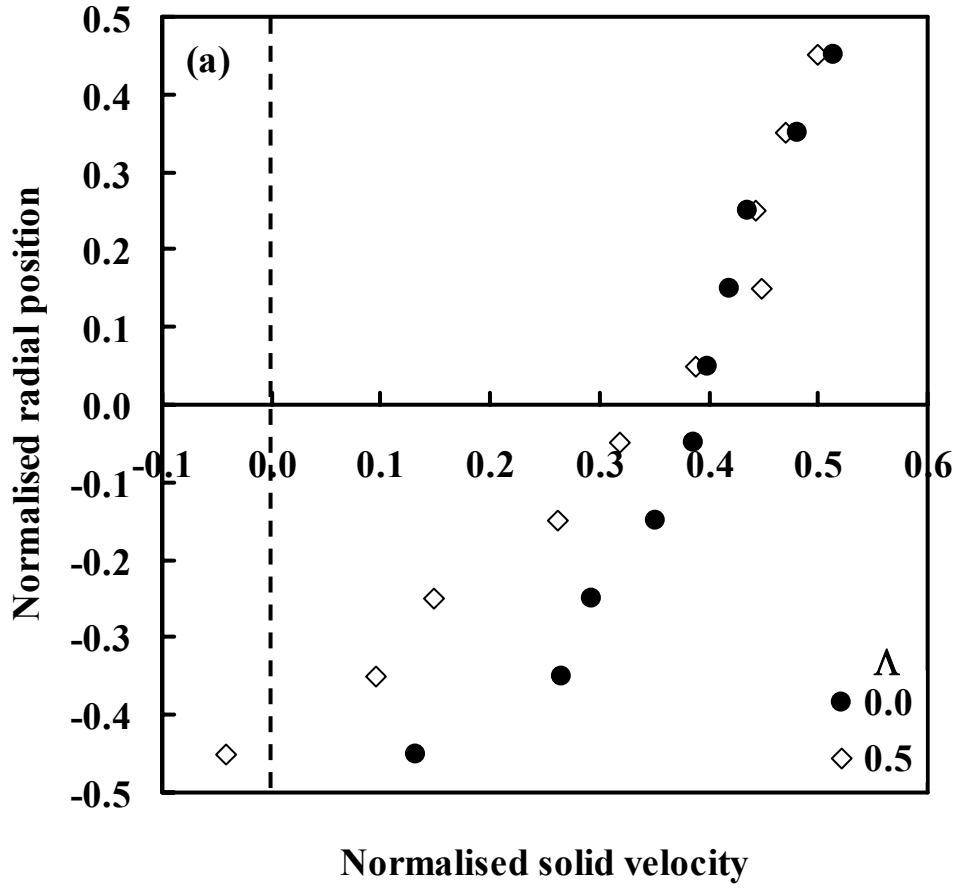

Figure 5.27a Solids velocity profiles normalized with respect to the inlet gas velocity of 3 m s^{-1} (α = 0.16) for Λ = 0.0 and 0.5. Radial position normalized with respect to pipe diameter.

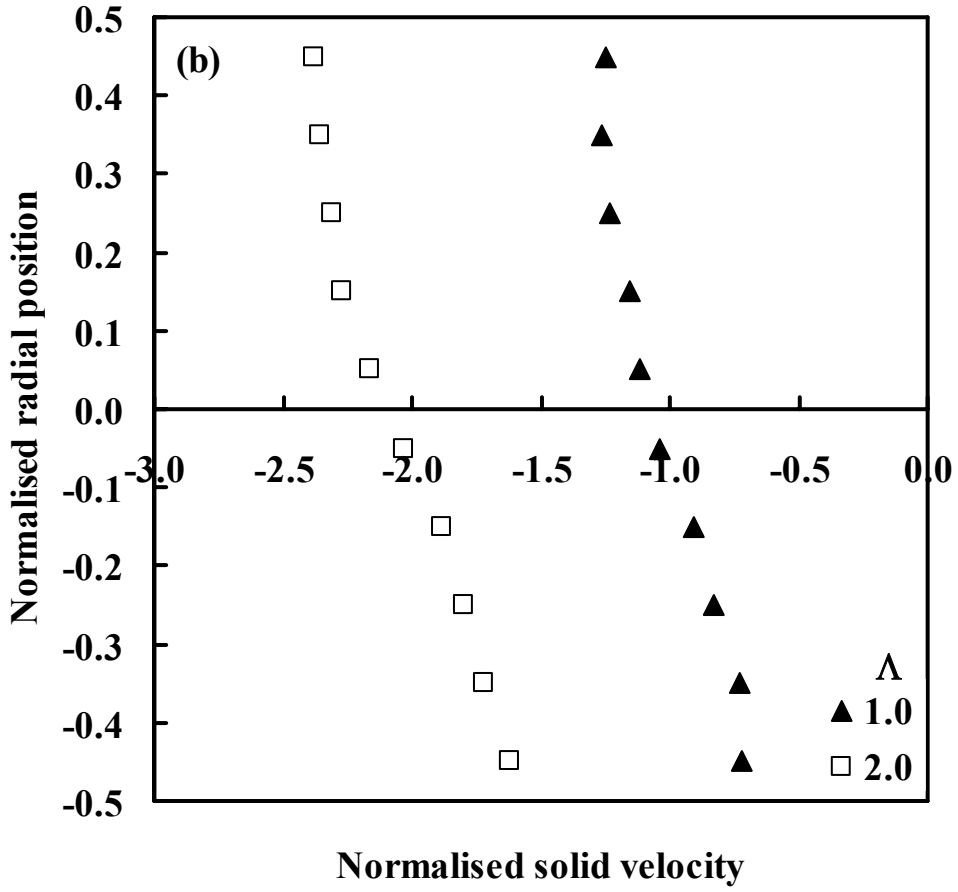

Figure 5.27b Solids velocity profiles normalized with respect to the inlet gas velocity of 3 m s^{-1} (α = 0.16) for Λ = 1.0 and 2.0. Radial position normalized with respect to pipe diameter.

When the gas velocity was increased to 5 m s^{-1}, the solid axial velocity profiles were fully positive for both $\Lambda = 0.5$ and 1.0 as shown in Figure 5.28a. This also means that an inlet gas velocity of 5 m s^{-1} was necessary to sustain a positive flow of solids in the presence of an electrostatic field of magnitude $\Lambda = 1.0$ when the solids could have been conveyed with a gas velocity of only 3 m s^{-1} under normal operating conditions when no electrostatic effects were present. In comparison with the velocity profiles seen previously in Figure 5.27a, no overlapping of the profiles takes place indicating that the electrostatic effects in these cases may not be confined to only the lower part of the conveying pipe. However, this gas velocity was again insufficient when the magnitude of Λ was further increased to 2.0 (Figure 5.28b). In contrast to previous velocity profiles, this exhibits both forward and reversed flow of solids along the upper and lower portions of the conveying pipe respectively. As such, physical conditions of inlet gas velocity and electrostatic effects may exist to allow both forward and reversed flow to occur in different parts of the conveying pipe at the same time. Finally, Figure 5.28c shows that a gas velocity of about 10 m s^{-1}, which was more than three times that needed in the absence of an electrostatic field, was required to ensure positive solids flow in a strong field represented by $\Lambda = 5.0$. This figure also shows that reversed flow occurs over a smaller region of the conveying pipe at the higher gas velocity of 10 m s^{-1} than at 8 m s^{-1} and thus illustrates that inlet gas velocity may also be used to control the spatial extent of reversed flow in an inclined conveying pipe.

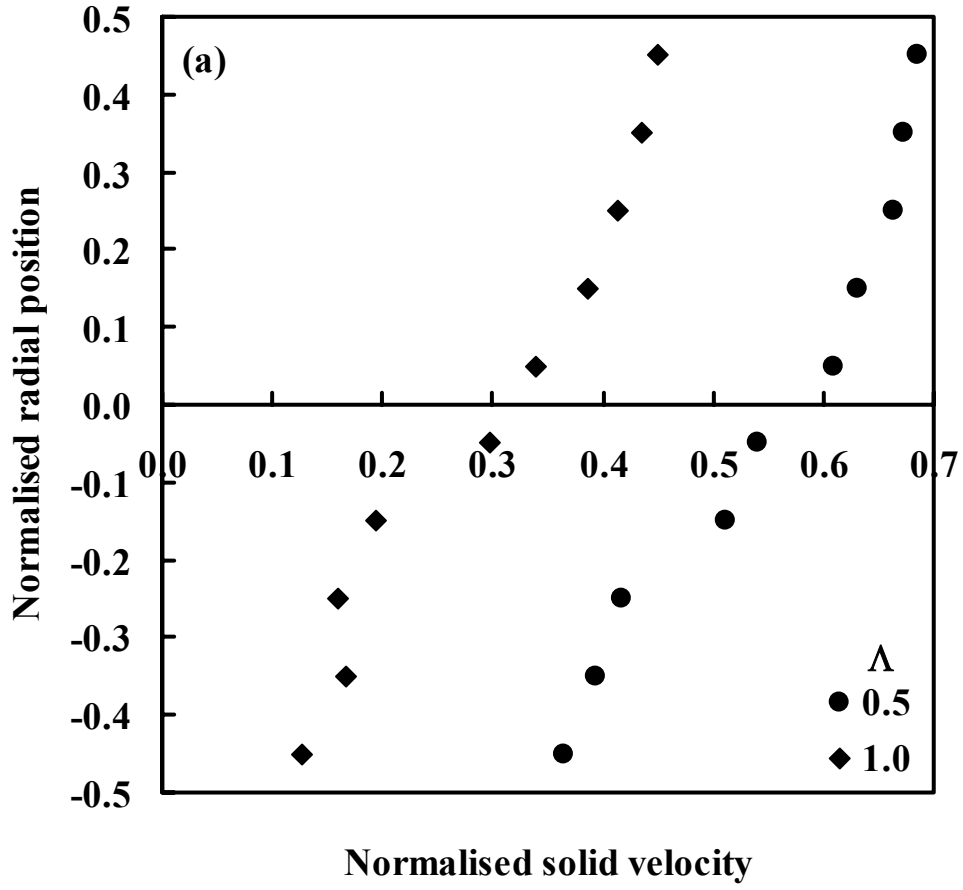

Figure 5.28a Solids velocity profiles normalized with respect to the inlet gas velocity of 5 m s^{-1} (α = 0.16) for 5 m s^{-1} and Λ = 0.5 and 1.0. Radial position normalized with respect to pipe diameter.

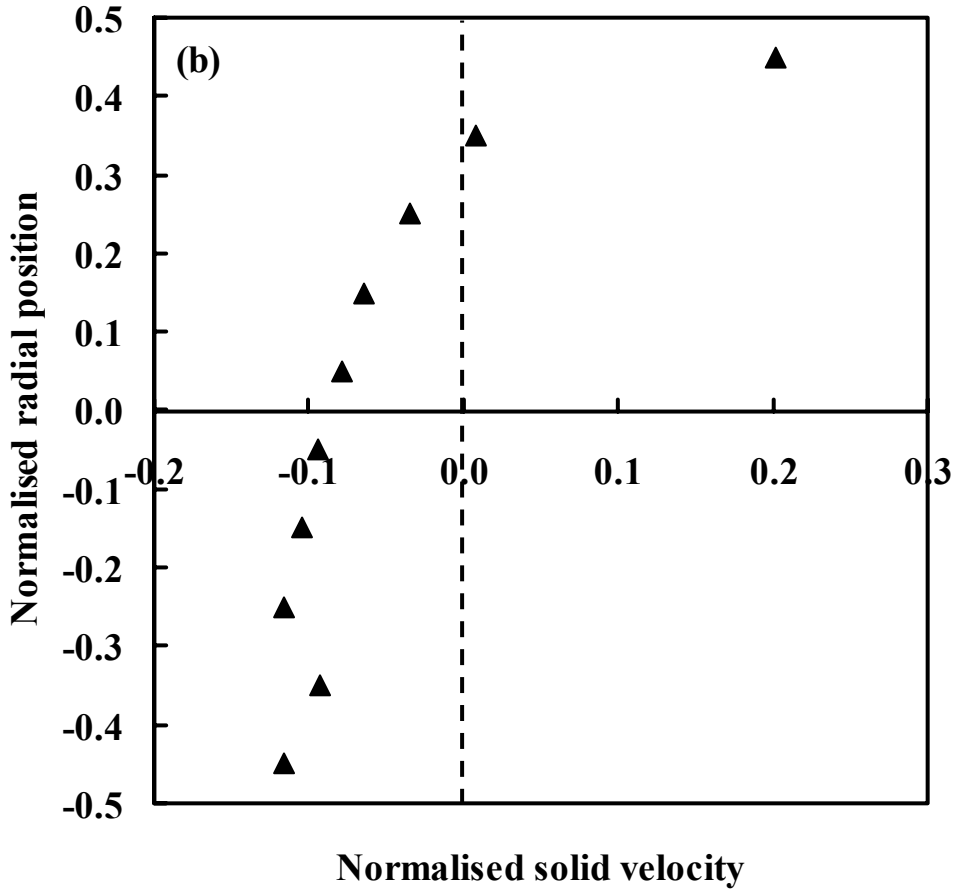

Figure 5.28b Solids velocity profiles normalized with respect to the inlet gas velocity of 5 m s^{-1} (α = 0.16) for 5 m s^{-1} and Λ = 2.0. Radial position normalized with respect to pipe diameter.

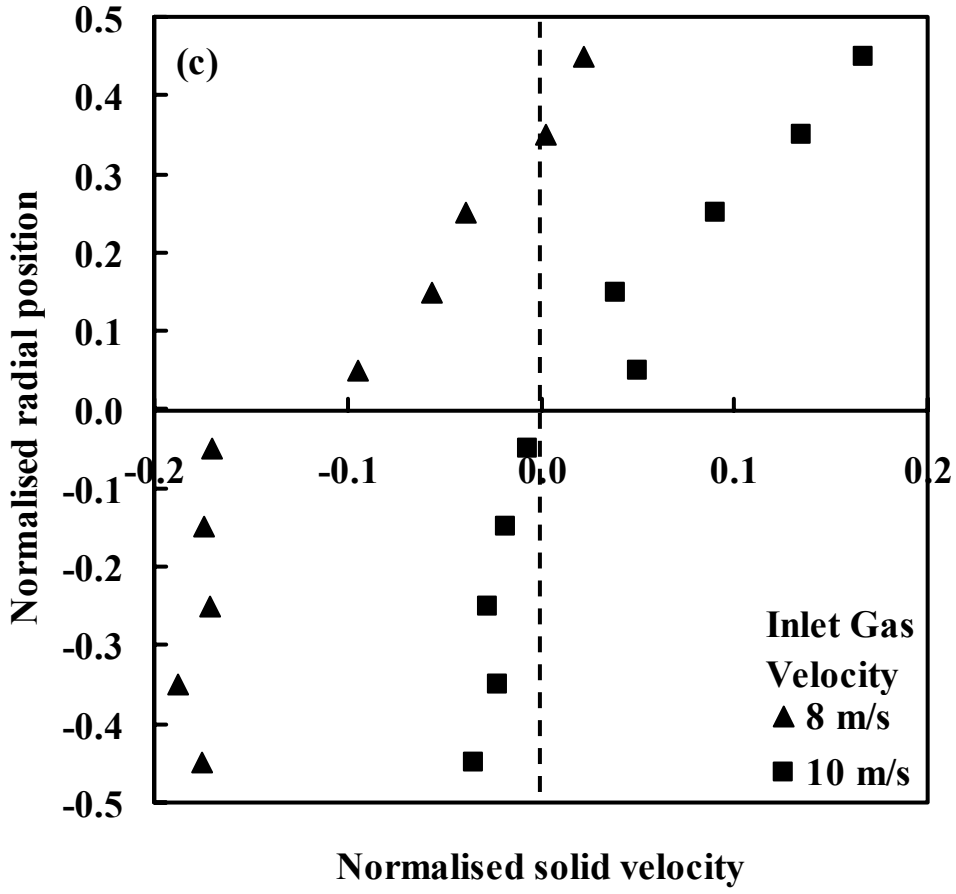

Figure 5.28c Solids velocity profiles normalized with respect to the inlet gas velocity of 5 m s^{-1} (α = 0.16) for 8 m s^{-1} and 10 m s^{-1} with Λ = 5.0. Radial position normalized with respect to pipe diameter.

The general consensus of numerous researchers is that pneumatic conveying through inclined pipes should be avoided as much as possible. Such a configuration may result in shorter pipe lengths compared with one made up of a combination of horizontal and vertical sections. However, the major disadvantages associated with inclined pneumatic conveying include low solid conveying velocities relative to the inlet gas velocity applied which corresponds to high energy requirements, tendency for particles to drop out of suspension and flow backwards, and higher minimum conveying gas velocity requirements (Mills *et al.*, 2004). Low conveying velocities may be associated with lower amount of solid attrition but the process would be uneconomical if a large inlet gas velocity is required to achieve limited solid motion along an inclined conveying pipe. As such, it was generally not recommended for use in any type of applications. However, it is important to realize that such views on inclined pneumatic conveying were established on limited published information on the subject. Furthermore, past experimental investigations on inclined pneumatic conveying seemed to have neglected the influence of electrostatics on solids flow behaviors while results obtained in the present study have confirmed the importance of such effects in such processes. In particular, electrostatic effects may play an important role in contributing towards the various problems assumed to be inherent in inclined pneumatic conveying. This would of course have to be further validated through experimental investigations.

5.6.3 Pressure Drops

Following from the previous point, it has also been mentioned by Mills *et al.* (2004) that pressure drop is another major issue to be considered when designing an inclined pneumatic conveying line. The general rule of the thumb is that it is better to

use a series of vertical and horizontal sections to achieve a vertical rise rather than an inclined section as the pressure drop in the latter may be larger than that for both vertical and horizontal pneumatic conveying. Here, it will be shown that, as with the issue of conveying velocities, anomalously large pressure drops may also be the result of electrostatic effects in the system.

Figures 5.29a, b show the pressure profiles in the 1 m section of conveying pipe under various effects of electrostatics when the inlet gas velocities were 3 m s^{-1} and 8 m s^{-1} respectively. In general, it may be seen that the stronger the effects of electrostatics, the larger the pressure drop within the conveying line. However, the higher pressure drops may not necessarily result in a positive flow of solids at very high Λ values, as have been seen from the solids axial velocities in the previous sections. In fact, the pressure drops observed for the cases Λ = 1.0 and 2.0 in Figure 5.29a and Λ = 5.0 in Figure 5.29b correspond to reversed flow of solids. This implies that an even larger pressure drop has to be created within the system in order to move the solids forward in each case. Conversely, for the same granular material and operating conditions (such as gas velocity), pressure drops required over an inclined pneumatic conveying pipe are smaller in the absence of electrostatic effects than otherwise. The pressure profiles exhibit fluctuations in regions where large clusters of solids are present. As such, Figures 5.29a and 5.29b show scatter at various positions for most cases simulated. Although such electrostatic pressure drop effect has been investigated previously for pneumatic conveying through vertical pipes, its counterpart in inclined conveying has never been studied till now. Based on the results of this and the previous sections, it is anticipated that the approach towards

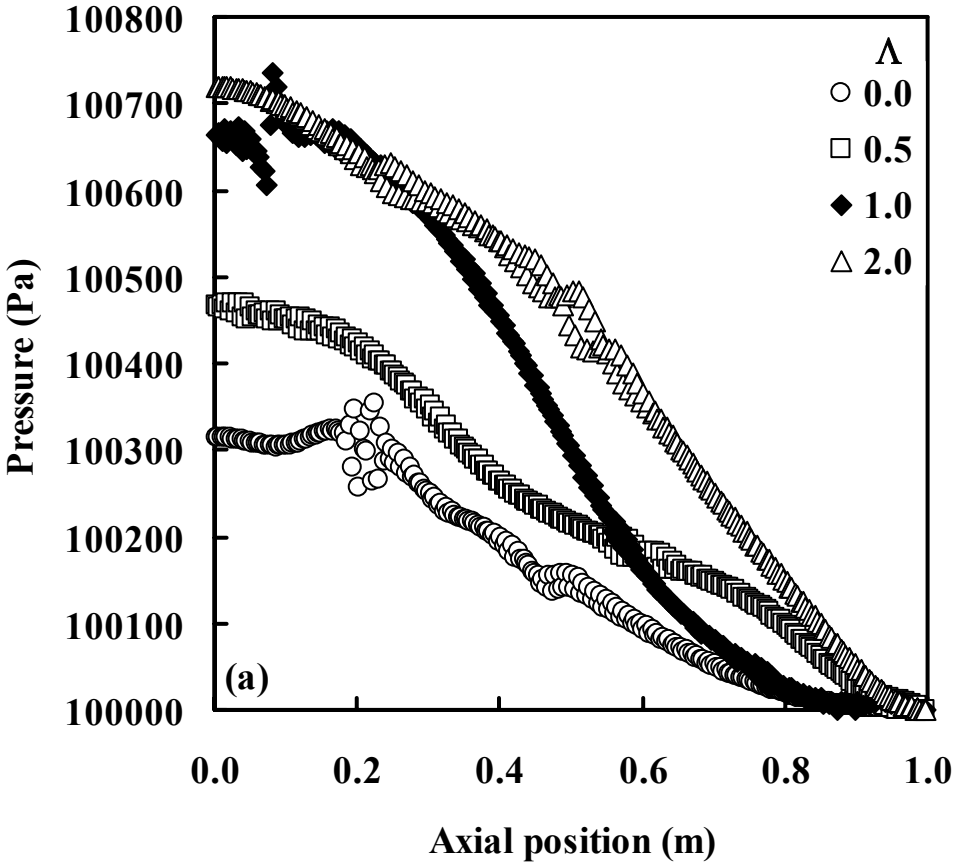

Figure 5.29a Pressure profiles along the conveying line for various values of Λ (α = 0.16) and inlet gas velocity of 3 m s^{-1}.

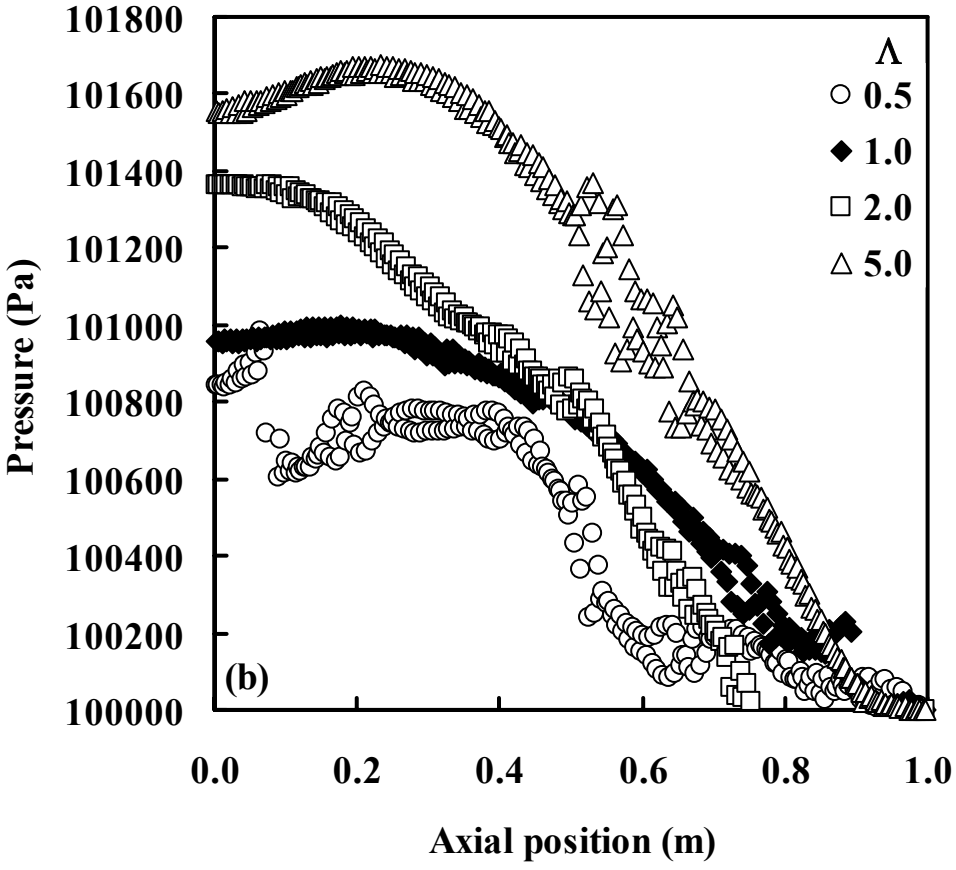

Figure 5.29b Pressure profiles along the conveying line for various values of Λ (α = 0.16) and inlet gas velocity of 8 m s^{-1}.

making pneumatic conveying through inclined pipes a feasible type of operation for transporting granular material may involve resolving the electrostatic charge generation problem.

5.6.4 Solids Fraction

The quantitative effects of electrostatic forces on the solids flow pattern would be discussed in the present section. The various flow regimes which can arise under different effects of electrostatics have been discussed in a previous section. Figures 5.30a, b show the typical spatially averaged solid fraction profiles when the gas inlet velocity is 3 m s^{-1} and the solids flow has become fully developed. It may be observed that the profiles for $\Lambda = 0.0$ and 0.5, corresponding to the moving dunes and eroding dunes regimes described earlier, are almost indistinguishable from each other. In the latter, a small amount of solids is flowing in the reversed direction causing erosion of the dunes but this does not result in a significant shift in solids fraction profiles from the case of no electrostatic effects. Figure 5.30a also shows that under similar electrostatic conditions, the solids fraction profile extracted from Electrical Capacitance Tomography (ECT) measurements and time averaged over a 30 s interval shows a fair correspondence with those obtained from CFD-DEM simulations. The simulations have thus been successful in reproducing quantitatively the eroding dunes flow pattern with backflow of solids under the influence of electrostatics. Such a flow pattern may be characterized by a high concentration of solids towards the bottom half of the inclined pipe and a relatively dilute upper region.

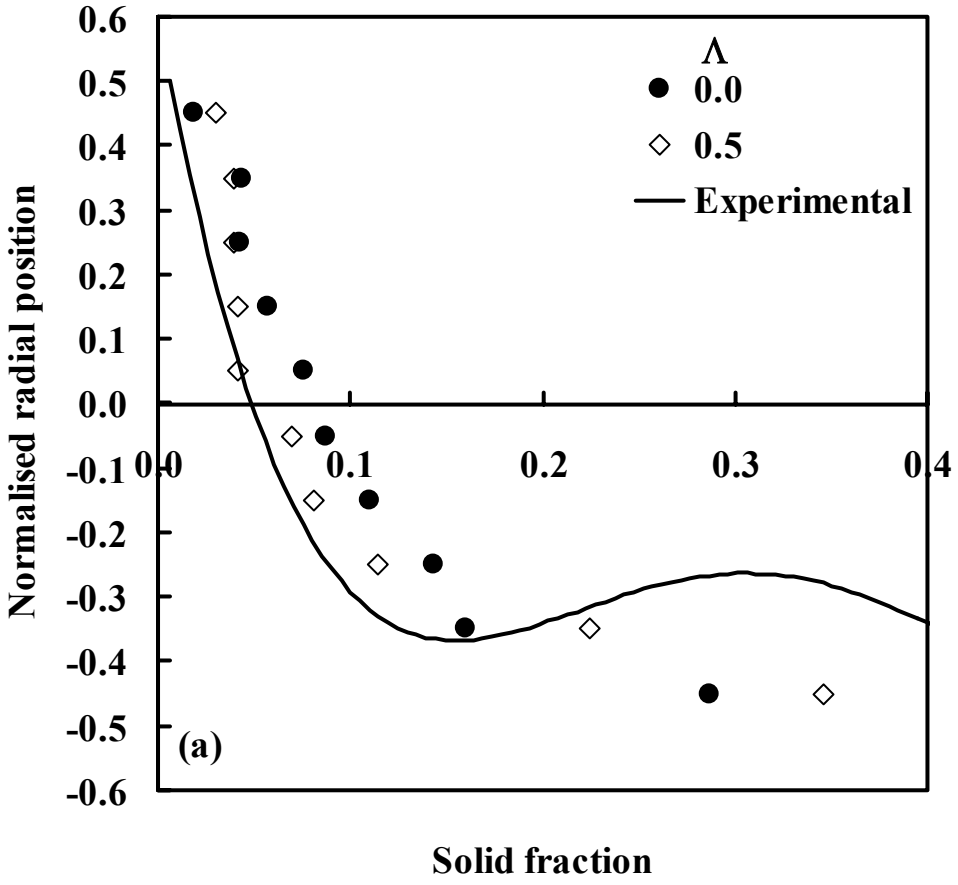

Figure 5.30a Solid fraction profiles for inlet gas velocity of 3 m s^{-1} (α = 0.16) and Λ = 0.0 and 0.5. Comparison with ECT data time-averaged over 30 s. The value of Λ observed in the experiment was about 0.1. Radial position normalized with respect to pipe diameter.

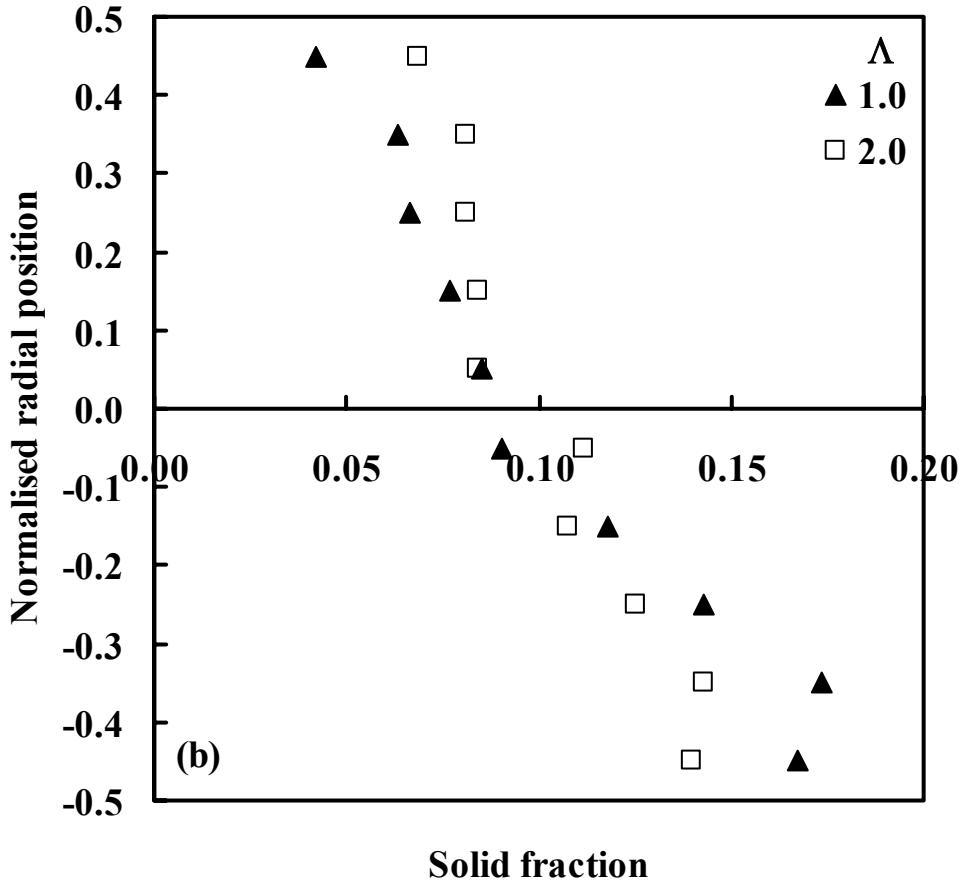

Figure 5.30b Solid fraction profiles for inlet gas velocity of 3 m s^{-1} (α = 0.16) and Λ = 1.0 and 2.0. Radial position normalized with respect to pipe diameter.

On the other hand, when electrostatic forces are sufficiently strong (Λ = 1.0 and 2.0) to cause disruption to the structure of the solids dunes and severe reversed flow of solids, the corresponding solid fraction profiles are also altered quantitatively (Figure 5.30b). It may be seen that with the dispersal of solids from the dunes during backflow, the solid fraction profiles become flatter. The important implication for the formation of such profiles is that the pneumatic conveying line may now become much more vulnerable to blockages. This may also explain why blockages occur frequently in inclined pneumatic conveying pipes, especially when conveying velocities are too low. Such occurrences are more predominant in inclined pneumatic conveying than both vertical and horizontal conveying and contribute towards the unpopularity of the former.

5.6.5 Solids Flow Rate

Figure 5.31 shows the solids flow rate and the associated time required to achieve a steady or fully developed state of flow under different conditions of electrostatic forces and at a gas velocity of 3 m s^{-1}. The solids flow rate presented has been non-dimensionalized with respect to the maximum possible solids flow rate where each particle moves at the inlet gas velocity of 3 m s^{-1}. In the absence of electrostatic effects, the solids flow rate becomes steady after about 2 s of flow. In view of this and the high computational demands of each simulation case carried out in the present study, it was deemed justifiable to simulate for a relatively short physical time of 10 s in each case before quantitative characterization was carried out. The CFD-DEM simulations show that the time required for the system to reach a steady state becomes longer with increasing effects of electrostatics (Figure 5.31). In addition, at Λ = 0.5, the final steady state flow rate of solids is lower than that for Λ =

0.0. When Λ is increased to 1.0, there is almost no net flow of solids through the conveying pipe, indicating almost equal reversed flow as forward flow of solids under such a condition. Finally, the case for $\Lambda = 2.0$ results in a very negative solids flow rate, corresponding to severe reversed flow of solids and a long transient state.

5.6.6 Phase Diagram

The subject of the present study on the effects of electrostatics on reversed flow behavior in pneumatic conveying through inclined pipes is a poorly understood area due primarily to the limited amount of research efforts which have been devoted to its study. The conditions under which reversed flow of solids can occur for various types of granular materials, operating conditions and strength of an induced electrostatic field cannot, in general, be predicted accurately. In the absence of a general theory for making such predictions, it would be useful, especially to industrialists and designers of pneumatic conveying systems, to have a general flow map or phase diagram showing combinations of conditions which can give rise to positive solids flow in inclined pneumatic conveying. Such phase diagrams would necessarily have to be constructed from voluminous experimental data rather than computational results, given the current status of computational power. In this section, a simple phase diagram constructed out of the data obtained from the simulations carried out is presented as an illustration of this approach towards a better understanding of inclined pneumatic conveying systems.

Figure 5.32a shows the relationship between solids flow rate and gas inlet velocity for various electrostatic field strengths. The solids flow rates have been non-

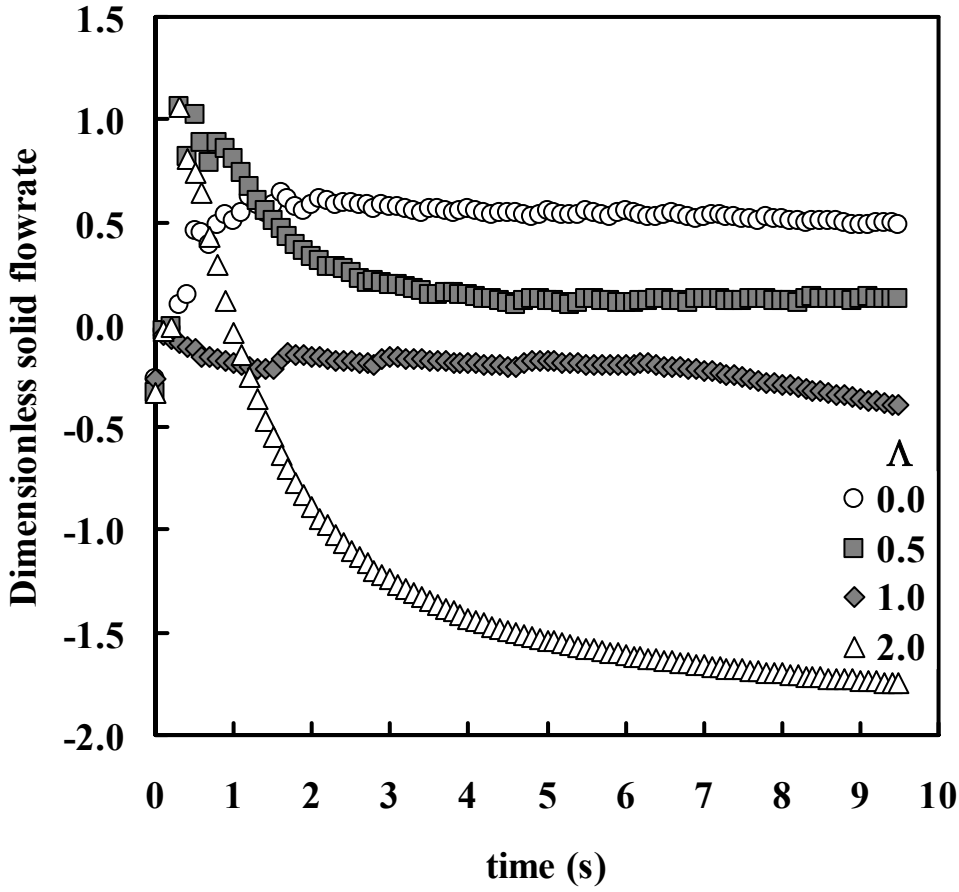

Figure 5.31 Transient development of solid flow rates with inlet gas velocity of 3 m s^{-1} for various values of Λ and α = 0.16. Solid flow rates are non-dimensionalized with respect to the maximum possible solid flow rate where each particle moves at the inlet gas velocity.

dimensionalized with respect to the maximum possible solids flow rate where all particles move at the respective inlet gas velocities. Areas above and below the horizontal axis correspond to net forward and reversed flow of solids respectively. It may be observed that the solids flow rate varies nonlinearly with gas velocity. For example, the dimensionless solids flow rate for $\Lambda = 0.5$ increases fairly linearly in the positive solids flow regime from about 0.13 to 0.46 to 0.92 when the gas velocity is increased from 3 to 5 to 8 m s^{-1} respectively. However, the relationship between solids flow rate and gas velocity becomes nonlinear with higher values of Λ (such as for Λ = 1.0, 2.0, 5.0) over the range of gas velocities, 2 – 10 m s^{-1}, investigated. This may be seen from the curves joining the data points added in Figure 5.32a to aid in the visualization of these trends. The gas velocity required to achieve a particular solids flow rate increases with increasing electrostatic effects. In particular, intersections between each curve and the horizontal axis indicate the minimum gas velocities required to ensure net positive flows of solids. For Λ = 0.5, 1.0, 2.0 and 5.0 these minimum gas velocities are observed to be about 3.0, 3.9, 5.6 and 7.9 m s^{-1} respectively. These are plotted with respect to the corresponding values of Λ in Figure 5.32b. It may be seen that the relationship between the two is also nonlinear and non-decreasing. Such a characteristic map of the flow conditions in an inclined pneumatic conveying system may be useful to designers of such systems. However, such data are unavailable in the scientific literature to date. The present work represents the first attempt at constructing such a flow map diagram for inclined pneumatic conveying systems with electrostatic effects. The flow map shows conditions under which reversed flow of solids might occur and the minimum gas velocities required to ensure minimum forward flow for various extents of electrostatic effects. This was

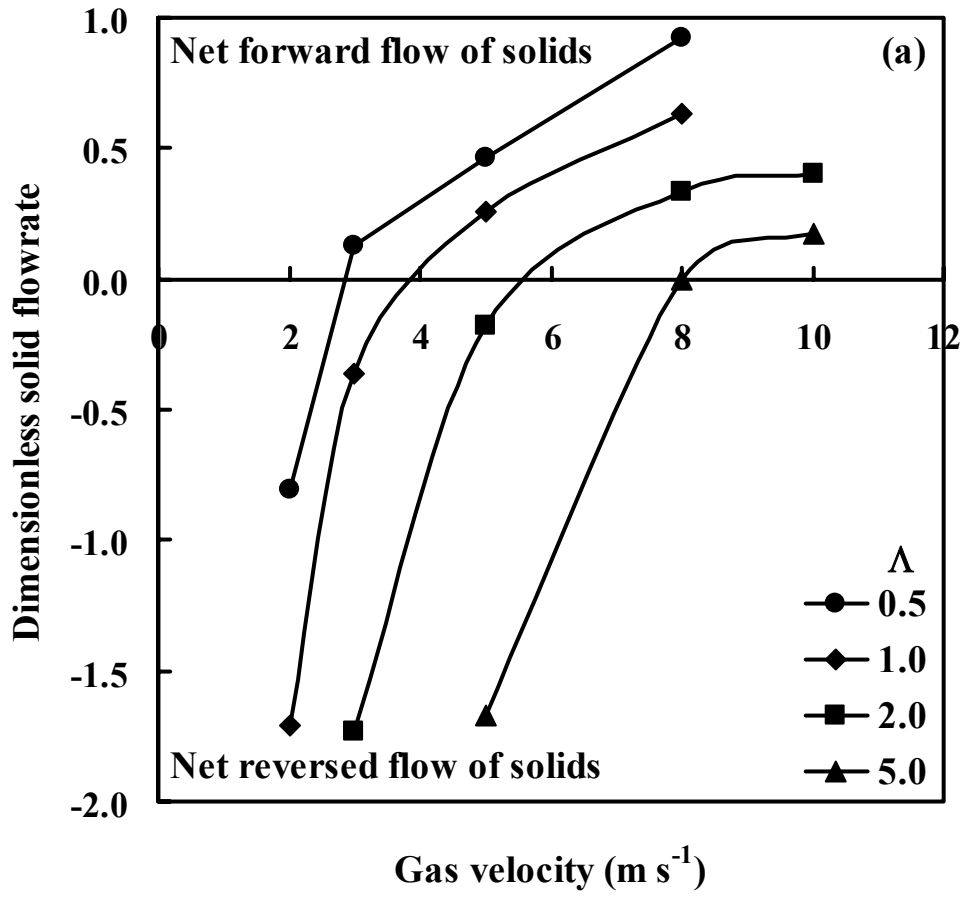

Figure 5.32a Phase diagrams showing relationship between solid flow rate and inlet gas velocity for various values of Λ. Solid flow rates are non-dimensionalized with respect to the maximum possible solid flow rate where all particles move at the respective inlet gas velocities. Curves are added to aid visualization.

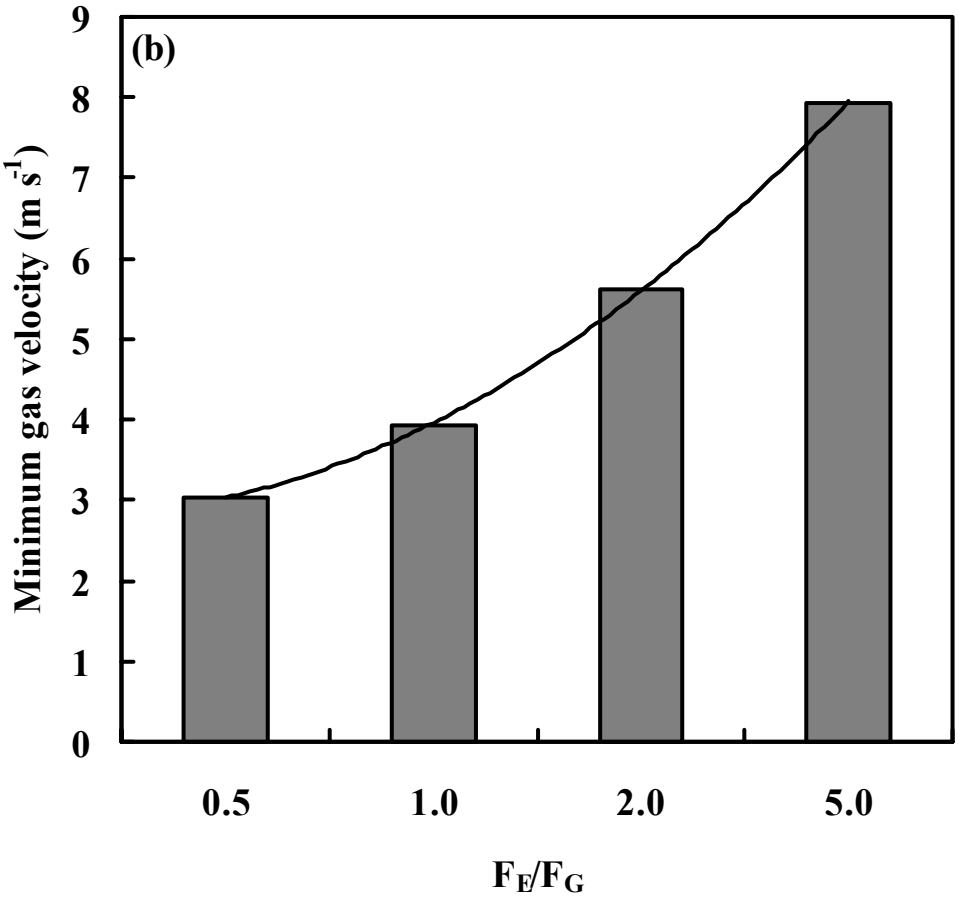

Figure 5.32b Phase diagrams showing minimum gas velocity required to ensure net positive flow of solids. Solid flow rates are non-dimensionalized with respect to the maximum possible solid flow rate where all particles move at the respective inlet gas velocities. Curves are added to aid visualization.

constructed out of data obtained from the CFD-DEM simulations carried out in this study. As mentioned previously, this may be a good approach for studying such electrostatics phenomenon as the amount of such effects can be imposed and controlled definitely for a very 'clean' study. However, it may also be noted that the present map is applicable only to the specific system investigated in the present study and may not be generalized to other pneumatic conveying systems with different operating parameters and conditions. To construct a more universal phase diagram for general inclined pneumatic conveying operations, the type of data presented here may have to be collected for a wide variety of pneumatic conveying systems with different types of particles, pipes and configurations. The practical approach of doing so would be through experiments due to the high computational demands of CFD-DEM simulations. However, this would first encompass overcoming the mentioned technical difficulties associated with controlling precisely the amount of electrostatic effects which are generated within a pneumatic conveying system and so would definitely pose a major technical challenge to experimentalists in this area of research.

5.6.7 Electrostatic Effects in Vertical Pneumatic Conveying

The predominant effect of an electrostatically charged pipe wall in vertical pneumatic conveying is to cause the formation of a fairly symmetrical but non-homogeneous solids distribution over the cross-section of the pipe. Figure 5.33a shows a typical snapshot of the particle distribution during the conveying process with an inlet gas velocity of 16 m s^{-1} when no electrostatic effects were present. Particles are dispersed throughout the entire space within the pipe and do not show any tendency to form clusters. This type of flow pattern has been studied previously using

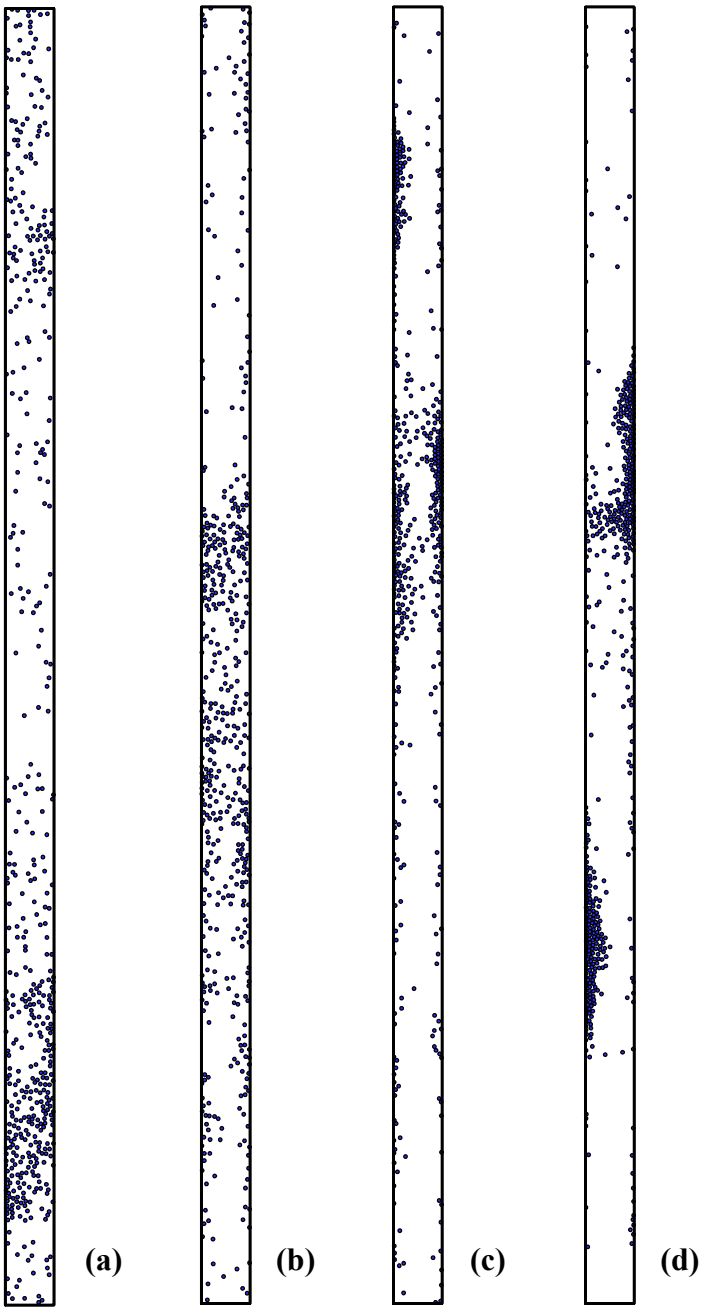

Figure 5.33 Pneumatic conveying through a vertical pipe with an inlet gas velocity of 16 m s^{-1} (α = 0.08) and (a) Λ = 0.0 (b) Λ = 1.0 (c) Λ = 5.0 (d) Λ = 10.0.

CFD-DEM simulations without consideration of electrostatic effects. Here, when an electrostatic field is imposed to simulate the presence of charged pipe walls, particles are observed to cluster towards both walls. Figures 5.33b, c, d show that the extent of this clustering increases with increasing field strength or Λ value. In particular, at Λ = 5.0 and 10.0, it may be seen that the effects of electrostatic attraction towards both walls of the vertical pipe are sufficiently significant to result in the formation of a new type of flow pattern. Most particles are now transported up the pipe in the form of dunes sliding against the two pipe walls, much like the moving dunes seen in horizontal or inclined pneumatic conveying. There is a high concentration of particle along the walls and a relatively empty region in the centre of the pipe, giving an interesting core-annular structure. Such a flow pattern was observed experimentally by Zhu *et al.* (2003) and Yao *et al.* (2004) and was referred to as the annular flow and ring flow regimes respectively. The present CFD-DEM simulation incorporating an electrostatic field model has successfully reproduced such a flow pattern computationally for the first time. This flow pattern was not reproduced by the CFD-DEM simulations carried out previously where no electrostatic effects were considered. As such, the present simulations have also confirmed the formation of the annular flow regime in vertical pneumatic conveying to be a consequence of electrostatic rather than pure hydrodynamic effects.

The solids fraction profiles are compared with the experimental data obtained by Zhu *et al.* (2003) under similar operating conditions so as to provide a more quantitative basis for the points put forward earlier. Figure 5.34 shows that the solids fraction is uniform across the conveying pipe in the dispersed flow regime represented

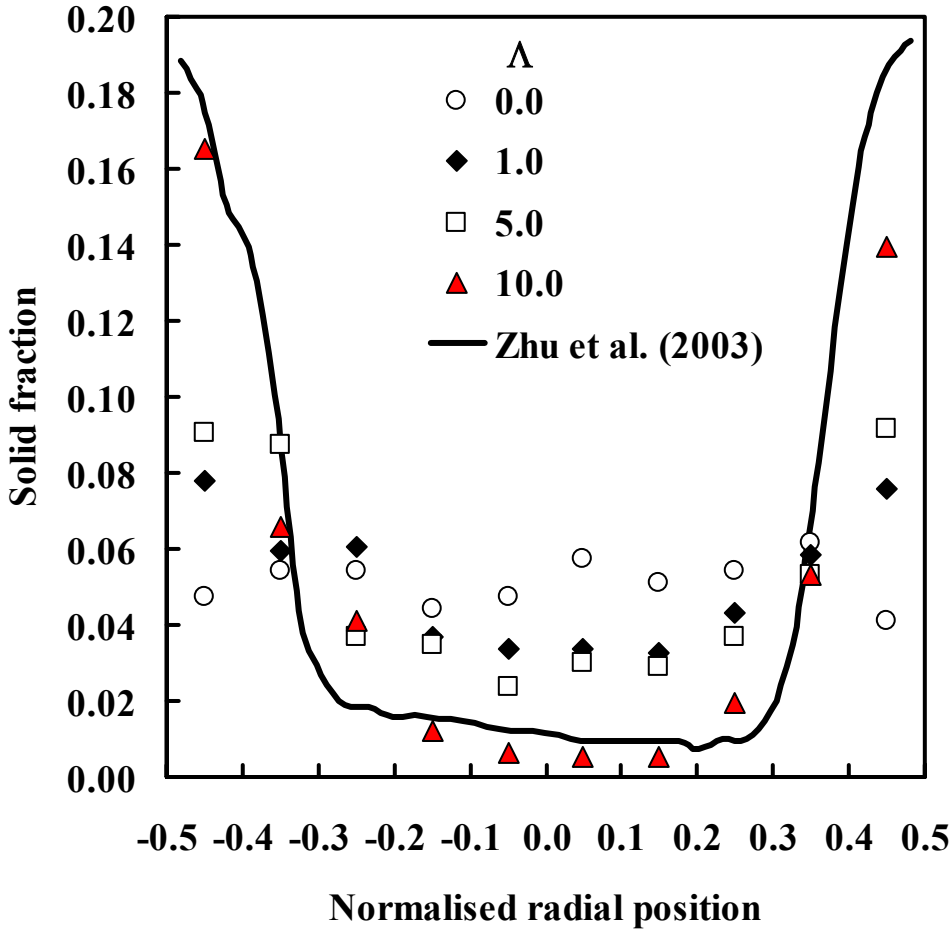

Figure 5.34 Solid fraction profiles for vertical pneumatic conveying with inlet gas velocity of 16 m s^{-1} for various values of Λ and α = 0.08 (500 particles). Radial position normalized with respect to pipe diameter. Comparison with experimental results obtained by Zhu *et al.* (2003) under the same operating conditions.

by Λ = 0.0. With increasing values of Λ, the solids fraction profiles become increasingly less uniform, showing higher solids concentration near the walls than at the pipe centre. When the typical value of Λ = 10.0 as observed in the experiments carried out in the present study is applied, the solids fraction profile matches the experimental data from Zhu *et al.* (2003). This confirms quantitatively the claim made earlier that electrostatics is the predominant factor giving rise to such a flow regime in vertical pneumatic conveying.

Zhu *et al.* (2003) reported that the formation of a core-annular structure in vertical pneumatic conveying was rather unusual and further investigated the cause of such a phenomenon by measuring the induced current in the pipe wall with a digital electrometer. They observed that the induced current and amount of accumulated charges were greater in the annular flow regime than in the dispersed flow regime. Furthermore, the addition of an antistatic powder to the pneumatic conveying system resulted in the disappearance of the annular flow regime altogether. They thus concluded qualitatively that electrostatic effects played a major role in the formation of this type of flow regime. Figure 5.35 shows a further comparison of the solids distribution obtained from the present CFD-DEM simulations when a value of Λ = 10.0 was applied at a gas velocity of 13 m s^{-1} with ECT data obtained by the previous workers using the same air flow rate. The presence of strong electrostatic forces resulted in the formation of a ring structure along the pipe walls in the experiment conducted. Similarly, the strong electrostatic field applied in the simulations led to the clustering of particles against the walls of the vertical pipe. The good agreement

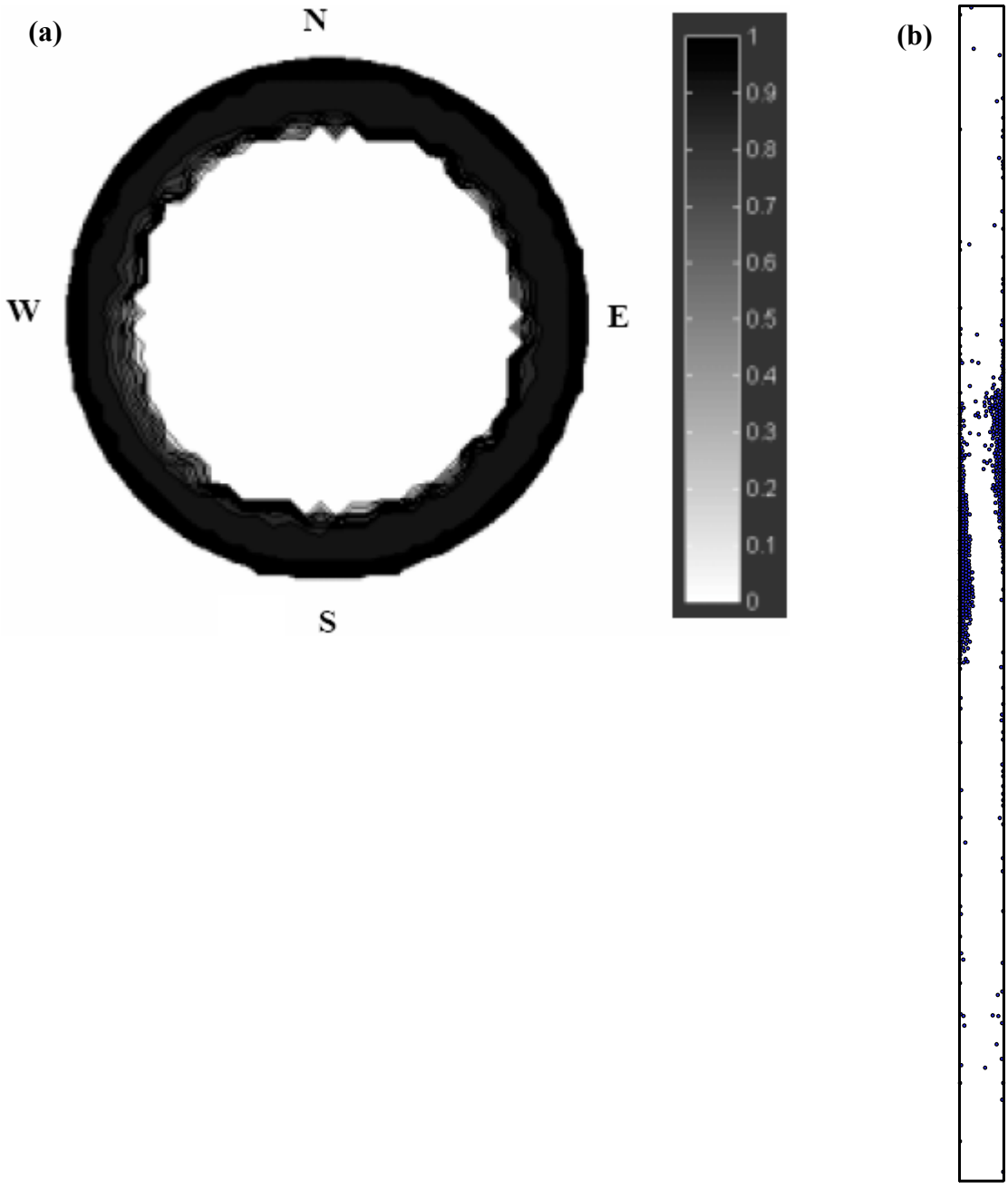

Figure 5.35 (a) ECT image of solids distribution in the annular flow regime (Zhu *et al.*, 2003) and (b) Annular flow obtained from CFD-DEM simulations with Λ = 10.0 and α = 0.08. Inlet gas velocity is 13 m s^{-1} for both cases.

between the numerical and experimental results further supports the conclusions reached earlier in both the previous and present studies.

5.6.8 Effects of Friction

With reference to the mechanism for the development of reversed flow in pneumatic conveying through inclined pipes proposed in a previous section, it may be expected that friction also plays an important role, in addition to electrostatic effects, in causing such behavior. In order to carry out a sensitivity analysis on the effects of friction in giving rise to the various flow patterns which have been observed in the simulation results shown earlier, a few more simulation cases on inclined pneumatic conveying have been carried out using the coefficient of friction as the variable. Specifically, the conditions which have been kept fixed include: an inlet gas velocity of 3 m s^{-1}, α = 0.16 (1000 particles) and Λ = 1.0. Cases where the coefficient of friction is 0.1, 0.5 and 1.0 were simulated and the flow patterns compared with that presented in Figure 5.25c where the value of coefficient of friction used was 0.3. These are shown in Figures 5.36a, b, c respectively. It may be seen that the eroding dunes flow regime may still be identified in each of these cases. Each dune picks up particles at the front and loses particles at its tail due to reversed flow. In addition, as in Figure 5.25c, a dilute solids phase with particles flowing backwards is present near the top of the inclined pipe. As such, it seems that within the range of coefficient of friction investigated in this sensitivity analysis study, friction does not cause a significant change in the flow pattern which is exhibited. The operating parameters which play a more important role in this aspect may include the gas velocity, solid concentration and electrostatic effects.

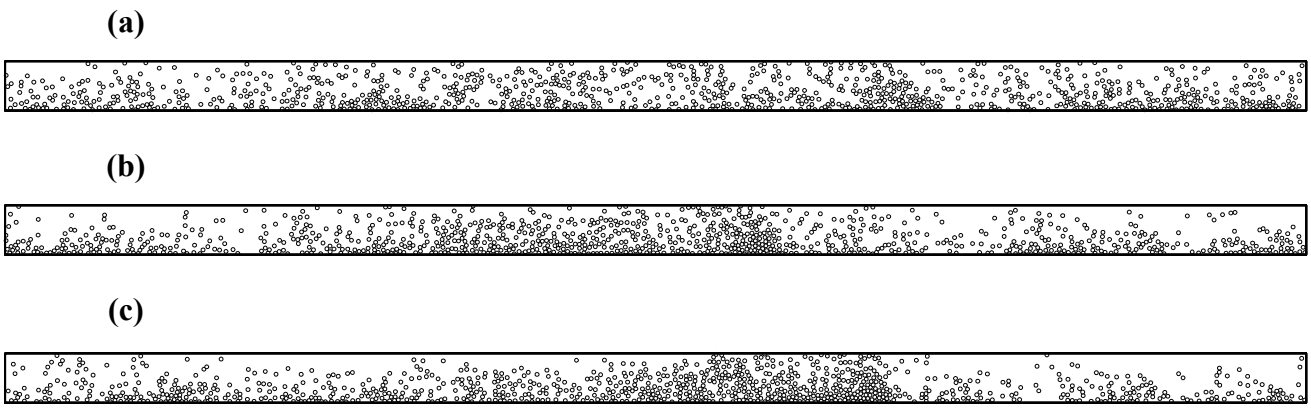

Figure 5.36 Pneumatic conveying through a pipe inclined at 45^{o} to the horizontal with an inlet gas velocity of 3 m s^{-1}, α = 0.16 (1000 particles), Λ = 1.0 and coefficient of friction equal to (a) 0.1 (b) 0.5 (c) 1.0. The orientation of the pipe relative to the direction of gravity and the horizontal plane and the direction of gas flow may be inferred from the inset to Figure 3.1.

5.6.9 Practical Applications

A better understanding of electrostatic effects in pneumatic conveying processes, in addition to the possible resolution of the undesirable characteristics of inclined pneumatic conveying, may also have important implications for future technological development. For example, one important industrial application of electrostatics is in a type of process known as electrostatic precipitation. This involves the removal of fine suspended particles from a gas by charging the particles in a corona discharge and separating them from the gas by means of an electric field (Robinson and Moore, 1973). The precipitator may consist of a grounded cylinder or parallel plates with discharge electrodes or wires. Charged particles are attracted to a collecting surface where they adhere and thus are extracted from the gas stream. The accumulated layer of particles has to be dislodged periodically and allowed to fall into a hopper or sump for subsequent removal. With reference to the subject of the present study, one possible improvement in the design of electrostatic precipitators may involve the use of suitably charged, inclined cylinders or parallel plates. This may allow charged particles that adhere onto the collecting surface to flow backwards naturally under the effects of gravity into the hopper or sump. Such a design would allow the electrostatic precipitation process to be operated in continuous rather than semi-continuous mode. One other important application of electrostatics which makes use of fluidization and pneumatic conveying through vertical pipes is referred to as electrostatic separation. This involves charging the components in particulate mixtures with opposite polarities and subsequently separating the components either by mutual repulsion or an external electric field, and possibly aided by gravity (Jonassen, 2002). For example, in the electrostatic separation of iron ore from sand in a fluidized bed, the mixture is fluidized over a perforated stainless steel plate which is

kept at a high potential. The positively charged ore particles will be pneumatically conveyed upwards because of the field while the sand particles will be retained. Following the present study, it may be expected that transport of charged particles through vertical pipes may lead to the formation of annular or ring structures within the pipe. This may also have important implications for specific industrial applications of such electrostatic separation processes. The CFD-DEM method coupled with a simple electrostatic field model may also be a useful tool for the study and design of such electrostatic processes.

5.7 Granular Attrition

5.7.1 Theoretical Modeling

Figure 5.37 shows attrition data obtained by Paramanathan and Bridgwater (1983a; 1983b) using granular NaCl and molecular sieve beads as the granular material in an annular shear cell while Figure 5.38 shows those reported by Ghadiri *et al.* (2000) for porous silica catalyst particles in the same type of equipment. It may be seen that the theoretical model developed in the present study based on a diffusion analogy (Equation 3.6) has been successful in reproducing the attrition behavior in terms of the weight fraction of particles attrited at various times for these different types of granular material in an annular shear cell. Similarly, attrition data obtained using gas-fluidized beds (Ayazi Shamlou *et al.*, 1990; Cook *et al.*, 1996; Stein *et al.*, 1998; Kage *et al.*, 2000) are compared with the model in Figures 5.39 – 5.42 respectively and good agreements are also observed. As mentioned previously, the attrition diffusivity D may be interpreted to be the propensity of particles to undergo

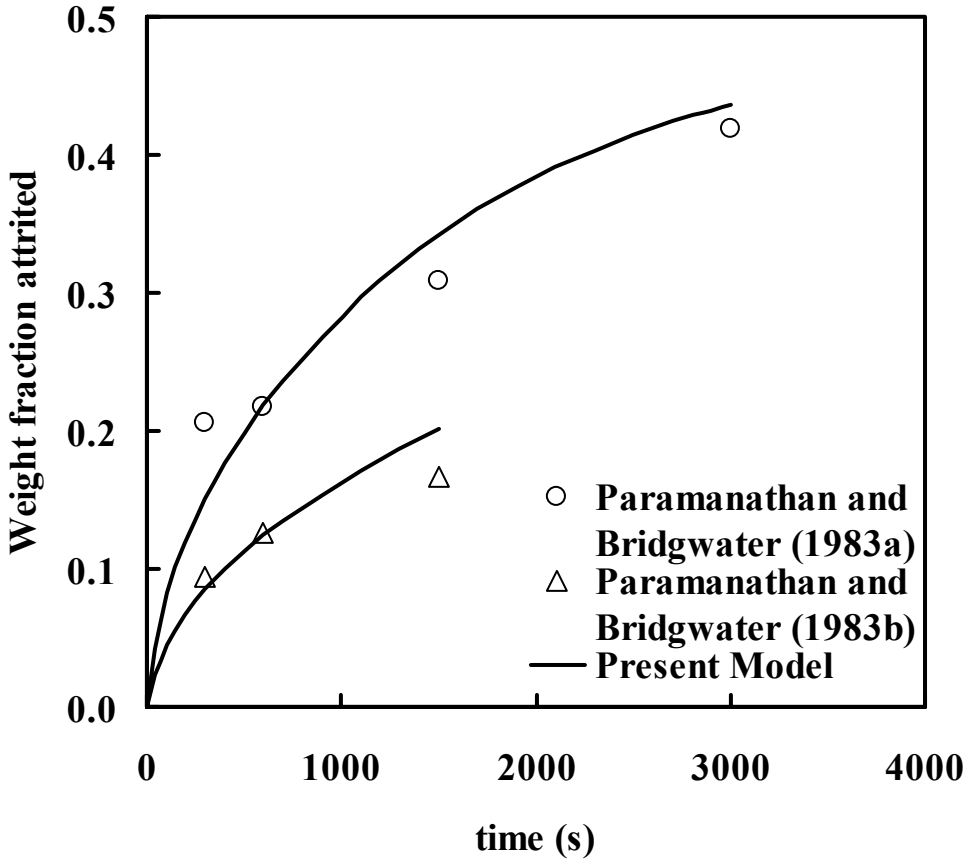

Figure 5.37 Comparisons of model with attrition data reported for experiments conducted using annular shear cells. The granular material used were 1.7 – 2.0 mm sodium chloride granules (Paramanathan and Bridgwater, 1983a) ($D = 6.82 \times 10^{-5}$ s^{-1}) and molecular sieve beads (Paramanathan and Bridgwater, 1983b) ($D = 2.36 \times 10^{-5}$ s^{-1}) with a constant applied normal stress of 41 kPa.

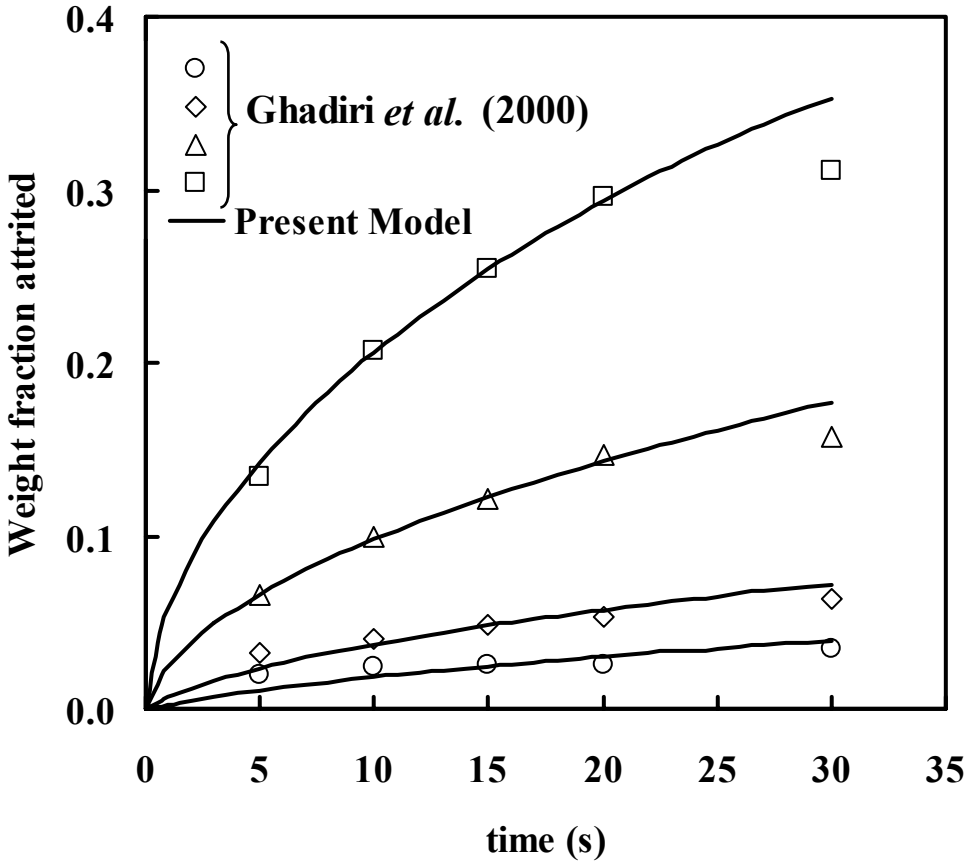

Figure 5.38 Comparisons of model with attrition data reported for experiments conducted using annular shear cells. The granular material used were 2.0 – 2.36 mm porous silica catalyst carrier beads (Ghadiri *et al.*, 2000) with varying applied normal stresses of 25 (○), 50 (◊), 100 (Δ) and 200 (□) kPa ($D = 6.39 \times 10^{-5}$, 1.77×10^{-4}, 9.20×10^{-4}, 3.67×10^{-3} s^{-1} respectively).

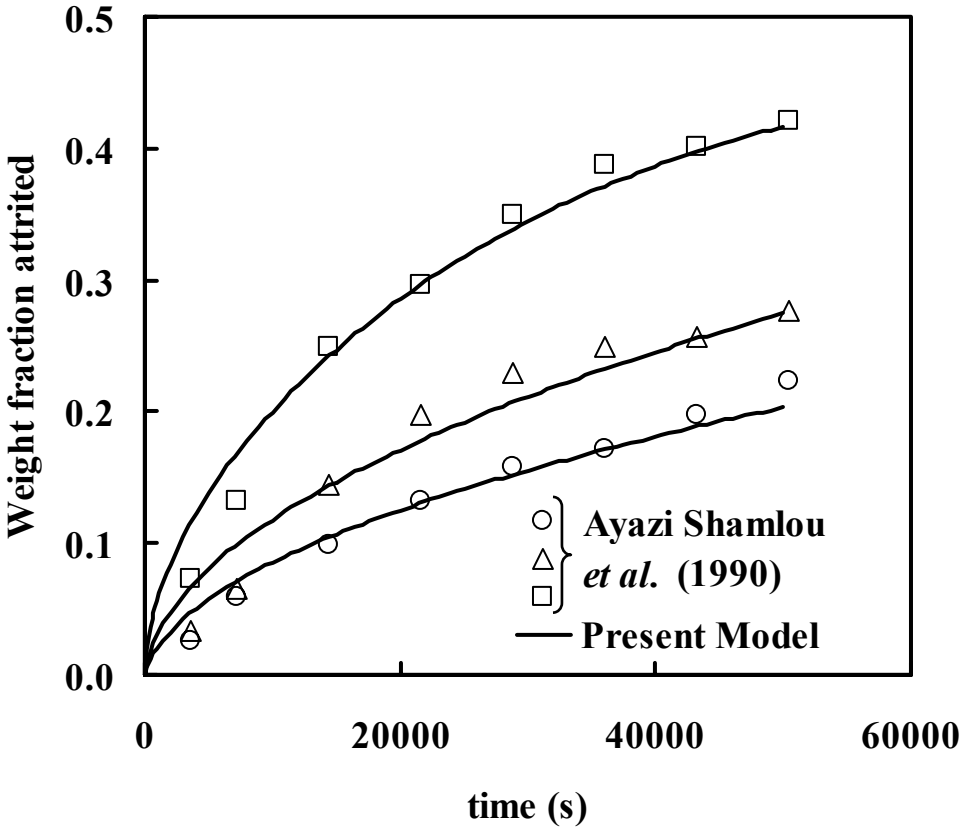

Figure 5.39 Comparisons of model with attrition data reported for experiments conducted using fluidized beds. The granular material used were 2 mm agglomerate particles made up of 63 – 90 μm soda glass beads (Ayazi Shamlou *et al.*, 1990) with varying superficial gas velocities of 1.1 (○), 1.2 (Δ) and 1.3 (□) times the minimum fluidization velocity ($D = 7.16 \times 10^{-7}$, 1.28×10^{-6}, 3.46×10^{-6} s^{-1}).

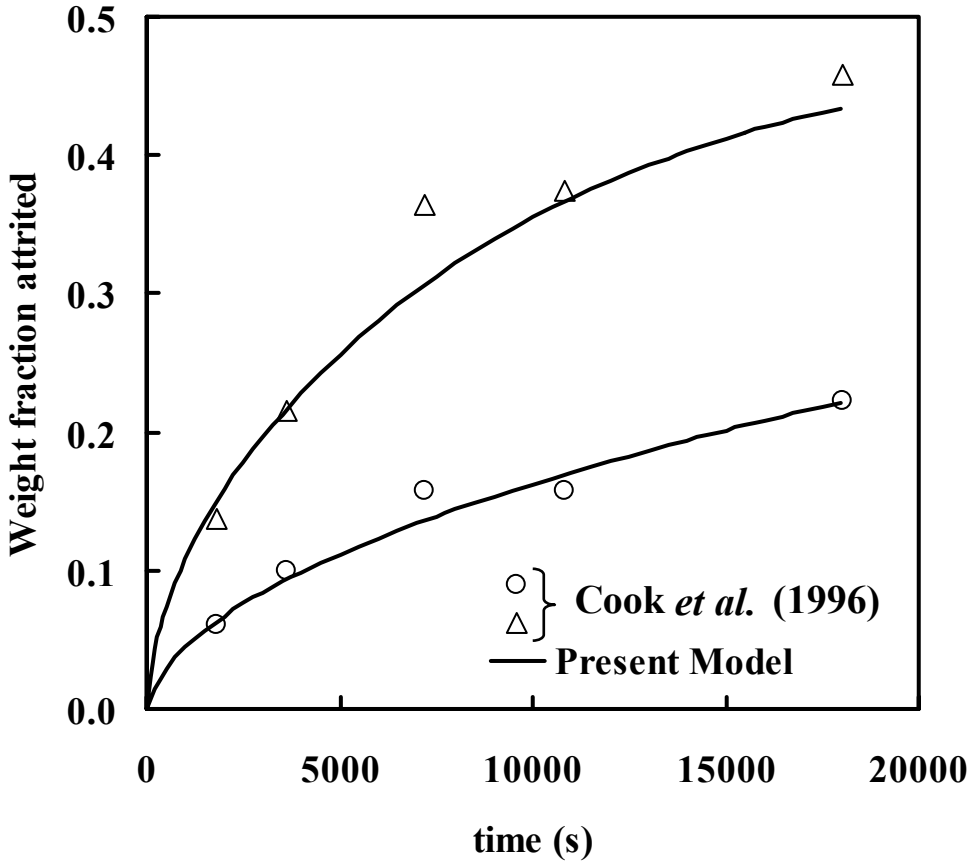

Figure 5.40 Comparisons of model with attrition data reported for experiments conducted using fluidized beds. The granular material used were 1764 μm lime sorbents in a circulating fluidized bed (Cook *et al.*, 1996) with fluidizing velocities of 2 (○) and 4 (Δ) m s^{-1} (D = 2.33 × 10^{-6}, 1.11 × 10^{-5} s^{-1}).

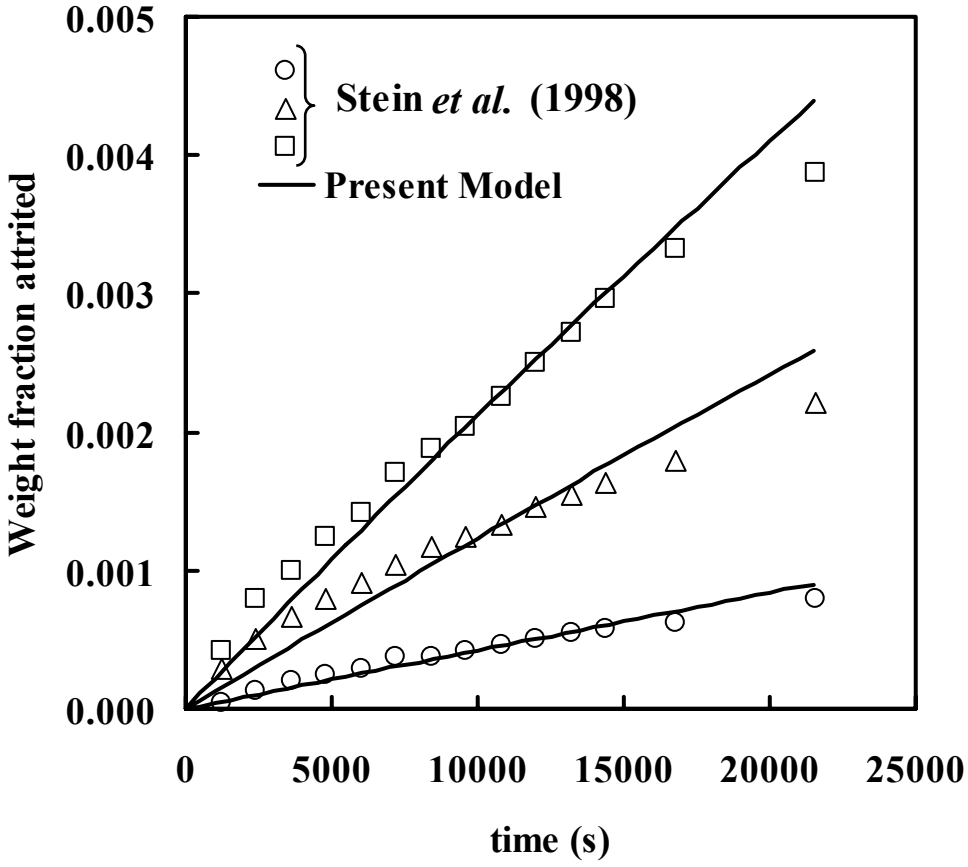

Figure 5.41 Comparisons of model with attrition data reported for experiments conducted using fluidized beds. The granular material used were 2.0 – 2.36 mm foamed glass particles (Stein *et al.*, 1998) with gas velocities 0.412 (○), 0.463 (Δ) and 0.512 (□) m s^{-1} (D = 1.06 × 10^{-9}, 3.15 × 10^{-9}, 5.49 × 10^{-9} s^{-1}).

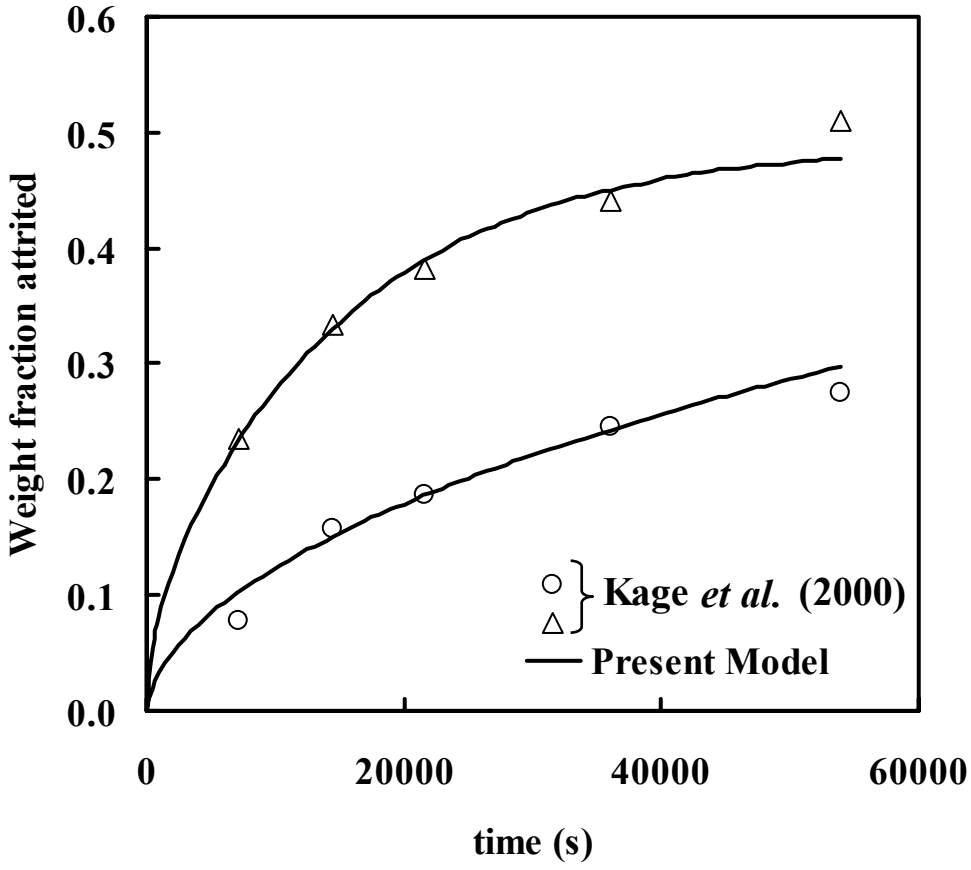

Figure 5.42 Comparisons of model with attrition data reported for experiments conducted using fluidized beds. The granular material used were 351 – 417 μm granular slug particles (Kage *et al.*, 2000) with jet velocities of 47.2 (○) and 70.7 (Δ) m s^{-1} (D = 1.40 × 10^{-6}, 6.55 × 10^{-6} s^{-1}).

attrition under the specific conditions applied. It shows larger magnitudes with increasing severity of the operating conditions used and may be functions of various system parameters or material properties of the granular materials undergoing attrition. Here, the attrition diffusivity, D, is used as the only fitting parameter. In comparison with other rate based single parameter model, the present model shows good agreement with various experimental data obtained by different research groups using different types of equipment (such as fluidized beds and annular shear cells) and granular materials. With rate based models, the inherent disadvantage is that the order of the rate equation to be used is unknown *a priori* and is often selected arbitrarily based on goodness of fit with experimental data. Consequently, a variety of rate based models have been applied and reported by different research workers. The application of any one particular model to data obtained by a different group would usually result in unsatisfactory fitting. As reviewed previously, some of these models contain two or three parameters. On the other hand, the present model contains only one parameter and reproduces the attrition behavior of all physical systems that have been reported in the published literature. It may also be mentioned at this point that the present diffusion model is not a special case of the general population balance equation which has been increasingly used to model both attrition and aggregation processes. The heart of the population balance equation is a “reaction” term, not unlike those used in simpler kinetics models, to account for the rate of disappearance of particles of a particular size range due to attrition. As such, it shares the inherent disadvantage associated with such modeling approaches as discussed above. Secondly, the general population balance equation is usually represented in the form of a continuous integro-partial-differential equation. It can also be discretized and represented as a series of ordinary differential equations. In both cases, exact solutions only exist for

some special cases and the equation usually has to be solved numerically. In contrast, the diffusion equation can be solved analytically in a relatively straightforward manner and the resulting solution can be fitted with experimental data obtained from various systems using the attrition diffusivity as the only fitting parameter.

5.7.2 DEM Simulation

Similarly, attrition data obtained from the numerical simulations are compared with the model. Figure 5.43 shows the variation of the weight fraction of particles attrited with respect to time and the corresponding values calculated using equation (3.6). In general, the higher the coefficient of restitution of particles, the larger the impact velocities during collision with other particles or with the walls of the system. This in turn gives rise to a larger overall extent of attrition. However, the relationship between coefficient of restitution and extent of attrition may be a highly nonlinear one. This is the main reason why there is a larger difference in weight fraction attrited between coefficients of restitution 0.3 and 0.4 than between 0.06 and 0.3. It may also be observed that the time scale of the attrition process is different from those seen previously. In most physical experiments, attrition may be allowed to occur over long time intervals and to large extents while in the present DEM simulations, attrition due to the flow of granular materials around a sharp bend occurs over a very short time interval and results in smaller extents of breakage. However in all cases, good agreements are obtained between the experimental or simulation results and the proposed model. Figure 5.44 shows a direct comparison of all experimental and simulation data presented earlier with the corresponding values calculated from the model.

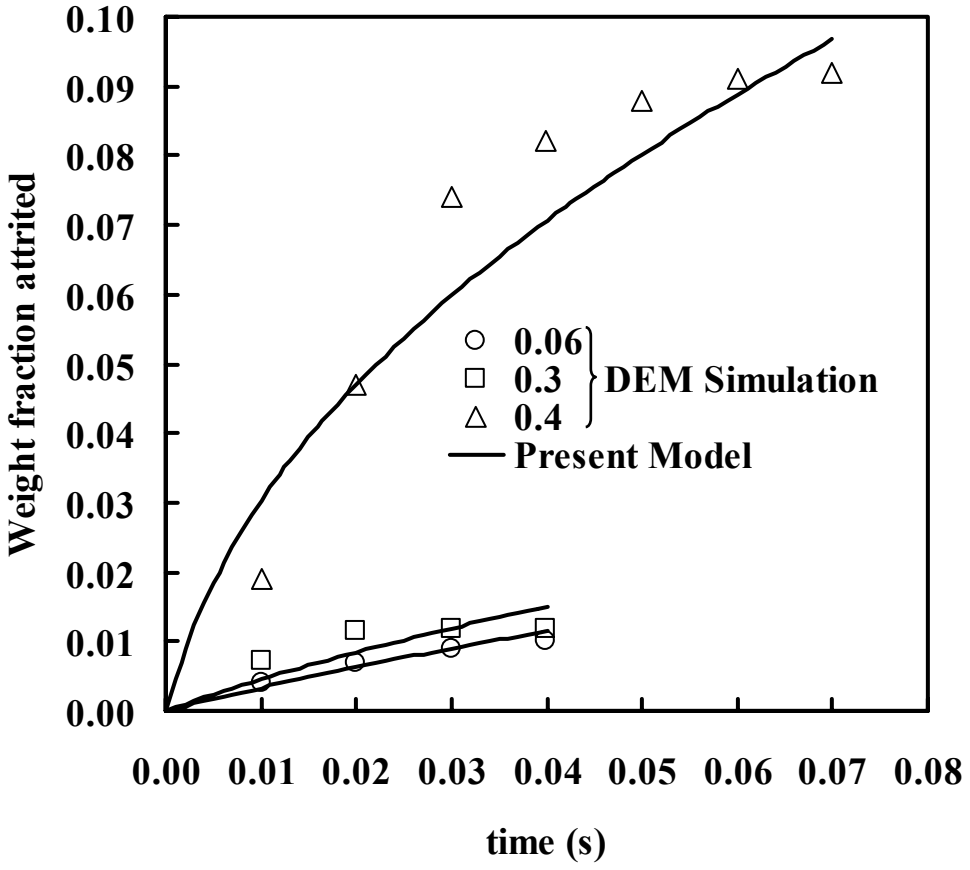

Figure 5.43 Comparisons of model with attrition data obtained from DEM simulations of pneumatic conveying around a sharp bend. The particles were simulated to have coefficients of restitution 0.06, 0.3 and 0.4 as indicated for the three cases studied respectively. The attrition diffusivities are 8.74×10^{-3}, 1.22×10^{-2} and 0.128 s^{-1} respectively.

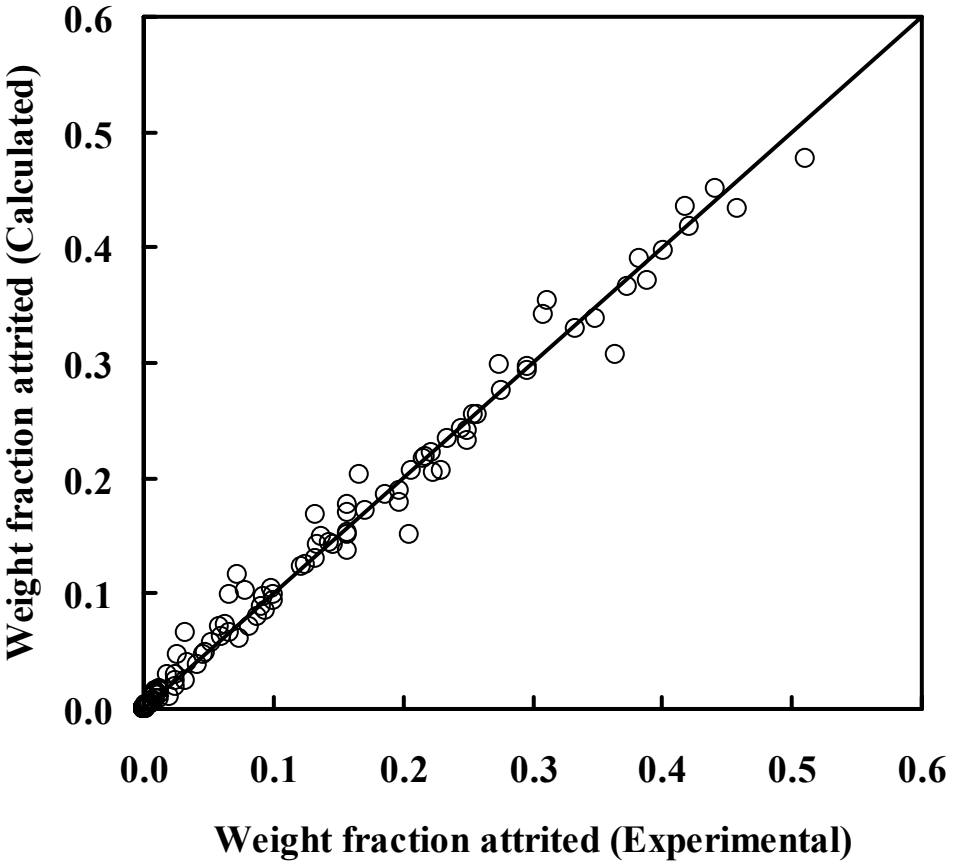

Figure 5.44 Plot of weight fractions of attrited particles calculated from the model against the corresponding data obtained either through experimentation or numerical simulations. There are a total of 130 data points taken from all previous figures presented.

The DEM simulations give further insights to the attrition processes occurring in pneumatic conveying about a sharp bend with regards to the relative importance of the two mechanisms depicted in Ghadiri's attrition model in giving rise to particle breakages. Figure 5.45 shows the number of chipping and fragmentation occurrences in the course of the attrition process for particles with different coefficients of restitution when the gas velocity used was 8 m s^{-1}. In general, chipping is a more important mechanism than fragmentation especially for particles with high values of coefficient of restitution. This is in accordance with the expectation that the proportion of particles with velocities higher than that required for chipping to take place is larger with higher coefficients of restitution. In contrast, particles which collide inelastically lose energy quickly and so have lower tendencies to undergo chipping or fragmentation. It may be noted that the same argument may also be presented in terms of granular temperature of particles and attrition diffusivity instead of particle velocities and tendencies for chipping or fragmentation to occur. That is, a system containing particles with high granular temperatures may also have a correspondingly large attrition diffusivity. Figure 5.46 shows the corresponding data obtained with a gas velocity of 10 m s^{-1}. Here, we see that the higher gas velocity used has reduced the relative effects of different values of the coefficient of restitution towards the number of chipping and fragmentation occurrences. Finally, with the use of perfectly elastic particles, Figure 5.47 shows that attrition via both mechanisms becomes very significant for all gas velocities applied. As particles do not lose energy upon collisions, two or more particles moving in opposite directions may undergo head-on collisions with sufficiently large relative impact velocities for fragmentation to occur. This explains the significant increase in the number of fragmentation

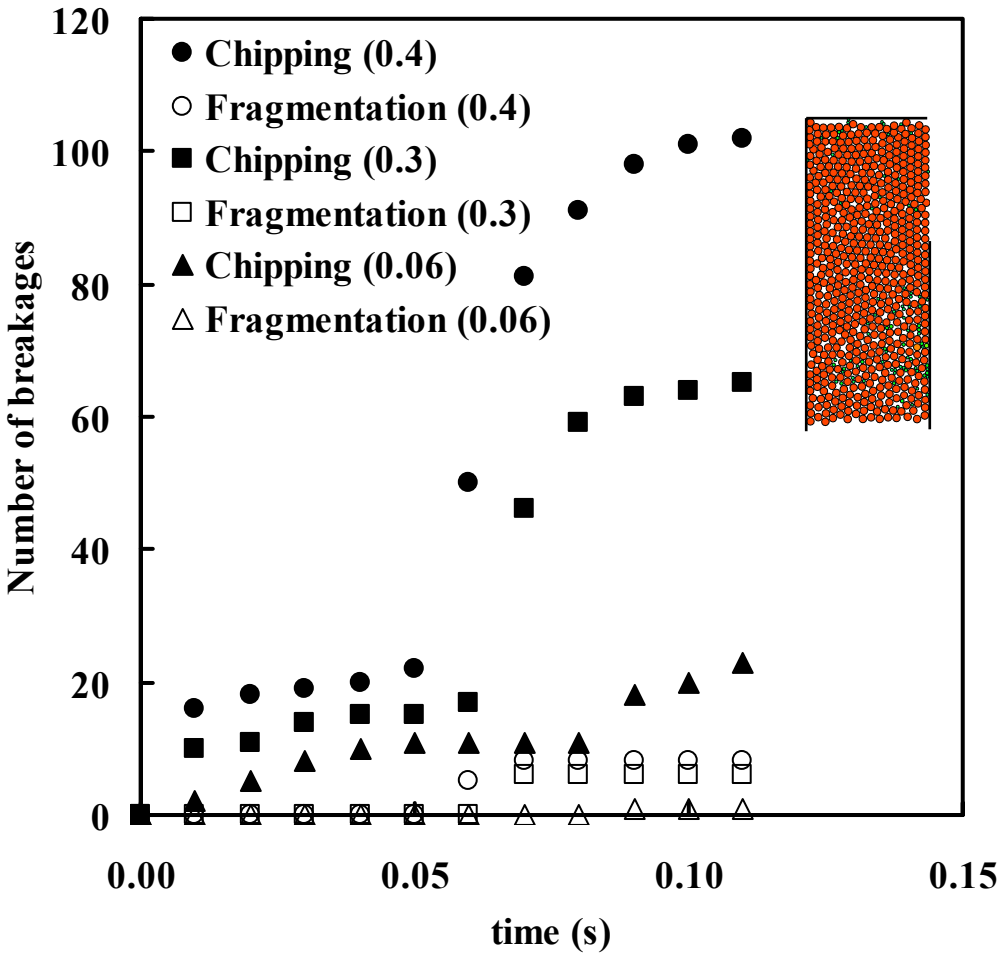

Figure 5.45 The mechanisms for granular attrition during pneumatic conveying about a sharp bend with a gas velocity of 8 m s^{-1}. The numbers indicated in the legend refer to coefficients of restitution of the particles simulated. The inset shows a snapshot of a portion of the computational domain at the end of a typical simulation illustrating the size distribution of particles for the case where coefficient of restitution equals 0.4.

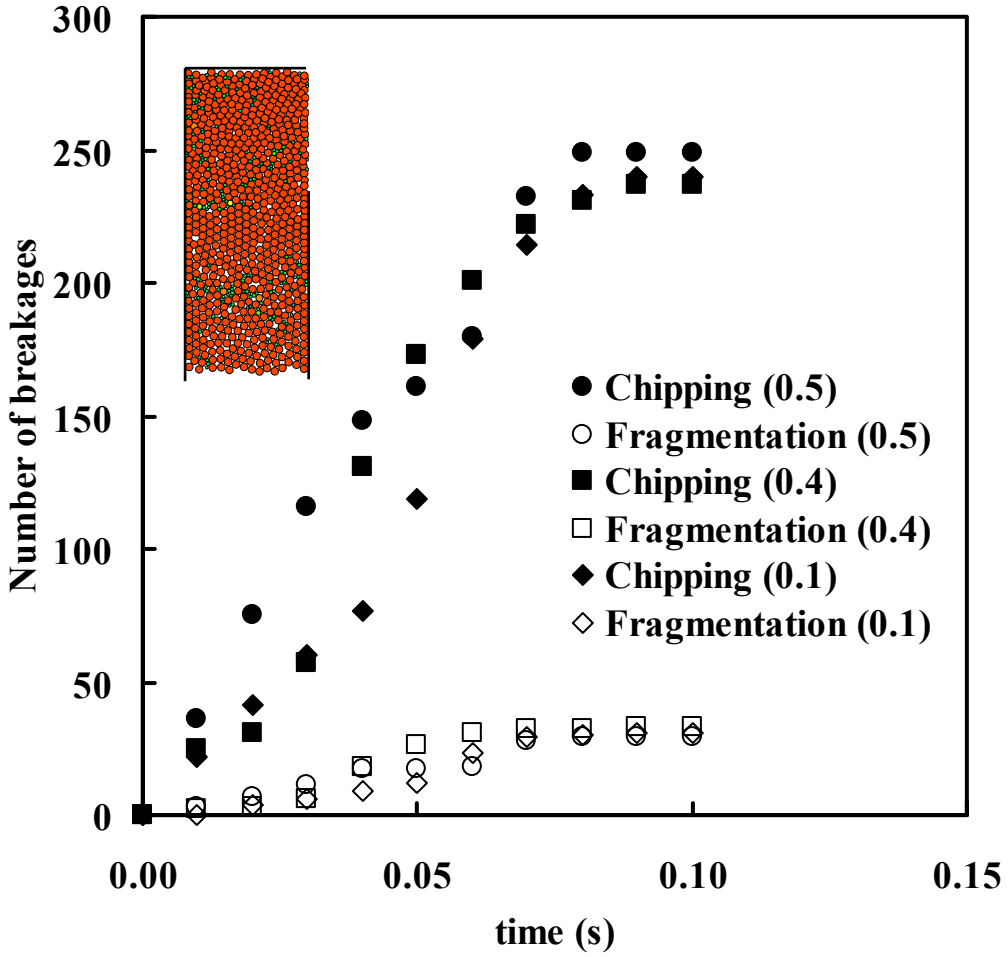

Figure 5.46 The mechanisms for granular attrition during pneumatic conveying about a sharp bend with a gas velocity of 10 m s^{-1}. The numbers indicated in the legend refer to coefficients of restitution of the particles simulated. The inset shows a snapshot of a portion of the computational domain at the end of a typical simulation illustrating the size distribution of particles for the case where coefficient of restitution equals 0.4.

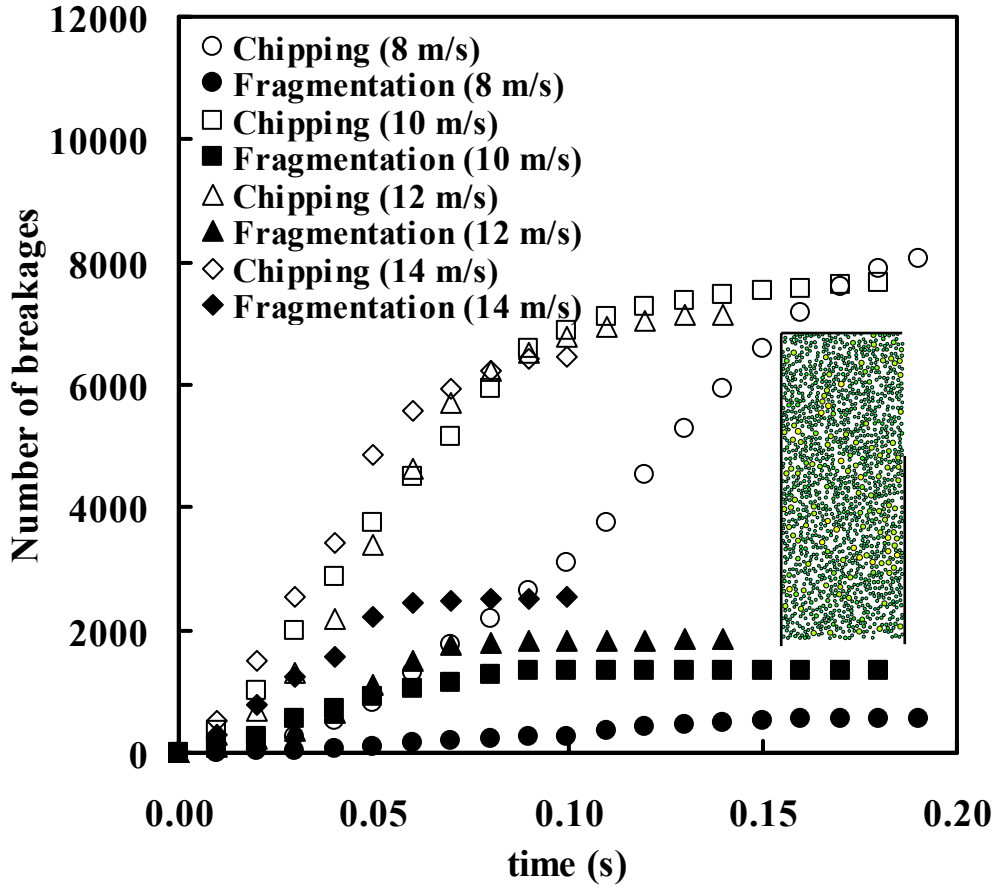

Figure 5.47 The number of chipping and fragmentation occurrences for perfectly elastic particles conveyed at various gas velocities. The inset shows a snapshot of a portion of the computational domain at the end of a typical simulation illustrating the size distribution of particles for the case where gas velocity equals 8 m s^{-1}.

occurrences compared with those seen in the previous two figures. Figure 5.48 shows the particle size distribution obtained at the end of the attrition process for each simulation case described above.

5.7.3 Further Analysis

A further analysis of the model presented in equation (3.6) will now be made to show a possible correspondence with the Gwyn formulation. The exponential term is expressed as a Taylor series and after some rearrangements, the resulting equation is written as (Appendix C):

$$W' = \sum_{\substack{n=1 \\ (n\ \text{odd})}}^{\infty} \sum_{m=1}^{\infty} K_{n,m} t^m \tag{5.1}$$

where $K_{n,m} = \dfrac{4(-1)^{m+1}\left(n^2\pi^2\right)^{m-1} D^m}{m!}$. In comparison with the Gwyn formulation given by $W' = Kt^m$, it seems that the latter is one term from the infinite series in equation (5.1) or an averaged representation of it. As such, the present model may be a generalization of this empirical formulation. Equation (3.6) also shows correct asymptotic behaviors with W' approaching the physically realistic value of 1.0 at large times. The Gwyn formulation, on the other hand, allows weight fraction to become larger than one and thereafter increase without bound as time approaches infinity.

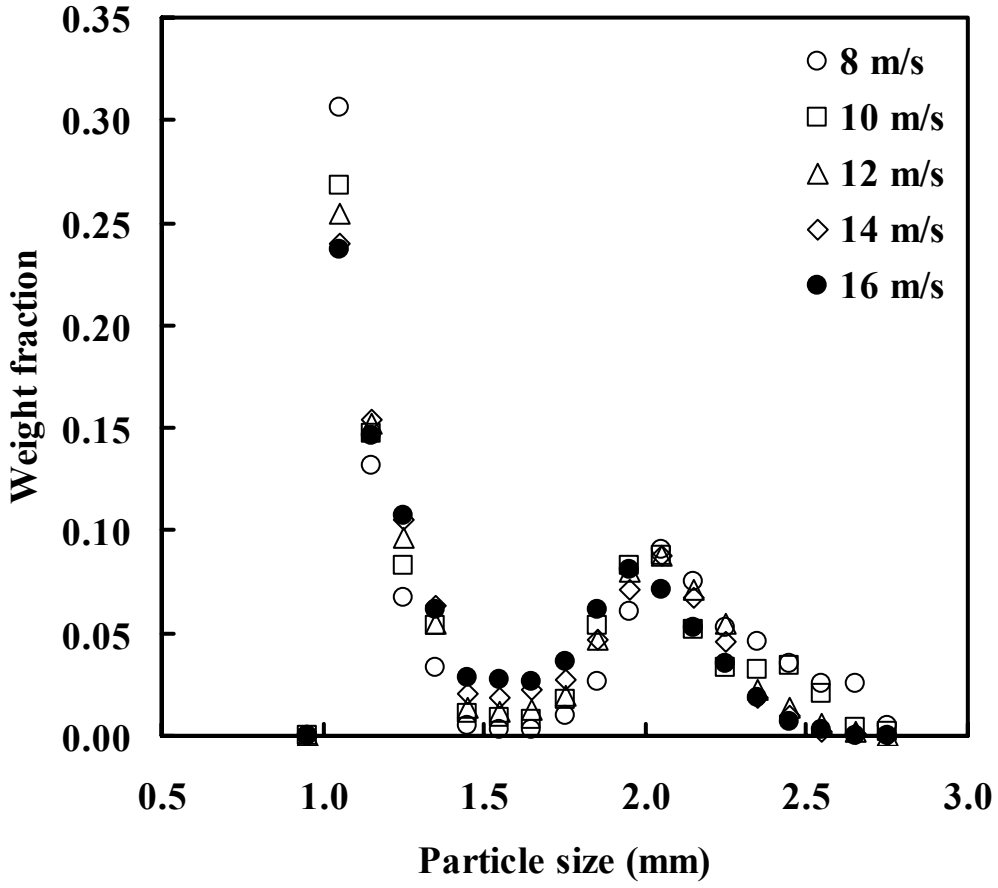

Figure 5.48 Particle size distribution obtained at the end of the attrition process for perfectly elastic particles at different gas velocities

5.8 Liquid Fluidization

5.8.1 CFD-DEM Simulation of Voidage Waves

Figure 5.49 shows 4 consecutive snapshots of the fluidized bed system obtained from the CFD-DEM simulation. The time interval between each snapshot is 0.05 s and the dimensions are 16 cm (height) by 2 cm (width). Alternating bands of dense and dilute solid concentrations may be clearly discerned from the figure. There are approximately two major dense and dilute phases present in the system under the present set of operating conditions. The coherent motion of these phases of the voidage wave up along the fluidized bed may also be observed. As such, the present simulation has been successful in reproducing the main qualitative feature of the phenomenon associated with voidage wave instability in a liquid fluidization system. It may also be stated that in the absence of a vibrating base, the fluidized bed was observed to expand slightly upon introduction of liquid with a superficial velocity and remain homogeneously fluidized with minimal tendency to develop such voidage wave instability (data not shown for brevity). This implied that the system was intrinsically stable in the absence of external perturbations while any internal noises were not sufficiently significant to cause instability. This was true for both liquid superficial velocities of 0.018 m s^{-1} and 0.030 m s^{-1} investigated in the initial phase of the present study. At the lower liquid superficial velocity of 0.018 m s^{-1} and in the presence of a vibrating base, a small amount of voidage waves could be observed in the system. These formed at the vibrating base but were propagated only a short distance up the bed. As the fluidized bed at this low superficial velocity was only expanded slightly and close to a packed condition, the likely reason for attenuation of the voidage waves could be the high effective solid viscosity. In contrast, when the

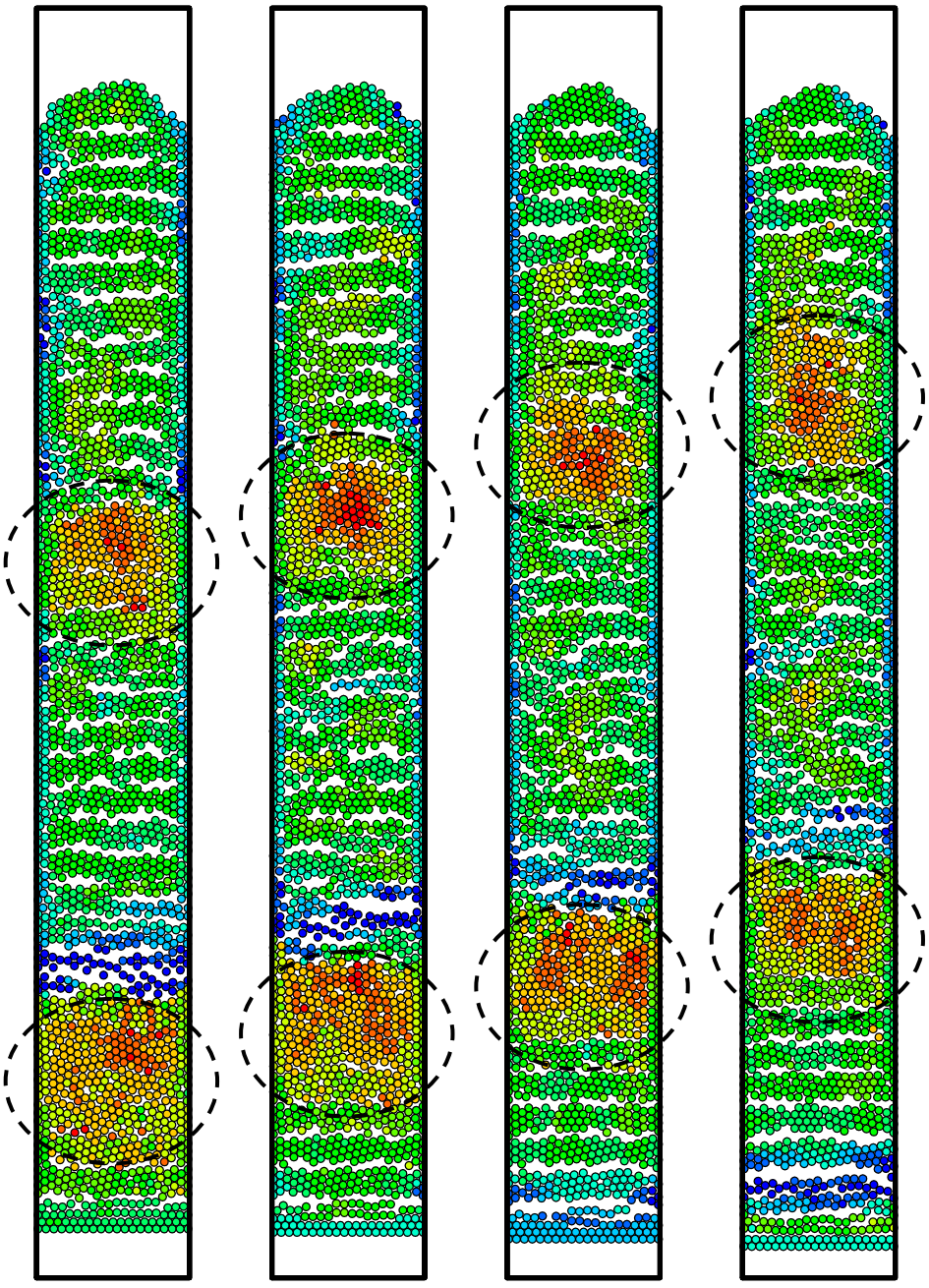

Figure 5.49 Voidage waves in a liquid fluidized bed operating at the following conditions: Liquid superficial velocity at inlet of 0.030 m s^{-1}, vibrating amplitude and frequency of base of 1.5 mm and 2 Hz respectively. Time interval between each frame shown is 0.05 s. Dimensions of the system are 16 cm (height) by 2 cm (width). The center of each major dense region of the voidage wave is enclosed in a dashed circle to aid in visualizing the propagation of the wave along the bed. Color online: Particles are color-coded according to the vertical velocity, increasing from blue (-0.030 m s^{-1}) to green to red (0.030 m s^{-1}).

liquid superficial velocity applied was 0.030 m s^{-1} such that the bed was expanded to a larger extent, voidage instabilities in the form of waves of high and low solid concentrations could be observed traveling up the expanded bed as shown in Figure 5.49. These clearly show the unstable nature of the system towards external perturbations and the convective characteristic of the resulting instability.

It may be noted that Duru *et al.* (2002) demonstrated in their experimental investigation of such voidage wave instabilities that the shape of these waves evolves along the bed and may reach a saturated state after a sufficient distance of wave propagation. Nicolas *et al.* (1999) applied a cnoidal function to describe quantitatively the shapes of such waves after attaining the state of saturation. In the present study, a shorter bed height of about 12 cm was used in the CFD-DEM simulations in consideration of the computational requirements involved. A similar bed height was also used in the experiments so as to have a good basis for comparison between the two approaches. As seen in Figure 5.49 previously, the structure of the voidage wave formed is such that about two wavelengths of the wave are developed over the entire bed. In other words, the voidage wave propagates for a distance of about two wavelengths along the bed and so may not reach the state of saturation. This may also be the reason why in the absence of an imposed external perturbation, where the natural or intrinsic perturbations due to flow of liquid at the base would then be only infinitesimally small in such cases, no voidage wave was seen to develop over the entire fluidized bed simulated. However, it may be noted that the state of saturation of the voidage waves or lack thereof does not affect the interpretation of the results obtained throughout this entire study. Duru *et al.* (2002) observed empirically the bed height required for saturation of voidage waves to occur by measuring experimentally

the shapes of the waves at various vertical positions along the bed. Nevertheless, this aspect of the voidage waves observed in the present fluidization system used will be discussed more quantitatively in a later section.

The nature of particle-particle and particle-wall collisions may be an important factor which affects the structure of the voidage waves formed, especially in the relatively dense fluidization system used in the present study where every particle is almost certainly always in contact with one or more other particles at any instant of time. In particular, the coefficient of restitution of particles may play an important role in such voidage wave phenomenon. Derksen and Sundaresan (2006) carried out direct numerical simulations of voidage waves in liquid fluidization systems similar to those considered in the present study by applying the lattice-Boltzmann method to compute the fluid flow field and a hard sphere collision model to simulate solid particles. They reported that the coefficients of restitution and friction had only weak influences on the structure of the voidage waves formed when these parameter values were varied in the range 0.8 – 1.0 and 0.0 – 0.2 respectively. In this study, in order to characterize the importance of the coefficient of restitution of particles on the voidage wave structure, the previous simulation where a liquid superficial velocity of 0.030 m s^{-1} was applied was repeated for the case where the coefficient of restitution of the solid particles was 0.1. All other operating conditions were maintained identical to those applied in the previous case. Figure 5.50 shows the resulting structure of the voidage waves formed in the fluidization system. The dense and dilute phases and the coherent motions of these phases are similar to those seen in Figure 5.49 previously for particles with a coefficient of restitution of 0.9. As such, the elasticity of collisions

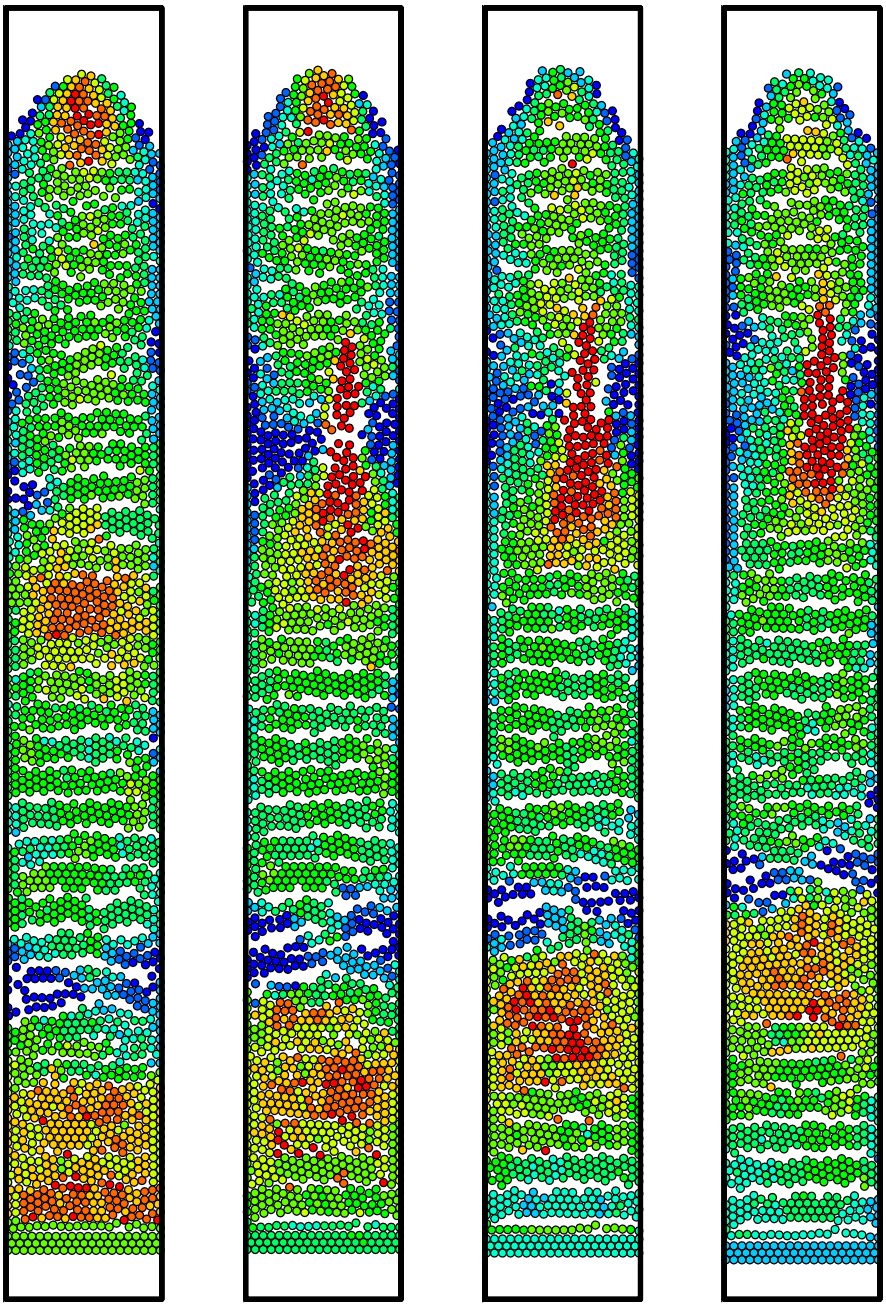

Figure 5.50 Voidage waves in a liquid fluidized bed containing inelastic solid particles with coefficient of restitution 0.1. Other parameters and operating conditions are as described in the caption of Figure 5.49.

among particles does not seem to have a significant effect, at least in a qualitative sense, on voidage wave formation in the present liquid fluidization system. However, there may be subtle quantitative differences such as a thicker layer of particles descending along the side walls of the column and the formation of streaks of particles having relatively high velocities near the top of the bed, as may be discerned from the snapshots shown in Figure 5.50.

Similarly, the frequency of vibration of the base may also play an important role in determining the structure of the voidage waves. It may be observed from Figure 5.51 that the macroscopic structure of the voidage wave has been changed with a reduction in the vibrating frequency to 1 Hz while keeping all other parameter values identical to those used in producing the simulation result shown in Figure 5.49. Both the solid distribution in the fluidized bed and the velocity vectors of the particles shown in the figure suggest that there is only one major dense and dilute phase present. Nevertheless, the characteristic ascending and descending behavior of particles in these dense and dilute phases, respectively, has remained unchanged. This aspect of voidage wave instabilities in liquid fluidized beds will not be within the scope of the present study. In the following sections, detailed quantitative analyses of the voidage wave phenomenon corresponding to the case where liquid superficial velocity is 0.030 m s^{-1}, coefficient of restitution of solid particles is 0.9 and vibrating frequency of the base is 2 Hz would be provided.

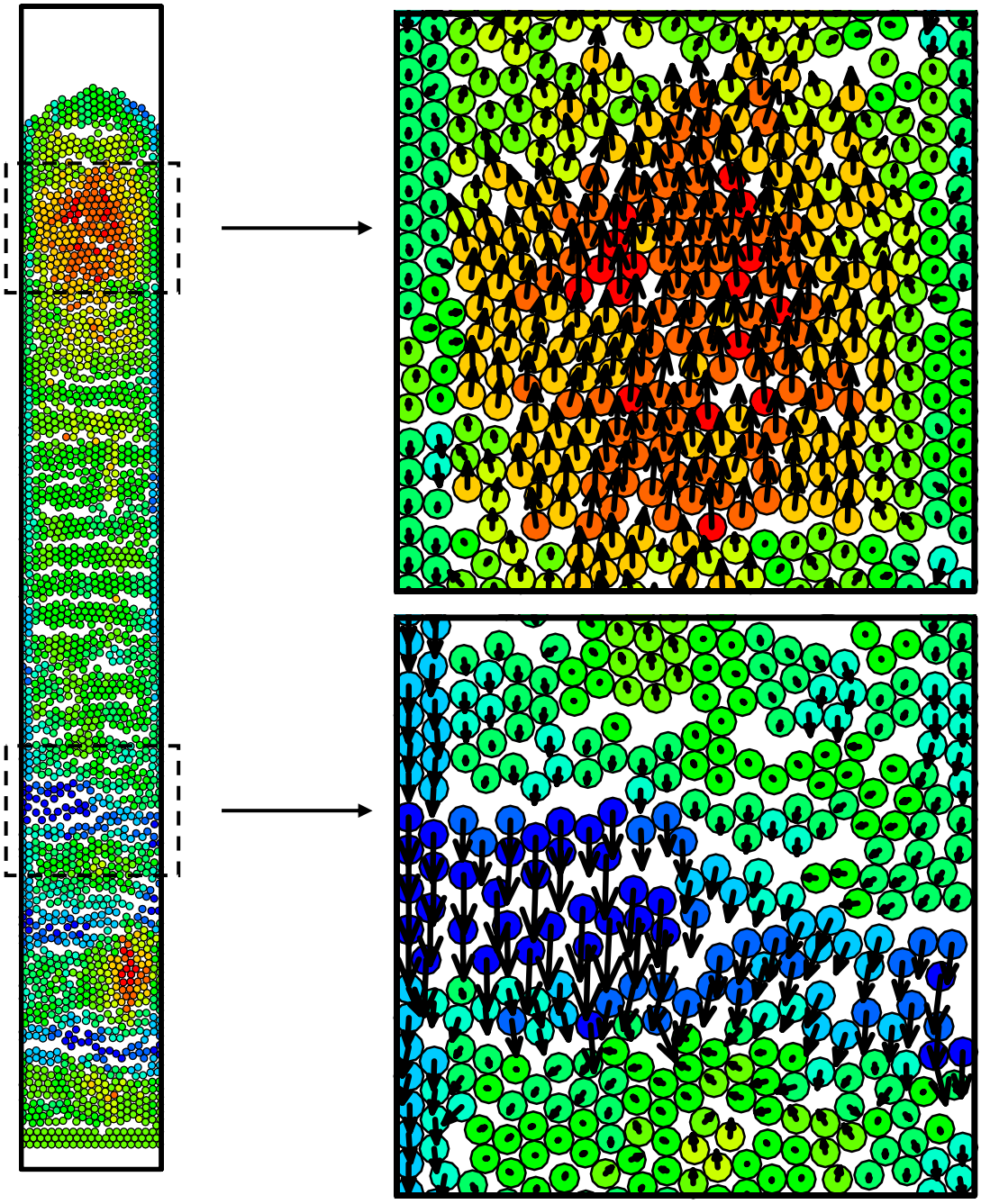

Figure 5.51 Voidage wave formed at a vibrating frequency of 1 Hz. Other operating parameters are as for Figure 5.49. Color online: Particles are color-coded according to the vertical velocity, increasing from blue (-0.030 m s^{-1}) to green to red (0.030 m s^{-1}).

5.8.2 Solid Volume Fraction

Figure 5.52 shows the calibration of light intensity transmitted against solid volume fraction obtained using the light scattering method. Each light intensity signal was averaged over 200 s and measurements were made at 1 cm, 5 cm and 10 cm above the base of the column. It may be observed that the transmitted light intensities varied strongly with both solid volume fraction and flow rate. This calibration curve was used for all subsequent solid volume fraction measurements.

Spatial averaging of solid fraction were performed at different instants of time by calculating the ratio of total volume of particles within a 2 mm (height) by 2 cm (width) domain 5 cm above the vibrating base to the volume of that domain. An ensemble average was then calculated by superimposing together a number of such profiles ensuring that the phases were matched to one another in this process. Figures 5.53a, b show the ensemble averaged solid fraction profile at 5 cm above the vibrating base with respect to time and the corresponding power spectrum obtained by fast Fourier Transform (FFT) of the instantaneous solid fraction signal respectively obtained from CFD-DEM simulations. Due to high computational requirements, the ensemble averaging was performed using 20 sets of solid fraction data from the CFD-DEM simulations, each over a time interval of 3 s. Figure 5.53c shows the corresponding data obtained from the experiments conducted and ensemble averaged over 120 waveforms for solid volume fraction. Similarly, Figure 5.53d shows quantitatively that the characteristic frequency of the voidage wave is also equal to that of the vibrating base. In addition, there may be higher or lower harmonics in the vicinity of this characteristic frequency (in the range 1 – 5 Hz) (Figure 5.53b).

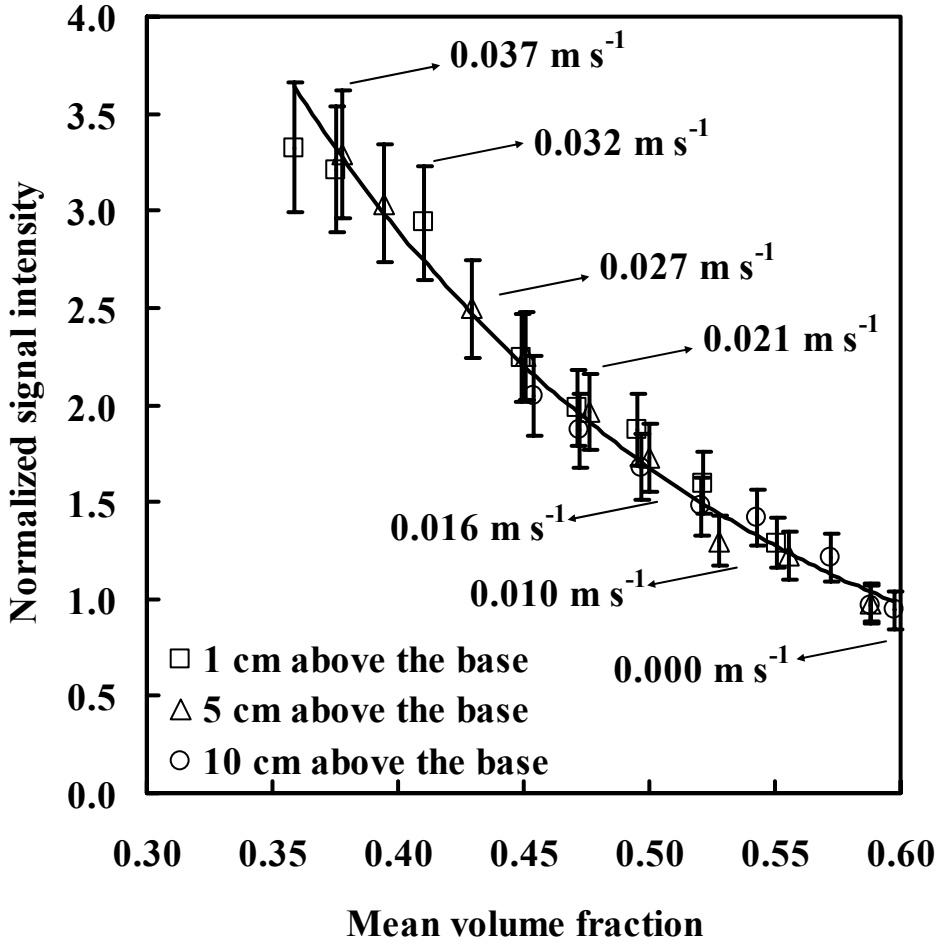

Figure 5.52 Calibration of light intensity transmitted against mean solid volume fraction using light scattering method. Signal intensities are normalized with respect to those obtained at zero flow rate (packed bed condition). Liquid superficial velocities required to achieve the respective mean volume fractions are indicated.

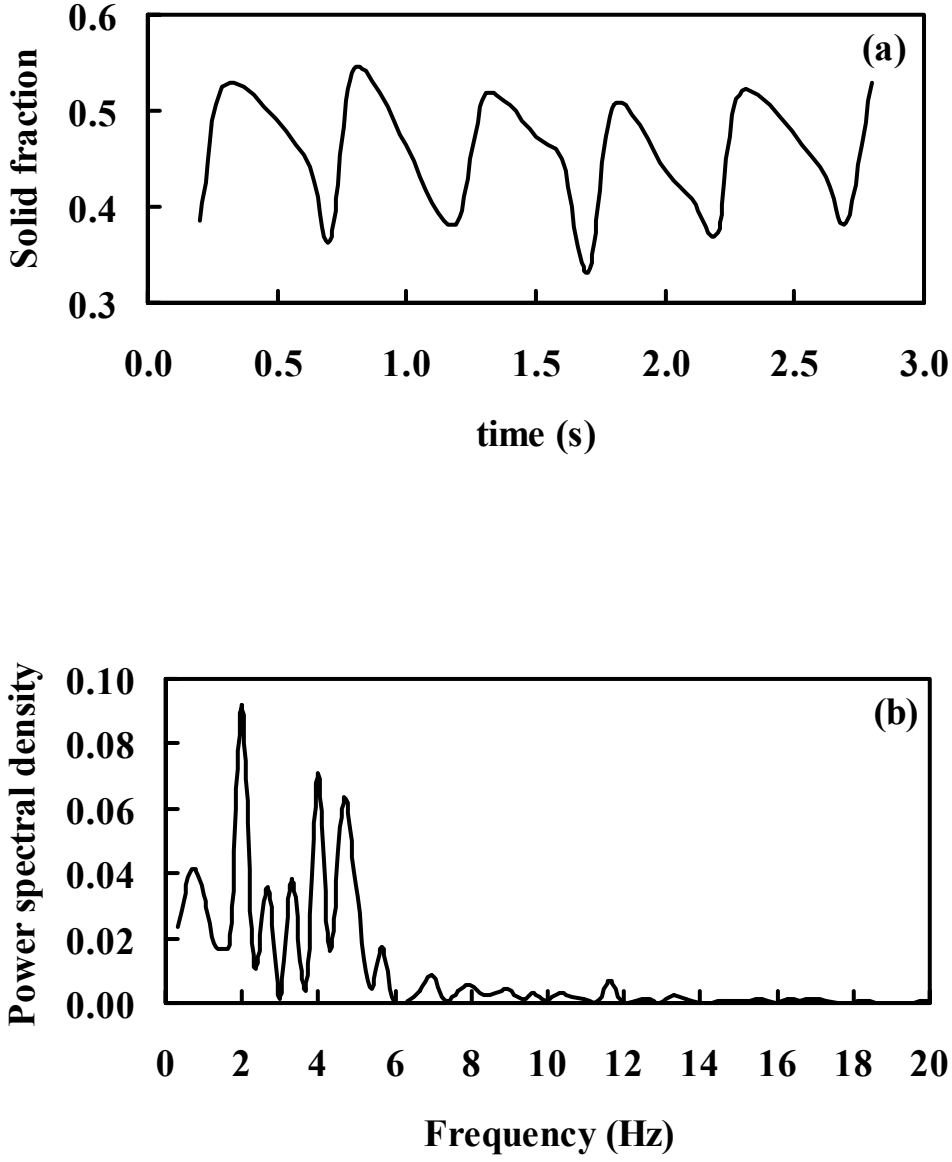

Figure 5.53 (a) Ensemble averaged variation of spatially averaged solid fraction at 5 cm above the vibrating base with respect to time obtained from CFD-DEM simulations. (b) Corresponding power spectral density of the time varying solid fraction.

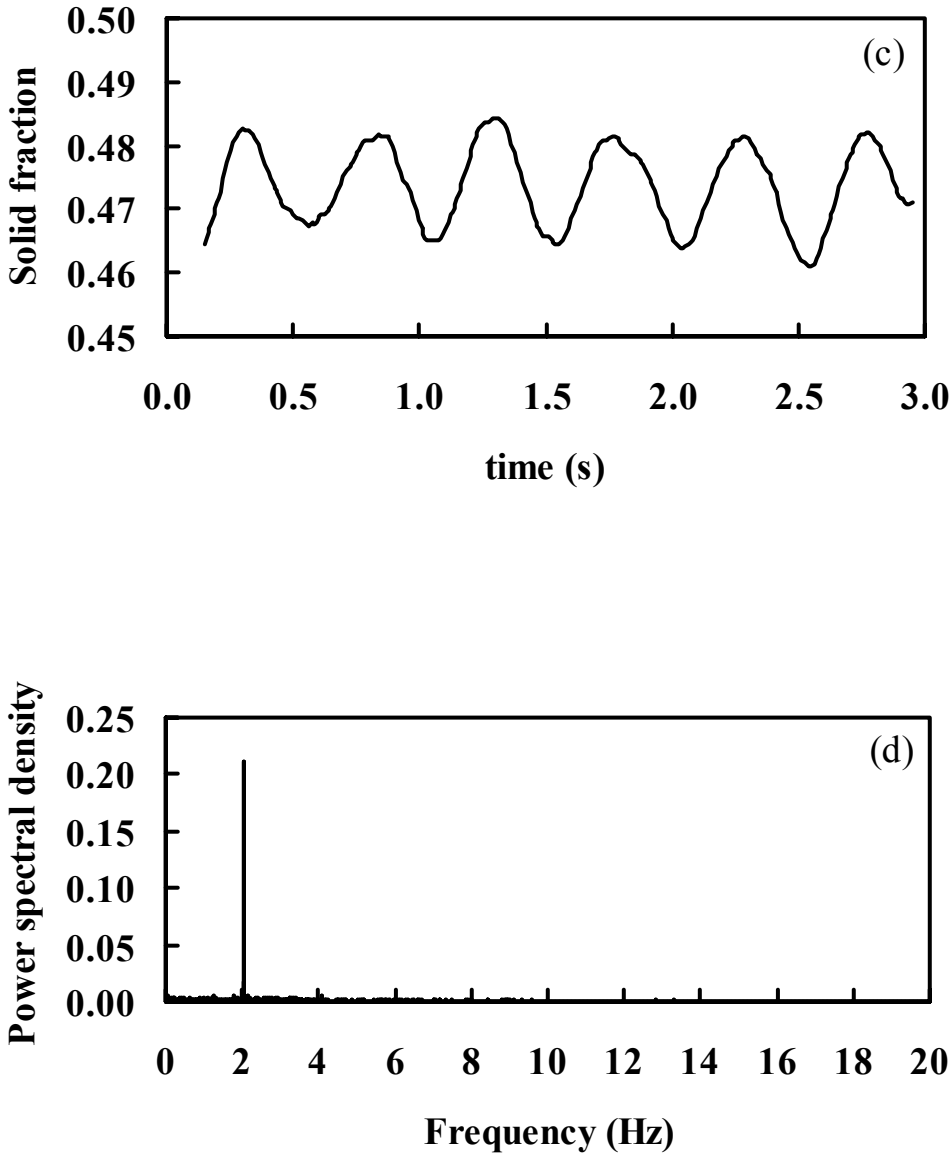

Figure 5.53 (c) Ensemble averaged variation of spatially averaged solid fraction at 5 cm above the vibrating base with respect to time obtained from experiments. (d) Corresponding power spectral density of the time varying solid fraction.

Figures 5.54a, b show the corresponding power spectral densities of solid fraction obtained at positions 1 cm and 10 cm above the vibrating base respectively from the CFD-DEM simulations. On comparison, it may be observed that the driving frequency of 2 Hz of the base has been manifested as the characteristic frequency of the voidage wave up to a height of 10 cm along the fluidized bed. However, the various harmonics mentioned are propagated a smaller distance. Other than the frequency which is exactly twice (4 Hz) that of the characteristic frequency, these are no longer present in the solid fraction signal at 10 cm from the vibrating base. The corresponding power spectral densities obtained from experiments show a similar attenuation of the voidage wave along the height of the bed. A qualitatively comparable disappearance of harmonics may also be observed (insets to Figures 5.54a, b). Duru *et al.* (2002) showed in their stability diagram that there exists a maximum limit of the frequency of an external perturbation for voidage wave instabilities to develop in such liquid fluidized bed systems. The higher harmonics of voidage waves discussed above may correspond to higher frequency modes of such instability waves which have been shown by the previous workers to be more stable. These have a tendency to be attenuated with vertical position along the bed. As such, the wave which persists at higher vertical positions as observed in the present study may be the dominantly unstable mode whose frequency matches that of the external perturbation imposed while other more stable modes are eventually damped out. Figure 5.54c shows the evolution of the shape of voidage waves obtained from the CFD-DEM simulations. It may be observed that the wave shape at 5 cm above the vibrating base is sinusoidal with a sharp peak while near the top of the expanded bed at 14 cm above the base, it becomes flatter showing signs of forming a plateau. This

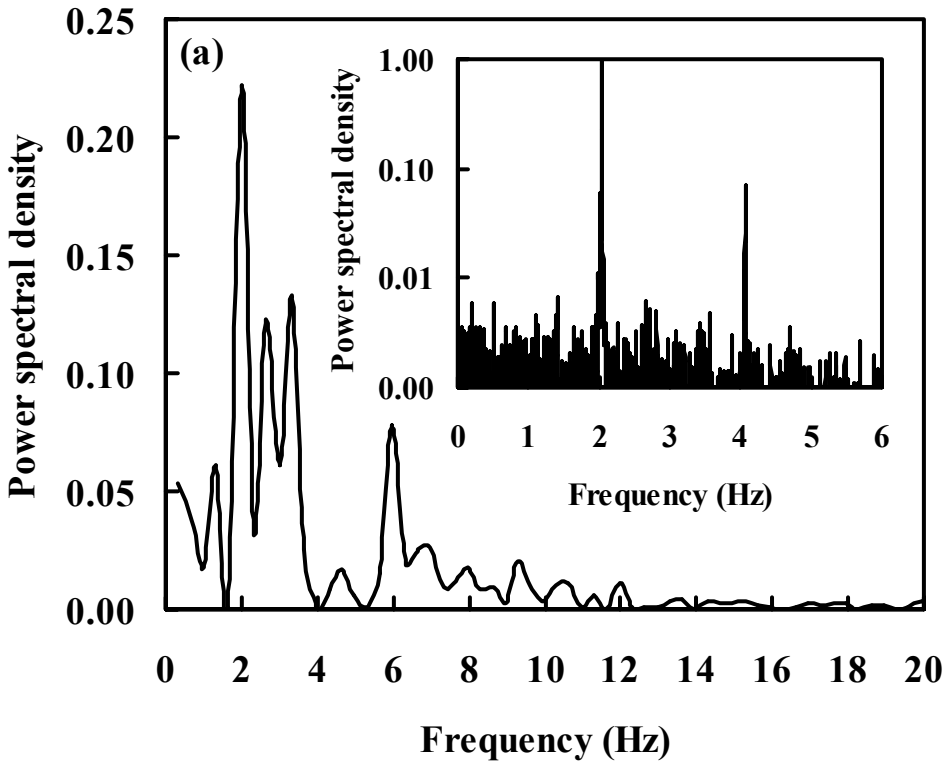

Figure 5.54a Power spectral density of solid fraction profile obtained at 1 cm above the vibrating base from CFD-DEM simulations. The inset shows the corresponding power spectral densities obtained from experiments.

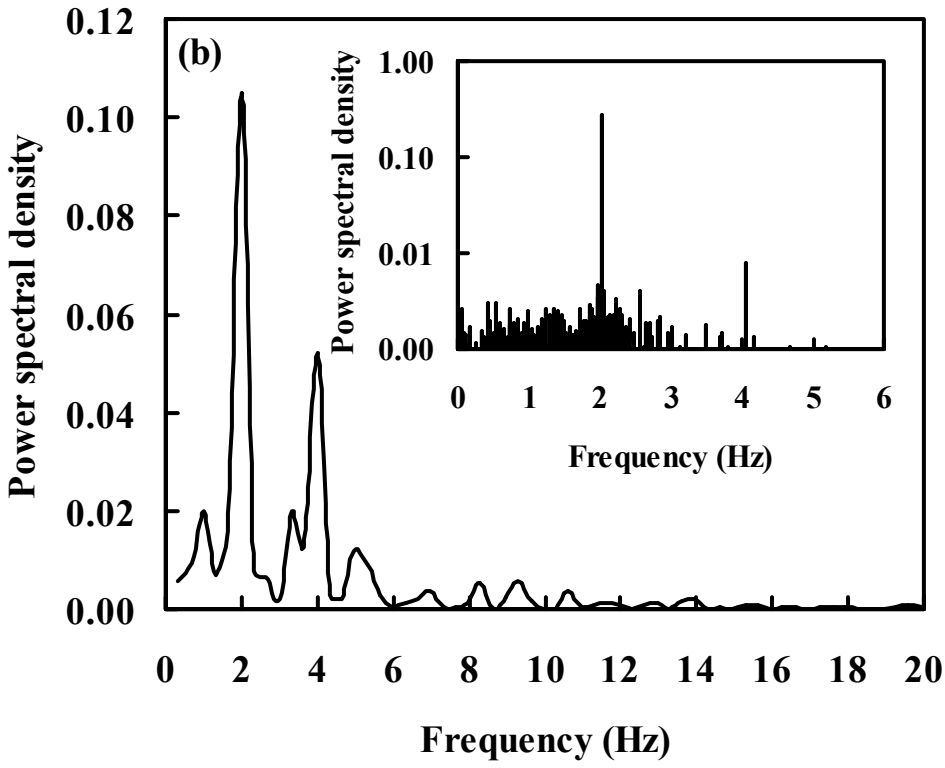

Figure 5.54b Power spectral density of solid fraction profile obtained at 10 cm above the vibrating base from CFD-DEM simulations. The inset shows the corresponding power spectral densities obtained from experiments.

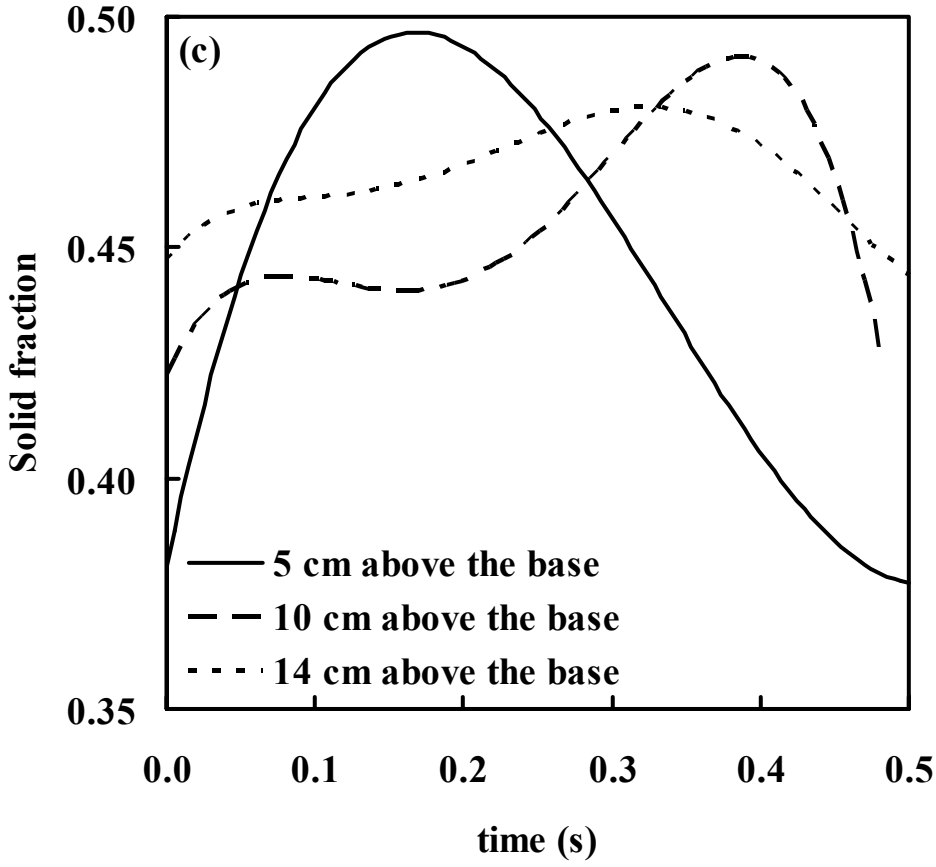

Figure 5.54c Evolution of voidage wave shape with vertical position along the bed.

indicates evolution of the voidage waves towards the state of saturation as they propagate along the bed and is consistent with the observations reported by Duru *et al.* (2002). It may be noted that a complete state of saturation of the voidage waves may not be attained in the present fluidization system as pointed out earlier. Nevertheless, the results shown here verify the adequacy of the current CFD-DEM model in capturing the physics involved and associated with voidage wave evolution and saturation.

Glasser *et al.* (1997) carried out linear stability analyses of a uniform base state of a solid-liquid suspension of 1.0 mm glass beads in water using the continuum continuity and momentum equations to determine the most unstable one-dimensional eigenvalue and the corresponding eigenfunction for solid fraction. The grey scale plot of this eigenfunction corresponding to the volume fraction of solids obtained by these authors is compared with a typical snapshot of the physical structure of a voidage wave obtained from the present CFD-DEM simulations (Figures 5.55a, b). The simulations were carried out using a base vibrating frequency of 3 Hz with other parameters and operating conditions identical to those of Figure 5.49. It may be seen in Figure 5.55b that four dense phases (regions of high solid concentration) are present in the section of the fluidized bed shown with a relatively more dilute region in between. On closer inspection, it may be easily discerned that this dilute region is further comprised of alternating layers of high and low solid concentrations. It is highly unlikely that such structures are voidage waves with higher wavenumbers corresponding to higher frequency perturbation modes as these are theoretically more stable (Duru *et al.*, 2002). Furthermore, no characteristic peak at the characteristic frequency of such structures was observed in the power spectral density profiles

shown earlier even though they were also present in those simulation results. As such, these layered structures may represent intermediate stages of decompactification of an originally dense phase whereby particles start to move downwards, causing the dense region to break up into smaller layers of particles. These structures will not be considered further in the present study. In Figure 5.55b, the characteristic wavelength of the voidage waves, λ_y, given by the distance between the two dense phases indicated is estimated to be about 3.5 cm. Following Glasser *et al.* (1997), the characteristic dimensionless wavelength, λ'_y, was obtained by non-dimensionalizing with respect to a characteristic length scale given by $L = \sqrt{\frac{Av_t}{\rho_p g}}$ and the corresponding dimensionless wavenumber was calculated by $k_y = \frac{2\pi}{\lambda'_y}$. Here, A is a constant equal to 50 cP and v_t is the particle terminal velocity. The resulting value for k_y was estimated to be about 0.103 which is lower than the value of 0.204 applied by Glasser *et al.* (1997) in their linear stability analysis. The corresponding solid fraction profiles are compared quantitatively in Figures 5.55c, d. There is a qualitative agreement in the voidage wave structure obtained from the two different calculation approaches. The present solid fraction profile shows lower overall solid fraction along one wavelength of the voidage wave in comparison with that obtained by Glasser *et al.* (1997). This may be due to the lower overall solid fraction used in the present simulation (~0.5) compared with that used by the previous researchers (~0.57). It may also be noted that the voidage waves computed by the previous researchers, following the principle of linear stability analysis, resulted from perturbations applied over a homogeneously fluidized system while in the present approach, an oscillating base

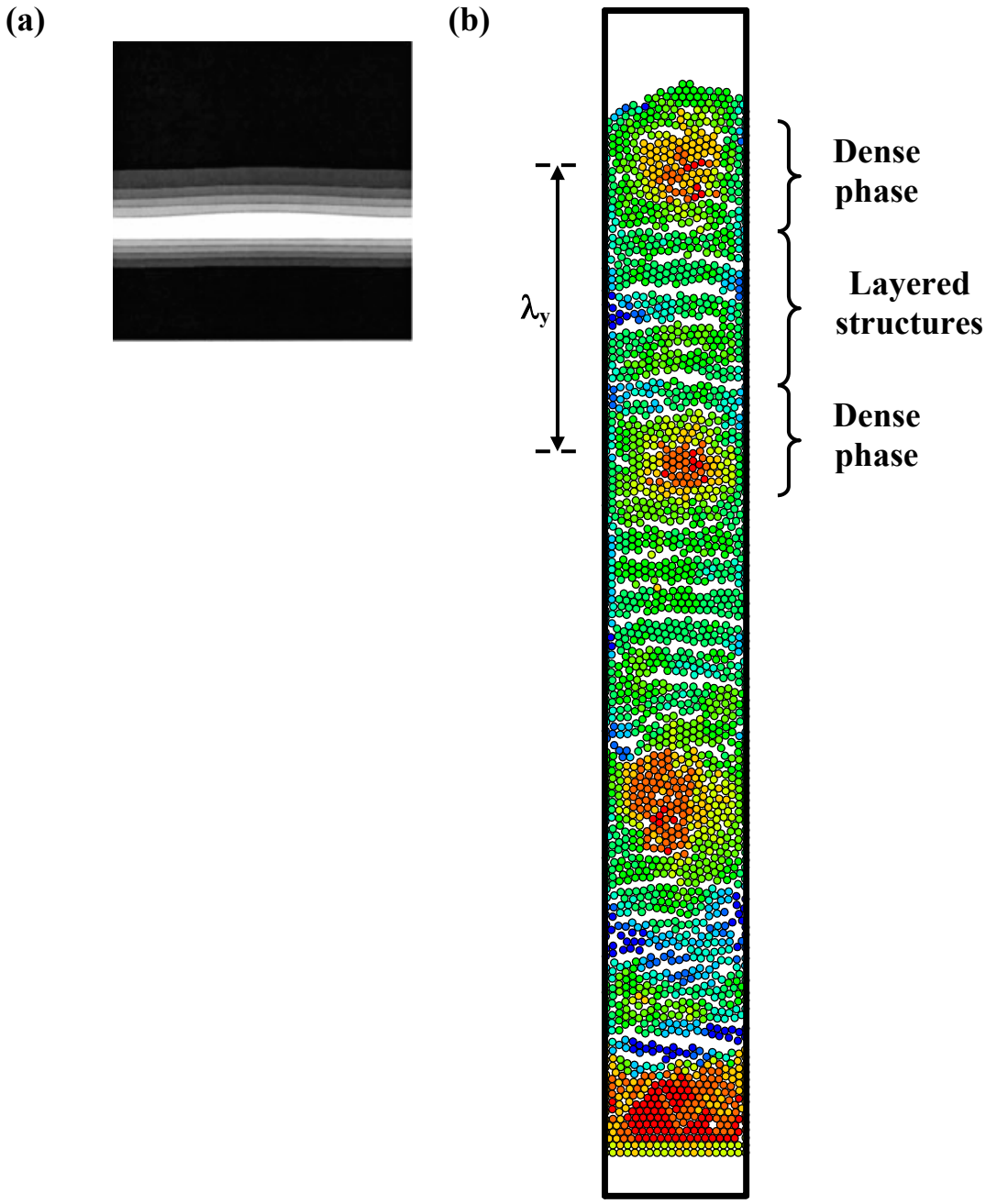

Figure 5.55 Voidage structure obtained from (a) linear stability analysis of continuum model (Glasser *et al.*, 1997) and (b) CFD-DEM simulations using base vibrating frequency of 3 Hz with other parameters and operating conditions as described in the caption of Figure 5.49. Color online: Particles are color-coded according to the vertical velocity, increasing from blue (-0.030 m s^{-1}) to green to red (0.030 m s^{-1}).

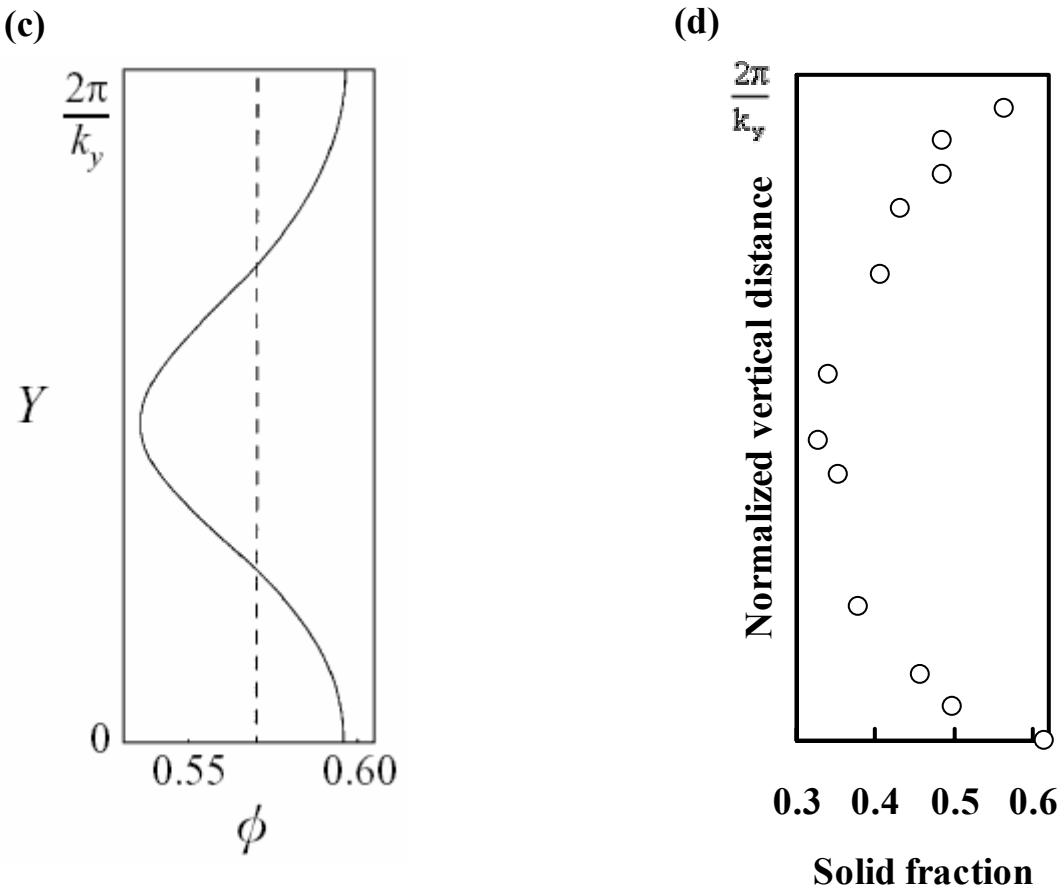

Figure 5.55 Solid fraction profile over a voidage wave from (c) Glasser *et al.* (1997) where k_y (dimensionless) = 0.204 and (d) CFD-DEM simulations where the corresponding dimensionless k_y is estimated to be ~0.103.

was simulated so as to introduce external perturbations into the system to produce the kind of voidage waves presented so far. This difference in the type of boundary conditions imposed may have a strong effect on the eigenfunctions calculated via linear stability analysis, although the method to impose an oscillating solid boundary in such analyses remains elusive to date. Nevertheless, the qualitative agreement in the structure of the voidage waves and their corresponding characteristic wavenumbers calculated using the two different approaches provides a strong indication that the combined CFD-DEM approach is also suitable for the numerical study of such voidage wave instabilities in liquid fluidized bed systems.

5.8.3 Solid Velocity

Figure 5.56a shows the instantaneous velocity vectors of particles in a section of the system about 5 cm above the vibrating base obtained from the CFD-DEM simulation. Correspondingly, Figure 5.56b shows the velocity vectors obtained from the experimental setup using the PIV system. Each frame of the figure shows approximately half a channel and has dimensions 1.5 cm (height) by 1.0 cm (width) with one wall of the channel on the left and the centerline on the right. The frames were captured at 0.2 s intervals. Each velocity vector was obtained by locally averaging over an interrogation window containing about 3 to 4 solid particles. In principle, this method can be applied anywhere within the column, including that close to the wall, as long as images of the solid particles can be captured by the PIV system. However, due to the presence of the wall, fewer solid particles are available within an interrogation window in this region for local averaging to calculate velocity vectors. Furthermore, the power of the laser had to be set sufficiently high so that it

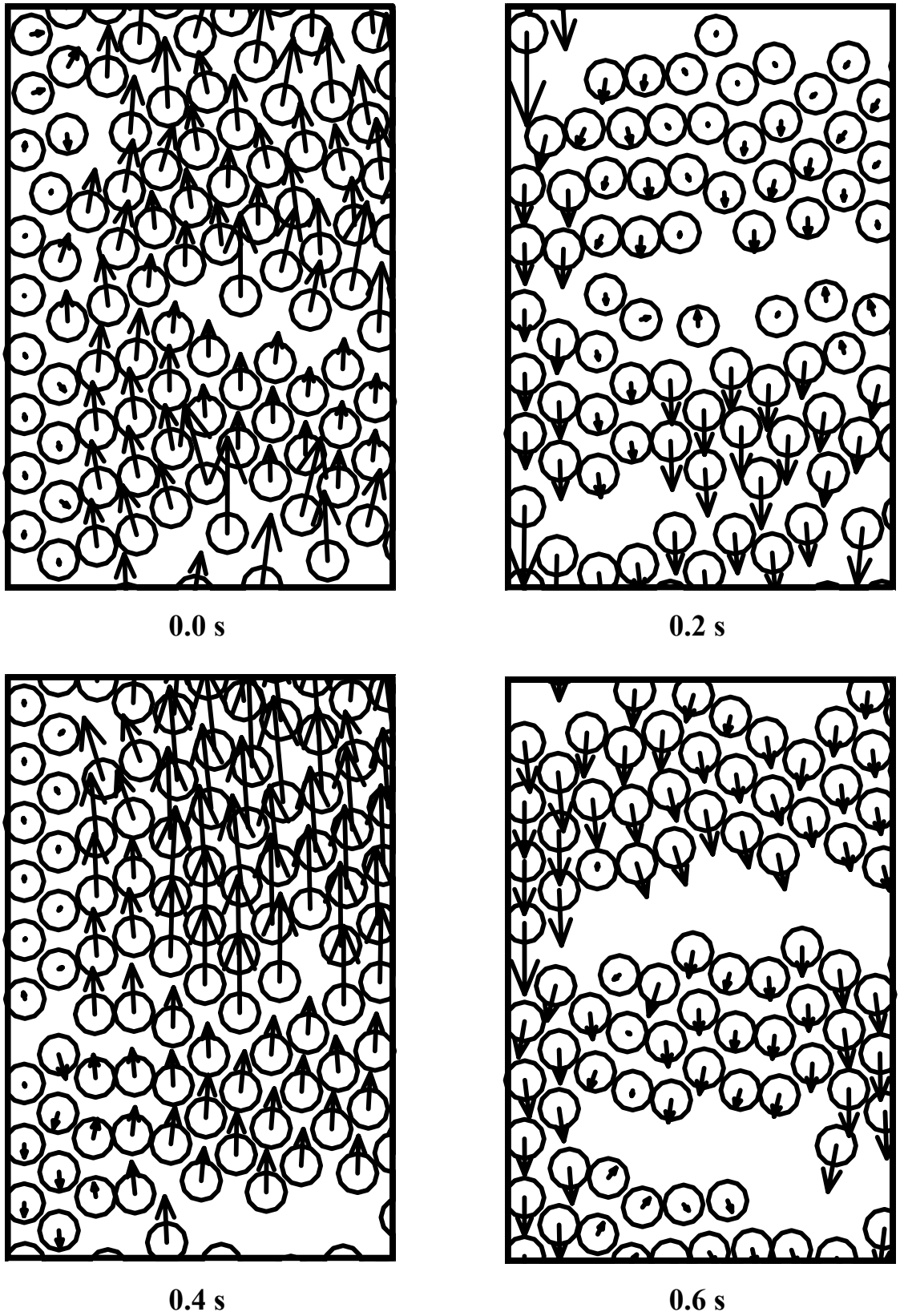

Figure 5.56a Instantaneous particle velocity vector field in a 1.5 cm (height) by 1.0 cm (width) section at 5 cm above the vibrating base obtained from CFD-DEM simulations. Snapshots are shown at 0.2 s intervals.

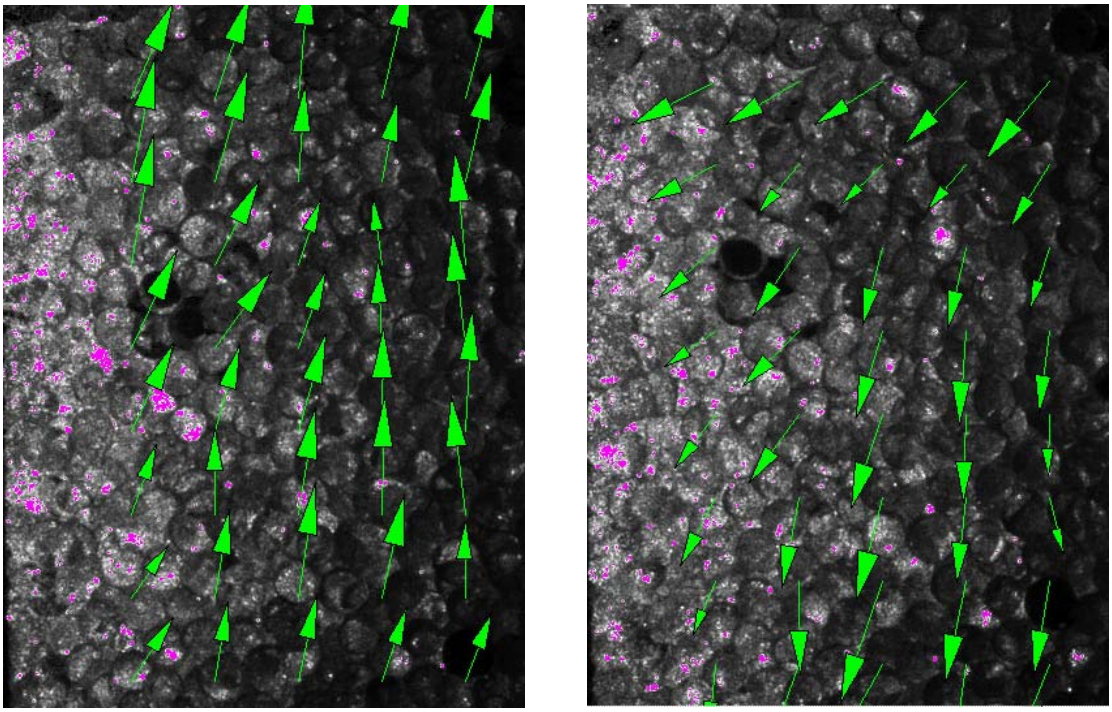

0.0 s **0.2 s**

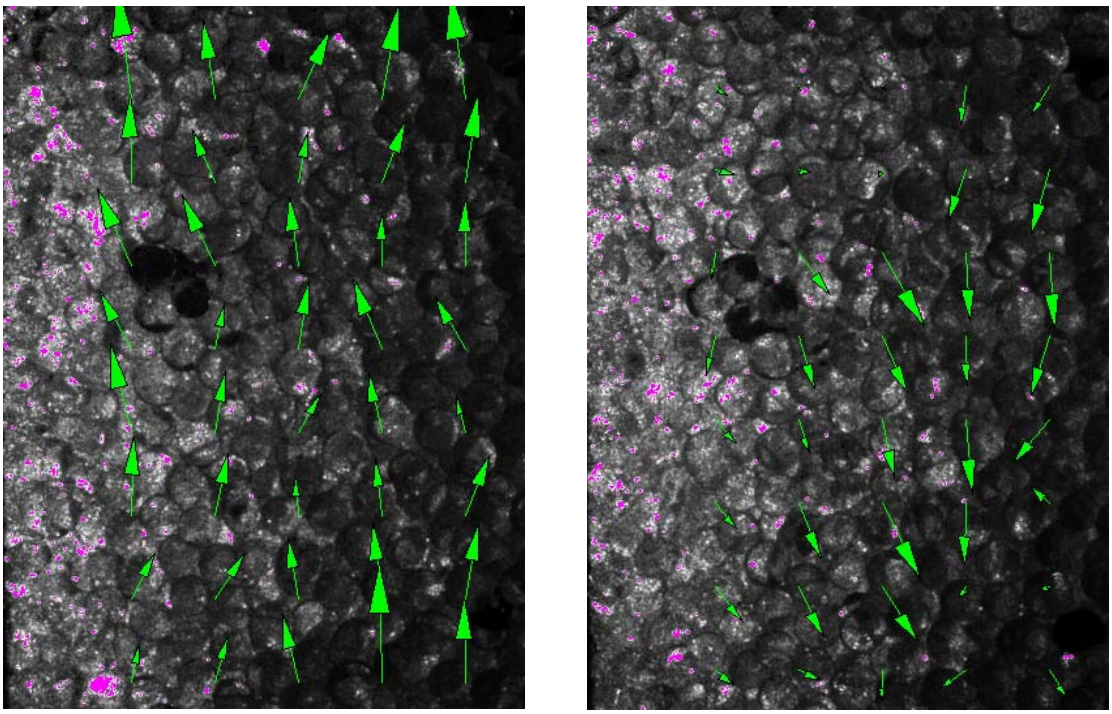

0.4 s **0.6 s**

Figure 5.56b Instantaneous particle velocity vector field in a 1.5 cm (height) by 1.0 cm (width) section at 5 cm above the vibrating base obtained from experiments. Snapshots are shown at 0.2 s intervals.

could penetrate the dense solid packing to illuminate those particles close to the center of the column. This resulted in over-reflection by some particles close to the wall which were nearer the laser source. As such, the region close to the column wall was not included in the calculation of velocity vectors to avoid possible inaccuracies. Nevertheless, the figure illustrates the unique behavior of solid particles in a liquid fluidization system in the presence of voidage waves. Here, adopting an Eulerian point of view, it may be seen that particles switch periodically between generally upward and downward motions. These correspond to the passage of dense and dilute phases of the voidage wave through the particles respectively. In other words, when a dense phase of the wave propagates through a section of the bed, particles in that section were observed to be moving in the upward direction and vice versa. For the present case studied, the frequency and amplitude of the vibrating base were 2 Hz and 1.5 mm respectively. Both Figures 5.56a and 5.56b show that the characteristic frequency of the periodic motion of the solid particles is also about 2 Hz.

Figure 5.57a shows the ensemble averaged profile of the vertical component of solid velocities at 5 cm above the vibrating base with respect to time. As with the case for solid fraction data described above, the ensemble averaging was performed using 20 sets of solid velocity data from the CFD-DEM simulations, each over a time interval of 3 s. This shows quantitatively the oscillatory behavior of particle motion over six cycles. Figure 5.57b shows the corresponding power spectrum obtained from the original instantaneous velocity signals. Instantaneous velocity data were collected at 0.01 s intervals from the CFD-DEM simulation for the calculation of the power spectrum. It may be observed that the characteristic frequency of the oscillatory solid velocity matches that of the vibrating base as mentioned earlier. Figure 5.57c shows

the waveform for solid velocity obtained by ensemble averaging over 120 sets of PIV experimental data. Each set of instantaneous solid velocity data was taken over a duration of 3 s and the periodicity of each waveform was observed to be fairly uniform and reproducible (data not shown for brevity). These individual sets of instantaneous solid velocity waveforms were then superimposed on one another, making sure that the phases were matched (peak to peak and trough to trough) before ensemble averaging was carried out. The number of experimental data sets used in the ensemble averaging has been verified to be sufficiently large to ensure statistical invariance of the resulting waveform. This is the first report of such a statistical representation of the solid velocity in a liquid fluidized bed exhibiting voidage wave instability. It may be noted that the instantaneous solid vertical velocity waveforms show both positive and negative values, in correspondence with the direction of the PIV velocity vectors seen in Figure 5.56b. However, such instantaneous velocity waveforms are not symmetrical about the zero velocity value. Instead, the magnitudes of the positive velocities are usually larger than those of their negative counterparts. This is most likely due to the mean background velocity provided by the net flow of liquid through the fluidization system. As such, the solid velocity waveform after ensemble averaging only exhibits negative solid velocity values at the trough positions and positive values elsewhere. Nevertheless, the power spectral densities for both simulation and experimental data (Figures 5.57b, d) show that the dominant oscillating frequency of solid velocity is equal to that of the driving frequency of the external perturbation imposed.

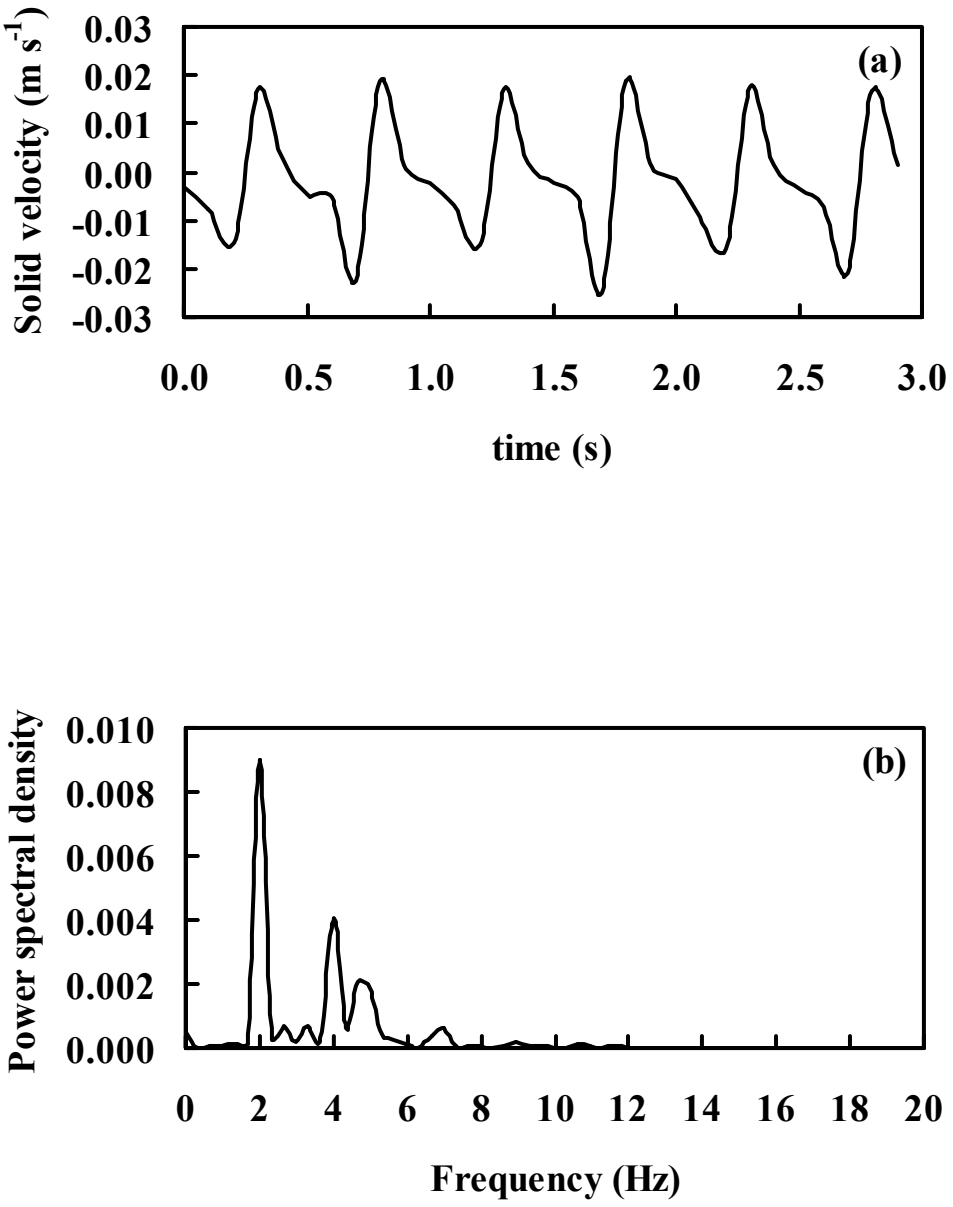

Figure 5.57 (a) Ensemble averaged variation of spatially averaged vertical component of solid velocities at 5 cm above the vibrating base with respect to time obtained from CFD-DEM simulations. (b) Corresponding power spectral density of the time varying solid velocities.

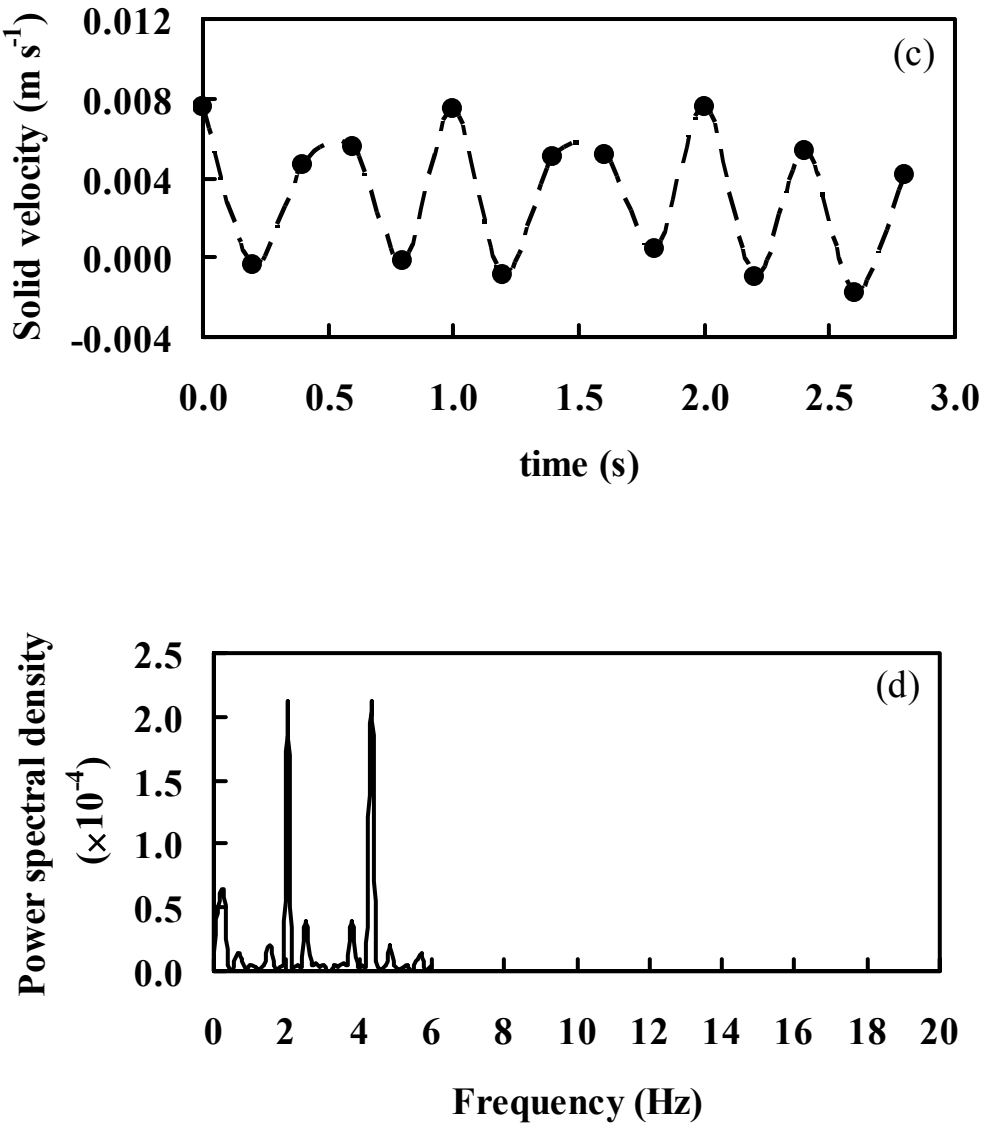

Figure 5.57 (c) Ensemble averaged variation of spatially averaged vertical component of solid velocities at 5 cm above the vibrating base with respect to time obtained from experiments. (d) Corresponding power spectral density of the time varying solid velocities.

5.8.4 Granular Temperature

Figures 5.58a, b show the granular temperature profiles of the solids in the liquid fluidized bed at 1 cm, 5 cm and 10 cm above the base obtained from the CFD-DEM simulations and experiments respectively. The local granular temperature was calculated based on the average of the sum of squared fluctuating velocity components over a domain 2 mm (height) by 1 mm (width):

$$T = \frac{1}{2}\sum_{i=1}^{N}\left[u(i) - \bar{u}\right]^2 + \left[v(i) - \bar{v}\right]^2 \tag{5.2}$$

where N is the number of particles in the local domain, u(i) and v(i) are the i^{th} horizontal and vertical velocity components, and $\bar{u}$ and $\bar{v}$ are mean horizontal and vertical velocity components respectively. It may be observed that granular temperatures are higher at the bottom of the bed and decrease with increasing bed heights. The granular temperatures calculated from both simulation and experimental data are of similar orders of magnitude (~10^{-5} m^2 s^{-2}). There is closer agreement at larger bed heights and some deviations between the two sets of profiles near the bottom of the bed. Specifically, the granular temperature at 10 cm above the base is approximately in the range 3.0 – 5.0 × 10^{-5} m^2 s^{-2} for both simulation and experimental data. At 5 cm above the base, the corresponding values are about 10.0 and 5.0 × 10^{-5} m^2 s^{-2} respectively while at 1 cm above the base the average granular temperatures obtained from simulation and experiments are approximately 12.0 and 6.0 × 10^{-5} m^2 s^{-2} respectively. The granular temperature profile over the entire bed can also be seen from a plot constructed from the simulation data (inset to Figure 5.58a). The plot shows that the bed has higher energy in the near base region and the energy is dissipated as one progresses up along the bed. This characteristic of the system

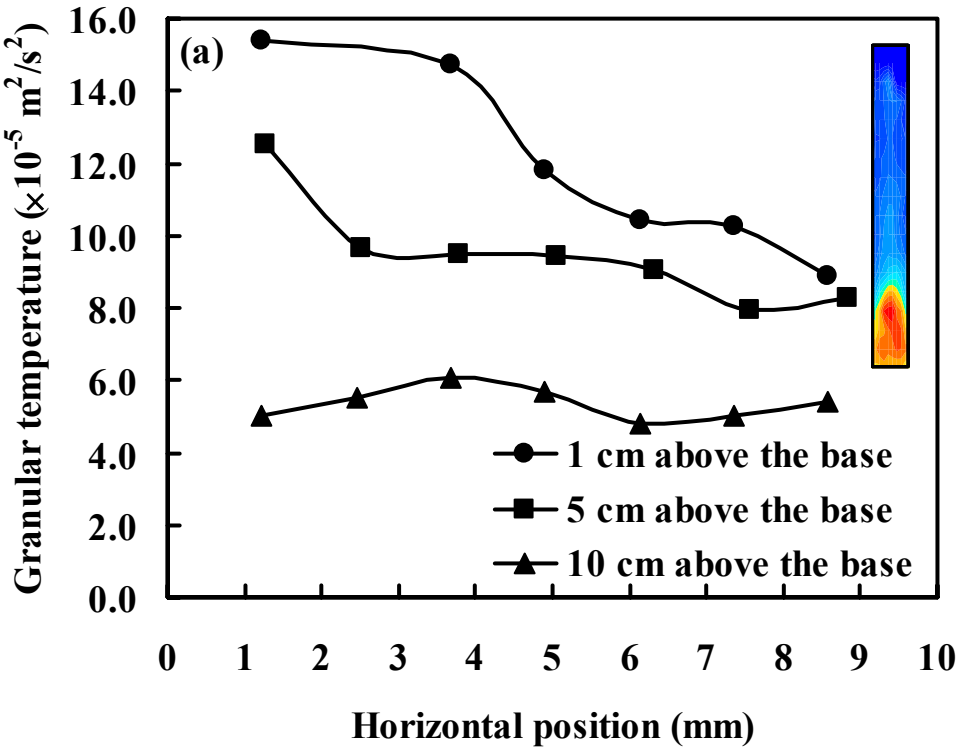

Figure 5.58a Granular temperature profiles of solids at various positions above the vibrating base obtained from CFD-DEM simulations. Color online: The inset shows the granular temperature plot over the entire fluidized bed from the CFD-DEM simulation. The range of the color scale used is 2.1×10^{-5} m^2 s^{-2} (blue) to 3.2×10^{-4} m^2 s^{-2} (red). Granular temperatures are higher at the bottom of the bed and decrease with vertical position along the bed. The origin of the horizontal position is the left lateral wall of the bed.

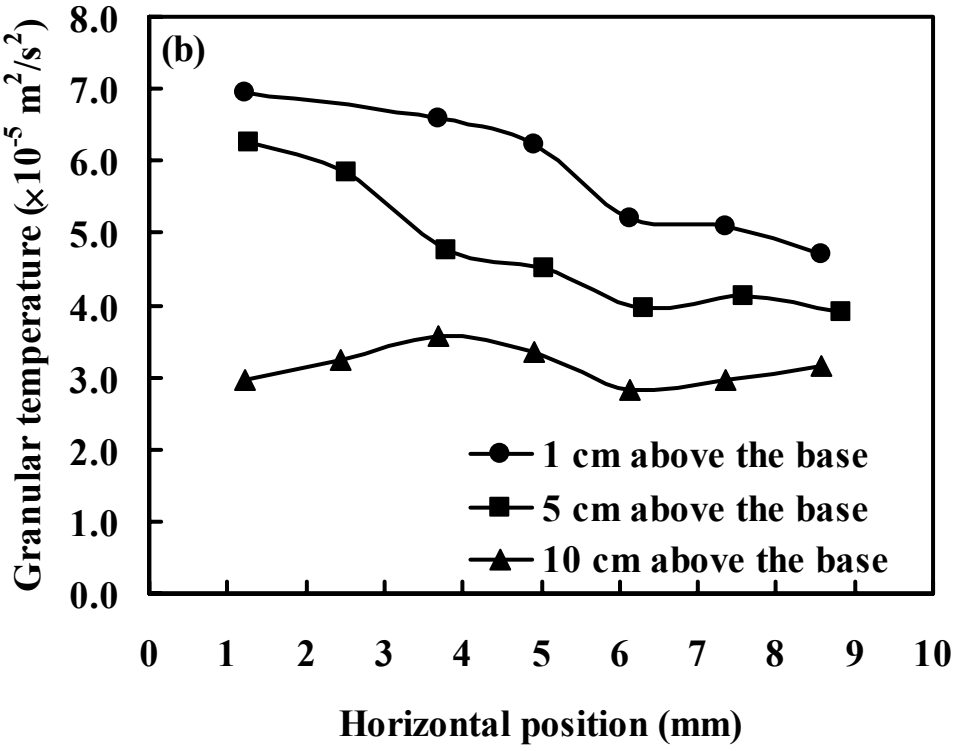

Figure 5.58b Granular temperature profiles of solids at various positions above the vibrating base obtained from experiments

whereby granular temperature is a function of bed height over the entire fluidized bed also supports the point made earlier that voidage waves formed in the fluidized bed system used in the present study do not reach a state of saturation. On the other hand, granular temperature values would be expected to reach saturated values beyond a certain bed height where the voidage waves do reach saturation. The granular temperature profile shown in the inset to Figure 5.58a also indicates the presence of high and low Reynolds stresses near the bottom and top of the bed respectively and seems to suggest possible correlations between such stresses and the onset of instability. Instabilities in the form of voidage waves originate at the vibrating base where the granular temperature is highest and are gradually attenuated as they travel up along the bed towards regions of lower granular temperatures. This observation is consistent with the conclusion made by Ham *et al.* (1990) whose flow visualization experiments and detailed quantitative measurements showed Reynolds stresses due to particle velocity fluctuations to be the main contributor to the formation of voidage instabilities.

5.8.5 Localization of Solids

Despite the convective nature of the voidage waves which originate at the vibrating base and travel up along the length of the fluidized bed, one interesting feature of such instabilities observed in the present CFD-DEM simulations is the highly localized motion of individual particles. As discussed earlier, solid particles move upwards when a dense phase of the voidage wave passes through and settle downwards in the dilute phase of the wave. However, the overall motion of some particles was observed to be highly restricted to a small region within the system. Taking a Lagrangian point of view, the positions of four representative particles were

tracked for a period of 6 s corresponding to 12 cycles of the vibrating base. Figure 5.59a shows the position of each particle at 1 s intervals. Regardless of the precise starting location of the particle within the system, it may be seen that there is very restricted motion in both the axial (vertical) and lateral (horizontal) directions. Each particle seems to be 'trapped' within a small region in space. On comparison with the structure of the voidage wave presented in Figure 5.49, the dimensions of such regions are also comparable with the length scale of each dense phase of the wave. However, when the base is vibrated at a frequency of 1 Hz, with all other operating parameters unchanged, the size of the region in which each particle is trapped remains substantially similar (Figure 5.59b). The extent of motion of individual particles does not seem to be significantly affected by the frequency of the vibrating base. Similar observations were made from the experiments conducted where a few arbitrarily selected particles were dyed and tracked visually for a period of time (Figures 5.59c, d). For characterization of such localized particle motion on a relatively short time scale, the time interval of 6 s as used here was deemed sufficiently long compared with the characteristic periodic time of 0.5 s and 1.0 s of the system when the base was vibrated at 2 Hz and 1 Hz respectively. This phenomenon of localized solid motion in a liquid fluidized bed exhibiting voidage wave instabilities does not seem to have been reported previously. Such behaviors of solids in a liquid fluidized bed system may have important implications in actual applications such as with regards to the type of mixing behavior which can be achieved during operations.

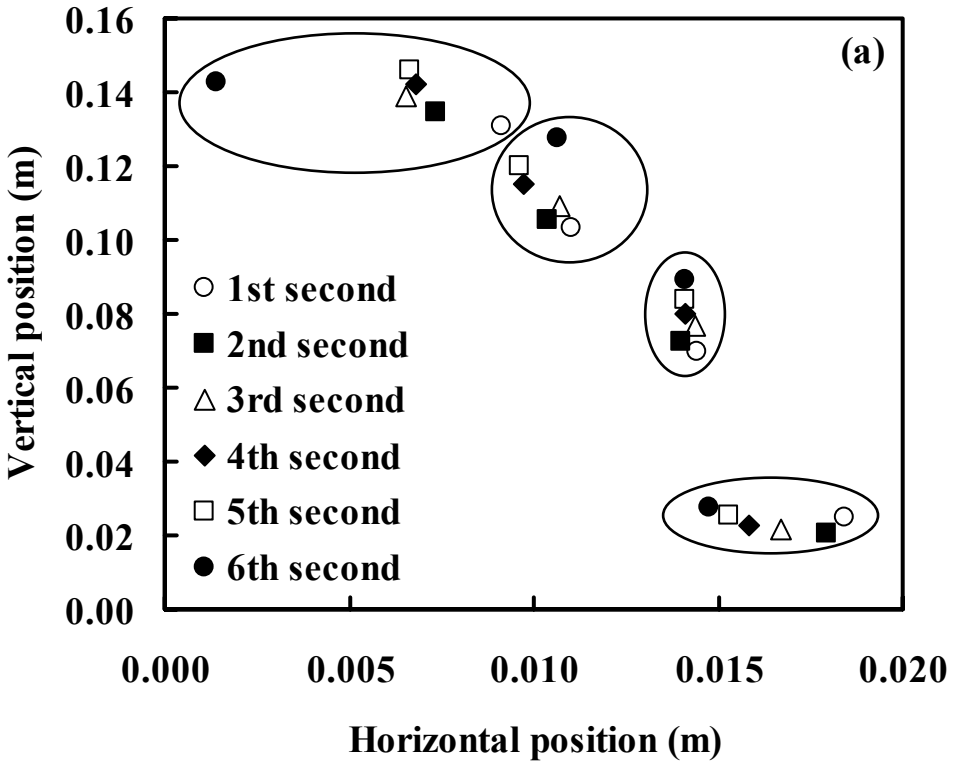

Figure 5.59a Positions of four arbitrarily selected particles at 1 s intervals from CFD-DEM simulations. Vibrating frequency of the base applied is 2 Hz.

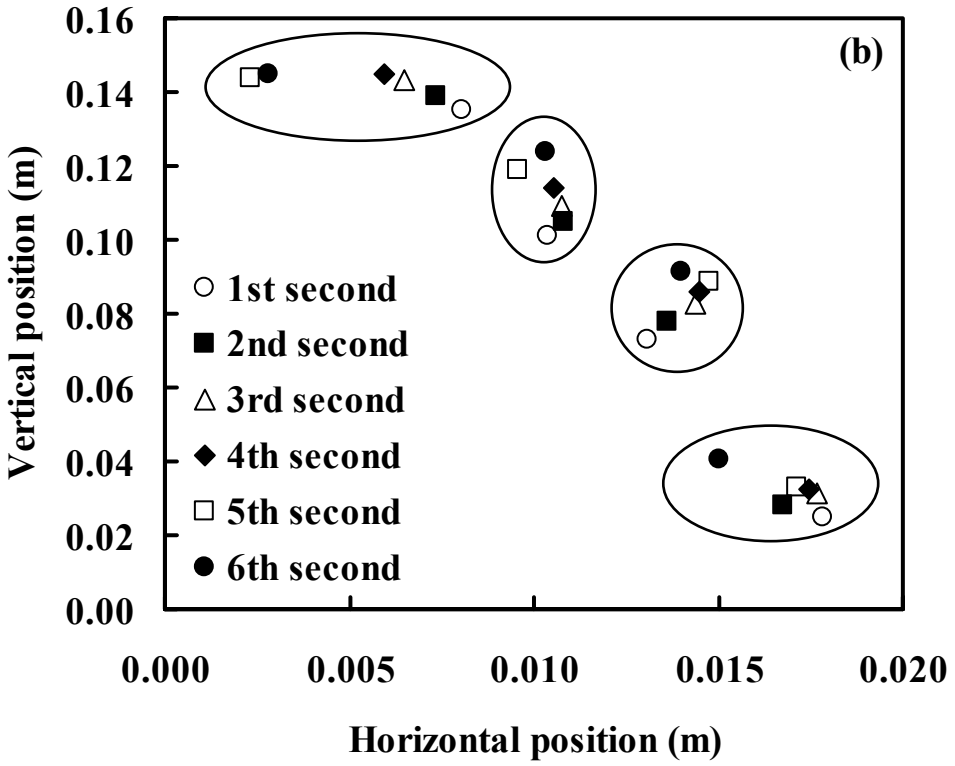

Figure 5.59b Positions of four arbitrarily selected particles at 1 s intervals from CFD-DEM simulations. Vibrating frequency of the base applied is 1 Hz.

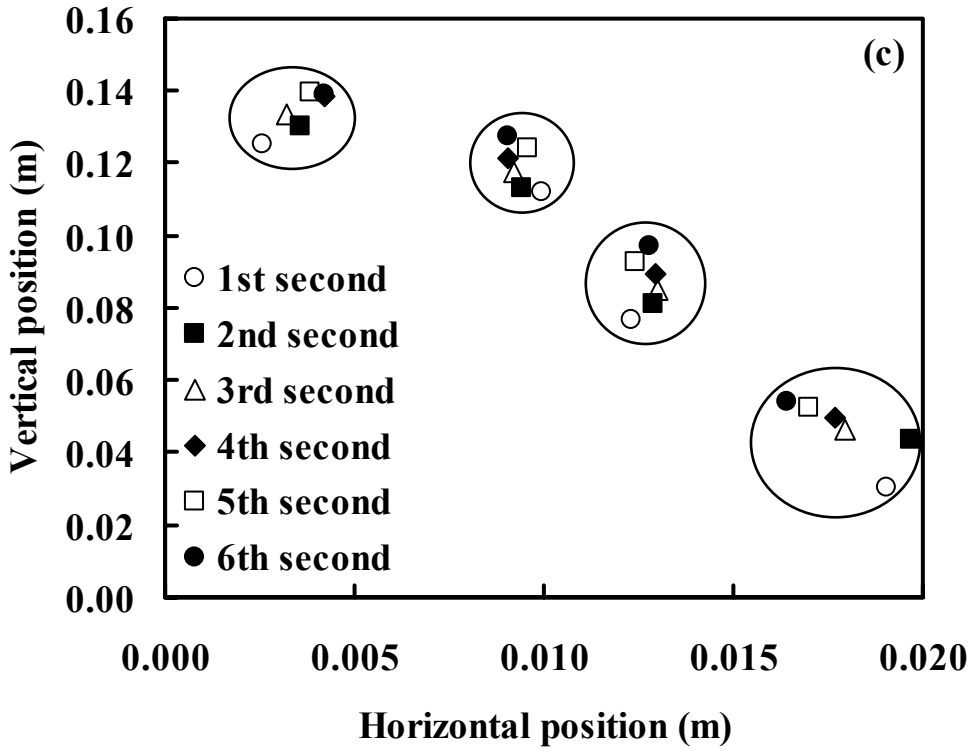

Figure 5.59c Positions of four arbitrarily selected particles at 1 s intervals from experiments. Vibrating frequency of the base applied is 2 Hz.

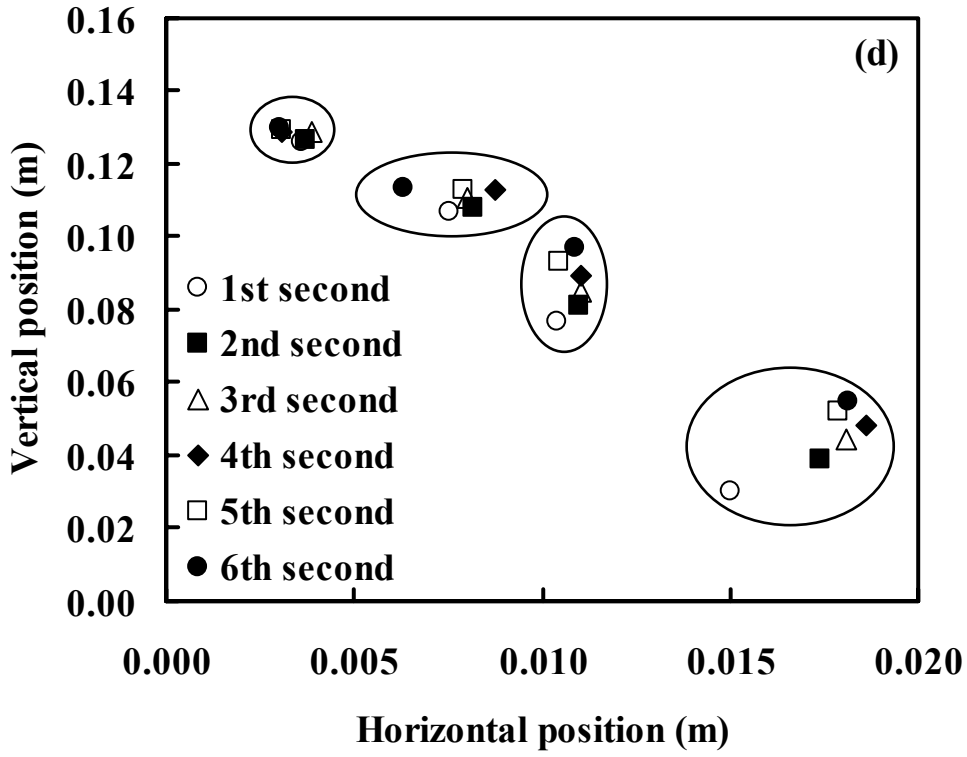

Figure 5.59d Positions of four arbitrarily selected particles at 1 s intervals from experiments. Vibrating frequency of the base applied is 1 Hz.

This study of localized solid motion was extended to include its characterization over longer time scales. It was observed in both the CFD-DEM simulations and experiments that some particles within the fluidized bed continued to exhibit such localized motion over a 60 s period corresponding to 120 cycles of the vibrating base when its frequency was set at 2 Hz (Figures 5.60a, b respectively). Figure 5.60a shows examples of the periodic type of movements that such particles undergo which result in their localization. It may be seen that particles tend to ascend near the center of the column and descend along the wall, giving rise to a local recirculation pattern. The spatial extension over which such restricted motion takes place is now seen to be larger than those observed previously over shorter time scales. In addition, most of the particles illustrated here seem to lie fairly close to the tube walls. Similarly, those captured clearly using a high speed video camera and observed to exhibit localized motion in Figure 5.60b are in close proximity to the near wall of the tube. The six dyed particles labeled '1' to '6' in each of the panels in the figure are observed to remain close to their original positions within the bed throughout 60 s of observation. Such observations seem to imply that two types of recirculation patterns of solid particles may be present with the liquid fluidized bed system exhibiting voidage wave instabilities. A global recirculation pattern results in solid particles traversing throughout the entire height of the bed while a local recirculation pattern gives rise to the localization behavior of solid particles reported in the present study. As mentioned previously, such behaviors may lead to uneven mixing, poor heat or mass transfer rates and even unexpected dead zones within a liquid fluidized bed and so should be of practical relevance to industrial applications.

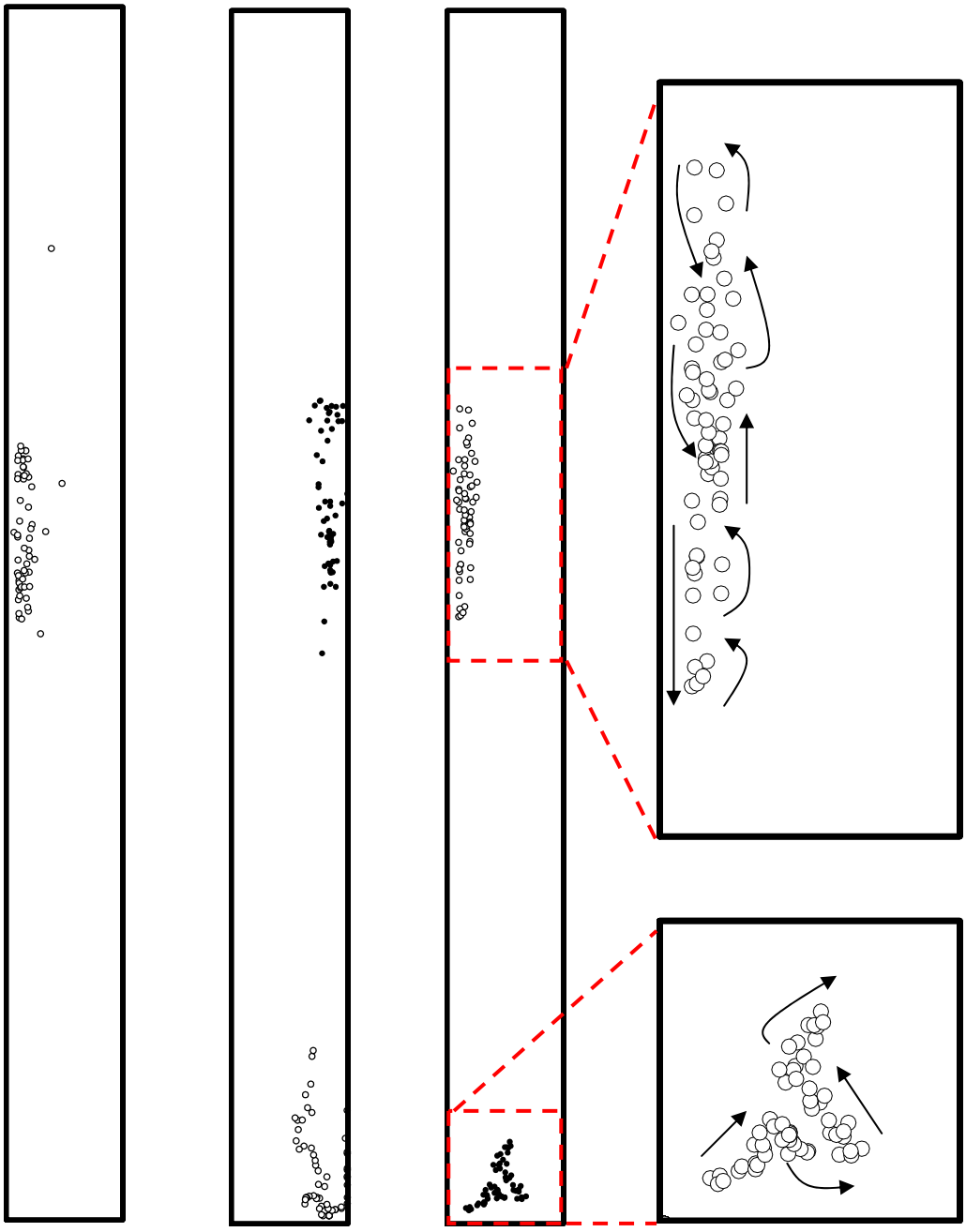

Figure 5.60a Positions of particles exhibiting localized motion over a 60 s period at 1 s intervals observed in CFD-DEM simulations. Vibrating frequency of the base applied is 2 Hz.

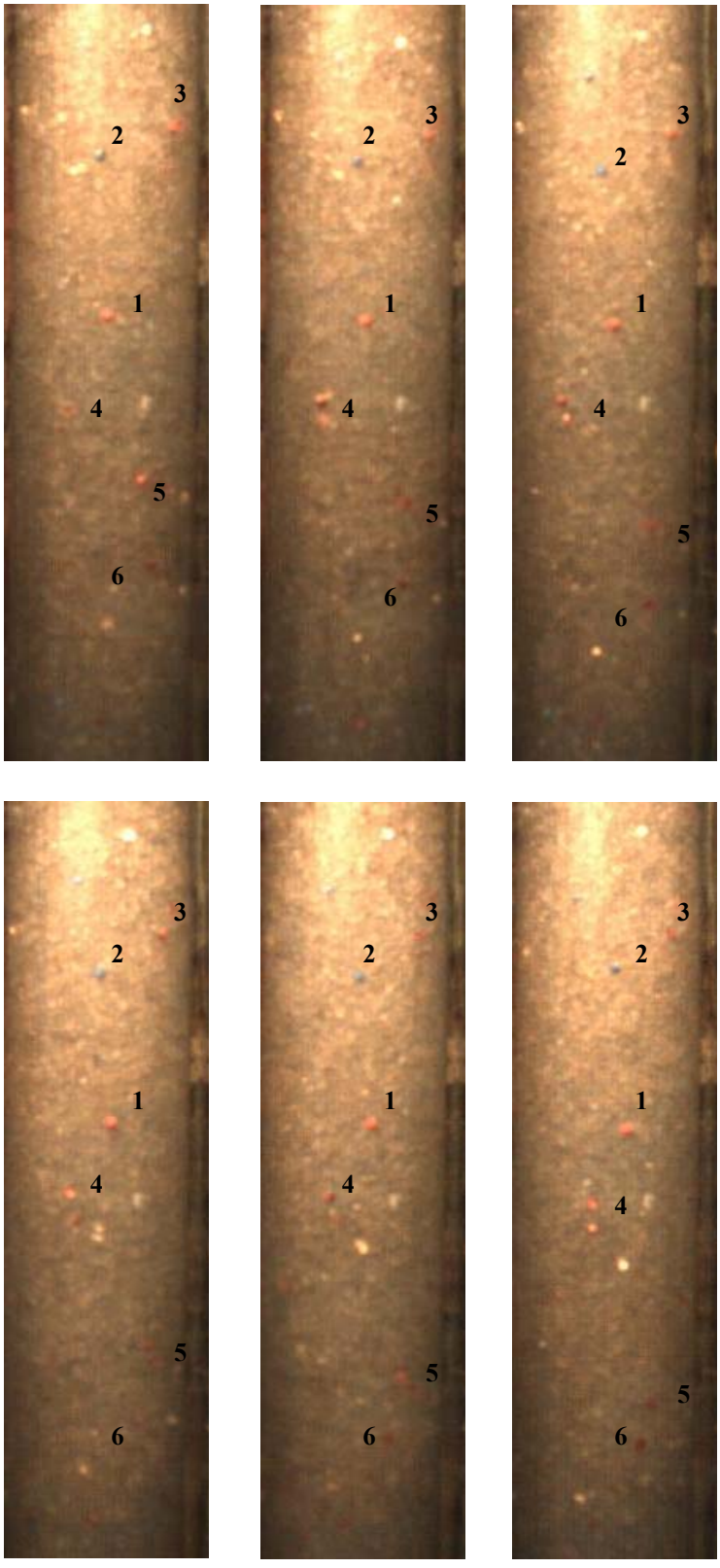

Figure 5.60b Snapshots of a section of the fluidized bed at 5.0 cm above the vibrating base containing some dyed particles captured using a high speed video camera at 10 s intervals. Vibrating frequency of the base applied is 2 Hz.

5.8.6 Dispersion of Solids

Following the previous qualitative discussion on localization of solid motion, a more quantitative approach was used to characterize the nature of such motions. Solids drifted away from their initial positions gradually much like the diffusion of material from a region of high concentration to another of lower concentration. In order to characterize this phenomenon quantitatively, the concept of dispersion was used to examine this drifting behavior of particles within the liquid fluidized bed. The following dispersion model developed in analogy to diffusion in unbounded systems was applied:

$$\left|\mathrm{r}(\mathrm{t})-\mathrm{r}(0)\right|^2 = 2\mathrm{Dt} \tag{5.3}$$

where r is the position vector of the tagged particle, D is the dispersion coefficient and t is the time over which the tagged particle has been tracked. Here, data from the CFD-DEM simulations were used to calculate the dispersion coefficient.

Figure 5.61a shows the mean squared vertical displacement of an arbitrarily selected particle over a 3 s interval. The excellent fit between the simulation data and the dispersion model used confirms that particles in the bed indeed exhibited a diffusion type of motion. This has not been reported in previous studies of voidage wave instabilities in liquid fluidized beds. The corresponding dispersion coefficient can be calculated from the gradient of the straight line fitted to the simulation data. Figure 5.61b shows that the same type of diffusion behavior of individual particles could be observed at various other positions of the fluidized bed exhibiting voidage wave instabilities. Furthermore, dispersion coefficients were found to be larger at higher bed levels, in contrast to the trend observed previously for granular temperatures (Figure 5.61c). However, as with the study of granular temperature

profiles discussed earlier, this feature also suggests that the voidage waves formed in the present fluidized bed system have not reached the state of saturation after propagating over the entire bed height. The values of dispersion coefficients may also be expected to become saturated beyond a sufficient bed height once the voidage waves become saturated. Thus, a consistent conclusion regarding the state of saturation of the voidage waves developed within the present system may be inferred from qualitative inspections of the wave structure obtained from CFD-DEM simulations as well as quantitative analyses of the granular temperature and dispersion coefficient profiles. The inter-relationships between granular temperature, dispersion coefficient and their influences on the formation, propagation and attenuation of voidage wave instabilities in a liquid fluidized bed may be the basis of an interesting study beyond the present work.

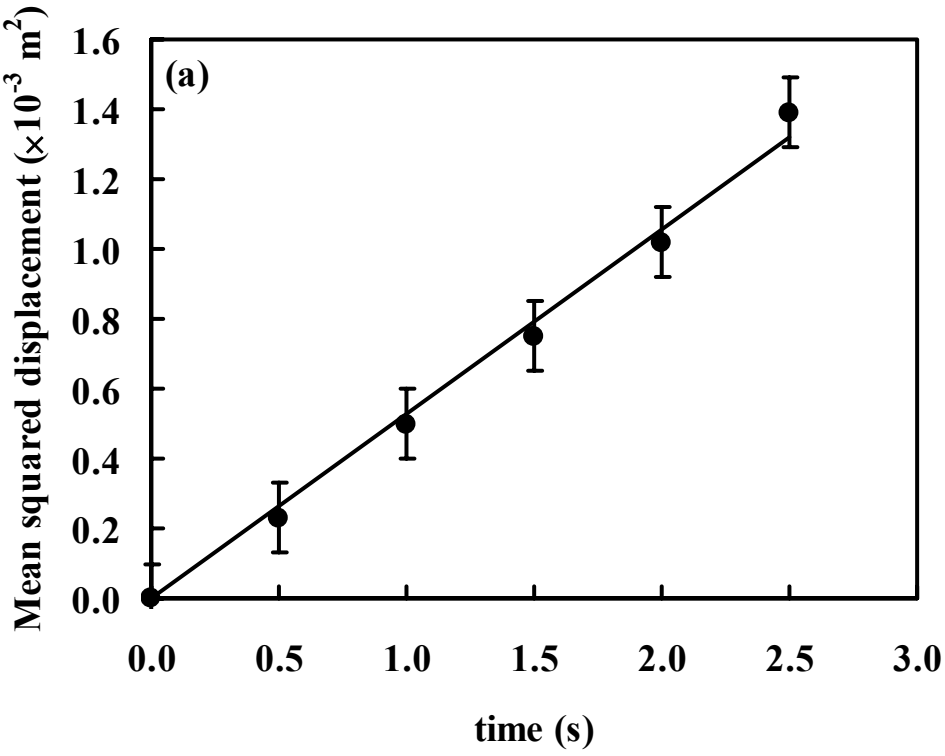

Figure 5.61a Variation of mean squared vertical displacement with time of an arbitrarily selected particle

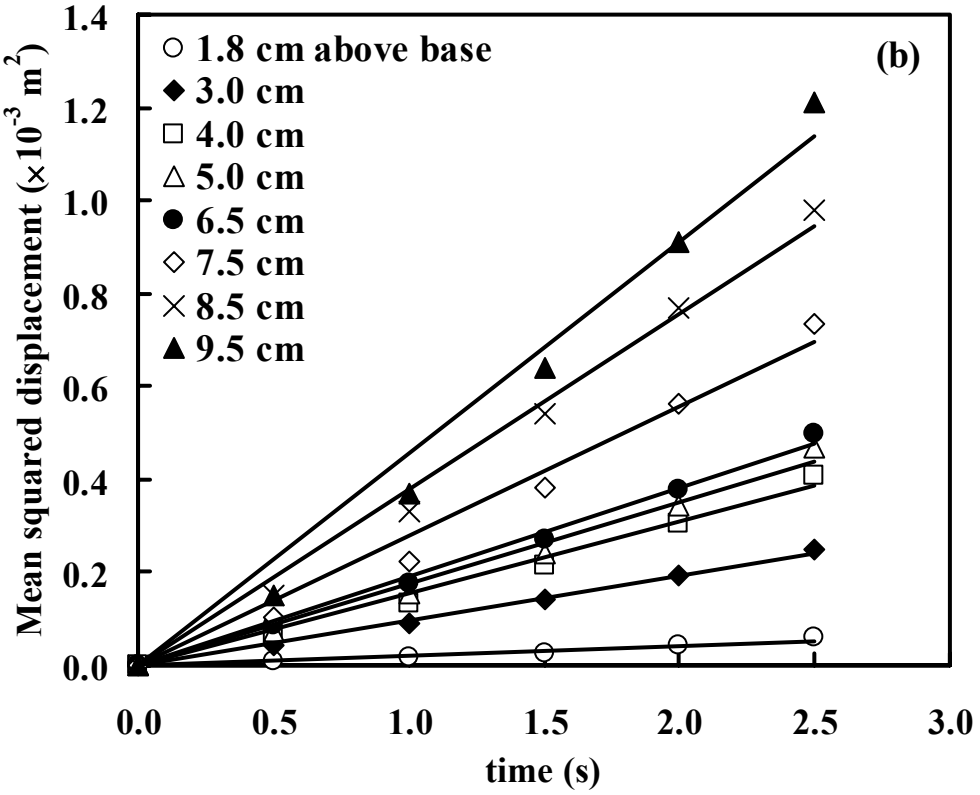

Figure 5.61b Variation of mean squared vertical displacement with time of particles with different initial positions (1.8 cm, 3.0 cm, 4.0 cm, 5.0 cm, 6.5 cm, 7.5 cm, 8.5 cm, 9.5 cm above the base) within the bed

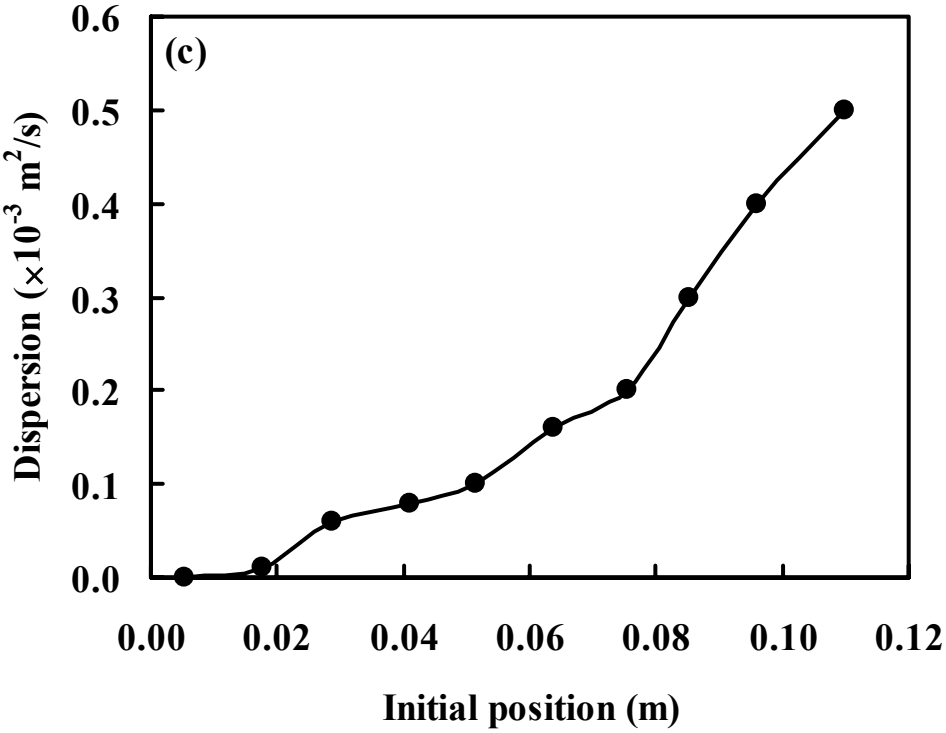

Figure 5.61c Variation of particle dispersion coefficient with different initial positions above the base

CHAPTER 6 CONCLUSIONS

Pneumatic conveying of granular materials is an essential component of any solids processing operation in the chemical, petrochemical and pharmaceutical industries. It is also an example of a complex multiphase flow process, the understanding of which has remained largely elusive and incomplete to the scientific community to date. In this research project, a detailed study of various aspects of the pneumatic conveying process has been carried out through a combination of numerical, experimental and theoretical approaches and the following main conclusions are drawn: The various solid flow regimes in pneumatic conveying through vertical, horizontal and inclined pipes arise from hydrodynamic interactions and other physical factors such as gas flow rates, solid concentration, coefficient of restitution of solid particles and electrostatic forces if present. They can be reproduced in computer simulations by applying the Discrete Element Method combined with Computational Fluid Dynamics. Bulk granular attrition was found to resemble a diffusion process in a theoretical analysis carried out in this project and a new empirical model was proposed as a possible starting point for the development of a new theory for such processes. The phenomenon of voidage wave instability in a vibrated liquid fluidized bed was studied numerically as well as experimentally using Particle Image Velocimetry for the first time and quantitative data on solid fraction, velocities and granular temperature profiles were reported. A new behavior of solid particles in such a system referred to as localization of solids was identified and characterized in this study. These conclusions will be elaborated in greater details in the following paragraphs of this chapter.

The Discrete Element Method (DEM) utilizing a linear spring-dashpot-friction slider force-displacement model was coupled with Computational Fluid Dynamics (CFD) and used for the simulation of pneumatic conveying of granular material in both vertical and horizontal pipes in this study. The motions of solid particles and gas were obtained by time integration of Newton's second law of motion and the Navier-Stokes equations respectively. Fluid drag forces were calculated using a fluid-particle drag force model and also represented as a source term in the gas momentum equation to ensure satisfaction of Newton's third law between the two phases. The effects of rolling friction and collision dynamics have also been considered in the computational model developed.

The simulation results obtained were in good agreement with previously reported experimental observations in terms of the types of flow patterns arising at different operating conditions used. In vertical pneumatic conveying, particles tend to be dispersed throughout the pipe at high gas velocities and low solid concentrations. On the other hand, particles tend to cluster together and move in the form of a dense plug when gas velocities are low or solid concentrations are high. These flow patterns have been referred to as the dispersed and plug flow regimes respectively. The solid concentration profile for dispersed flow was observed to be symmetrical and with a minimum near the center of the pipe while that for plug flow was almost flat. In horizontal pneumatic conveying, the simulations also show the presence of homogeneous or slug flow regimes where particles are distributed along the length of the pipe or packed together as a large cluster respectively. In addition, due to the effects of gravitational forces which cause particles to settle towards the bottom wall of the horizontal pipe, the stratified and moving dunes flow regimes where particles

are transported by traction along the pipe wall are observed at low gas velocities and solid concentrations. The solid concentration profile for stratified flow was unsymmetrical with higher concentration near the lower wall of the pipe while that for slug flow was similar to the flat profile seen for plug flow in vertical pneumatic conveying. The various flow regimes and their corresponding operating conditions have been represented in the form of phase diagrams. In the range of gas velocity values where transition between two flow regimes might be taking place in a vertical pipe, hysteresis of the solid flow rates was observed to occur. The types of flow regimes obtained at the different operating conditions were observed to be insensitive to parameters used in the mathematical model within the range of values investigated in a sensitivity analysis of these parameters. However, the steady state solid flow rate showed a marginal decrease with increasing coefficient of friction. Solid particles with a low viscous contact damping coefficient or equivalently high coefficient of restitution have a low tendency to form large clusters and the plug flow regime normally observed in vertical pneumatic conveying may not exist under such conditions. The mathematical model used in the present study may also be extended to include the effects of electrostatics or particle attrition to investigate the influences of such effects in pneumatic conveying systems. In particular, it may be possible to simulate the few other types of flow regimes mentioned earlier which have been observed in physical experiments with the incorporation of such effects.

In the second part of this study, DEM was coupled with CFD and a simple electrostatic field model for the numerical simulation of pneumatic conveying of granular materials through an inclined pipe. The simulation results obtained were in good agreement with previously reported experimental observations and

measurements carried out using Electrical Capacitance Tomography and high-speed camera techniques. In particular, it was shown that the eroding dunes regime observed experimentally by previous research workers to occur in pneumatic conveying through an inclined pipe where significant electrostatic effects were present could be reproduced computationally by incorporating a simplified electrostatic field model into the CFD-DEM method. The flow behavior of solid particles in this regime obtained from the simulations was validated quantitatively by experimental observations and measurements. Reversed flow of particles was seen in a dense region close to the bottom wall of the conveying pipe and forward flow in a more dilute region in the space above. The effects of a charged bottom wall may be confined to the lower half of the conveying pipe for the solid concentrations investigated when the strength of the field is mild. However, such effects may be a determining factor in causing reversed flow of the granular materials along an inclined pipe. At sufficiently high field strengths, complete backflow of solids in the pneumatic conveying pipe may be observed and a higher inlet gas velocity would be required to sustain a net positive flow along the pipe. However, this may be at the expense of a larger pressure drop over the entire conveying line. In addition, the time required for such a pneumatic conveying system to reach a steady state whereby the solids flow rate remains substantially constant with respect to time is also dependent on the amount of electrostatic effects present within the system. The transient period was observed to be longer when the electrostatic field strength was higher. Finally, a flow map or phase diagram was proposed in the present study as a useful reference for designers of inclined pneumatic conveying systems and a means for a better understanding of such systems. The current phase diagram which was constructed out of simulation data showed the conditions under which reversed flow of solids would

occur and the minimum gas velocities required to ensure net positive flow for the various electrostatic field strengths investigated. In pneumatic conveying through a vertical pipe, the presence of electrostatically charged pipe walls results in the formation of the annular flow regime whereby particles are concentrated against the walls of the pipe, leaving a relatively dilute core region. The solids distribution profiles obtained computationally in the present study are shown to be in good quantitative agreement with Electrical Capacitance Tomography data obtained by previous researchers. As such, it is concluded that electrostatic effects play a dominant role in the formation of such a flow regime in vertical pneumatic conveying.

In the granular attrition study carried out in this project, a simple empirical model for bulk granular attrition derived based on a diffusion analogy to the process was introduced. Granular attrition was treated as a process involving diffusion of the weight fraction of granular materials in a particle-size space. The behavior of the model compares well with experimental data reported in the literature for a wide variety of systems as well as DEM simulation results for attrition in pneumatic conveying about a sharp bend carried out in the present study. Attrition in the latter occurs over a much smaller time scale than those observed in physical experiments. Nevertheless, the model was found to be capable of reproducing the various attrition profiles observed. In addition, it exhibits correct asymptotic behaviors at large times and so is considered more sound than other empirical correlations. A secondary contribution from the DEM simulations carried out in this study is the characterization of the attrition process occurring in pneumatic conveying about a sharp bend. The resulting particle size distribution depends on the relative amounts of chipping and fragmentation occurrences which in turn depend on system parameters and material

properties such as gas velocities and coefficient of restitution respectively. This aspect has been investigated for a reasonable range of parameter values in the present study. Despite the relevance of attrition in pneumatic conveying systems to industrial applications, it has not been investigated very extensively in the scientific literature and it is hoped that the present work would motivate more work to be carried out in this direction. DEM is particularly suited for such investigations as it models attrition from the microscopic or particle level and allows for extensive parametric sensitivity analyses. Future work may involve the study of such attrition processes in systems with various particle-to-pipe diameter ratios, other material properties such as particle densities and hardness, initial particle sizes and particle size distributions. Finally, from comparison of the diffusion model proposed in this study with the well-established Gwyn correlation, it seems likely that the general success of such a power-law type correlation may have arisen from the diffusion-like nature of attrition processes occurring in particle-size space. This suggests that a diffusion analogy for granular attrition may also be a good starting point for further theoretical studies of such processes. It would be pertinent in future studies to develop closures for the attrition diffusivity such that this quantity can be calculated from measurable quantities such as the various material properties of the granular material used for attrition.

Finally, the characteristics of one-dimensional voidage waves in a liquid fluidized bed have been investigated both experimentally and computationally in the present study. The CFD-DEM computer simulations have successfully reproduced the phenomenon of voidage wave formation in a liquid fluidized bed system subjected to external perturbations. A uniform inlet velocity was applied and the base of the

system was allowed to undergo simple harmonic motions to simulate the introduction of small external disturbances. Voidage waves consisting of alternating regions of high and low solid concentrations were observed to form and travel in a coherent manner along the fluidized bed. Solid particles were seen to move upwards when a dense phase of the wave passed through their positions and settle downwards otherwise. The characteristic frequency of such oscillatory motions of solid particles was obtained by a fast Fourier Transform of the vertical component of solid velocities and observed to match the vibrating frequency of the base. Similarly, the characteristic frequencies of solid fraction which also exhibited periodic variations with respect to time were found to be equal to the vibrating frequency of the base. The voidage waves formed as a result of instability in such liquid fluidized bed systems are traveling waves with dense and dilute phases being convected along the bed. The effective wavelength of such waves in terms of the distance between two adjacent major dense or dilute phases was found to depend substantially on the frequency of vibration of the base. However, the motion of individual particles was observed to be highly restricted to a small region or cell whose dimensions did not seem to depend significantly on the vibrating frequency. Despite the convective nature of such waves, the phenomenon is a highly localized one at the individual particle level. This may have important implications for the operations of such liquid fluidization system such as with regards to the effectiveness with which solids mixing can be accomplished in such systems and others. Quantitatively, such motions of individual particles were found to be diffusive in nature. This type of behavior was adequately described by a simple dispersion model used in the present study. Following the work completed on voidage waves in liquid fluidization, an important point of consideration is the fate of such voidage wave instabilities in solid-liquid systems when they are allowed to

evolve over both time and space. Instead of restricting the evolution of such instabilities to within a closed fluidization system, it would be pertinent to explore the consequences of transporting the solid particles together with the voidage waves over longer distances. Such types of operation involving open, solid-liquid flow systems have traditionally been referred to as hydraulic conveying of granular materials and have been extensively studied by various research workers for the past few decades. However, the main focus of early studies in this area was mainly on the development of empirical correlations for predicting pressure drops during hydraulic conveying operations. The study of the formation and development of voidage wave instabilities, albeit fairly well established for liquid fluidization systems, has been almost completely neglected by research workers in the area of hydraulic conveying. An understanding of the various phenomena and characteristics of hydraulic conveying operations is important for such traditional applications as well-drilling and transportation of slurry materials through pipelines. It may also find applications in more modern areas of research such as microfluidic transportation for example.

REFERENCES

Al-Adel, M. F., D. A. Saville, S. Sundaresan. The effect of static electrification on gas-solid flows in vertical risers. Industrial and Engineering Chemistry Research, *41*, 6224–6234. 2002.

Ally, M. R. and G. E. Klinzing. Inter-relation of electrostatic charging and pressure drops in pneumatic transport. Powder Technology, *44*, 85–88. 1985.

Ayazi Shamlou, P., Z. Liu, J. G. Yates. Hydrodynamic influences on particle breakage in fluidized beds. Chemical Engineering Science, *45*, 809–817. 1990.

Beer, F. P. and E. R. Johnson. Mechanics for Engineers – Statics and Dynamics. New York: McGraw-Hill. 1976.

Boerefijn, R., N. J. Gudde, M. Ghadiri. A review of attrition of fluid cracking catalyst particles. Advanced Powder Technology, *11*, 145–174. 2000.

Bridgwater, J. Attrition of high-density polyethylenes. Powder Technology, *50*, 243–252. 1987.

Cook, J. L., S.-J. Khang, S.-K. Lee, T. C. Keener. Attrition and changes in particle size distribution of lime sorbents in a circulating fluidized bed absorber. Powder Technology, *89*, 1–8. 1996.

Cundall, P. A. and O. D. L. Strack. A discrete numerical model for granular assemblies. Geotechnique, *29*, 47–65. 1979.

Dallimore, M. P. and P. G. McCormick. Dynamics of planetary ball milling – a comparison of computer simulated processing parameters with CuO/Ni displacement reaction milling kinetics. Materials Transaction Jim, *37*, 1091–1098. 1996.

Derksen, J. J. and S. Sundaresan. DNS of dense suspensions: wave instabilities in liquid-fluidized beds. Submitted to Journal of Fluid Mechanics. 2006.

Didwania, A. K. and G. M. Homsy. Flow regimes and flow transitions in liquid fluidized beds. International Journal of Multiphase Flow, *7*, 563–580. 1981.

Di Felice, R. The voidage function for fluid-particle interaction systems. International Journal of Multiphase Flow, *20*, 153–159. 1994.

Duru, P., M. Nicolas, J. Hinch, É. Guazzelli. Constitutive laws in liquid-fluidized beds. Journal of Fluid Mechanics, *452*, 371–404. 2002.

El-Kaissy, M. M. and G. M. Homsy. Instabilities waves and the origin of bubbles in fluidized beds. Part 1: Experiments. International Journal of Multiphase Flow, *2*, 379–395. 1976.

Drake, T. G. and O. R. Walton. Comparison of experimental and simulated grain flows. ASME Journal of Applied Mechanics, *62*, 131–135. 1995.

Fasso, L., B. T. Chao, S. L. Soo. Measurement of electrostatic charges and concentration of particles in the freeboard of a fluidized bed. Powder Technology, *33*, 211–221. 1982.

Feng, Y. Q., B. H. Xu, S. J. Zhang, A. B. Yu, P. Zulli. Discrete particle simulation of gas fluidization of particle mixtures. AIChE Journal, *50*, 1713–1728. 2004.

Gajewski, A. Measuring the charging tendency of polystyrene particles in pneumatic conveyance. Journal of Electrostatics, *23*, 55–66. 1989.

Ghadiri, M., Z. Ning, S. J. Kenter, E. Puik. Attrition of granular solids in a shear cell. Chemical Engineering Science, *55*, 5445–5456. 2000.

Glasser, B. J., I. G. Kevrekidis, S. Sundaresan. Fully developed traveling wave solutions and bubble formation in fluidized beds. Journal of Fluid Mechanics, *334*, 157–188. 1997.

Gwyn, J. E. On the particle size distribution function and the attrition of cracking catalysts. AIChE Journal, *15*, 35–39. 1969.

Ham, J. M., S. Thomas, É Guazzelli, G. M. Homsy, M.-C. Anselmet. An experimental study of the stability of liquid-fluidized beds. International Journal of Multiphase Flow, *16*, 171–185. 1990.

Han, T., A. Levy, H. Kalman. DEM simulation for attrition of salt during dilute-phase pneumatic conveying. Powder Technology, *129*, 92–100. 2003.

Homsy, G. M., M. M. El-Kaissy, A. Didwania. Instability waves and the origin of bubbles in fluidized beds – II Comparison with theory. International Journal of Multiphase Flow, *6*, 305–318. 1980.

Huber, N. and M. Sommerfeld. Modelling and numerical calculation of dilute-phase pneumatic conveying in pipe systems. Powder Technology, *99*, 90–101. 1998.

Jonassen, N. Electrostatics. pp. 155–157, The Netherlands: Kluwer Academic Publishers. 2002.

Joseph, S. and G. E. Klinzing. Vertical gas-solid transition flow with electrostatics. Powder Technology, *36*, 79–87. 1983.

Kage, H., K. Kawaji, H. Ogura, Y. Matsuno. Attrition of granular slug by single horizontal jet equipped in fluidized bed. Journal of Chemical Engineering of Japan, *33*, 605–611. 2000.

Kaneko, Y., T. Shiojima, M. Horio. DEM simulation of fluidized beds for gas-phase olefin polymerization. Chemical Engineering Science, *54*, 5809–5821. 1999.

Klinzing, G. E. Clustering under the influence of electrostatic forces. International Journal of Multiphase Flow, *12*, 853–857. 1986.

Levy, A. Two-fluid approach for plug flow simulations in horizontal pneumatic conveying. Powder Technology, *112*, 263–272. 2000.

Matsusaka, S. and H. Masuda. Electrostatics of particles. Advanced Powder Technology, *14*, 143–166. 2003.

Mikami, T., H. Kamiya, M. Horio. Numerical simulation of cohesive powder behavior in a fluidized bed. Chemical Engineering Science, *53*, 1927–1940. 1998.

Mills, D., M. G. Jones, V. K. Agarwal, L. L. Faulkner (ed). Handbook of pneumatic conveying engineering. pp. 252, New York. 2004.

Neil, A. U. and J. Bridgwater. Attrition of particulate solids under shear. Powder Technology, *80*, 207–219. 1994.

Neil, A. U. and J. Bridgwater. Towards a parameter characterising attrition. Powder Technology, *106*, 37–44. 1999.

Nicolas, M., J.-M. Chomaz, D. Vallet, É. Guazzelli. Experimental investigations on the nature of hte first wavy instability in liquid-fluidized beds. Physics of Fluids, *8*, 1987–1989. 1996.

Nicolas, M., J.-M. Chomaz, É. Guazzelli. Absolute and convective instabilities of fluidized beds. Physics of Fluids, *6*, 3936–3944. 1994.

Nicolas, M., J. Hinch, É. Guazzelli. Wavy instability in liquid-fluidized beds. Industrial and Engineering Chemistry Research, *38*, 799–802. 1999.

Nieh, S. and T. Nguyen. Effects of humidity, conveying velocity, and particle size on electrostatic charges of glass beads in a gaseous suspension flow. Journal of Electrostatics, *21*, 99–114. 1988.

Patankar, S. V. Numerical Heat Transfer and Fluid Flow. New York: Hemisphere. 1980.

Paramanathan, B. K. and J. Bridgwater. Attrition of solids – I cell development. Chemical Engineering Science, *38*, 197–206. 1983a.

Paramanathan, B. K. and J. Bridgwater. Attrition of solids – II material behaviour and kinetics of attrition. Chemical Engineering Science, *38*, 207–224. 1983b.

Rao, S. M., K. Zhu, C.-H. Wang, S. Sundaresan. Electrical capacitance tomography measurements on the pneumatic conveying of solids. Industrial and Engineering Chemistry Research, *40*, 4216–4226. 2001.

Robinson, M. and A. D. Moore (ed). Electrostatic precipitation. In Electrostatics and its applications, pp. 180. 1973.

Sharmene Ali, F., I. I. Inculet, A. Tedoldi. Charging of polymer powder inside a metallic fluidized bed. Journal of Electrostatics, *45*, 199–211. 1999.

Stein, M., J. P. K. Seville, D. J. Parker. Attrition of porous glass particles in a fluidised bed. Powder Technology, *100*, 242–250. 1998.

Tashiro, H., X. Peng, Y. Tomita. Numerical prediction of saltation velocity for gas-solid two-phase flow in a horizontal pipe. Powder Technology, *91*, 141–146. 1997.

Tsuji, Y., T. Tanaka, T. Ishida. Lagrangian numerical simulation of plug flow of cohesionless particles in a horizontal pipe. Powder Technology, *71*, 239–250. 1992.

Tsuji, Y., T. Kawaguchi, T. Tanaka. Discrete particle simulation of two-dimensional fluidized bed. Powder Technology, *77*, 79–87. 1993.

Verlet, L. Computer "Experiments" on classical fluids. I. Thermodynamical properties of Lennard-Jones molecules. Physical Review, *159*, 98–103. 1967.

Wang, F.-J., J.-X. Zhu, J. M. Beeckmans. Pressure gradient and particle adhesion in the pneumatic transport of cohesive fine powders. International Journal of Multiphase Flow, *26*, 245–265. 2000.

Werther, J., E. U. Hartge. Modeling of industrial fluidized-bed reactors. Industrial and Engineering Chemistry Research, *43*, 5593–5604. 2004.

Wolny, A. and W. Kazmierczak. Triboelectrification in fluidized bed of polystyrene. Chemical Engineering Science, *44*, 2607–2610. 1989.

Xiang, J. and D. McGlinchey. Numerical simulation of particle motion in dense phase pneumatic conveying. Granular Matter, *6*, 167–172. 2004.

Xu, B. H. and A. B. Yu. Numerical simulation of the gas-solid flow in a fluidized bed by combining discrete particle method with computational fluid dynamics. Chemical Engineering Science, *52*, 2785–2809. 1997.

Xu, B. H., A. B. Yu, S. J. Chew, P. Zulli. Numerical simulation of the gas-solid flow in a bed with lateral gas blasting. Powder Technology, *109*, 13–26. 2000.

Yang, R. Y., R. P. Zou, A. B. Yu. Computer simulation of the packing of fine particles. Physical Review E, *62*, 3900–3908. 2000.

Yao, J., Y. Zhang, C. H. Wang, S. Matsusaka, H. Masuda. Electrostatics of the granular flow in a pneumatic conveying system. Industrial and Engineering Chemistry Research, *43*, 7181–7199. 2004.

Yao, J., Y. Zhang, C. H. Wang. Granular electrostatics and the energy in a pneumatic conveying system, AIChE Annual Meeting. 2005.

Zhang, Y.-F., Y. Yang, H. Arastoopour. Electrostatic effect on the flow behavior of a dilute gas/cohesive particle flow system. AIChE Journal, *42*, 1590–1599. 1996.

Zhou, Y. C., B. D. Wright, R. Y. Yang, B. H. Xu, A. B. Yu. Rolling friction in the dynamic simulation of sandpile formation. Physica A, *269*, 536–553. 1999.

Zhu, K., S. M. Rao, C.-H. Wang, S. Sundaresan. Electrical capacitance tomography measurements on vertical and inclined pneumatic conveying of granular solids. Chemical Engineering Science, *58*, 4225–4245. 2003.

Zhu, K., S. M. Rao, Q. H. Huang, C. H. Wang, S. Matsusaka, H. Masuda. On the electrostatics of pneumatic conveying of granular materials using electrical capacitance tomography. Chemical Engineering Science, *59*, 3201–3213. 2004.

APPENDICES

Appendix A

Solution of diffusion equation for bulk granular attrition

Governing Equation:

$$\frac{\partial W}{\partial t} = D\frac{\partial^2 W}{\partial x^2} \tag{A.1}$$

where $x = \frac{d}{d_o}$

Boundary Conditions:

$x = 0,\ W = 0$

$x = 1,\ W = 1$

Applying Finite Fourier Transform:

$$\Phi_n(x) = \sqrt{2}\sin(n\pi x)$$

$$\frac{d^2\Phi_n}{dx^2} = -\lambda_n^2\Phi_n$$

$$W_n(t) = \int_0^1 W(x,t)\Phi_n(x)dx$$

Transforming L.H.S. of (A.1):

$$\int_0^1 \frac{\partial W}{\partial t}\Phi_n dx = \frac{\partial W_n}{\partial t}$$

Transforming R.H.S. of (A.1):

$$\int_0^1 \frac{\partial^2 W}{\partial x^2}\Phi_n dx = \Phi_n \frac{dW}{dx}\bigg|_0^1 - \int_0^1 \frac{dW}{dx}\frac{d\Phi_n}{dx}dx$$
$$= -\left[\frac{d\Phi_n}{dx}W\bigg|_0^1 - \int_0^1 W\frac{d^2\Phi_n}{dx^2}dx\right]$$
$$= -\left[\frac{d\Phi_n}{dx}\bigg|_{x=1} - \int_0^1 -(n\pi)^2 W\Phi_n dx\right]$$
$$= -\left[n\pi\sqrt{2}\cos(n\pi x)\big|_{x=1} + (n\pi)^2 W_n\right]$$
$$= -\sqrt{2}n\pi\cos(n\pi x) - (n\pi)^2 W_n$$
$$= -\sqrt{2}n\pi(-1)^n - (n\pi)^2 W_n$$

Transformed Governing Equation:

$$\frac{dW_n}{dt} = D\left[-\sqrt{2}n\pi(-1)^n - (n\pi)^2 W_n\right]$$

$$\frac{dW_n}{dt} + (n\pi)^2 DW_n = -D\sqrt{2}n\pi(-1)^n$$

Auxiliary Equation:

$$m + (n\pi)^2 D = 0 \Rightarrow m = -(n\pi)^2 D$$

Complementary Function:

$$W_n = A\exp\left[-(n\pi)^2 Dt\right]$$

Particular Integral:

$$W_n = a_o$$
$$(n\pi)^2 Da_o = -D\sqrt{2}n\pi(-1)^n$$
$$a_o = \frac{-\sqrt{2}(-1)^n}{n\pi}$$

General Solution:

$$W_n = A\exp\left[-(n\pi)^2 Dt\right] - \frac{\sqrt{2}(-1)^n}{n\pi}$$

General Solution of (A.1):

$$W = \sum_{n=1}^{\infty} W_n \Phi_n(x)$$
$$= \sum_{n=1}^{\infty} \left\{ A \exp\left[-(n\pi)^2 Dt \right] - \frac{\sqrt{2}(-1)^n}{n\pi} \right\} \sqrt{2} \sin(n\pi x) \qquad \text{(A.2)}$$

Initial Condition:

$t = 0, W = 0$

$$\sum_{n=1}^{\infty} \left\{ A - \frac{\sqrt{2}(-1)^n}{n\pi} \right\} = 0$$
$$\Rightarrow A = \frac{\sqrt{2}(-1)^n}{n\pi}$$

Substituting into (A.2):

$$W = \sum_{n=1}^{\infty} \left\{ \frac{\sqrt{2}(-1)^n}{n\pi} \exp\left[-(n\pi)^2 Dt \right] - \frac{\sqrt{2}(-1)^n}{n\pi} \right\} \sqrt{2} \sin(n\pi x)$$
$$= \sum_{n=1}^{\infty} \frac{\sqrt{2}(-1)^n}{n\pi} \left\{ \exp\left[-(n\pi)^2 Dt \right] - 1 \right\} \sqrt{2} \sin(n\pi x)$$

$$\therefore W = \frac{2}{\pi} \sum_{n=1}^{\infty} \frac{(-1)^n}{n} \left\{ \exp\left[-(n\pi)^2 Dt \right] - 1 \right\} \sin(n\pi x) \qquad \text{(A.3)}$$

Appendix B

Weight fraction of solid particles attrited

$$W' = \int_0^1 W dx \tag{B.1}$$

Substituting (A.3) into (B.1):

$$W' = \frac{2}{\pi}\int_0^1 \sum_{n=1}^{\infty} \frac{(-1)^n}{n}\left\{\exp\left[-(n\pi)^2 Dt\right]-1\right\}\sin(n\pi x)dx$$

$$= \frac{2}{\pi}\sum_{n=1}^{\infty} \frac{(-1)^n}{n}\left\{\exp\left[-(n\pi)^2 Dt\right]-1\right\}\left[\frac{-\cos(n\pi x)}{n\pi}\right]\Bigg|_0^1$$

$$= \frac{2}{\pi}\sum_{n=1}^{\infty} \frac{(-1)^n}{n}\left\{\exp\left[-(n\pi)^2 Dt\right]-1\right\}\left(-\frac{1}{n\pi}\right)\left[\cos(n\pi)-1\right]$$

$$= \frac{2}{\pi}\sum_{n=1}^{\infty} \frac{(-1)^n}{n}\left\{\exp\left[-(n\pi)^2 Dt\right]-1\right\}\left(-\frac{1}{n\pi}\right)\left[(-1)^n-1\right]$$

$$= \frac{2}{\pi^2}\sum_{n=1}^{\infty} \frac{(-1)^{n+1}}{n^2}\left\{\exp\left[-(n\pi)^2 Dt\right]-1\right\}\left[(-1)^n-1\right]$$

$$= \frac{4}{\pi^2}\sum_{\substack{n=1 \\ (n\ \text{odd})}}^{\infty} \frac{(-1)^{n+2}}{n^2}\left\{\exp\left[-(n\pi)^2 Dt\right]-1\right\}$$

$$= \frac{4}{\pi^2}\sum_{\substack{n=1 \\ (n\ \text{odd})}}^{\infty} \frac{-1}{n^2}\left\{\exp\left[-(n\pi)^2 Dt\right]-1\right\}$$

$$= \frac{4}{\pi^2}\sum_{\substack{n=1 \\ (n\ \text{odd})}}^{\infty} \frac{1}{n^2}\left\{1-\exp\left[-(n\pi)^2 Dt\right]\right\}$$

$$\therefore W' = \frac{4}{\pi^2}\sum_{\substack{n=1 \\ (n\ \text{odd})}}^{\infty} \frac{1}{n^2}\left\{1-\exp\left[-(n\pi)^2 Dt\right]\right\} \tag{B.2}$$

Appendix C

Further analysis of diffusion model for bulk granular attrition

Taylor Series Expansion:

$$\exp\left[-(n\pi)^2 Dt\right] = 1 + \sum_{m=1}^{\infty} \frac{(-1)^m \left[(n\pi)^2 Dt\right]^m}{m!} \tag{C.1}$$

Substituting (C.1) into (B.2):

$$W' = \frac{4}{\pi^2} \sum_{\substack{n=1 \\ (n\ \text{odd})}}^{\infty} \frac{-1}{n^2} \left\{ \sum_{m=1}^{\infty} \frac{(-1)^m \left[(n\pi)^2 Dt\right]^m}{m!} \right\}$$

$$= \sum_{\substack{n=1 \\ (n\ \text{odd})}}^{\infty} \sum_{m=1}^{\infty} \frac{-4\left[-(n\pi)^2 Dt\right]^m}{(n\pi)^2 m!}$$

$$\therefore W' = \sum_{\substack{n=1 \\ (n\ \text{odd})}}^{\infty} \sum_{m=1}^{\infty} \frac{4(-1)^{m+1} \left(n^2\pi^2\right)^{m-1} D^m}{m!} t^m \tag{C.2}$$

LIST OF JOURNAL PUBLICATIONS

Zhang, Y., E. W. C. Lim and C. H. Wang. Pneumatic Transport of Granular Materials in an Inclined Conveying Pipe: Comparison of CFD-DEM, ECT and PIV Results. Industrial and Engineering Chemistry Research, Article in Press, 2007.

Lim, E. W. C., Y. S. Wong, C. H. Wang. Particle Image Velocimetry Experiment and Discrete-Element Simulation of Voidage Wave Instability in a Vibrated Liquid-Fluidized Bed. Industrial and Engineering Chemistry Research, *46(4)*, 1375–1389. 2007.

Lim, E. W. C., Y. Zhang, C. H. Wang. Effects of an Electrostatic Field in Pneumatic Conveying of Granular Materials through Inclined and Vertical Pipes. Chemical Engineering Science, *61(24)*, 7889–7908. 2006.

Lim, E. W. C. and C. H. Wang. Diffusion Modeling of Bulk Granular Attrition. Industrial and Engineering Chemistry Research, *45(6)*, 2077–2083. 2006.

Yao, J., C. H. Wang, E. W. C. Lim, J. Bridgwater. Granular Attrition in a Rotary Valve: Attrition Product Size and Shape. Chemical Engineering Science, *61(11)*, 3435–3451. 2006.

Lim, E. W. C., C. H. Wang, A. B. Yu. Discrete Element Simulation for Pneumatic Conveying of Granular Material. AIChE Journal, *52(2)*, 496–509. 2006.

LIST OF CONFERENCE PRESENTATIONS

Lim, E. W. C., Y. Zhang, C. H. Wang, Recent Developments on the Dynamics of Particulate Systems, The 5th International Symposium on Measurement Techniques for Multiphase Flows, Macau, China, 10–13 December, 2006.

Lim, E. W. C., Y. Zhang, C. H. Wang, Effects of an Electrostatic Field in Pneumatic Conveying of Granular Materials through a Vertical Pipe, The 10th Asian Conference on Fluidized-Bed and Three-Phase Reactors, Busan, Korea, 26–29 November, 2006.

Zhang, Y., E. W. C. Lim, C. H. Wang, Pneumatic Transport of Granular Materials in a 45° Inclined Conveying Pipe, The 10th Asian Conference on Fluidized-Bed and Three-Phase Reactors, Busan, Korea, 26–29 November, 2006.

Lim, E. W. C. and C. H. Wang, Voidage Wave Instability in a Vibrated Liquid-Fluidized Bed, AIChE Annual Meeting, San Francisco, California, United States, 12–17 November, 2006.

Lim, E. W. C. and C. H. Wang, A Computational Study of the Various Flow Regimes in Pneumatic Conveying of Granular Materials, AIChE Annual Meeting, Ohio, United States, 30 October – 04 November, 2005.

Lim, E. W. C. and C. H. Wang, Granular Attrition as a Diffusion Phenomenon, AIChE Annual Meeting, Ohio, United States, 30 October – 04 November, 2005.

Lim, E. W. C., Y. S. Wong, C. H. Wang, Voidage Instabilities in Liquid Fluidized Beds, AIChE Annual Meeting, Ohio, United States, 30 October – 04 November, 2005.

Wong, Y. S., E. W. C. Lim, C. H. Wang, Instabilities in Liquid Fluidization Systems, AIChE Annual Meeting, Ohio, United States, 30 October – 04 November, 2005.

Lim, E. W. C. and C. H. Wang, Discrete Element Modeling for Flows of Granular Material, AIChE Annual Meeting, Texas, United States, 7–12 November, 2004.